PhD Thesis

# Development of synthetic ionophores for therapeutics and molecular communication

A dissertation submitted to the
Indian Institute of Technology Guwahati
As partial fulfilment of the Degree of
Doctor of Philosophy in Chemistry


By

Soumya Srimayee




Department of Chemistry
Indian Institute of Technology Guwahati
Guwahati - 781039, Assam, India


An offering to The Mother and Sri Aurobindo

# Declaration

I hereby proclaim that the thesis entitled "Development of synthetic ionophores for therapeutics and molecular communication" is the research work performed under the guidance of Prof. Debasis Manna. This thesis has been submitted by me to the Department of Chemistry, Indian Institute of Technology Guwahati, for the award of the degree of Doctor of Philosophy. In keeping with the general practice of reporting scientific observations, due acknowledgments have been made wherever the work described is based on the findings of other investigators. I declare that I have adhered to all principles of academic honesty and integrity and have not misinterpreted or falsified any idea/data/fact/source in my submission. I further declare that this work has not been submitted anywhere else for any degree, diploma, associateship, or membership, etc., of any Institute or University to the best of my knowledge.

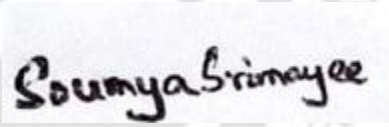

(Soumya Srimayee)

भारतीय प्राद्योगिक संसथान गुवाहाटी
Indian Institute of Technology Guwahati
Prof. Debasis Manna
Department of Chemistry
Phone: +91-0361-258-2325
Fax: +91-0361-258-2349
E-mail: dmanna@iitg.ac.in

To whom it may concern

This is to certify that the thesis entitled "Development of synthetic ionophores for therapeutics and molecular communication" being submitted by Ms. Soumya Srimayee (Roll No. 206122032) for the award of the Ph.D. degree in Chemistry to the Indian Institute of Technology Guwahati, is genuinely her own research work which was carried out by her during her PhD tenure. All the information and data she reported are entirely her original findings. She has meticulously performed all the scientific investigations and also followed the guidelines of my laboratory. Neither this thesis nor any part of it has been submitted for the award of any degree/diploma anywhere before.

**(Prof. Debasis Manna)**

Dr. Debasis Manna
Professor
Department of Chemistry
Indian Institute of Technology Guwahati
Guwahati-781 039, Assam, INDIA

# Contents

# *Acknowledgements*

*First and foremost, I thank Almighty God for His abundant grace, guidance, and blessings throughout the course of this work.*

*I would like to express my sincere gratitude to my thesis supervisor,* ***Prof. Debasis Manna, for his continuous support, guidance,*** *and constructive suggestions throughout my PhD, which have enriched my scientific knowledge. From day one of my PhD enrollment, I found a motivating and happy environment, which helped me greatly in experiencing this wonderful journey through many learning experiences. His guidance, encouragement, advice, and involvement in every aspect of research work actually flourished my scientific knowledge. I am really grateful to have a mentor like him who always tries to extend his helping hand for students' well-being. I am truly honored and blessed to be part of his research group. As a guardian, a perfect supervisor, and a mentor, I humbly bow down at his feet with gratitude. With immense respect and gratitude, I thank you, Sir, for everything.*

*I would like to extend my deepest gratitude to all my collaborators, Dr. Purushottam Mohapatra (NIPER, Guwahati), Prof. Mathias Winterhalter (Constructor University, Germany) Sir, for their support in my thesis work.*

*I would like to thank my doctoral committee members, Prof. Gopal Das, Prof. Subhas Chandra Pan, and Dr. Rajkumar P. Thummer, for their constructive suggestions and evaluation throughout my research journey.*

*I would like to express my gratitude to all the faculty and staff members of the Department of Chemistry, IIT Guwahati, for their continuous help and support. Also, I am immensely thankful to the Department of Chemistry, Central Instrument Facility (CIF, IIT Guwahati), and the Centre for the Environment for providing me with the opportunities to improve the quality of my research through the numerous sophisticated instrument facilities. I will always be thankful to IIT Guwahati for providing me the scholarship to carry out my research work.*

*I sincerely thank my past senior lab members for helping me out during the initial learning phase, which includes Dr. Nirmalya Pradhan, Dr. Nasim Akhtar, Dr. Subhasis Dey, Dr. Oindrila Biswas, Dr. Anjali Patel, and Dr. Sribash Das. I acknowledge my current lab members, Ms. Priyanka Mazumder, Mr. Biswa Mohan Prusty, Mr. Gunanka Hazarika, Ms. Niku Moni Das, Ms. Rama Karn, Mr. Mrinal Kanti Kar, Mr. Rahul Kumar, Ms. Suravi Chauhan, Mr. Joydip Pal, Mr. Pritam Kumar Mohanto, Ms. Ritama Mukherjee, Mr. Yousuf Sk, Mr. Soumajit Saha for providing me a healthy and friendly atmosphere in the lab which helped me a lot to reduce the stress of my research as well as my personal life.*

*I am deeply grateful to my dear friends, whose love, laughter, companionship, and constant encouragement have made this journey unforgettable and less painful. Thank you, Ms. Sima,*

*Ms. Smrutilipi, Ms. Ankita, Ms. Aastha, Ms. Akshara, Ms. Pritishree, Ms. Alpana, and Dr. Abhijeet, for supporting me through ups and downs.*

*I owe everything to my family, whose love is the foundation of all that I am and all that I achieve. I would like to acknowledge my parents, Ms. Swagatika Sahu and Mr. Manoj Kumar Sahoo, for their ardent support and love, which have been my pillar of strength throughout this journey. Last but not least, I thank my elder brother, Mr. Nirod Baran, and my sister-in-law, Ms. Sonali Sahoo, for their constant encouragement and support. Also, I would like to extend my gratitude to my cousins, family, and relatives who have blessed me throughout this journey. Especially, I would like to thank Biswa for being my constant companion and support, my strength on this journey, and in the future.*

*Thank you all for being a special part of my life*
***Ms. Soumya Srimayee***

# Abstract

The thesis, entitled "Development of synthetic ionophores for therapeutics and molecular communication," provides a brief description of numerous new classes of anionophores with promising therapeutic potential. Within this thesis, the recognition, transmembrane transport, and the possible therapeutic and non-therapeutic prospects/applications are reported. The thesis has been divided into four chapters based on the experimental results obtained throughout the research period.

**Chapter 1** provides a brief discussion of the importance of ion transporters in maintaining normal physiological functions, the use of ionophores as therapeutic agents, and their non-therapeutic applications. Compact literature on stimuli-responsive ion-transporting molecules and their numerous potentialities, along with methodologies for detecting and exploring ion transport, is mentioned.

**Chapter 2** presents a series of bis-thiourea moieties appended to the RGD peptide and the carbonate linker, forming a multi-stimuli-responsive ion transporter for specific targeted delivery. The detailed transport mechanism and its correlation with apoptosis have also been demonstrated using in vitro experiments.

**Chapter 3** presents a salicylaldehyde-based imine that forms self-assemblies in a lipophilic environment for selectively transporting $Zn^{2+}$ ions across the membrane. The transported $Zn^{2+}$ ions form a functional complex with tyrosine, catalyzing the conversion of non-fluorescent precursors into fluorescent reporters. This process establishes a transmembrane signal amplification mechanism functioning as a three-input AND logic gate.

**Chapter 4** describes a molecular system comprising a tripodal moiety that self-assembles in hydrophobic conditions to form an ion channel that transports $Zn^{2+}$ ions into lipid vesicles. Inside, $Zn^{2+}$ forms a complex with a photosensitizer, which, upon light irradiation, generates reactive oxygen species. These reactive oxygen species further show oxidation reaction mimicking enzyme-like activity.

# List of Abbreviation

| | |
|---|---|
| ATP | Adenosine triphosphate |
| DNA | Deoxyribonucleic acid |
| CFTR | Cystic fibrosis transmembrane conductance regulator |
| ABC | ATP-binding cassette |
| NBD | Nucleotide binding domain |
| ZnT | Zinc transporter protein |
| ZIP | Zinc and iron-regulated proteins |
| SLC 30 | Solute carrier 30 protein |
| RyR | Ryanodine receptor |
| ClC | Chloride channel protein |
| GSH | Glutathione |
| ROS | Reactive oxygen species |
| EYPC | Egg yolk phosphatidyl choline |
| CHOL | Cholesterol |
| $EC_{50}$ | Half maximal effective concentration |
| BLM | Black lipid membrane |
| ISE | Ion-selective electrode |
| DPhPC | Diphytanoyl phosphatidylcholine |
| LUV | Large unilamellar vesicle |
| HPTS | 8-Hydroxypyrene-1,3,6-trisulfonate |
| Lucigenin | *N*,*N*′-Dimethyl-9,9′-biacridinium dinitrate |
| MgG | Magnesium Green |
| HEPES | 4-(2-Hydroxyethyl)-1-piperazineethanesulfonic acid |
| CF | Carboxyfluorescein |
| RGD | Arginylglycylaspartic acid |
| PBS | Phosphate buffer saline |
| A375 | Human malignant melanoma cell line |
| HEK293T | Human Embryonic Kidney 293 cells |
| GUV | Giant unilamellar vesicles |
| TBACl | Tetrabutylammonium chloride |
| FCCP | Carbonyl cyanide-p-trifluoromethoxy phenylhydrazone |

| | |
|---|---|
| DPPC | Dipalmitoyl phosphatidylcholine |
| HBSS | Hank's Balanced Salt Solution |
| DMSO | Dimethyl sulfoxide |
| DMF | Dimethylformamide |
| DCM | Dichloromethane |
| $IC_{50}$ | The concentration of an inhibitor which causes 50% inhibition of a maximal activity |
| DMEM | Dulbecco's Modified Eagle Medium |
| FBS | Fetal bovine serum |
| MTT | 3-(4,5-dimethylthiazol-2-yl)-2,5-diphenyltetrazolium bromide |
| HPLC | High-performance liquid chromatography |
| MALDI-TOF | Matrix-Assisted Laser Desorption/Ionization-Time Of Flight |
| $\lambda_{ex}$ | Excitation wavelength |
| $\lambda_{em}$ | Emission wavelength |
| Tyr | Tyrosine |
| AHPTS | Sodium 8-acetoxypyrene-1,3,6-trisulfonate |
| CFDASE | Carboxyfluorescein diacetate succinimidyl ester |
| FESEM | Field emission scanning electron microscopy |
| EDTA | Ethylene diamine tetraacetic acid |
| CAC | Critical aggregation constant |
| pPOR | Protochlorophyllide oxidoreductase |
| PPIX | Protoporphyrin IX |
| Trp | Tryptophan |
| Nfk | N-formyl kynurenine |
| Kyn | Kynurenine |
| IDO1 | Indoleamine-2,3-dioxygenase |
| DCF | dichlorofluorescein |
| $H_2$DCFDA | 7′-dichloro dihydro fluorescein diacetate |
| TCA | Trichloroacetic acid |
| PDMAB | p-Dimethylaminobenzaldehyde |
| $Et_3N$ | Triethyl amine |
| EtOH | Ethanol |
| m/z | Mass to charge ratio |

## For symbols/units

| | |
|---|---|
| Å | Angstrom |
| atm | Atmosphere |
| β | Beta |
| C | Celsius |
| *J* | Coupling constant |
| ° | Degree |
| *δ* | Delta |
| Hz | Hertz |
| K | Kelvin |
| MHz | Megahertz |
| *m* | Meta |
| µg | Micro gram |
| µM | Micro molar |
| mL | Millilitre |
| mV | Mili Volt |
| min | Minute |
| h | Hour |
| nM | Nano mole |
| *o* | Ortho |
| *p* | Para |
| % | Percentage |
| s | Second |

## Chapter 1: Introduction to ion transport and its therapeutic and non-therapeutic applications

The movement of solute particles and molecules across cellular membranes is central to essential biological processes like energy generation, intercellular communication, metabolic regulation, and biosynthetic pathways.[1] Spontaneous solute passage is restricted by a steep thermodynamic energy barrier due to the presence of the hydrophobic interior of lipid bilayers. To overcome these cells, rely on highly specialized classes of membrane proteins that mediate selective and regulated transport of ions and other solutes by lowering the energy barrier. This intricate process of regulating the ionic gradient is essential for maintaining osmotic balance, controlling cell volume, regulating cell-cycle progression, facilitating signal transduction, and initiating apoptosis.[2]

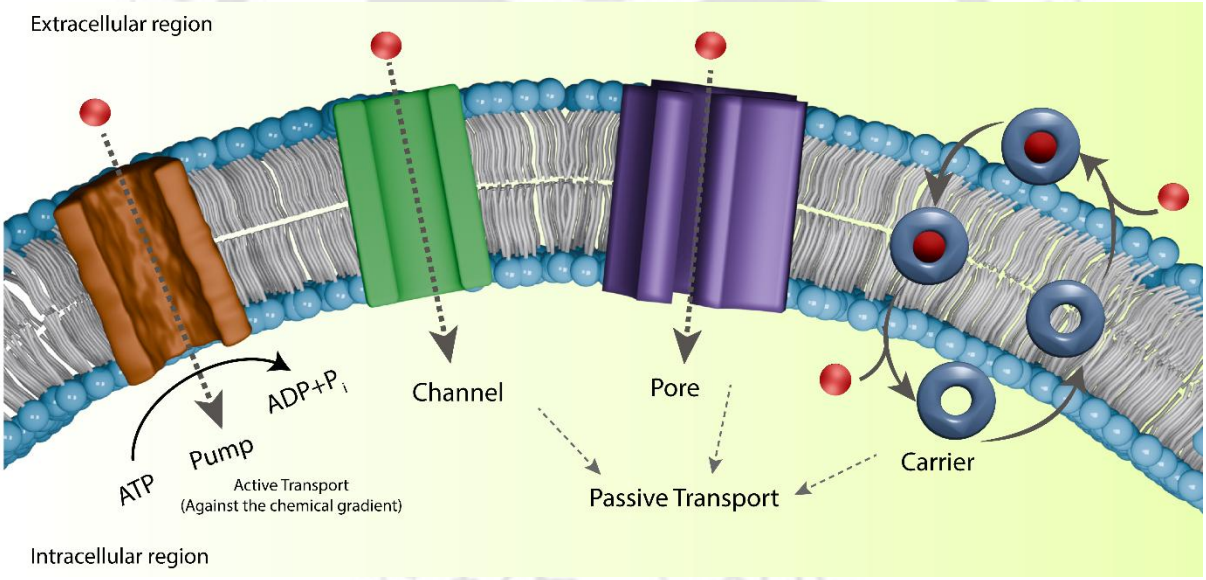


**Figure 1.** Schematic description of the ion transport process through the plasma membrane.

Physiologically relevant ions are fundamental to life, as they regulate communication, energy flow, and homeostasis in living systems. Both anions, such as chloride, phosphate, and bicarbonate, and cations, such as sodium, potassium, calcium, magnesium, zinc, and iron, play essential yet distinct roles in cellular processes.[1,2] $Na^+$ and $K^+$ gradients across membranes create electrical conduction required for neuronal signalling and muscle contraction, while calcium ions act as universal messengers that control processes from cell division to neurotransmitter release. $Mg^{2+}$ stabilizes ATP, the cell's primary energy source, whereas trace

metals like $Fe^{3+}$, $Zn^{2+}$, and $Cu^{2+}$ serve as cofactors in enzymatic catalysis and redox reactions. Anions are equally important, like $Cl^-$, which regulates osmotic balance, acid–base homeostasis, and apoptosis, while bicarbonate acts as a vital buffer to maintain physiological pH. Together, the harmonious regulation of these ions supports nearly all crucial biological processes, and disruptions in their balance cause profound physiological disorders.[3]

Synthetic ion transporters have emerged as vital tools for addressing limitations in biological transport systems. These are artificially designed molecules that can mimic or replace disrupted ion channels. These supramolecular systems are designed to facilitate selective ion passage across lipid bilayers, thereby bypassing the constraints of natural protein expression or mutation with high precision and tunability. Their biological importance is evident in their potential to restore impaired ionic gradients in a wide range of channelopathies, including synthetic chloride transporters that can be programmed to disrupt ionic homeostasis in targeted cells, offering innovative strategies for inducing apoptosis in cancer therapy. Synthetic $Zn^{2+}$ transporters have been explored to restore or modulate $Zn^{2+}$ flux, which is critical in cellular signaling, enzyme activity, and antimicrobial activity. $Cu^{2+}$ synthetic transporters control cellular redox balance, triggering cancer cell death by utilising $Cu^{2+}$ driven reactive oxygen species (ROS) generation.[4]

In addition to their medicinal uses, synthetic ionophores are increasingly popular for non-clinical applications, offering simple yet powerful ways to replicate natural signal transduction processes. These systems can be designed to replicate cellular communication pathways by enabling regulated ion flow across artificial membranes. This lays the framework for molecular communication networks. These techniques might be investigated to develop intelligent biotechnological devices that respond to environmental signals with exceptional spatial and temporal accuracy. Additionally, the incorporation of synthetic transporters into lipid vesicles and protocell models represents a pivotal advancement in the development of artificial cells, providing insight into the prerequisites for life-like functionalities and facilitating the development of programmable, bio-inspired technology.

Overall, we have devoted our work to the design and synthesis of diverse ion-transporting molecules, with a focus on their therapeutic and non-therapeutic relevance. The therapeutic potential was particularly investigated in the context of cancer treatment using in vitro cellular studies. For non-therapeutic applications, we have explored molecular communication-based cascading reactions for chemical-to-optical signal conversion and for photoregulated catalytic oxidation. The research is presented in four chapters, each dedicated to a distinct class of ionophores and their potential applications in biological and non-clinical settings.

**Chapter 1** provides a brief discussion of the importance of ion transporters in maintaining normal physiological functions, the use of ionophores as therapeutic agents, and their non-therapeutic applications. Compact literature on stimuli-responsive ion-transporting molecules and their numerous potentialities, along with methodologies for detecting and exploring ion transport, is mentioned.

**Chapter 2** presents a series of bis-thiourea moieties appended to the RGD peptide and the carbonate linker, forming a multi-stimuli-responsive ion transporter for specific targeted delivery. The detailed transport mechanism and its correlation with apoptosis have also been demonstrated using in vitro experiments.

**Chapter 3** presents a salicylaldehyde-based imine that forms self-assemblies in a lipophilic environment for selectively transporting Zn2+ ions across the membrane. The transported $Zn^{2+}$ ions form a functional complex with tyrosine, catalyzing the conversion of non-fluorescent precursors into fluorescent reporters. This process establishes a transmembrane signal amplification mechanism functioning as a three-input AND logic gate.

**Chapter 4** describes a molecular system comprising a tripodal moiety that self-assembles in hydrophobic conditions to form an ion channel that transports $Zn^{2+}$ ions into lipid vesicles. Inside, $Zn^{2+}$ forms a complex with a photosensitizer, which, upon light irradiation, generates reactive oxygen species. These reactive oxygen species further show oxidation reaction mimicking enzyme-like activity.

## Chapter 2: Development of Stimuli-responsive release of active anionophore from RGD peptide-linked proanionophore

The present study provides an integrated exploration of synthetic anion transporters, with an emphasis on the rational design and biological evaluation of stimuli-responsive systems targeting cancer cells with improved selectivity. Ion transport across lipid membranes is a fundamental biological process. Its disruption underlies a range of channelopathies, including cystic fibrosis, Dent's disease, and cancer.[5, 6] In this context, synthetic ionophores represent powerful chemical tools not only to mimic natural transport proteins but also to overcome their limitations, including genetic defects, poor stability, or resistance mechanisms.[7]

In this work, we have designed thiourea-based chloride transporters appended with an RGD peptide via a glutathione-responsive disulfide and ROS-responsive carbonate linker. This dual-responsive strategy aimed to achieve two critical goals: first, the internalization of the ionophore into cancer cells via integrin receptor-mediated endocytosis; and second, the activation of the proionophore in response to elevated intracellular glutathione (GSH), thereby releasing the active transporter specifically within malignant cells. The structural design relied on a 1,3-phenylenedimethanamine thiourea scaffold, known for its chloride recognition capabilities, further optimized by aryl substitutions to enhance activity.

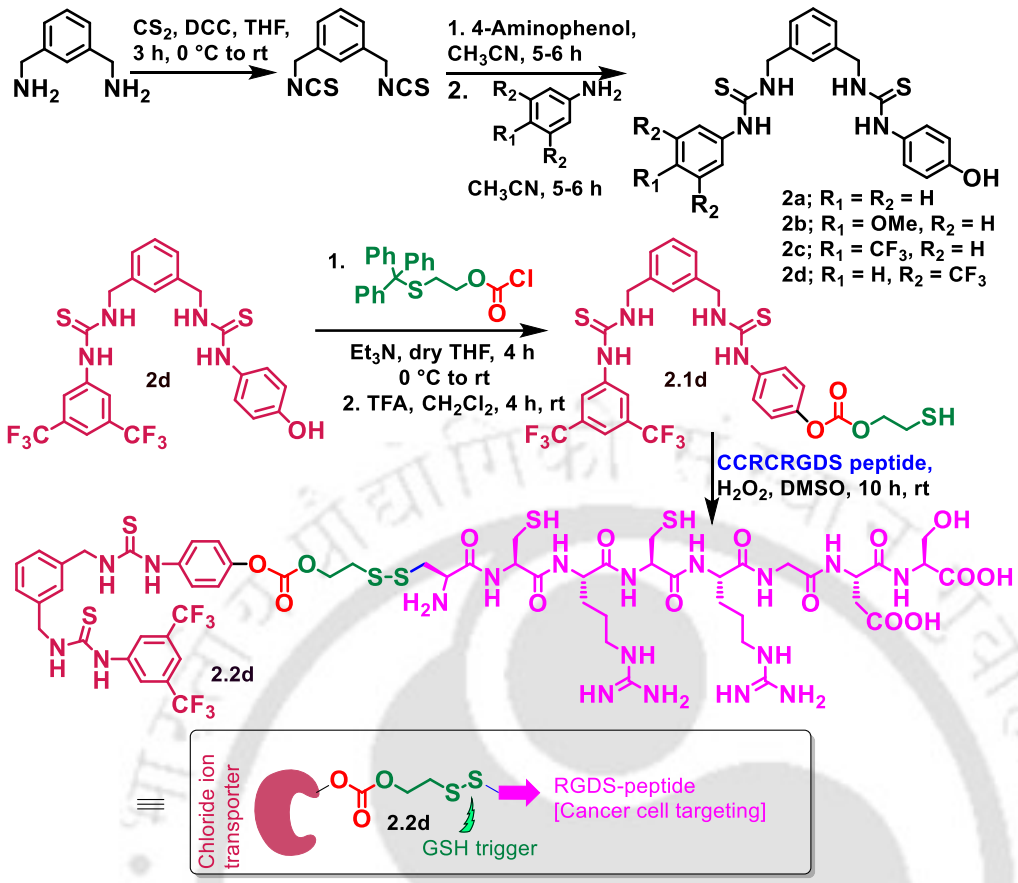


**Scheme 2.1.** Schematic representation of bis-thiourea-based ionophore and RGD peptide-linked proionophore synthesis.

Transport analysis in large unilamellar vesicles (LUVs) with EYPC/cholesterol, 8:2 ratio, demonstrated that compound **2d** exhibited the highest chloride transport activity among the other synthesized derivatives (Figure 2.1 B). Fluorescence-based kinetics assays in EYPC/CHOL-LUVs⊃lucigenin (halide sensitive dye, $\lambda_{ex}$ = 455 nm, $\lambda_{em}$ = 505 nm ) revealed an $EC_{50}$ of 4.15 ± 0.81 μM (0.01 mol% relative to lipid) with a Hill coefficient (n) of 0.78, representing 1:1 transporter to anion binding stoichiometry (Figure 2.1 C). More evidence from ion-selective chloride electrodes (ISE-Cl) confirmed comparable transport efficiency ($EC'_{50}$ = 5.24 ± 1.29 μM, n′ = 0.82) (Figure 2.1 D). The binding study by $^1$H NMR titration and UV titration of the compound **2d** and TBACl salt further established a binding constant of 14.63 $M^{-1}$ ± 5.98% and 8957.67 $M^{-1}$±9.56% respectively, indicating moderate yet effective anion recognition. Using FCCP and valinomycin, studies have determined that the transport mechanism is $H^+/Cl^-$ symport, followed by the ionophore **2d**.[8] U-tube analysis and

temperature-dependent DPPC assay confirm the carrier mechanistic pathway followed by the ionophore for $H^+/Cl^-$ transport.

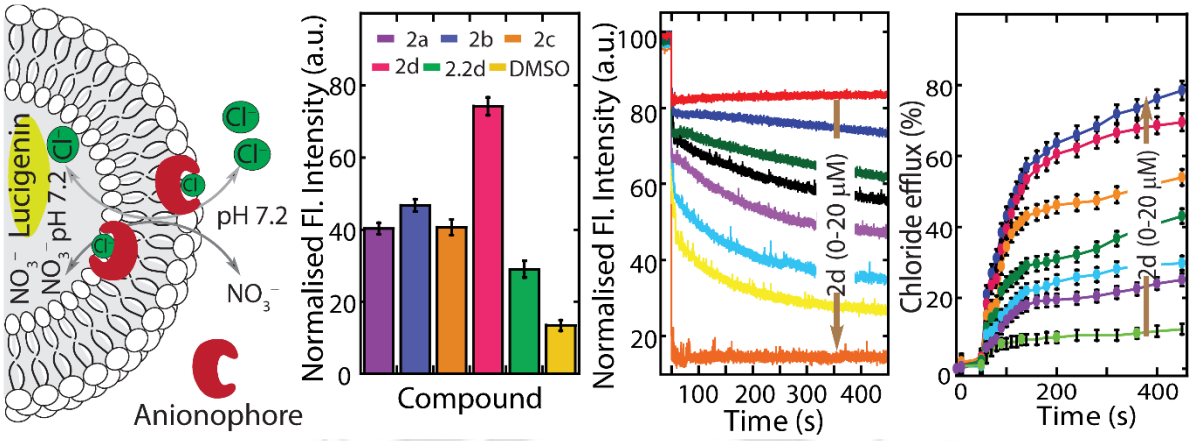


**Figure 2.1.** (A) Schematic representation of the lucigenin assay for $Cl^-$ transport. (B) Comparative $Cl^-$ transport activities of the compounds. (C) Concentration-dependent $Cl^-$ transport activities of **2d** across the lipid bilayers of EYPC/CHOL-LUVs⊃lucigenin. (D) The extent of $Cl^-$ efflux ability of **2d** across the EYPC/CHOL-LUV.

The development of RGD-linked proionophore **2.2d** for target-specific delivery is crucial. Proionophore **2.2d** effectively regenerated the active ionophore **2d** when exposed to physiological levels of GSH (10 mM), as evidenced by HPLC analysis (Figure 2.2 A) and lucigenin assays (Figure 2.2 B). This chloride transport efficacy to levels nearly identical to that of the free ionophore, confirming successful GSH-mediated cleavage of the disulfide and carbonate linkers. These results provide strong support for the proposition that the proionophore strategy is chemically robust and physiologically viable.

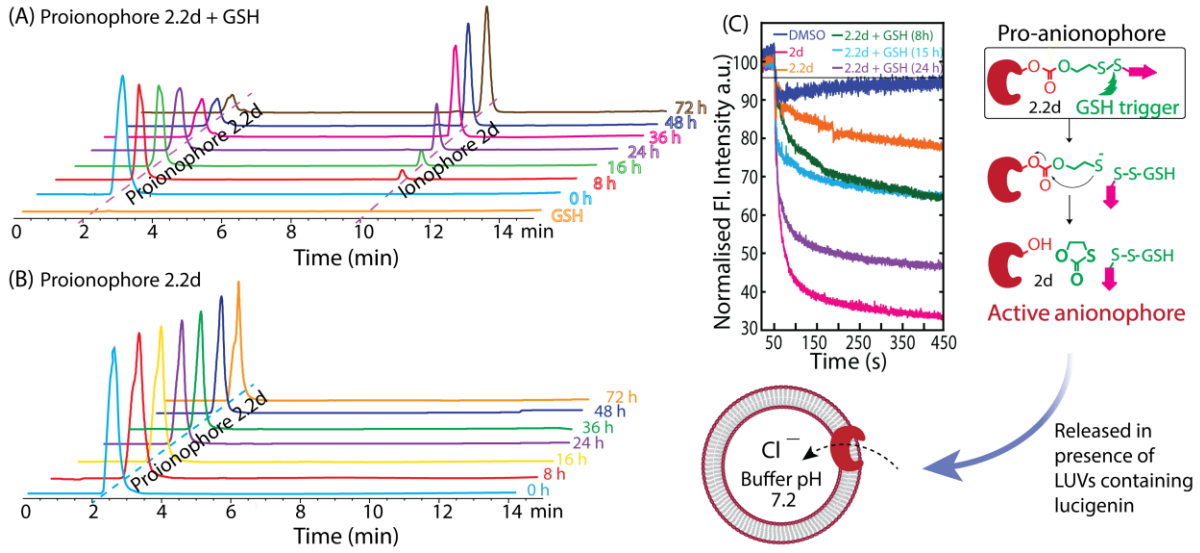


**Figure 2.2.** (A) Pro-ionophore to ionophore **2d** release study in HPLC post-GSH treatment for 72 h. (B) Stability checking of the pro-ionophore for 72 h. (C) Fluorescence-based spectral study of released ionophore **2d** in EYPC/CHOL-LUV⊃lucigenin and schematic representation of the process.

Cell-based experiments further confirmed the therapeutic potential of this method. The parent transporter **2d** exhibited dose-dependent cytotoxicity against both melanoma A375 and normal HEK293T cells, with IC50 values of 19.9 ± 4.05 µM and 21.0 ± 1.68 µM, respectively (Figure 2.3A). The lack of selectivity restricted the clinical significance of the ionophore. In contrast, proionophore **2.2d** exhibited selective cytotoxicity against cancer cells. $IC_{50}$ values were 28.21 ± 1.73 µM for A375 cells and 38.43 ± 2.57 µM for HEK293T cells under standard conditions (10% FBS) (Figure 2.3 B). Under serum starvation conditions (1% FBS), which elevate intracellular ROS levels, the $IC_{50}$ of proionophore **2.2d** against A375 cells decreased to 12.30 ± 2.33 µM, but it remained elevated in HEK293T cells at 35.80 ± 3.05 µM (Figure 2.3C).[9] The threefold difference in cytotoxicity underlines the synergistic function of intracellular redox stress in activating the proionophore and selectively eliminating cancer cells. Control trials utilising a non-targeted proionophore (compound **2.3**, lacking the RGD peptide) showed the significance of integrin-mediated transport. Compound **2.3** demonstrated superior action against HEK293T cells relative to A375 cells, thus affirming that RGD targeting was crucial to the discerned selectivity of proionophore **2.2d**. The integrin receptor $\alpha_v\beta_3$, which is overexpressed in tumour cells, provided a biologically relevant targeting route for the proionophore, thereby improving tumor-specific delivery and reducing off-target effects.

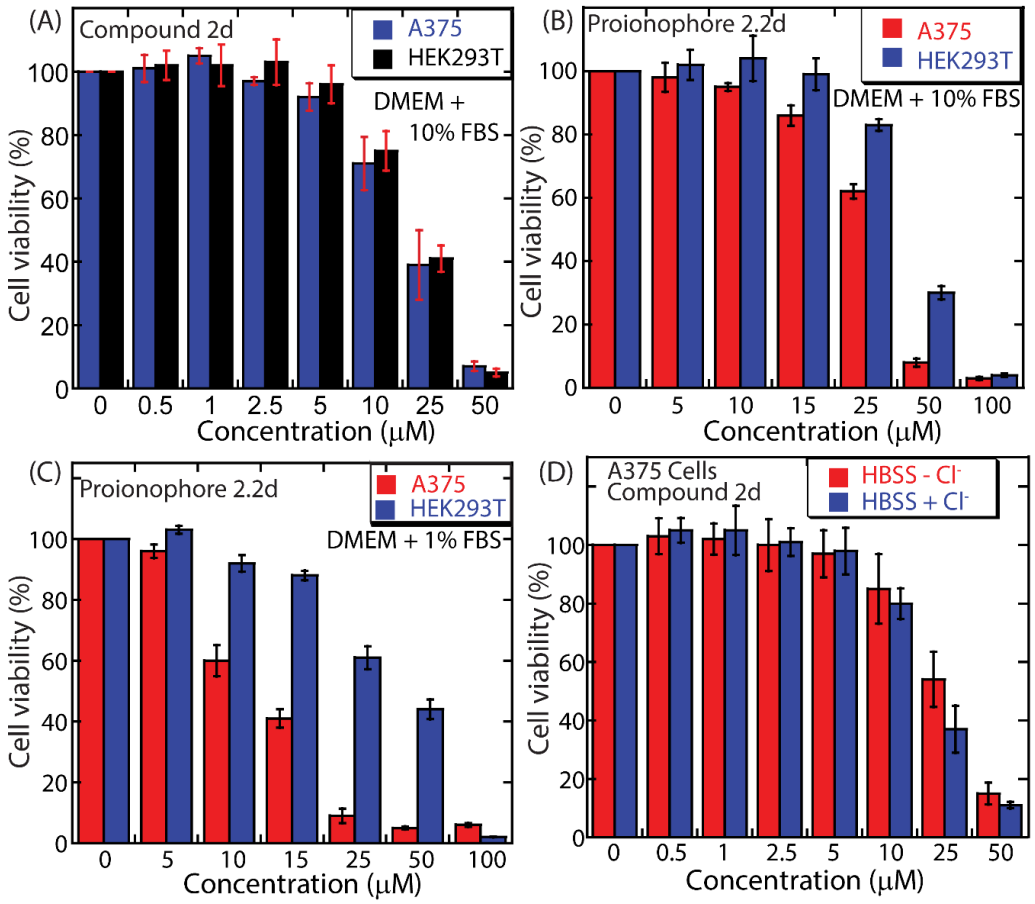


**Figure 2.3.** (A)The viability of compound **2d** in A375 and HEK293T cell lines. (B)Viability of A375 and HEK293T cells treated (24 h) with different concentrations of proionophore **2.2d** in the presence of 10% FBS. (C)Viability of A375 cells in DMEM containing 10% FBS or 1% FBS. (D) Viability of A375 cells in HBSS buffer with or without $Cl^-$ at different concentrations of compound **2d**.

**Chapter 3: Development of supramolecular ion channels to engineer $Zn^{2+}$ ion transport mediated chemical-to-optical signal transduction**

The previous chapter has shown a new stimuli-responsive bis-thiourea-based chloride ion transporter as a potential anti-cancer agent. Synthetic chloride ion transporters have been well explored for therapeutic applications, especially in tumor treatment. To explore other metal ion-based ionophores, we decided to construct supramolecular channels from a series of salicylaldehyde-based imine derivatives of 2-(6-(6-amino-1H-benzo[d]imidazol-2-yl) pyridine-2-yl)-1H-benzo[d]imidazol-5-amine (**3.2a-d**) scaffold optimized for selective $Zn^{2+}$ recognition. Structure-activity relationship studies revealed that substitution patterns on the aromatic rings and side-arm functionalities significantly impacted channel formation and ion

selectivity.[10] Among the synthesized molecules, compound **3.2a** exhibited the highest $Zn^{2+}$ transport activity, attributed to an optimal balance between lipophilicity, binding affinity within the lipid bilayer. The lack of examples in the direction of metal-ionophore-based development and its utilisation in non-therapeutic applications is a loophole we have sought to address through our work.

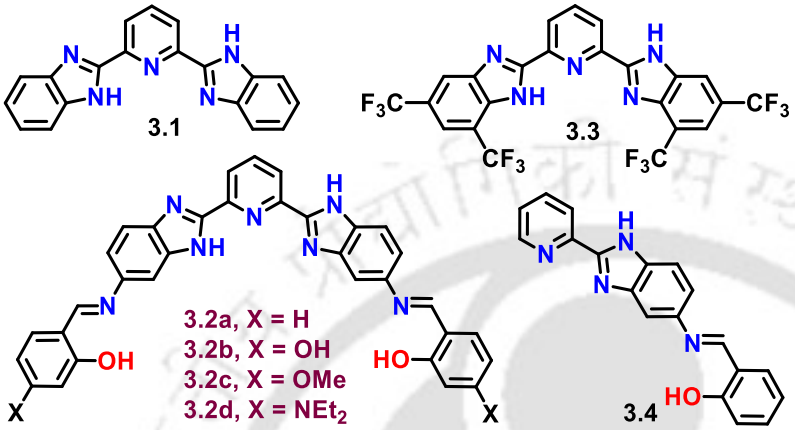


**Figure 3.1**: Structures of synthesized transporters.

Transport analysis has been performed in LUVs containing pentapotassium salt of magnesium green (MgG, $\lambda_{ex}$ = 506 nm, $\lambda_{em}$ = 531 nm) along with 10 mM HEPES buffer, 100 mM NaCl, 100 µM ethylenediaminetetraacetic acid (EDTA), pH 7.0 (Figure 3.2 A). In this liposomal condition, EDTA was used at a low concentration to avoid interference from transition-metal ions. Compound screening studies revealed that compound **3.2a** had the highest transport efficacy (78%) among its derivatives (Figure 3.2B). However, compound **3.3** (with a logP value comparable to that of **3.2a**) showed negligible transport efficacy for $ZnCl_2$. This suggests either its lack of involvement or a strong complexation ability of the core moiety, which may hinder its transport efficacy. To assess the significance of the imine bond and hydroxyl group, control compound **3.4** was synthesized, and its transport study revealed a transport efficacy of approximately 37% for $Zn^{2+}$ ions. This comparative study concluded that the imine-N and hydroxyl –OH groups of salicylaldehyde are responsible for the reversible binding of $Zn^{2+}$ ions. The concentration-dependent MgG assay of compound **3.2a** showed an $EC_{50}$ value of 167.19 ± 10.32 nM and Hill coefficient (n) 1.92 ± 0.08 (Figure 3.2 C and D). The calculated Hill coefficient of ≈2 indicates that more than one molecule of compound **3.2a** (positive cooperativity) might form supramolecular ion channels for transporting $Zn^{2+}$ ions.[11]

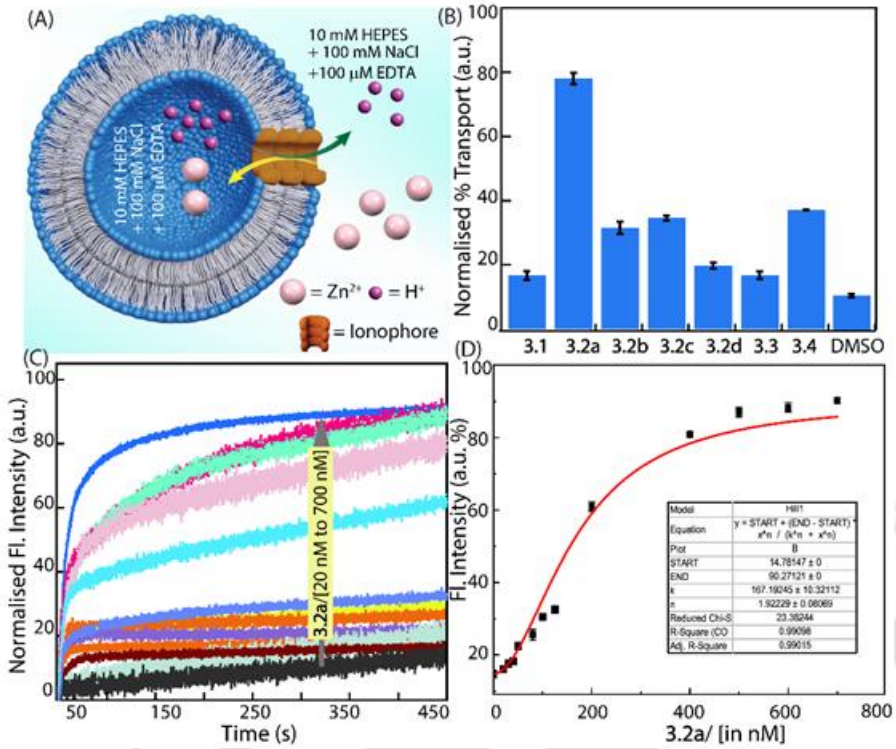


**Figure 3.2** (A) Schematic representation of ion transport studies across EYPC/CHOL-LUVs⊃MgG vesicles. (B) Assessment of the $Zn^{2+}$ ion transport activity (at t = 450 s) of the synthesized compounds (300 nM) across EYPC/CHOL-LUVs⊃MgG prepared in 10 mM HEPES buffer, 100 mM NaCl, 100 µM EDTA, 50 µM MgG, pH 7.0, and dispersed in 10 mM HEPES buffer, 100 mM NaCl, 100 µM EDTA. The LUVs were equilibrated with $ZnCl_2$, and a pulse of compound **3.2a** (300 nM) was added to initiate the transport studies. (C) Concentration-dependent transmembrane $Zn^{2+}$ ion transport activities of compound **3.2a**. (D) Concentration-dependent transmembrane $Zn^{2+}$ ions transport efficacy of compound **3.2a** across EYPC/CHOL-LUVs⊃MgG. The $EC_{50}$ value was calculated using the Hill equation.

The association constant ($K_a$) for the interaction was found to be 313.29 ± 5.4 $M^{-1}$. The selectivity study for **3.2a** revealed the compound's specific $Zn^{2+}$ selectivity and the absence of significant anion involvement in the transport process. The lucigenin assay suggested the inability of $Cl^-$ transport by compound **3.2a** under similar experimental conditions. FCCP (Figure 3.3A), valinomycin (Figure 3.3B), and a fluorescein dye-based mechanistic assay revealed involvement of $H^+$ transport in the mechanistic pathway, suggesting that the compound follows the $Zn^{2+}/H^+$ antiport process. The temperature-dependent DPPC assay and the classical U-tube assay indicated that the compound uses a channel-based mechanism to shuttle $Zn^{2+}$ across the membrane. So we proceed with real-time measurements of current across the diphytanoyl phosphatidylcholine (DPhPC) bilayer lipid membrane (BLM) to further

investigate the channel-forming ability of compound **3.2a**.[12] The lipid bilayer was prepared over the orifice in the Teflon foil connecting two electrolyte chambers containing $ZnCl_2$ (0.5 M) solution. Upon adding compound **3.2a** (4 μM), we observed rapid flickering events at various holding potentials, confirming the formation of an ion channel in the planar lipid bilayer (Figure 3.3C). In a symmetrical solution of 0.5 M $ZnCl_2$, we measured a single-channel conductance (G) of 88 ± 7 pS, corresponding to a simple pore model with a pore diameter (d) of 1.9 Å.

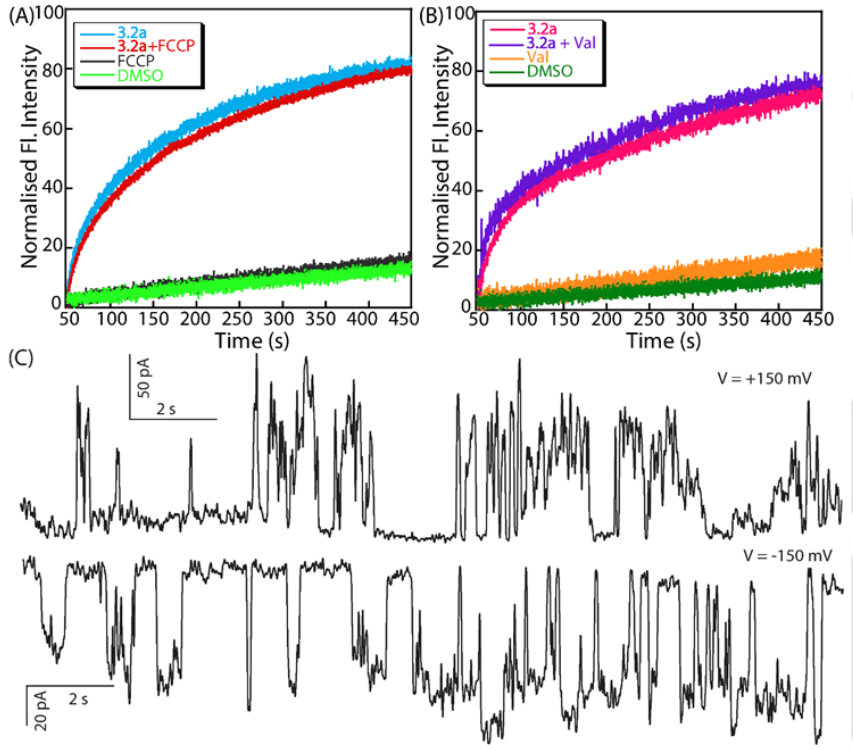


**Figure 3.3:** (A) Ion transport activity of compound **3.2a** (300 nM) in the absence and presence of FCCP (1 nM) across EYPC/CHOL-LUVs⊃MgG. (B) Ion transport activity of compound **3.2a** (300 nM) in the absence and presence of valinomycin (12 pM) across EYPC/CHOL-LUV⊃MgG prepared in 10 mM HEPES buffer containing 100 mM KCl and 100 μM EDTA, pH 7.0, and suspended in 10 mM HEPES buffer containing 100 mM NaCl and 100 μM EDTA, pH 7.0. Val = valinomycin. DMSO (10 μL) was used as a control. (C) Ion conductance measurements of compound **3.2a** (4 μM) at +150 mV and −150 mV in symmetrical $ZnCl_2$ solution (0.5 M).

We then attempted to utilise this Zn2+ ion-transport efficacy to develop a molecular communication system. We have used the natural amino acid tyrosine (Tyr) as our pre-catalyst, which showed esterase-like activity upon complexation with the $Zn^{2+}$ ion. We tried to utilise this artificial catalytic system to convert non-fluorescent AHPTS to fluorescent HPTS. The Tyr-

$Zn^{2+}$ complex serves as the catalyst for hydrolysing the ester derivatives of HPTS; however, the absence of either Tyr or Zn2+ failed to generate an optical fluorescent response (Figure 3.4 A). For rate determination, we monitored the hydrolysis of AHPTS to HPTS via fluorometric measurements. The change in reaction rate with substrate concentration was analysed using the Michaelis–Menten equation ($R^2$ = 0.99). The maximum catalytic rate ($V_{max}$) and Michaelis constant ($K_m$) values were found to be 91.57 ± 1.51 µM $min^{-1}$ and 106.06 ± 7.51 µM, respectively. We have incorporated this into the liposomal condition to test our hypothesis. Therefore, EYPC/CHOL-LUV⊃AHPTS/Tyr were prepared in 20 mM HEPES buffer containing 100 mM $NaNO_3$ at pH 7.0. Initially, no generation of HPTS was observed due to the impermeability of $Zn^{2+}$ ions without transporter **3.2a**. When transporter **3.2a** and $Zn^{2+}$ were introduced into the extravesicular solution, rapid HPTS generation was observed, confirming that ester hydrolysis occurred inside the vesicle. We performed a real-time catalytic activity assay using EYPC/CHOL-LUV⊃AHPTS/Tyr, varying the concentration of **3.2a**, and observed an increase in catalytic activity with increasing compound concentration (Figure 3.4B). Further, chemical-to-optical signal transfer in this molecular communication system was found to be a perfectly coordinated interaction among three essential components: $Zn^{2+}$, transporter **3.2a**, and Tyr, which led us to formulate a 3-input AND logic gate system.

In brief, we have optimised a molecular communication system using a synthesized Zn2+ ion transporter that forms a supramolecular ion channel in a lipid bilayer. Utilising its ion-transport ability, we have shown esterase-like activity inside the vesicle using the Tyr amino acid and the non-fluorescent esterified substrate AHPTS. The ester hydrolysis reaction releases the fluorescent HPTS as a product, indicating successful coordination of the molecular communication process to generate an optical response to the chemical signal ($Zn^{2+}$).

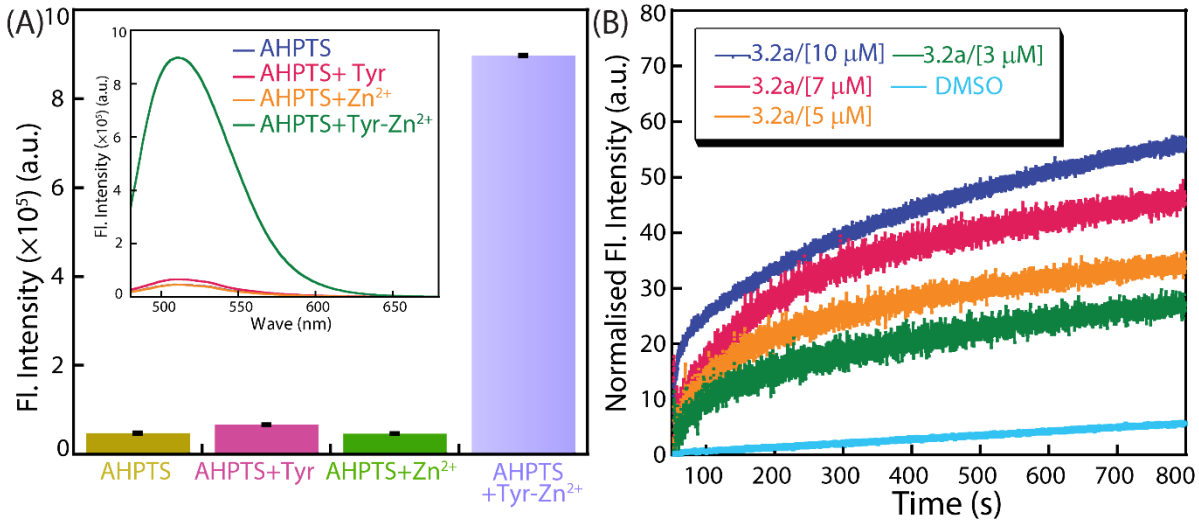


**Figure 3.4:** (A) Fluorescence intensity changes due to the hydrolysis of AHPTS to HPTS in 50 mM HEPES buffer, pH 7.0. The inset depicts the fluorescence spectral change due to the hydrolysis of AHPTS. (B) Concentration-dependent (**3.2a**; 0-10 μM) hydrolysis of AHPTS to HPTS in the presence of $ZnCl_2$ (3 mM) across EYPC/CHOL-LUV⊃AHPTS/Tyr.

**Chapter 4: Development of molecular communication system using $Zn^{2+}$ selective supramolecular nanochannel to induce photo-regulated catalysis**

In the previous work (Chapter 3), we have successfully developed a molecular communication system as an application of the signal transduction process. We further investigated the feasibility of conducting additional such applications to establish a transport-mediated molecular communication process. In this study, we reported another class of $Zn^{2+}$ transporter of 2-(pyridin-2-yl)-1H-benzo[d]imidazole moiety attached to a tripodal (1,3,5-triethyl-2,4,6-tris(isothiocyanatomethyl)benzene) core molecule.[13] The series of molecules was tested for $Zn^{2+}$ ion transport efficacy with EYPC/CHOL-LUVs⊃MgG in 10 mM HEPES buffer, 100 mM NaCl, 100 μM EDTA, pH 7.0. with compound **4.1d** (~85%) showing the highest transport ability. (Figure 4.2 B)

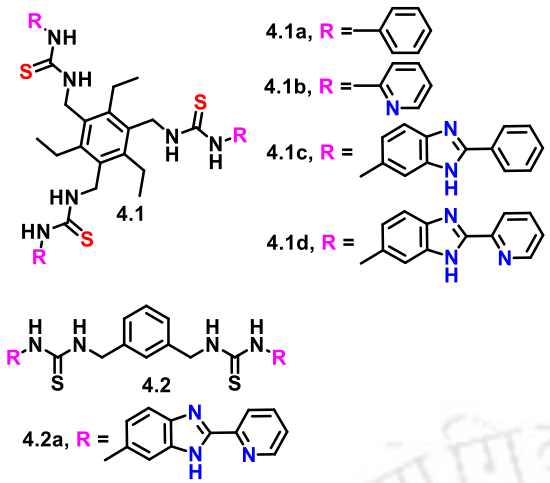


**Figure 4.1**: Structural representation of the synthesized compounds.

The concentration-dependent MgG assay of compound **4.1d** showed a half-maximal effective concentration ($EC_{50}$) of 44.83 ± 1.74 nM (compound 3d: lipid = 1: $5.58\times10^{8}$) and the Hill coefficient (n) value of 1.87 ± 0.09. (Figure 4.2 C and D) The Hill coefficient (~2) suggests that compound **4.1d** exhibits positive cooperativity in forming supramolecular channels within the hydrophobic environment of the lipid bilayers. The selectivity study revealed that compound **4.1d** shows high Zn2+ selectivity, and that the anionic counterpart is not involved in the mechanistic pathway (Figure 4.2E and F). The UV-Vis absorption spectroscopy-based titration study revealed the binding constant of compound **4.1d** (10 µM) with $Zn^{2+}$ (0-85 µM) to be around 7439 ± 3 $M^{-1}$.

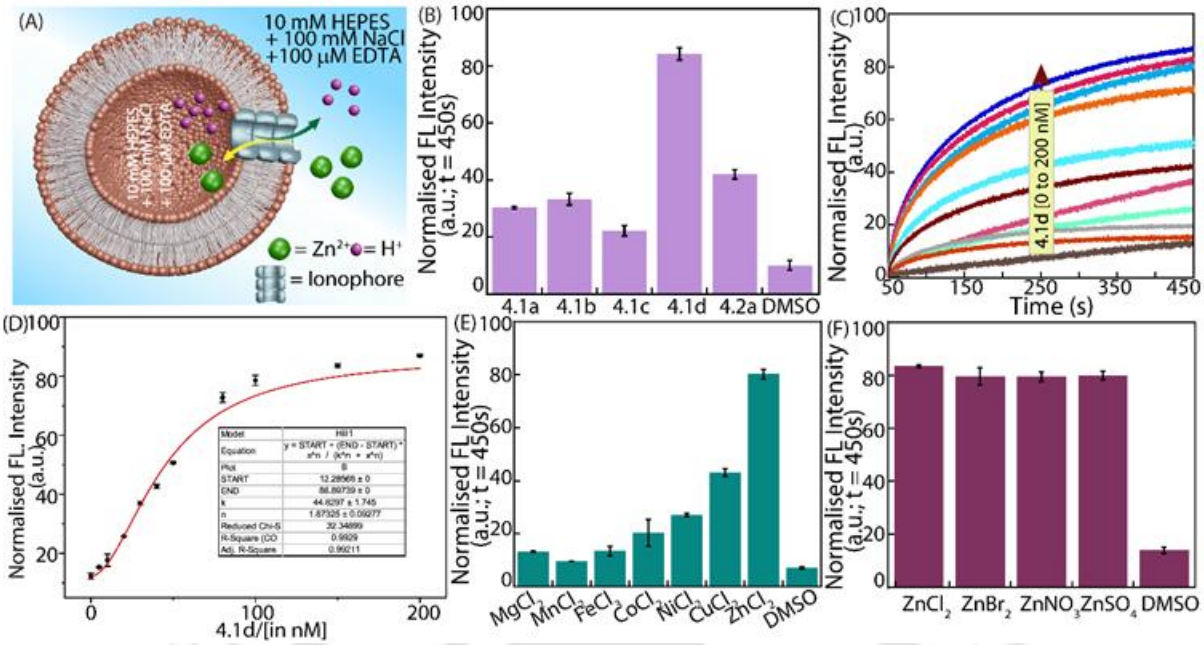


**Figure 4.2:** (A) Schematic representation of ion transport studies across EYPC/Chol-LUVs⊃MgG. (B) Evaluation of the $Zn^{2+}$ transport activity of the synthesized compounds (50 nM) across EYPC/Chol-LUVs⊃MgG prepared in 10 mM HEPES buffer, 100 mM NaCl, 100 µM EDTA, 50 µM MgG, pH 7.0, and dispersed in 10 mM HEPES buffer, 100 mM NaCl, 100 µM EDTA, pH 7.0. The LUVs were equilibrated with $ZnCl_2$, and a pulse of compound **4.1d** was added to initiate the ion transport studies. (C) Concentration-dependent $Zn^{2+}$ transport activities of compound **4.1d**. (D) Concentration-dependent transmembrane $Zn^{2+}$ transport efficacy of compound **4.1d** across EYPC/Chol-LUV⊃MgG. The $EC_{50}$ value was calculated using the Hill equation. (E) Cation and (F) anion transport selectivity of compound **4.1d** (50 nM) across EYPC/Chol-LUVs⊃MgG.

Mechanistic studies revealed that the compound has a $Zn^{2+}/H^+$ antiport pathway via FCCP and valinomycin, as demonstrated by a fluorescein-based liposomal assay. Cholesterol dependency assay and classical U-tube assay showed that compound **4.1d** follows a channel-mediated rather than a carrier-based mode of $Zn^{2+}$ transport across the model lipid bilayer membrane. To further investigate the channel-forming ability, the real-time change in current at a constant voltage in the presence of compound **4.1d** was monitored through an electrophysiological experiment. The BLM study with DPhPC lipid, 0.5 M $ZnCl_2$ solution, and 4 µM compound concentration showed instantaneous channel formation by fluctuation of current upon voltage application. The measured single-channel conductance (G) of 54 ± 11 pS indicates the formation of ion channels with a pore diameter of 1.5 Å, according to a simple pore model. Morphological analysis in hydrophobic and hydrophilic media supported the channel-

formation theory, where the compound showed agglomeration in the hydrophilic medium but nanowire-like properties in the hydrophobic medium. The 2D-NOESY measurement of compound **4.1d** (in DMSO-$d_6$) revealed a strong spatial correlation between the pyridyl aromatic proton ($\delta$ 7.51 ppm) and the thiourea N–H proton ($\delta$ 9.49 ppm). These observations suggest a probable architecture in which the pyridyl arms of two molecules engage in interlocking non-covalent interactions to form a self-assembly channel for $Zn^{2+}$.

Utilizing this concept, we have attempted to develop a photo-responsive molecular communication system by integrating a nanochannel-forming synthetic $Zn^{2+}$ transporter with a protoporphyrin IX (PPIX)-based $Zn^{2+}$-mediated catalytic module to monitor ion-transport-regulated biochemical transformation under red light.[14] (Figure 4.3 A) The complexation of transported

$Zn^{2+}$ with the PPIX resulted in the formation of a catalytic system to promote singlet oxygen ($^1O_2$) mediated oxidation of tryptophan (Trp) amino acid to N-formyl kynurenine (Nfk) exclusively in the presence of red light within the intravesicular environment. This was confirmed by HRMS analysis, which showed the formation of Nfk ($[M+H]^+$ = 237.0905). Nfk is known to undergo hydrolysis to kynurenine (Kyn) in the presence of trichloroacetic acid (TCA).[15] The resulting Kyn was subsequently quantified using UV-vis spectroscopy following derivatization with p-dimethylaminobenzaldehyde (p-DMAB). The UV-Vis spectral analysis revealed a significant enhancement of the peak at 480 nm, which corresponds to the formation of the imine complex of p-DMAB with Kyn. The time-dependent HPLC analysis confirmed increasing Kyn formation with light exposure (retention time of 2.8 min) (Figure 4.3 B), while no significant amount of Kyn was detected without light. We also conducted a similar reaction under alternating 60-minute light and dark cycles for a total duration of 5 hours. The UV-Vis spectral analysis showed that light-dependent Trp to Kyn conversion is associated with the photo-induced $^1O_2$ generation by the in-situ generated PPIX-$Zn^{2+}$ complex within the vesicles (Figure 4.3 C). The PPIX-$Zn^{2+}$ mediated selective transformation of Trp to Nfk in the presence of red-light mimics the indoleamine 2,3-dioxygenase 1 (IDO1) enzyme activity.[15]

In brief, we have developed a molecular communication system in which $Zn^{2+}$ serves as the signal and is transported within the vesicle. Inside the vesicle, we incorporated PPIX, a photosensitizer that interacts with $Zn^{2+}$. Upon photoirradiation, this PPIX-$Zn^{2+}$ complex generates singlet oxygen, which oxidizes tryptophan to N-formyl kynurenine.

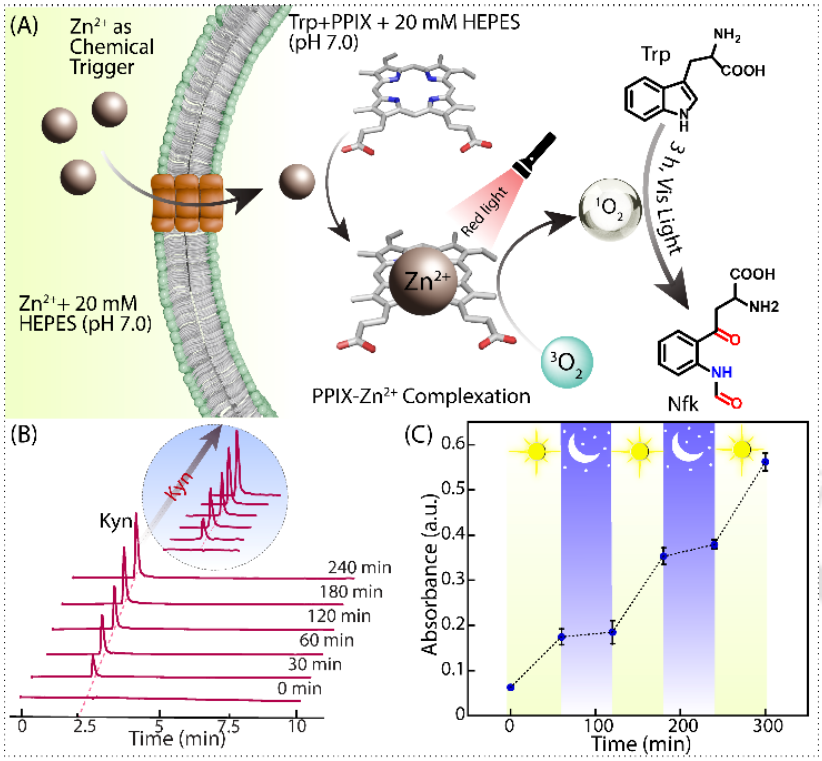


**Figure 4.3:** (A) A schematic illustration shows the in-situ complexation of $Zn^{2+}$ with PPIX, initiating light-regulated catalysis that significantly increases the generation of ROS and leads to the oxidation of Trp to Nfk. (B) HPLC analysis at different time intervals demonstrates the production of Kyn within the EYPC/Chol-LUVs⊃Trp/PPIX system after photo-irradiation in the presence of compound **4.1d** and $Zn^{2+}$. (C) Stepwise red-light irradiation ON/OFF experiment using EYPC/CHOL-LUVs⊃Trp/PPIX in 20 mM HEPES buffer, pH 7.0, with compound **4.1d** and $Zn^{2+}$ to detect Kyn generation.

**References**

1. Gokel, G. W.; Carasel, I. A., Biologically active, synthetic ion transporters. *Chem. Soc. Rev.* **2007,** *36* (2), 378-389.

2. Davis, J. T.; Gale, P. A.; Quesada, R., Advances in anion transport and supramolecular medicinal chemistry. *Chem. Soc. Rev.* **2020,** *49* (16), 6056-6086.

3. Gouaux, E.; MacKinnon, R., Principles of selective ion transport in channels and pumps. *Science* **2005,** *310* (5753), 1461-1465.

4. Bouraguba, M.; Schmitt, A. M.; Yelisetty, V. S.; Vileno, B.; Melin, F.; Glattard, E.; Orvain, C.; Lebrun, V.; Raibaut, L.; Ilbert, M., Quest for a Stable Cu-Ligand Complex with a High Catalytic Activity To Produce Reactive Oxygen Species. *Metallomics* **2024**, *16* (5), mfae020.

5. Jentsch, T. J.; Hübner, C. A.; Fuhrmann, J. C., Ion channels: function unravelled by dysfunction. *Nat. Cell Biol.* **2004,** *6* (11), 1039-1047.

6. Dworakowska, B.; Dołowy, K., Ion channels-related diseases. *Acta Biochim. Pol.* **2000,** *47* (3), 685-703.

7. Akhtar, N.; Biswas, O.; Manna, D., Biological applications of synthetic anion transporters. *Chem. Commun.* **2020,** *56* (91), 14137-14153.

8. Saha, A.; Akhtar, N.; Kumar, V.; Kumar, S.; Srivastava, H. K.; Kumar, S.; Manna, D., pH-Regulated anion transport activities of bis (iminourea) derivatives across the cell and vesicle membrane. *Org. Biomol. Chem.* **2019,** *17* (23), 5779-5788.

9. Okon, I. S.; Zou, M.-H., Mitochondrial ROS and cancer drug resistance: Implications for therapy. *Pharmacol. Res.* **2015,** *100*, 170-174.

10. Fares, M.; Wu, X.; Ramesh, D.; Lewis, W.; Keller, P. A.; Howe, E. N.; Pérez-Tomás, R.; Gale, P. A., Stimuli-Responsive Cycloaurated "OFF-ON" Switchable Anion Transporters. *Angew. Chem. Int. Ed.* **2020,** *59* (40), 17614-17621.

11. Paul, R.; Dutta, D.; Mukhopadhyay, T. K.; Müller, D.; Lala, B.; Datta, A.; Schwalbe, H.; Dash, J., A non-B DNA binding peptidomimetic channel alters cellular functions. *Nat. Commun.* **2024,** *15* (1), 5275.

12. Gutsmann, T.; Heimburg, T.; Keyser, U.; Mahendran, K. R.; Winterhalter, M., Protein reconstitution into freestanding planar lipid membranes for electrophysiological characterization. *Nat. Protoc.* **2015,** *10* (1), 188-198.

13. Schiffmann, R.; Neugebauer, A.; Klein, C. D., Metal-Mediated Inhibition of *Escherichia coli* Methionine Aminopeptidase: Structure−Activity Relationships and Development of a Novel Scoring Function for Metal−Ligand Interactions. *J. Med. Chem.* **2006**, *49* (2), 511−522.

14. Rajasree, S. S.; Li, X.; Deria, P., Physical properties of porphyrin-based crystalline metal–organic frameworks. *Commun. Chem.* **2021,** *4* (1), 47.

15. Pradhan, N.; Akhtar, N.; Nath, B.; Peña-García, J.; Gupta, A.; Pérez-Sánchez, H.; Kumar, S.; Manna, D., Inhibition of immunosuppressive indoleamine 2, 3-dioxygenase by targeting the heme and apo-form. *Chem. Commun.* **2021,** *57* (3), 395-398.

# *Chapter 1*

## Introduction to ion transport and it's therapeutics and non-therapeutics applications

## 1.1 Introduction to Ion Transport

Synthetic ion transporters that reversibly bind hydrophilic ions have emerged over the past two decades as promising tools for modulating ion concentrations across cellular membranes. By disrupting cellular ion homeostasis, these systems can disrupt critical electrochemical gradients and signalling processes, ultimately triggering programmed cell death.[1,2] Recent developments, including the design of proionophores for better solubility, aim to enhance targeted delivery, improve membrane permeability, and minimize unintended cytotoxicity toward healthy cells.[3] Beyond applications linked to uncontrolled cell proliferation, synthetic ion transporters hold promise for correcting ion imbalance disorders such as channelopathies, and for designing molecular devices that replicate or mimic the function of natural ion channels.[4] Advances in supramolecular chemistry have led to transporters capable of self-assembly within lipid bilayers, improving both stability and efficiency. Furthermore, incorporating stimuli-responsive features that respond to pH changes, redox potential, or light enables precise spatial and temporal control over ion transport activity. Current research also explores the dynamic interactions between synthetic transporters and complex cellular environments, including effects on membrane potential and downstream signalling pathways. Collectively, these interdisciplinary efforts underscore the potential of synthetic ion transporters not only as therapeutic agents but also as fundamental tools for probing membrane biology and developing next-generation biomimetic materials and molecular devices.

## 1.2 Cell and cellular membrane:

A cell is the basic unit of life, capable of executing vital functions such as metabolism, signal transduction, and reproduction. Despite varying morphology and roles, all cells possess core components, including a plasma membrane, cytoplasm, and genetic materials (DNA). The plasma membrane serves as a selectively permeable barrier not only by defining the boundaries of the cell and its organelles, but also by preserving internal homeostasis by precisely regulating the transport of nutrients, ions, and waste products. The cytoplasm, composed of organelles and cytosol, provides a dynamic milieu in which a multitude of biochemical reactions and metabolic pathways occur, facilitating biosynthesis and energy production. Genetic material transmits and

stores the instructions vital for cell function, growth, and inheritance. These features collectively enable cells to sustain and regulate life processes.[5]

The cellular membrane, primarily made up of a phospholipid bilayer with embedded proteins, serves as a dynamic barrier that maintains cellular integrity and regulates the exchange of substances between the cell and its environment (Figure 1.1). These phospholipid bilayers are composed of amphiphilic molecules with a hydrophobic tail and a hydrophilic head, including key components such as lipids, proteins, and carbohydrates, which contribute to membrane fluidity, facilitate signal transmission, and ensure selective transport necessary for cellular function.[6] The plasma membrane, with a hydrophobic nature, serves as a selective barrier separating the cell's interior from its external surroundings, allowing the passage of specific solutes while limiting others. Its bilayer architecture supports the regulated transport of various substances, including inorganic ions, small polar molecules, nonpolar solutes, and large polar compounds. This selective exchange is crucial for maintaining vital cellular processes, including pH regulation, osmotic balance, cell volume control, and signal transduction. Nonpolar molecules diffuse readily across the membrane; small polar molecules traverse more slowly; and large polar molecules and ions face significant resistance due to the hydrophobic core. To enable the transport of these critical solutes, specialized transmembrane proteins form channels or pores, providing hydrophilic pathways to facilitate their movement across the bilayer[7].

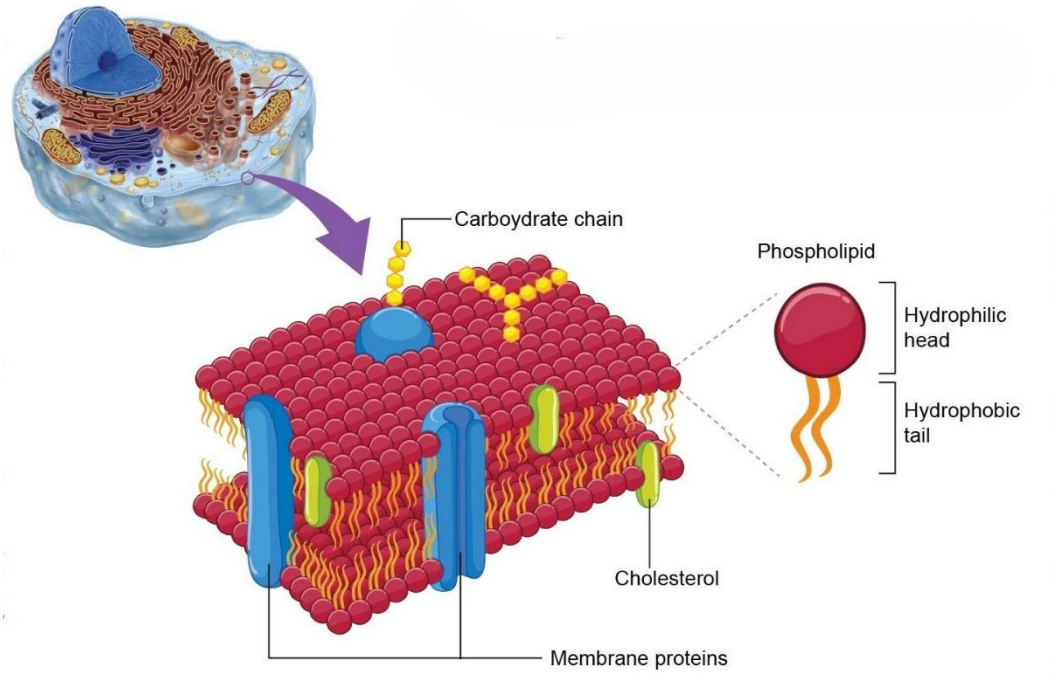


**Figure 1.1.** Representative image of the plasma membrane of a eukaryotic cell. The image of a cell is obtained from the link https://rsscience.com/cell-membrane.

### 1.3 Ion transport pathway and mechanism across a cell membrane:

The transport of ions, molecules, and other polar and nonpolar molecules can happen by active or passive transport pathways (Figure 1.2). ATP hydrolysis-driven energy is utilised in primary active transport to move ions against their electrochemical gradients[8]. Major examples include the $Na^+$-$K^+$ pump, which actively transports three $Na^+$ ions out of the cell and two $K^+$ ions into the cell, and the calcium pump, which removes $Ca^{2+}$ ions from the cytosol or accumulates them in the endoplasmic reticulum. The movement of one ion down its electrochemical gradient can provide energy to drive the movement of other ions against their gradients in secondary active transport. Specific examples include the sodium-glucose symporter, which transports glucose into cells using the sodium gradient, and the sodium-calcium exchanger, which expels calcium ions from the cell by utilizing the inward sodium gradient.

Diffusion is a passive process in which molecules or ions move from areas of high concentration to areas of low concentration, either directly through ion channels or via the lipid bilayer. For example, $O_2$ and $CO_2$ move across the membrane by simple diffusion, while $K^+$ ions cross through potassium channels. Facilitated diffusion can operate without energy input, but it requires specific proteins, such as ion channels or exchangers, to assist the transport of

substances across the membrane. Such examples include glucose entering cells via glucose transporters and chloride ions moving through chloride channels.

Transport of ions across bilayer membranes primarily takes place through ion channels or carrier pathways.[10] Ion channels are typically membrane-embedded proteins that form fixed, aqueous pores, allowing specific ion movement across the membrane. On the other hand, carriers are small amphiphilic molecules that bind specific ions and transport them across the hydrophobic core of the lipid bilayer. Channels offer a continuous passage, but carriers operate through partial conformational changes, temporarily encapsulating ions during transit.[11]

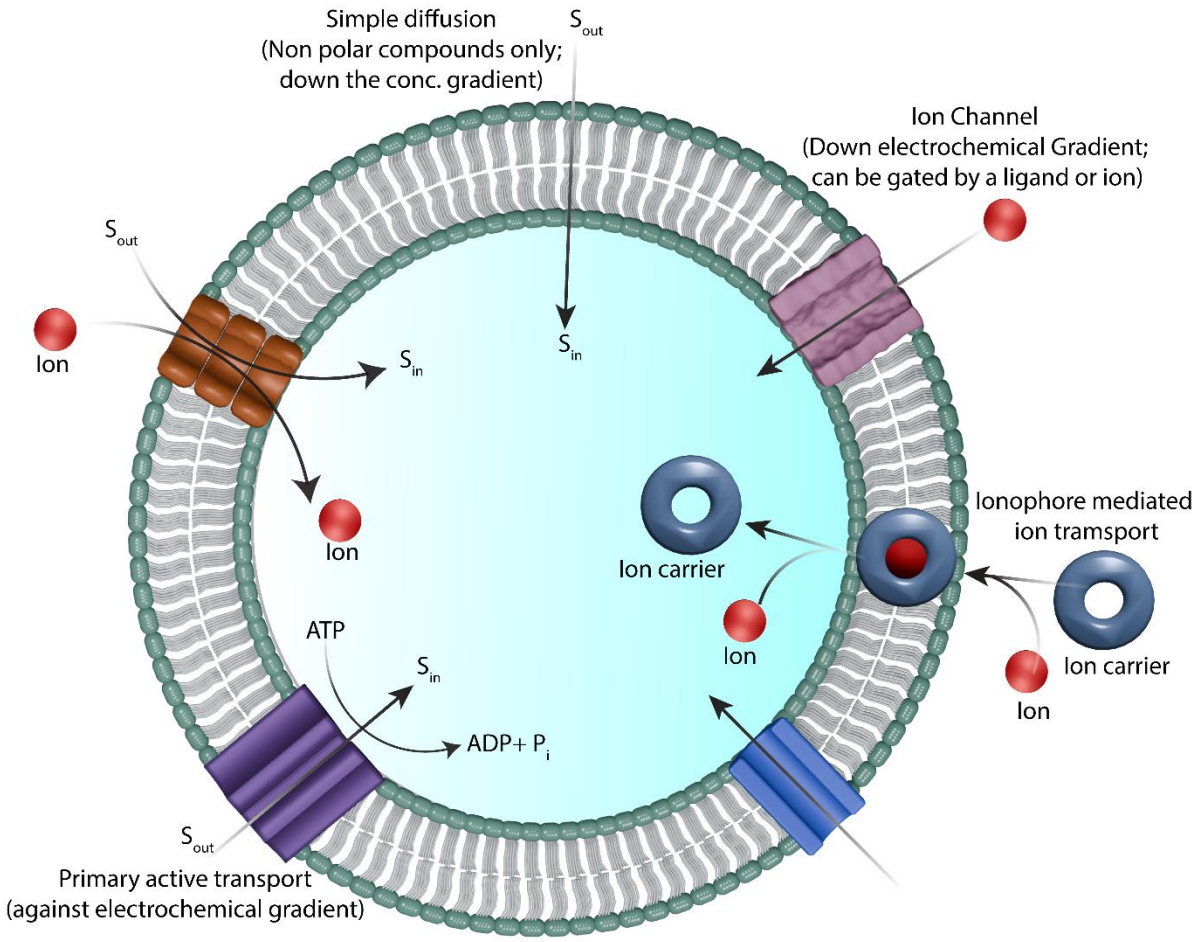


**Figure 1.2.** Different modes of transportation of ions and solutes across the bilayer membrane.

Differentiating transporters on the basis of the number of substances and the specific direction of movement, they are further divided into three categories: uniport, antiport, and symport (Figure 1.3). Uniport is a passive transport process in which a single ion or molecule moves across the membrane in a single direction, without utilizing cellular energy. Mostly, membrane-embedded uniporter proteins enable the diffusion of transported species down their concentration or potential gradients. Antiport involves the simultaneous movement of two

different ions (two positively charged cations or negatively charged anions) or molecules in opposite directions across the membrane. Antiporters are transmembrane proteins that often employ stored electrochemical energy rather than direct ATP hydrolysis to drive this exchange against one or both concentration gradients. Examples include the chloride-bicarbonate exchanger, which swaps chloride and bicarbonate ions across the membrane.[12]

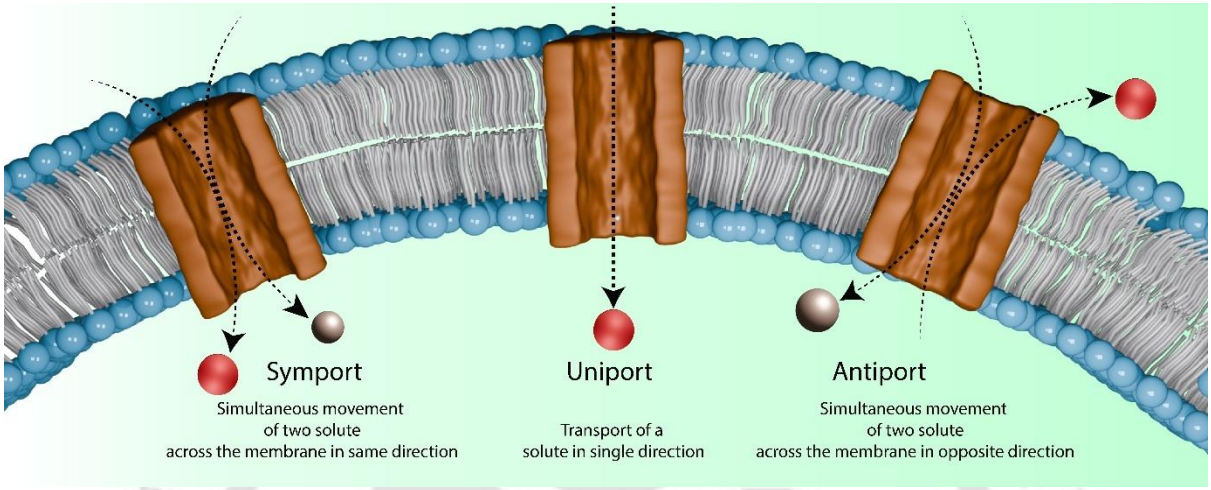


**Figure 1.3.** Different modes of transportation of ions according to direction.

### 1.4 Importance of developing robust ion-transport systems:

The ion transport systems are crucial to regulate the movement of charged particles such as $Na^+$, $K^+$, $Mg^{2+}$, $Ca^{2+}$, $Zn^{2+}$, and $Cl^-$, across biological membranes. In living organisms, these processes are tightly controlled, enabling muscle contraction, nerve conduction, intracellular signaling, and hormone release. Thus, exploring more effective synthetic ion transport systems is crucial for translating these biological principles into therapeutic applications and for creating artificial cellular platforms. Channelopathies arise from faulty ion channels or disrupted ion gradients across the cellular membrane. Artificial ion transporters offer a suitable alternative for restoring natural faulty proteins or disrupted ionic gradients. While controlled modulation of ion gradients can trigger cell death in diseased cells, such as cancer, while sparing healthy cells, it has the potential to act as a therapeutic.

Ion gradients influence processes like endosomal escape and vesicle fusion. To create stimuli-responsive release mechanisms, synthetic ion transporters can be integrated into drug carriers, enabling therapeutic activation only at the target site and improving efficiency. Ion flux is a key trigger for signal transduction pathways; for example, $Ca^{2+}$ regulates neurotransmission, $Zn^{2+}$ plays a role in immune signaling, and $H^+$ gradients drive ATP production. So synthetic transporters can mimic these ionic signals, enabling artificial systems to interface with natural

cellular communication networks. It makes it easier to send and receive information between synthetic cells, or between artificial and natural cells.

The futuristic and prophetic revolution this research field can bring is beyond imagination. Many truths and facts about the application of synthetic ion transport systems still need to be explored.

**1.5 Naturally occurring ion transporters and channels:**

Ion channels are molecular assemblies that are intricately regulated and enable rapid cellular responses to external and internal stimuli while maintaining cellular homeostasis. Structurally, these transmembrane protein macromolecules span the lipid bilayer, creating highly selective pathways for ions such as $Cl^-$, $Na^+$, $K^+$, and $Ca^{2+}$ to be transported across impermeable membranes. This selective permeability is critical for generating and maintaining electrochemical gradients, which underpin vital physiological processes, including hormone and neurotransmitter secretion, nerve impulse propagation, and muscle contraction. Ion channels achieve their specificity through finely tuned gating mechanisms responding dynamically to voltage changes, ligand binding, light, or even mechanical stress. Such gating induces conformational shifts that open or close the ion-conducting pore, tightly controlling ion flow in alignment with cellular needs. Moreover, their ability to rapidly switch between open and closed states enables cells to respond almost instantaneously to changing conditions. Through this precise regulation and remarkable selectivity, ion channels play an indispensable role in coordinating complex biological processes and sustaining life at the cellular level.

Various natural products having one or more protein subunits have been shown to facilitate the selective transport of cations and anions across bilayer membranes, regulating ionic balance and membrane potential. Voltage-gated ClC-1 chloride channel has a homodimer protein, predominantly expressed in skeletal muscle fibres, with each subunit forming an independent ion-conducting pore (Figure 1.4 A). It maintains chloride homeostasis in skeletal muscle by regulating ion flow during the restoration of the resting membrane potential by rapidly repolarizing the sarcolemma after muscle excitation by allowing passive flow of $Cl^-$ ions. Approximately 70% of the resting membrane conductance in skeletal muscle is attributed to ClC-1, which effectively suppresses electrical excitability and prevents involuntary muscle contractions. Mutations in the CLC-1 gene cause myotonia congenita, a disorder characterized by delayed muscle relaxation after voluntary contraction, highlighting its physiological significance. [13] The Cystic Fibrosis Transmembrane Conductance Regulator (CFTR) is an ATP-gated $Cl^-$ ion channel that facilitates chloride ion transport across epithelial membranes

(Figure 1.4 B). Its channel activity is essential for osmotic balance and mucus viscosity in exocrine tissues, and it also regulates transepithelial ion flux and fluid secretion. Structurally, CFTR belongs to the ATP-binding cassette (ABC) transporter family, but it actually functions as an ion channel. It comprises a regulatory (R) domain, two transmembrane domains, and two nucleotide-binding domains (NBDs), whose phosphorylation controls channel gating. Mutations in the CFTR gene disrupt $Cl^-$ conductance, leading to dehydrated mucus and clinical manifestations of cystic fibrosis, including chronic respiratory infections and pancreatic insufficiency. [14] The $Na^+/K^+$ is a P-type ATPase consisting of α and β subunits (Figure 1.4 C). It uses ATP hydrolysis to drive conformational rearrangement, pumping out three $Na^+$ ions and pumping in two $K^+$ ions per cycle, maintaining steep transmembrane $Na^+$ and $K^+$ gradients that are fundamental to cell physiology. The $Na^+/K^+$-ATPase also indirectly fuels secondary active transporters, such as $Na^+$-coupled glucose and amino acid symporters, enabling efficient nutrient uptake. Beyond ion transport, it interacts with signaling complexes, influencing cell adhesion, proliferation, and apoptosis. Dysregulation or mutations affecting its function are linked to neurological disorders, hypertension, and cardiomyopathies. This process is important for maintaining intracellular ion gradients, supporting nutrient transport, and enabling secondary active transport across the bilayer membrane.[15]

Zinc transporters are important integral membrane proteins that precisely regulate intracellular $Zn^{2+}$ distribution and provide optimal zinc availability for protein structural integrity, metalloenzyme function, and modulation of signal transduction pathways critical for cellular activity. $Zn^{2+}$ transporters of the ZnT (SLC30) and ZIP (SLC39) families maintain cellular $Zn^{2+}$ homeostasis through bidirectional regulation, like ZnT mediating $Zn^{2+}$ efflux or intracellular compartmentalization, while ZIPs promote cytosolic $Zn^{2+}$ influx (Figure 1.4 D and 1.4 E).[16] The ryanodine receptor (RyR), a $Ca^{2+}$ release channel located on the endoplasmic reticulum and sarcoplasmic membranes, is initiated by $Zn^{2+}$, which enhances its sensitivity and promotes $Ca^{2+}$ release into the cytosol (Figure 1.4 F). This $Zn^{2+}$-dependent activation of RyR is pivotal for regulating intracellular calcium signalling involved in neuronal responsiveness, muscle contraction, and other essential cellular processes.[17]

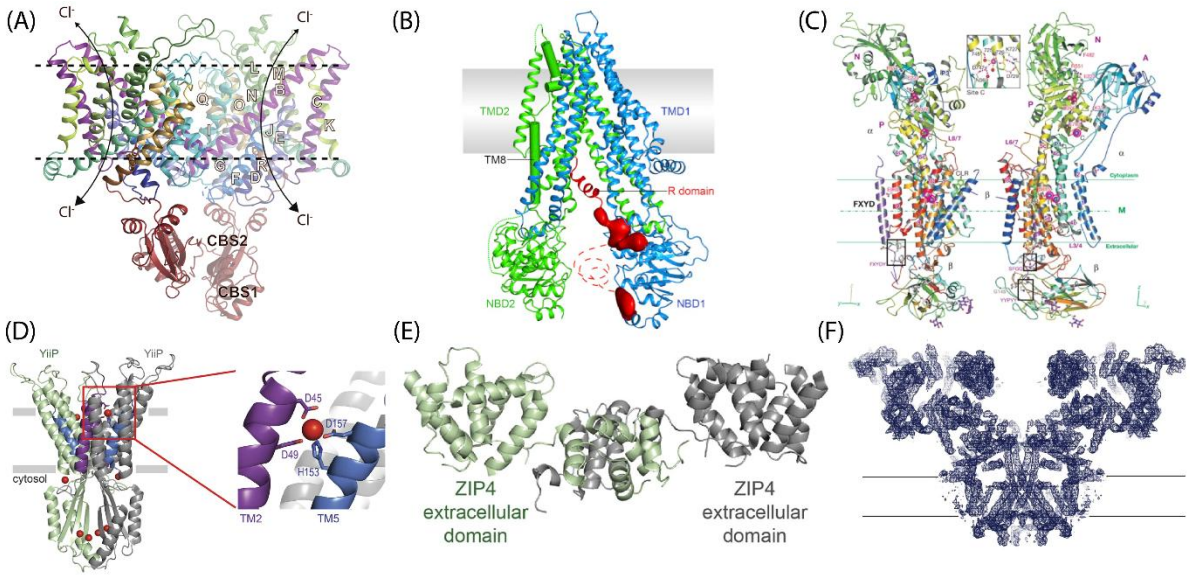


**Figure 1.4.** Representative image of naturally occurring protein channels (A) CLC-1 chloride channel protein, (B) CFTR chloride channel protein, (C) $Na^+/K^+$ ATPase pump, (D) ZnT protein for Zn2+, (E) ZIP protein for $Zn^{2+}$, (F) Ryanodine receptor channel (RyR) for $Ca^{2+}$.

Prodigiosin is a natural product notable for its vibrant red colour and unique ion-transporter properties (Figure 1.5 A). It facilitates $H^+/Cl^-$ symport across lipid bilayers, effectively dissipating membrane potential and transmembrane pH gradients. This transport relies on protonation at acidic sites and stabilisation of chloride ions through hydrogen bonding and electrostatic interactions. Structurally, prodigiosin consists of a lipophilic tripyrrole scaffold bearing alkyl substituents, thereby promoting efficient membrane partitioning. Its ion transport activity underlies its broad biological effects, including pro-apoptotic and anticancer actions, by disrupting ionic balance and triggering mitochondrial dysfunction. Prodigiosin also exhibits antibacterial and immunosuppressive properties, highlighting its multifunctional bioactivity.[18] Ceramides are bioactive sphingolipids that not only contribute to membrane architecture but also modulate chloride ion transport across cellular membranes (Figure 1.5 B). At lower concentrations, these molecules function via a mobile carrier mechanism, transiently binding and shuttling $Cl^-$ ions across the lipid bilayer. At higher concentrations, ceramides can self-assemble into stable, channel-like aggregates, facilitating sustained chloride flux. This dynamic ion transport capability is minutely linked to their role in regulating apoptosis, cell differentiation, and inflammation. Structurally, the amphiphilic nature of ceramides, comprising a sphingosine backbone and a fatty acid chain, promotes their integration into membranes, where they reorganise lipid domains and influence bilayer permeability. Additionally, ceramide-mediated ion transport affects mitochondrial membrane potential and

calcium signalling, further amplifying their role in cellular stress responses and programmed cell death.[19] Valinomycin is a naturally occurring uniporter ionophore produced by *Streptomyces* species, renowned for its exceptional selectivity for $K^+$ ions over $Na^+$ (Figure 1.5 C). Its cyclic structure features alternating ester linkages, creating a flexible yet highly specific cavity in which carbonyl oxygens coordinate $K^+$ ions with perfect geometry. Functionally, valinomycin facilitates rapid $K^+$ translocation across lipid bilayers via a carrier mechanism, thereby maintaining the membrane potential critical for processes such as oxidative phosphorylation and nerve impulse propagation. In biological systems, it uncouples oxidative phosphorylation by collapsing $K^+$ gradients across mitochondrial membranes, which can lead to ATP depletion and apoptosis. This ability to disrupt ionic gradients makes valinomycin a potent antibiotic and an experimental tool for studying ion transport, membrane potential regulation, and mitochondrial function.[20] Hinokitiol, a natural tropolone derivative, functions as a broad-spectrum metal ionophore capable of transporting $Fe^{3+}$, $Zn^{2+}$, $Cu^{2+}$, and $Mn^{2+}$ across lipid bilayers by forming neutral, lipid-soluble complexes (Figure 1.5 D). Beyond its established antimicrobial and anticancer activities, hinokitiol uniquely restores iron transport in cells lacking endogenous transporters, such as DMT1 or ferroportin, offering therapeutic potential in iron-deficiency conditions. Its capacity to modulate intracellular metal availability influences redox balance and enzyme activity, impacting key cellular processes. Moreover, hinokitiol's structural simplicity and efficient metal shuttling have inspired the development of synthetic tropolone-type ionophores designed for targeted and controlled metal delivery in biological systems.[21, 22]

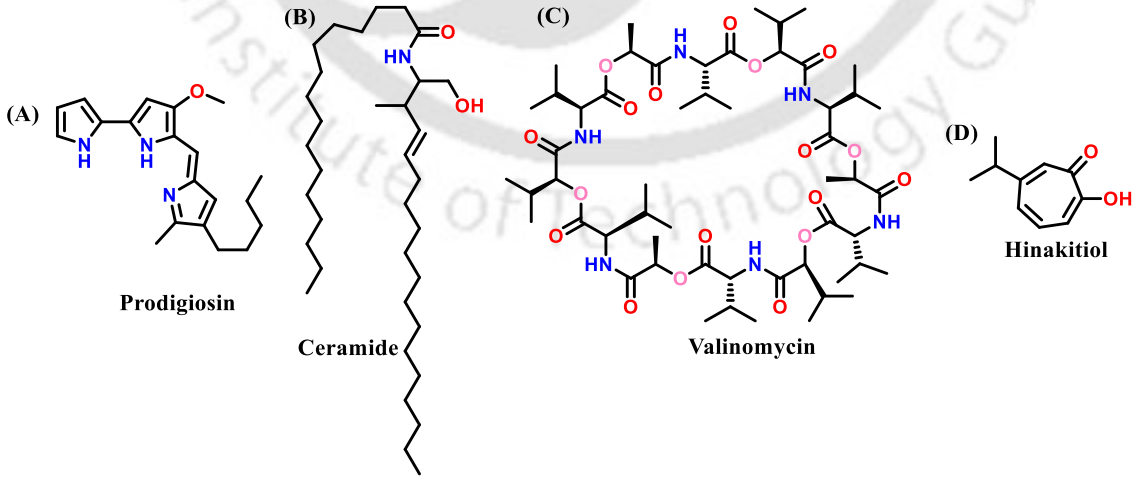


**Figure 1.5.** Representative structure of some naturally occurring ion carrier molecules.

### 1.6 Reported synthetic ion transporters

Designing synthetic ion transporters that overcome the energetic barrier between hydrophilic ions and the hydrophobic membrane is crucial for replicating the selective, directional ion movement observed in natural systems. Ions play indispensable roles in sustaining biological functions, with each ion contributing uniquely to cellular and physiological processes. These transporters facilitate the controlled flow of ions across lipid bilayers, enabling the reconstruction and regulation of essential ionic gradients. Mimicking these ion transport processes is vital for reconstituting cellular phenomena such as signal transduction, volume regulation, and apoptosis. Some recent work by Talukder et al. has shown the therapeutic potential of a synthetic chloride ion channel, in which a 2-hydroxyphenyl benzamide-based molecule forms a Barrel-Rosette-type ion channel that selectively targets apoptosis in cancer cells over normal cells.[23] (Figure1.6 [1]) Urea and thiourea-based moieties are quite well known for recognising anions and transporting across the bilayer membrane and showing apoptotic or autophagy activities. Gale and co-workers have shown that simple indole-based thio-urea moieties can transport $Cl^-/H^+$ and thus exhibit apoptotic activity due to their pH-dissipation ability.[24] (Figure1.6 [3]) Manna and co-workers have extensively explored the thiourea-based compounds' properties, where they have synthesized diphenylene ethylene diamine-based bis-urea moieties,[25] PITENINs[26] and quinine-based thio-urea derivatives.[27] These synthesized molecules were further explored in in-vitro cellular studies, which conclude these molecules have an apoptotic nature towards a variety of cancer cell lines because of their ability to smoothly dissipate pH gradient along with $Cl^-$ ion. Squaramide-based derivatives are also proven quite effective in demonstrating apoptotic activity. Chen and co-workers reported a squaramide containing a morpholine derivative that showed targeted lysosomal activity by dissipating the pH gradient.[28] (Figure 1.6 [4.1 a-c]). Recently, squaramide-hydroxamic acid conjugate molecules were synthesized, which have showcased excellent selectivity towards tumor cells over normal cells in both in vitro and in vivo conditions.[29] (Figure1.6 [4.1d])It showed increased lysosomal pH, decreased mitochondrial membrane potential, decreased intracellular iron concentration (due to iron chelating hydroxamic unit), and enhanced ROS generation. Moreover, $Cl^-$ transporters have been employed to replicate chloride efflux associated with CFTR function, offering potential therapeutic strategies for cystic fibrosis.[30, 31] (Figure1.6 [2 and 4]) Yang and co-workers reported detailed biological activity of isopthalamide derivative based compound which effectively showcased channel property in liposomal condition (proved through patch clamp technique) and these derivatives showcased increased $Cl^-$ conductance in CuFi-8 cell lines. (cells derived from human cystic fibrosis bronchial epithelial).[31] Benzimidazole-based anion transporters have also been extensively

explored, as they can modulate the pH gradient owing to the presence of a protonable NH group. Chen and co-workers have reported a new class of fluorinated 1,3-bis(benzimidazol-2-yl)benzene derivatives that function as efficient synthetic anion transporters capable of forming stable complexes with $Cl^-$ and mediating efficient transmembrane $Cl^-$ transport in liposomal systems. Enhanced transport activity correlates with the degree of fluorination due to increased lipophilicity, and transporters exhibit potent cytotoxicity in cancer cell lines, attributed to disruption of chloride homeostasis and induction of apoptosis. These transporters therefore represent promising drug-like anionophores with potential applications in chloride-mediated anticancer strategies.[32] (Figure1.6 [6.1a-c]) Manna and co-workers developed bis(iminourea) derivatives as a novel category of pH-responsive $Cl^-$ ion carriers that demonstrate reversible transport behavior across lipid bilayers, with optimal performance at approximately pH 6.6, correlating with their apparent membrane $pK_a$ values. The compounds facilitate selective $H^+/Cl^-$ co-transport in acidic conditions and exhibit weak $Cl^-/OH^-$ antiport at physiological pH. This pH-responsive mechanism was supported by ion-selective electrode measurements and DFT analysis. Notably, chloride-dependent cytotoxicity studies show that disruption of $Cl^-$ homeostasis leads to cell death, suggesting that these compounds can serve as useful chemical tools for exploring how pH-dependent anion transport contributes to cellular dysfunction in cancer.[33] Talukdar and co-workers synthesized pyridyl-linked benzimidazolyl hydrazones operating through an imino-amino tautomeric equilibrium function with efficient non-electrogenic $H^+/Cl^-$ cotransporters, achieving $EC_{50}$ values as low as $5.5 \times 10^{-5}$ and $2.2 \times 10^{-5}$ mol%, thereby outperforming prodigiosin and all previously reported synthetic HCl transporters. Structural, crystallographic, and mechanistic investigations reveal a cooperative proton-chloride recognition motif, driven by protonation at the pyridine nitrogen and stabilised chloride binding, which explains their exceptional transport activity. These hydrazone-based transporters induce chloride-mediated lysosomal deacidification and selective cytotoxicity in MCF-7 breast cancer cells, while exhibiting minimal toxicity toward noncancerous HEK293T cells, establishing them as useful chemical probes for studying HCl transport-driven biological effects.[34] Bicarbonate ($HCO_3^-$) is vital for pH regulation, metabolic waste, and $CO_2$ transport. Quesada et. al reported the first experimental evidence that the natural product prodigiosin can efficiently mediate $Cl^-/HCO_3^-$ antiport across lipid bilayers, demonstrating that small molecules can mimic protein-regulated bicarbonate transport processes. The higher transport efficiency of prodigiosin establishes the tri-pyrrolic hydrogen-bonding framework as a superior structural motif for bicarbonate transport and provides the first quantitative evidence that small molecules can functionally mimic protein-mediated bicarbonate exchange in bio-membranes.

Most synthetic bicarbonate transporters rely on NH-based hydrogen-bond donor motifs, including urea, thiourea, amides, and pyrrolic frameworks, which generally lack strict anion selectivity and often mediate $Cl^-/HCO_3^-$ antiport alongside $H^+/Cl^-$ symport. Mechanistic studies reveal that efficient transporters may switch from $CO_2$-diffusion-driven processes at low concentrations to genuine $HCO_3^-/Cl^-$ antiport at higher loadings. Notably, bambusurils uniquely achieve preferential bicarbonate antiport, though excessive lipophilicity currently limits their biological applicability.[35, 36] (Figure 1.6 [5])

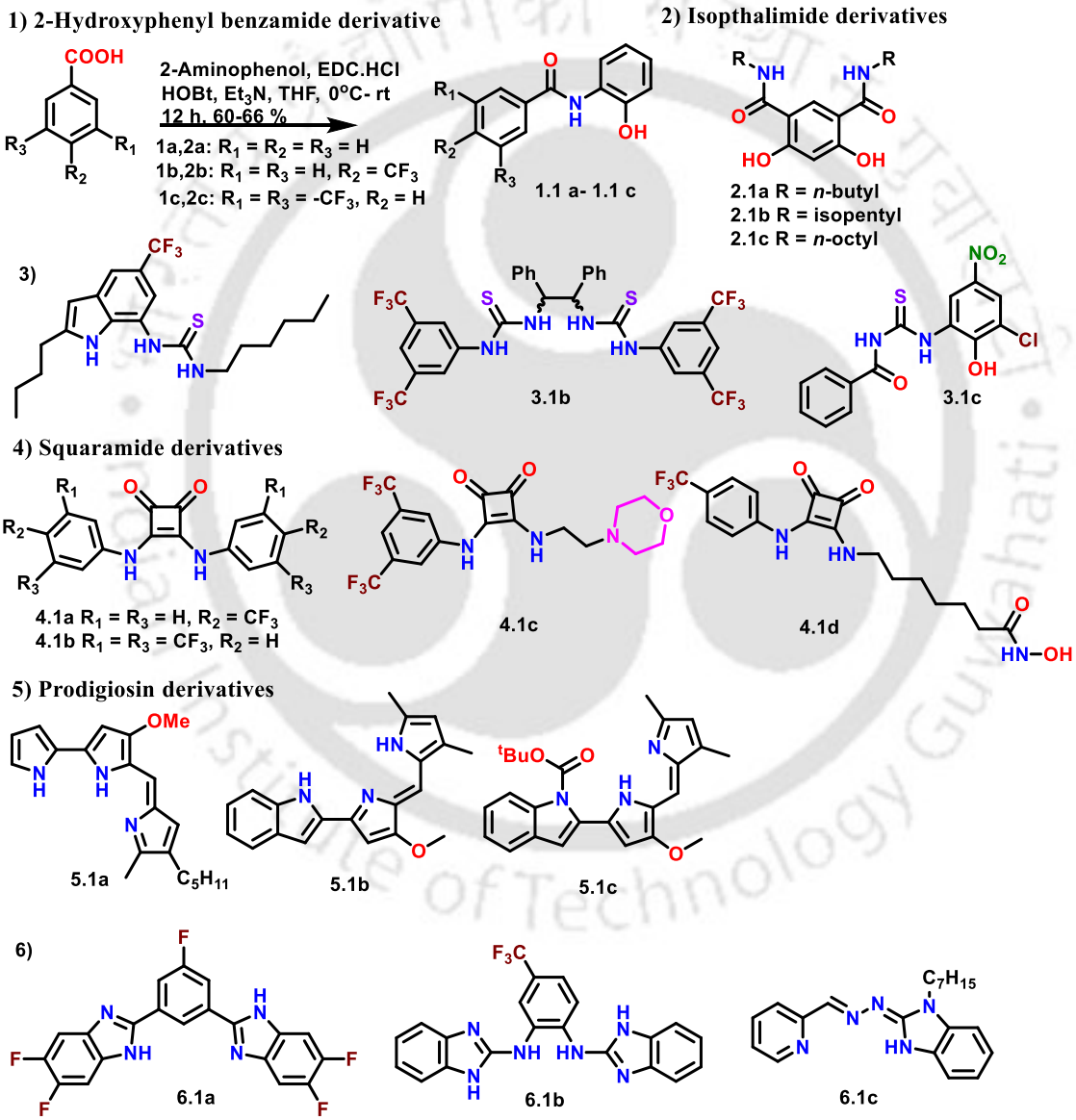


**Figure 1.6.** Schematics of reported anion transporters.

The $Na^+$ and $K^+$ ions are essential for maintaining intracellular ionic balance, and their dysregulation can trigger cellular stress responses. Synthetic $Na^+/K^+$ exchangers are reported by Ren et. al, where they showcased a significant advance in artificial ion transport by

demonstrating that highly selective $K^+$ transport was achieved through the cooperative action of two small-molecule $K^+$ transporters operating in a synergistic manner. The lead transporter, a synthetic $K^+$-selective system that operates through intermolecular cooperation, exhibits exceptional performance with an $EC_{50}$ of 0.28 μM and a $K^+/Na^+$ selectivity of 15.5, placing it among the most selective artificial $K^+$ transporters reported to date. Most importantly, this work provides the first in vitro and in vivo evidence that restoring intracellular $K^+$ homeostasis using artificial $K^+$ transporters can reverse liver fibrosis, establishing ion-transport modulation as a viable therapeutic strategy (Figure 1.7 [7.1 a]).[38] Another work by Yang and co-workers showed a simple α-aminoxy-acid-based small-molecule $K^+/H^+$ transporter that utilizes intrinsic subcellular pH gradients and membrane potential to facilitate site-selective ion transport at mitochondrial and lysosomal membranes in living cells. By selectively disrupting $K^+$ and proton homeostasis in these organelles, the transporter induces mitochondrial damage, lysosomal dysfunction, apoptosis, and suppression of autophagy, leading to highly selective cytotoxicity toward chemo-resistant ovarian cancer stem cells, with up to 47-fold selectivity over non-CSC populations. Furthermore, the depletion of cancer stem cells resulted in a significant inhibition of tumor formation in vivo, illustrating that the selective disruption of mitochondrial and lysosomal $K^+/H^+$ homeostasis by a synthetic cation transporter can yield targeted anticancer effects without causing nonspecific disturbances in cellular ion equilibrium.[39] (Figure 1.7 [7.1 b])

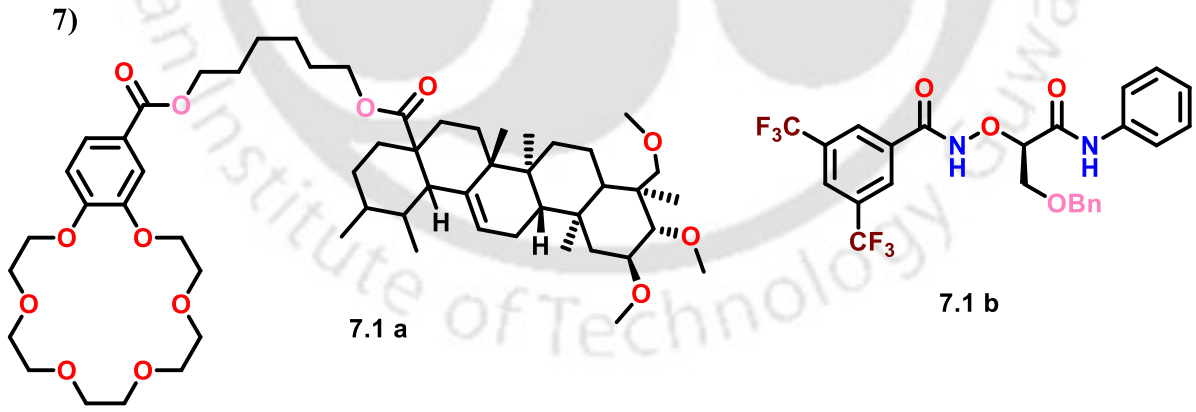


**Figure 1.7.** Schematics of $Na^+$ and $K^+$ synthetic ionophore.

$Zn^{2+}$ is a crucial trace element involved in over 300 enzymatic reactions; it regulates gene expression, stabilizes protein structures via zinc-finger motifs, and acts as a secondary messenger in intracellular signalling pathways. $Zn^{2+}$ demonstrates significant antimicrobial activity and contributes to therapeutic interventions in dermatological conditions. Pyrithione (Figure 1.8 [8]), a 2-mercaptopyridine-based $Zn^{2+}$ ionophore mostly used in skin treatment, has

been structurally modified by the J. L. Sessler group to explore its anticancer potential.[40] Recently, Choudhary et al. have reported a study on structural modification of a $Zn^{2+}$-chelating ligand with silyl groups (Figure 1.8 [10]), which is a specific $Zn^{2+}$ ionophore that exhibited enhanced antimicrobial activity by selectively disrupting zinc homeostasis in pathogens while maintaining low toxicity toward mammalian cells. The most potent compounds in this study are silyl-substituted $Zn^{2+}$ ionophores, in which silicon-containing groups positioned near the metal-binding site enhance lipophilicity and fine-tune $Zn^{2+}$ affinity. This structural modification enables efficient membrane permeation and selective $Zn^{2+}$ transport, resulting in strong antibacterial activity with reduced mammalian toxicity compared to conventional $Zn^{2+}$ ionophores.[41] Manna et al. also have reported a quinoline-based synthetic zinc ionophore capable of facilitating $Zn^{2+}$ transport and exhibiting significant antibacterial activity.[42] (Figure 1.8 [9]) Another well-known class of zinc ionophore, PBT2, which is a derivative of 8-hydroxyquinoline, has shown potential antibacterial activity. Shen et al. reported that PBT2 increases intracellular zinc levels in Klebsiella pneumoniae, which, in turn, reverses tigecycline resistance under higher $Zn^{2+}$ conditions. (Figure 1.8 [11]) The elevated $Zn^{2+}$ disrupts cell wall synthesis, bacterial growth, metabolism, and the balance of oxidative stress.[43] Another report on flavonoid-based molecule quercetin (QCT) (Figure 1.8 [12.1a]) and epigallocatechin-gallate (EGCG) Figure 1.8 [12.1b] is reported by Larrea and co-workers, which acts as a $Zn^{2+}$ ionophore and transports $Zn^{2}$ across lipid membranes independently of native $Zn^{2+}$ transporters. QCT and EGCG rapidly increase labile $Zn^{2+}$ levels in liposomes and in mouse hepatocarcinoma Hepa 1-6 cells.[44] $Cu^{2+}$ is essential for oxidative phosphorylation, functioning as a redox-active cofactor in enzymes like cytochrome c oxidase and superoxide dismutase, which are vital for cellular respiration and antioxidant defence.[45] Madhavan et al. have reported a tripeptide-based amphiphilic scaffold with a C-terminal pybox ligand forming dimeric pores which selectively transport $Cu^{2+}/H^{+}$ antiport mechanism, promoting targeted tumour cell death and antibacterial activity through precise modulation of ion homeostasis.[46] (Figure 1.8 [13]). Recently, Manna et al. have reported a light-activated Cu(I) transporter using a photolabile-modified pro-transporter in mammalian cells, enabling spatiotemporal control to minimize off-target effects and to investigate the role of Cu(I) in protein aggregation.[47]

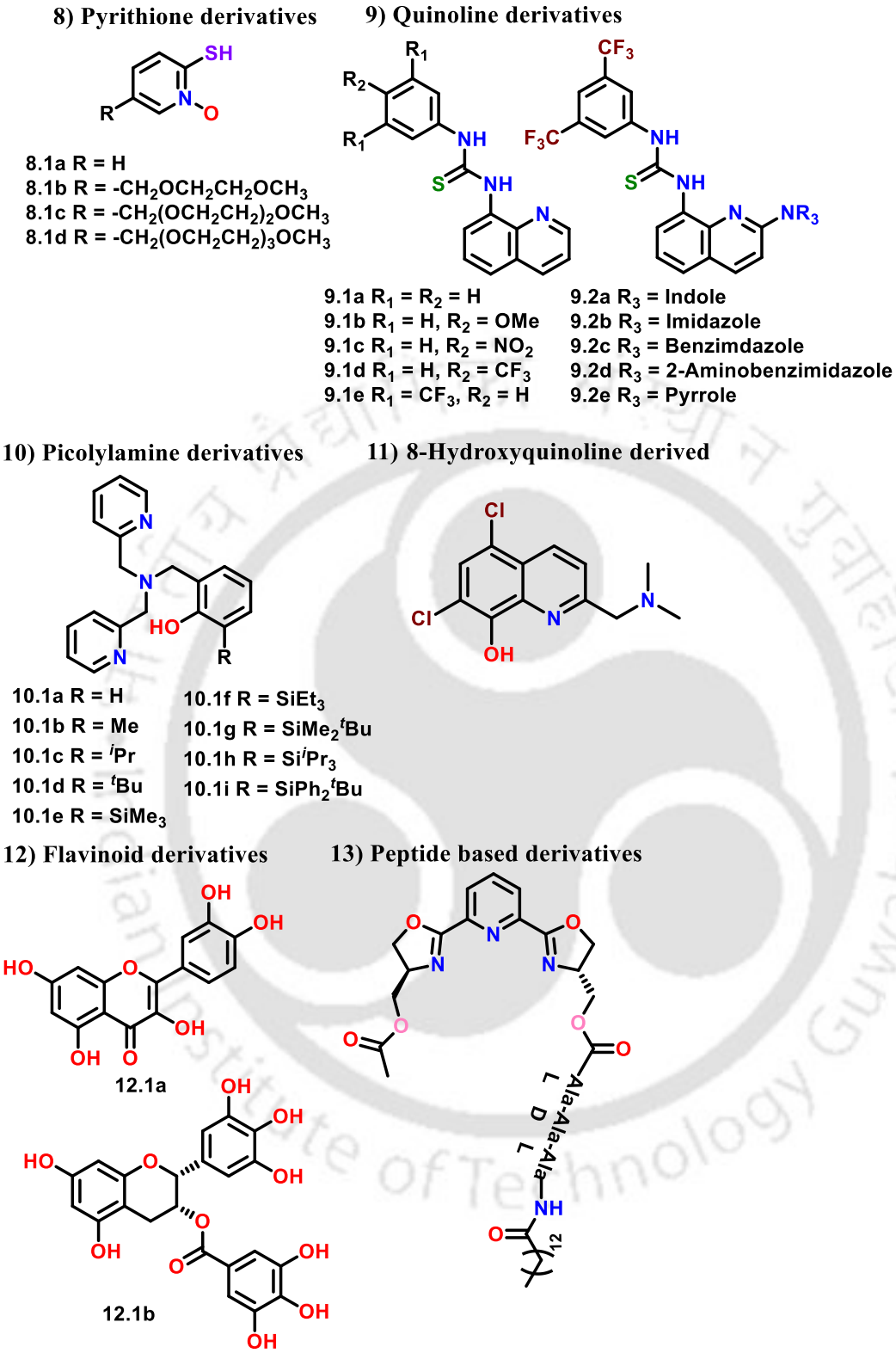


**Figure 1.8.** Synthetic ionophores reported for $Cu^{2+}$/$Zn^{2+}$ ion transport.

Que, E.L. et al. have reported a synthetic bio-stimulus-responsive $Fe^{3+}$ transporter that generates redox-active (GSH-based) ROS, leading to tumor cell apoptosis.[48] $Ca^{2+}$ ions are also abundant in our biological systems and are involved in many important physiological

processes. $Ca^{2+}$ flux across membranes is essential for muscle contraction, cardiac rhythm regulation, and neural signal transmission. Disruption of this process is linked to diseases like epilepsy, periodic paralysis, familial hemiplegic migraine, and Lambert–Eaton myasthenic syndrome.[49, 50] Madhavan and co-workers developed a peptide-based calcium ion transporter which presents alanine-derived peptides containing pyridyl-triazole motifs and hydrophobic alkyl chains, which help membrane insertion and efficiently transport $Ca^{2+}$. The pyridyl-triazole units serve as structural binding sites for $Ca^{2+}$, enabling $Ca^{2+}/OH^-$ symport transport with notable efficiency.[51] In another example reported by Yang and co-workers, they reported an artificial $Cl^-$ channel capable of modulating membrane potential toward the $Cl^-$ equilibrium, thereby indirectly regulating voltage-gated $Ca^{2+}$ channels and intracellular $Ca^{2+}$ levels. The channel effectively induces vasorelaxation in smooth muscle by controlling membrane excitability in living cells and tissues.[52] Thus, the precise regulation of these ions is essential for maintaining cellular homeostasis and supporting life processes.

The ability to tune a supramolecular system in response to external stimuli has emerged as a powerful direction in the design of therapeutic alternatives. Inspired by nature's specific use of environmental cues to regulate complex biological processes, scientists have developed synthetic systems whose structure and function can be dynamically tuned by specific stimuli such as light, pH, enzymes, redox conditions, or molecular ligands. This stimuli-responsiveness not only enables precise spatial and temporal control over ion transport or drug release but also enhances efficacy and selectivity, thereby addressing key challenges in therapeutic applications. In 2023, Wang and co-workers developed the rational design of a ClC-type single-molecule chloride channel that exhibits high transport efficiency, with an $EC_{50}$ of 0.10 μM (0.075 mol% relative to lipid) in lucigenin-based vesicle assays. Planar bilayer measurements demonstrate excellent chloride selectivity, with a $Cl^-/K^+$ permeability ratio up to 12.31 and anion selectivity comparable to that of natural ClC proteins. Mechanistically, the high selectivity arises from the cooperative action of hydrogen bonding and anion-π interactions within the central macrocyclic filter. The presence of pH-responsive terminal phenylalanine residues confers pH-dependent conductance, with enhanced activity at acidic pH, highlighting the potential relevance of this synthetic channel in cancer-associated microenvironments (Figure 1.9 [14]). Notably, the channel exhibits pH-dependent conductance and ion selectivity, highlighting its responsiveness to pH as a key external stimulus.[53] Manna and co-workers developed a quinazoline-thiourea molecular switch that becomes significantly more active in acidic conditions, thanks to proton-assisted chloride binding. Using anion-induced conformational changes to modulate transport activity, this work details the construction of a

molecular switch that acts as a selective $Cl^-$ carrier across lipid bilayers. Single-crystal X-ray diffraction, NOESY NMR, and fluorescence experiments collectively demonstrate that chloride binding triggers a cooperative interaction between $H^+$ and $Cl^-$ ions between the quinazoline core and thiourea moiety, facilitating effective $H^+/Cl^-$ cotransport. The transport efficiency significantly improves under acidic circumstances, indicating a pH-responsive gating mechanism. Notably, the compound also facilitates $H^+/Cl^-$ transport in Gram-positive bacteria, leading to antibacterial effects and underscoring the potential of such adaptive molecular switches for ion-transport-based biological and therapeutic applications[54] (Figure 1.9 [15]). Due to its non-invasive nature, light serves as an ideal external stimulus for modulating biological functions and provides precise spatiotemporal control. The design of photo-responsive synthetic ion transporters enables us to restore ion balance in channelopathies or disrupt ionic homeostasis in cancer therapy at a specific targeted site. Langton and coworkers reported an innovative photo-gating approach for supramolecular mobile anion carriers by controlling carrier mobility within lipid bilayers rather than altering the ion-binding site. By connecting the carrier to a membrane-anchoring alkyl chain via an ortho-nitro benzyl photo-cleavable linker, ion transport is effectively inhibited, resulting in minimal background activity due to reduced trans-bilayer shuttling. Light irradiation of 365 nm induces the cleavage of the linker, liberating the mobile carrier in situ, swiftly reinstating membrane mobility and activating anion transport. This mobility-driven photo-regulation offers exact spatiotemporal control of ion transport and creates a comprehensive, modular framework for the construction of stimuli-responsive ionophores for therapeutic and chemical, biological applications.[55] (Figure 1.9 [16]) Another recent work by the same group reported a photocaged pyridyl triazole carrier that enables light-activated transmembrane transport of Pd(II) ions into vesicles. The delivered Pd(II) forms catalytically active Pd(0)-phosphine complexes inside, triggering intravesicular de-allylation reactions with spatial and temporal precision[56] (Figure 1.9 [17]). Multi-responsive anion transporters are also reported to improve and systematize target specificity. Langton and co-workers reported arylhydrazone-based anionophores whose transport activity can be precisely switched off and on by external light or $H_2S$ stimuli, thanks to reversible intramolecular hydrogen bonding (Figure 1.9 [18]). De-caging these locked hydroxyl groups regenerates anion binding and transport, achieving efficient, controllable off and on profiles.[57] Manna et al. has reported thiourea-containing β-carboline ionophores that mediate $H^+/Cl^-$ cotransport, leading to selective cytotoxicity in cancer cells through apoptosis and autophagy. (Figure 1.9 [19]) Notably, the system features multi-stimuli responsiveness,

where photoactivation of a caged proionophore restores transport activity, anticancer effects, and lower pH enhances transport ability.[58]

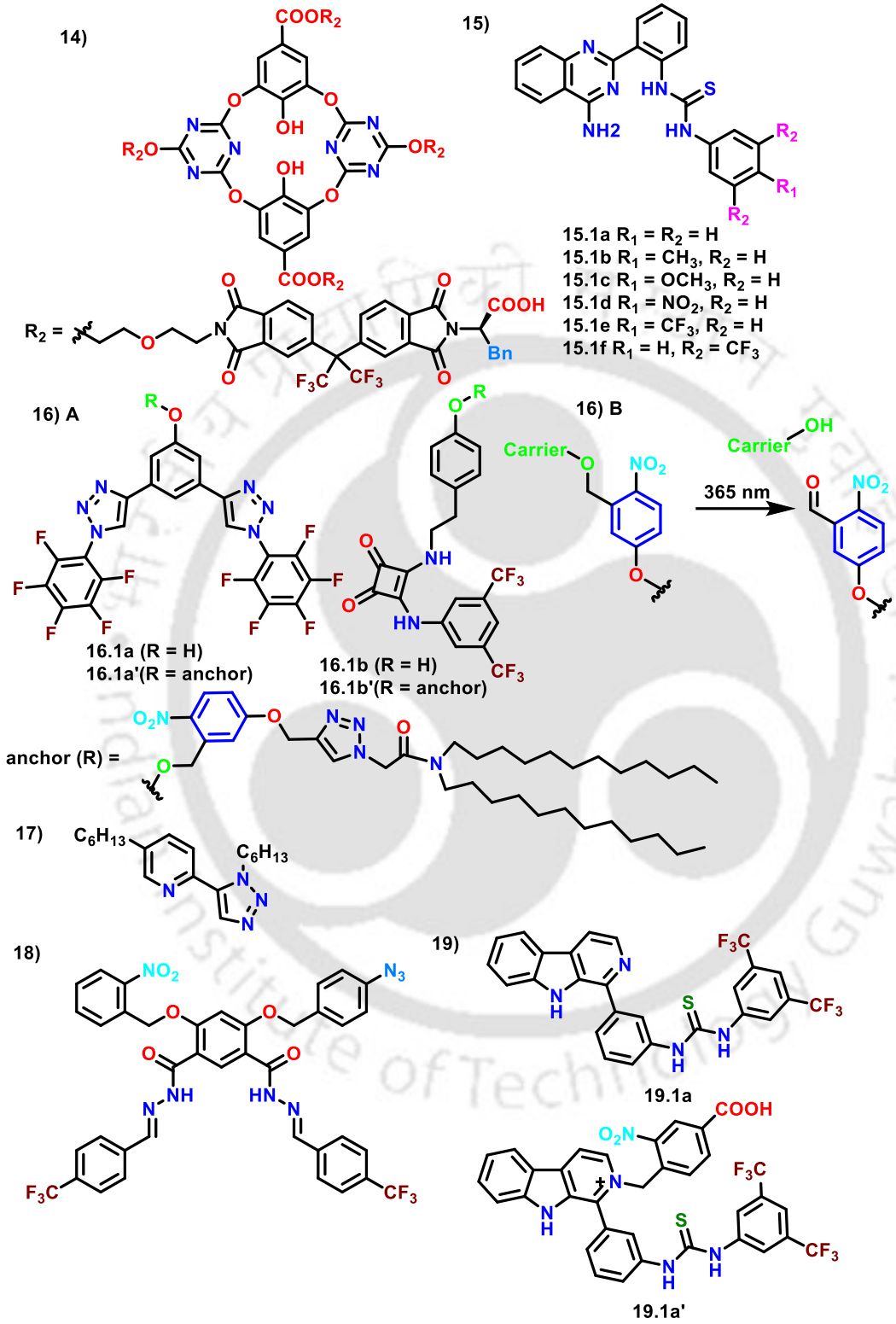


**Figure 1.9.** Schematic representation of a reported stimulus-responsive ion transporter.

## 1.7 Application beyond therapeutics

Synthetic ion transporters play an important role in therapeutic applications by enabling controlled ion transport across lipid membranes through ion imbalance. These molecules are conformationally tunable for ion selectivity and membrane permeability, enabling targeted action while minimizing cytotoxicity in healthy cells. The ability to selectively disrupt ion gradients in diseased cells (tumor cells) or impair ionic homeostasis in bacteria has been well explored and vastly studied. But beyond their therapeutic potential, synthetic ionophores are increasingly recognized for their ability to influence ion-mediated signal transduction, a fundamental mechanism of cellular communication. Nature exhibits many visually striking biological responses and precise ion reflexes, which make us wonder and curious to explore the underlying mechanisms of these processes. For instance, in glow fish, signal-induced $Ca^{2+}$ ion flux activates luciferase enzymes, facilitating controlled light emission as a form of biological communication.[59] Similarly, bioluminescence in fireflies is triggered by a precisely regulated influx of $O_2$ and ions into specialized cells, where ATP-dependent reactions generate light—a process governed by ion-controlled enzyme activation.[60] These naturally beautiful examples signify how transient ionic changes can result in complex, macroscopic biological phenomena.

The application of supramolecular chemistry and synthetic ionophores has allowed researchers to replicate finely tuned ionic events in simplified, controllable systems. By designing ionophores responsive to stimuli such as pH, light, or redox changes, scientists were able to recreate some ion signalling cascades within synthetic artificial vesicles or minimal cellular models. Through the rational design of molecular scaffolds such as calixarenes, crown ethers, porphyrins, and pyrroles, it becomes easier to engineer binding sites with precise charge, size, and electronic environments to selectively recognize and transport desired ions. Similarly, ligand-modified amphiphilic peptides with embedded ion-binding sites form transient pores that replicate proton or divalent-ion flux, similar to natural ion channels. These systems enable us to deal with molecular-level interactions, which can be programmed to reproduce cell-like physiological processes with near precision.

Synthetic ionophores have emerged as an essential component in developing protocells and artificial cellular systems. By incorporating synthetic ionophores into liposomal vesicles or supported lipid bilayers, we can recreate membrane potential, regulate osmotic balance, and introduce signal transduction pathways analogous to those in living cells. This biomimetic strategy helps unravel how ion gradients regulate key biological processes such as secretion, metabolic coordination, and neurotransmission. These synthetic platforms serve as exceptional

tools for engineering artificial cells capable of mimicking life-like behaviours such as environmental sensing, intercellular communication, and dynamic responses to external stimuli. Importantly, synthetic ionophores enable researchers to create programmable systems that replicate specific signalling events such as $Zn^{2+}$- or $Ca^{2+}$-mediated ionic fluxes mirroring those found in neuronal signalling or hormonal regulation. Moreover, synthetic ionophores enable communication between protocells through ion-mediated signalling. These systems enable the mimicking of complex biological phenomena such as quorum sensing, neuronal signalling, and ionic wave propagation across vesicle networks, which is a key element for replicating coordinated multicellular behaviours, including spatial patterning, tissue morphogenesis, and synchronized cellular dynamics. More complex systems can integrate multiple types of ionophores to build feedback loops and logic gate operations, laying the groundwork for synthetic cells that process information and respond intelligently—features commonly associated with biological cognition.

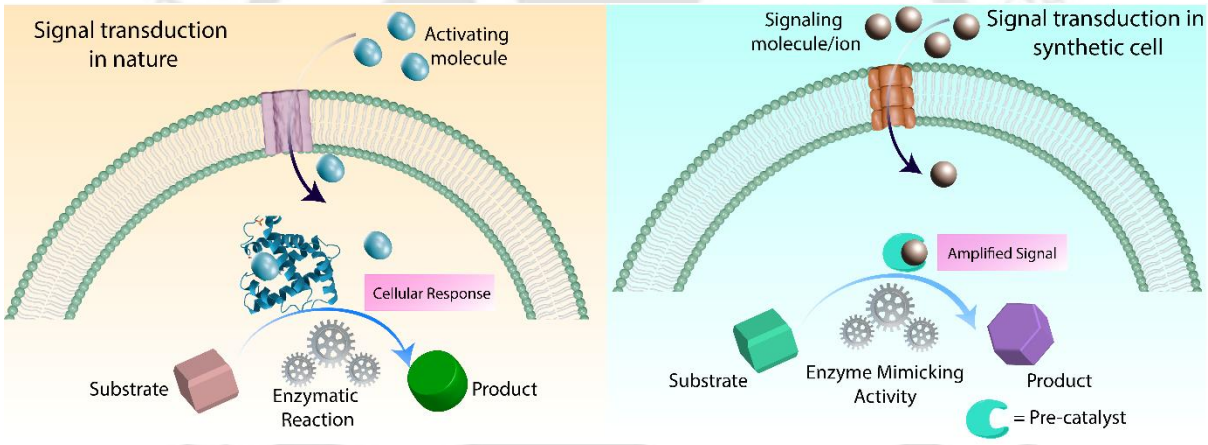


**Figure 1.10.** Schematic representation of the signal transduction process application in liposomal system

Biological systems consisting of membrane-spanning proteins that mediate highly specialized cellular signalling in response to various external stimuli, like small primary messengers, membrane potential, and light. The dimerization mechanism of transmembrane receptors, as observed in biological systems, was first replicated and investigated within a synthetic framework. Earlier, Schrader et al. has developed a membrane-spanning system in which binding of diethylenetriamine to bisphosphonate groups induces dimerization of the membrane-spanning receptor, enabling signal transduction in the inner leaflet of the membrane via FRET-based fluorescent output between donor- and acceptor-labelled molecules.[61] Liu and co-workers recently reported an artificial DNA-based receptor that gets dimerized in the

presence of an ATP trigger. This dimerized complex, coupled with G-quadruplex, induces peroxidase activity, which converts non-fluorescent Amplex red to fluorescent resorufin.[62] Artificial signal transduction systems have been widely explored by Hunter, Williams, and co-workers, utilising pH, redox switching, and metal complexation as the external trigger to activate the primary messenger. They have synthesized molecules with a variety of head groups attached to the two ends and connected by a hydrophobic spacer, like a steroid. One head group act as an external sensor, and the other as a pre-catalyst. Pyridine-oxime, a well-known ligand for transition metal ions, has been utilized as a pre-catalyst. This pyridine-oxime complex, when coordinated with $Zn^{2+}$ or $Cd^{2+}$, shows ester hydrolysis activity. The external sensors that have been explored are pH-sensitive morpholine compounds, readily forming a transition-metal-complexing ligand, phenanthroline, and the biotin sensor desthiobiotin. These external head groups, positioned on one side of the membrane, are triggered by appropriate stimuli to activate membrane translocation, thereby initiating a signal or releasing a secondary messenger on the opposite side of the membrane.[63-65] Clioquinol, a well-known zinc sensor, has been utilised by Langton and co-workers to develop photo-responsive $Zn^{2+}$ transmembrane ion carriers based on BODIPY-caged derivatives operable under visible light. Clioquinol, following the $Zn^{2+}/H^{+}$ antiport mechanism, has been used to establish a synthetic inter-vesicle communication model mimicking the naturally occurring quorum-sensing process.[66] These membrane translocating systems highlight how molecular binding-triggered transport can be harnessed to design synthetic ion transporters that generate and relay signals across membranes, mimicking natural signal transduction processes. Beyond therapeutics, synthetic small-molecule ion transporters could drive revolutionary advances in artificial cell preparation.

### 1.8 Structural requirements for designing ion transporters

The revolution of synthetic ionophores is very crucial for developing therapeutic alternatives to malfunctioning or faulty natural ion channels and for engineering artificial signalling systems that drive the construction of robust artificial cells. Precise knowledge of functional groups that act as ion-binding sites, the potency of reversible interactions, and the ability to enable selectivity for targeted ions help in the structural design of synthetic ion transporters. The spatial arrangement, coordination geometry, and polarity of these binding sites must mimic natural systems for effective transport across bilayer membranes. Besides that, cavity size, lipophilicity, and the presence of heteroatoms like O, N, S, etc., also play key roles in designing and hypothesizing ionophores with better transport efficacy and higher selectivity.

Designing an effective anionophore requires careful consideration of structural elements such as hydrogen and halogen bonding interactions, suitable binding sites for anion, and an optimal balance of lipophilicity to ensure efficient transport across lipid membranes. Considering these factors, reported examples include triazole/tetrazole derivatives, thiourea/urea derivatives, squaramide- and sulphonamide-based derivatives, isothiazolium derivatives, calixarene-based compounds, and others (Figure 1.11).

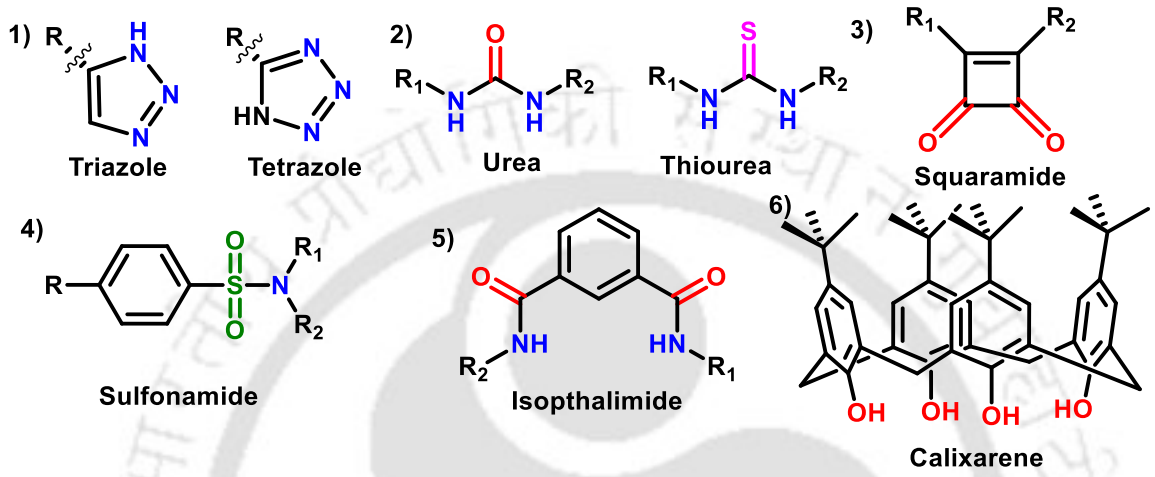


**Figure 1.11.** Representative example of a functional group responsible for an anion-based ion transporter.

In recent years, acyclic iodo-triazole motifs developed by Langton et al. have demonstrated efficient anion transport via halogen and hydrogen bonding interactions, enabling strong, directional binding of chloride ions. These halogen bonding systems show enhanced $Cl^-$ selectivity over $OH^-$ compared with their hydrogen-bonded prototriazole counterparts, highlighting differences associated with stronger, more directional interactions and increased charge delocalization within the halogen bonding complex.[67] Quesada et. al synthesized a triazole-based derivative of prodigiosin that demonstrated effective $Cl^-$ and $HCO_3^-$ transport in cellular models, indicating their potential as CFTR-independent therapeutic candidates for cystic fibrosis.[68] Thiourea and urea functional groups interact with anions via H-bonding and are well known for reversible binding upon proper incorporation in the system. Manna et al. has reported thio-urea-functionalized quinine derivatives that facilitate $H^+/Cl^-$ exchange across lipid bilayers through cooperative interactions between the quinuclidine ring and thiourea motifs, leading to intracellular chloride accumulation, pH disruption, and activation of mitochondria-mediated apoptotic signalling pathways in cancer cells. Squaramide compounds participate in reversible binding and transport of anions via H-bond interactions. It also plays a vital role in altering the pH gradient, providing an additional benefit for use as an anion

transporter. Gale and coworkers reported squaramide-based compounds that exhibit superior anion transport across lipid bilayers compared to urea- and thiourea-functionalised moieties, owing to their stronger anion-binding affinity and a favourable balance of lipophilicity and hydrophilicity.[69] Romański and coworkers have shown that a squaramide–crown ether-based ditopic receptor exhibited the ability to transport negatively charged amino acids like glutamate and arginine across lipid bilayers by facilitating ion-pair formation and exploiting strong hydrogen bonding and ion-dipole interactions.[70] Anions can be transported across the bilayer membrane by calixarene-based molecules through weak interactions, such as hydrogen bonding and π-anion-π attraction, via their cup-like structures. Their amphiphilic, rigid yet flexible conformational rearrangement ability facilitates the easy binding of ions and their efficient transport. Saha et al. have reported a two-wall calix [4] pyrrole with 3,5-bis(trifluoromethyl)phenyl groups in cis conformation efficiently transporting $F^-$ ions across membranes via selective π-anion-π interactions.[71] Recently, Valkenier and co-authors also showed Calix[6]arene derivatives having halogen bond donor groups effectively transport $Cl^-$ and $NO_3^-$ across membranes with better selectivity, as their tunable and directional halogen bonding interactions outperform traditional hydrogen bonds, enabling potent anion recognition and minimizing disruption to pH gradients.[72]

Designing a cationophore requires a careful balance of ion selectivity, membrane compatibility, and binding strength. The molecule must coordinate properly to the target metal ion while remaining sufficiently lipophilic to cross the cell membrane. An optimal transporter binds the metal ion reversibly, enabling controlled release, and mimics natural ion transport processes without disrupting cellular homeostasis. Considering the above key factors, functional groups that can be incorporated in the structure for metal or cation transport reversibly are benzimidazole derivatives, poly-ethers, hydroxamate derivatives, Thiols and thiocarbamate derivatives, -sp2 hybridised N-like imines, hydrazones, etc. (Figure 1.12).

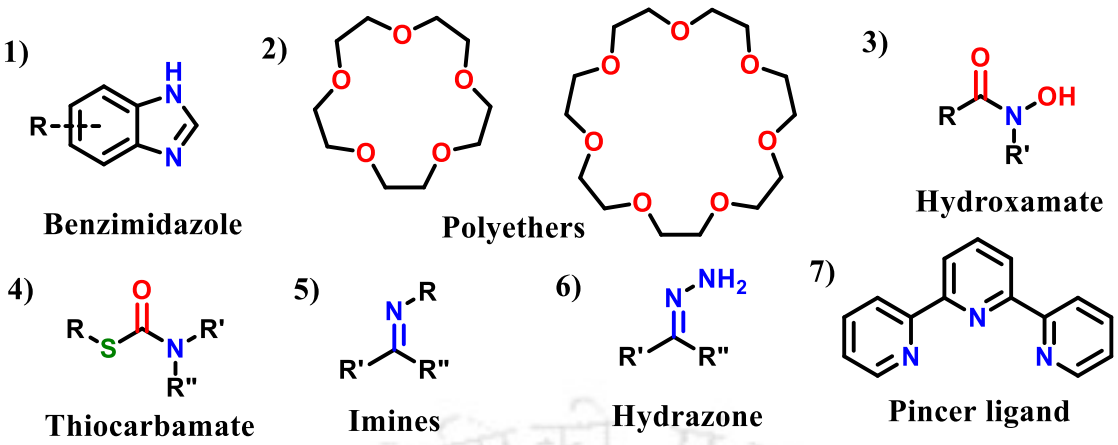


**Figure 1.12.** Representative example of a functional group responsible for a cation or metal-based ion transporter.

Earlier, Haupt et al. developed bis(thiosemicarbazone)-based copper ionophores that facilitate intracellular copper accumulation, leading to selective cytotoxicity in prostate cancer cells by disrupting metal homeostasis. They demonstrated efficacy both in vitro and in vivo, highlighting their potential as targeted anticancer agents.[73] This bis(thiosemicarbazone) based molecule provides a planar co-ordinating environment with two thiones and two imine donors. Also, the key factor governing its ion-transport behaviour is the ligand deprotonation upon metal binding, which renders the resulting Cu(II) complex electrically neutral and less hydrophilic, thereby facilitating efficient partitioning into lipid membranes. Tardito and co-workers have developed a pyrazole-pyridine-based scaffold for Cu-ion transport, which showed effective inhibition of fibrosarcoma cells.[74] Recently, Madhavan et. al developed a peptide-based $Cu^{2+}$ transporter where they incorporated a pybox ligand, a pyridine-2,6-bis(oxazoline) based moiety that has a tridentate coordination site and
attached to an alanine-based tri-peptide, which makes the synthesized molecule hydrophobic for membrane insertion.[75] Pyrithione, a N-oxide and thiolate functional group-based bidentate ligand, coordinating $Zn^{2+}$ to form a stable, charge-neutral 2:1 complex. These metal-ligand coordinated species passively diffuse across lipid membranes, facilitating intracellular metal delivery. Sessler et al. have reported a pyrithione derivative bearing oligoethylene glycol chains at the 5-position of the pyrithione ring, which efficiently transports $Zn^{2+}$ into A549 and PC-3 cancer cells, triggering apoptosis via intracellular zinc accumulation.[40] Clioquinol, a derivative of 8-hydroxyquinoline, acts as a bidentate $Zn^{2+}$ ionophore capable of forming a stable, lipophilic metal complex. It facilitates the passive diffusion of $Zn^{2+}$ across lipid membranes and has been shown to modulate metal-dependent enzymatic pathways in cellular systems by

disrupting intracellular metal ion distribution.[66] Recently, a benzimidazole-based Zn2+ transporter was reported by Manna et. al., which was incorporated with a β-cyclodextrin-based suprasomal delivery system to deliver the ionophore to the targeted site.[76] Poly-ether or crown ether-based derivatives are widely used for selectively transporting $Na^+$ and $K^+$ ions across the cell membrane.[77, 78]

**1.9 Principle for designing ion transporters**

Nature builds up ion channels through genetically encoded biosynthetic pathways. However, replicating these complex architectures synthetically is a tough challenge due to their intricate structures and large molecular sizes. Structural elucidation of peptide-based natural ion channels using methods such as crystallography has enabled the identification of conserved amino acid residues and other functional groups responsible for gating and ion selectivity. These insights have become increasingly important for rationally designing both protein-based and small synthetic organic ion channels. However, exploring the structure-function relationship through physical and analytical methods, such as sequence studies, can be time-consuming and resource-intensive. In contrast, small synthetic amphiphilic molecules offer a more cost-effective and accessible strategy for mimicking biological ion transport. Small synthetic or natural molecules can serve as practical and less demanding alternatives to natural ion channels, making it easier to study and mimic ion transport in simpler systems.

Membrane and supramolecular structures coherently move together dynamically, as embedding lipophilic supramolecular structures into bilayers offers a suitable way to connect hydrophobic

systems with biological and water-based environments. As most functional organic supramolecular compounds are poorly water-soluble, membranes serve as a perfect interface, which makes membrane-based supramolecular chemistry a promising avenue for advancing applications in biology and medicine.

In ion transport, the weak interaction force plays a crucial role. Ion transport across membranes involves careful navigation of hydration shells where layers of water molecules are tightly bound to ions in solution. Dissolving these ions requires significant energy, especially for highly charged or small ions like $Na^+$ or $Mg^{2+}$. The hydration barrier can be overcome by strong ion-binding receptors, but when interaction becomes too strong, the receptor can trap the ion and hinder its release on the other side of the membrane. Hence, synthetic ionophores are designed to interact with the hydrated ion or a partially de-solvated species, thereby maintaining effective transport efficiency. This balance between affinity and reversible binding is pivotal for dynamic ion transport and mimicking the working of natural ion channels.

Reversible non-covalent interactions, especially electrostatic interactions, are central to transmembrane transport processes and ion recognition. These interactions are influenced by the steric accessibility and charge density of the ions involved. Ions like $Na^+$ and $Cl^-$, which possess high, localized charge densities, can engage in strong electrostatic interactions, facilitating efficient transport and binding. In contrast, ions like $I^-$ with diffused charge density around it, as seen in tetrabutylammonium cations, experience weaker electrostatic interactions due to charge delocalization or shielding.

Ion transport across biological membranes occurs in aqueous environments and is governed by the thermodynamics of ion solvation and de-solvation. In water, ions are strongly stabilised by solvation shells, and the direct transfer of hydrated ions into the low-dielectric interior of a lipid bilayer is energetically highly unfavourable. Ionophores facilitate membrane transport by providing a preorganised, complementary binding environment that partially replaces the solvation shell and compensates for the associated dehydration penalty, while shielding the ion from the hydrophobic membrane core. Consequently, transport efficiency reflects a balance between the free-energy cost of ion de-solvation and the stabilising noncovalent interactions formed within the ionophore and ion complex, rather than any intrinsic reduction in ion solvation within the membrane phase.

In our biological systems, molecular interactions in the cytosolic environment or extracellular fluid are mostly governed by charge/charge, charge/dipole, or dipole/dipole forces, due to the polar nature of the environment. In contrast, the lipid bilayer presents a highly nonpolar, hydrophobic layer composed of lipid tails that actively exclude polar or charged species. This region accommodates molecules with hydrophobic core structures, like long alkyl chains or aromatic systems. For a molecule to effectively integrate or function within the membrane, it must exhibit amphiphilic character bearing both hydrophilic and hydrophobic (or lipophilic) domains. This amphiphilic nature allows proper alignment within the bilayer, with polar moieties interacting with the aqueous surroundings and ion-capturing and hydrophobic portions buried within the membrane, actively transporting ions across it.

Entropy plays a pivotal role in the process of ion transport, particularly in overcoming the hydrophobic barriers by the membrane. Unlike electrostatic attractions between cations and anions, hydrophobic regions of membrane-lipids do not attract each other; rather, these core parts repel water molecules. This repulsion causes water molecules near hydrophobic surfaces

to adopt highly ordered, constrained arrangements to maintain hydrogen bonding with neighbouring water molecules. Such structuring reduces the freedom of molecular motion, leading to a significant decrease in entropy, which is energetically unfavourable for the system. Ion transporters, being amphiphiles, reduce this loss by minimizing water-ion interactions, facilitating ion passage, and increasing overall system entropy, which makes transport energetically favourable.

Effective metal ionophores require a careful integration of structural architecture and chemical functionality. They must contain a polar coordination site capable of selectively binding metal ions, while also exhibiting a nonpolar exterior to interact favourably with the lipid bilayer. This dual nature allows the molecule to embed in the membrane and facilitate ion movement across it. To enhance permeability and transport activity, the molecule's lipophilicity, typically expressed as logP, should be close to 5, as suggested by Lipinski's rule. A variety of structural frameworks, including bipodal, tripodal, macrocyclic, and foldamer motifs, are employed to modulate ion-binding affinity and optimize transmembrane transport behaviour.

Designing synthetic metal-ion channels is complex, requiring precise control over noncovalent supramolecular interactions to achieve selective ion conduction. These channels must span or exceed the membrane thickness and consist of self-assembled units. A hydrophobic exterior ensures membrane compatibility, while a polar interior lining enables coordination with hydrated metal cations, facilitating their efficient transmembrane passage. Metal ionophores are ligands that reversibly bind metal ions under physiological conditions and enable their controlled transport across cellular membranes. They typically form neutral, lipophilic complexes with metal ions, allowing efficient membrane passage. Once inside the cell, metal release is triggered by localized ion concentrations or specific environmental stimuli, thereby modulating intracellular metal homeostasis.

Thus, lipid bilayer membranes are fundamental to cellular life, acting as selective barriers that separate internal and external environments. Membrane proteins, both integral and peripheral, enhance these structures by enabling ion and small molecule transport, facilitating molecular recognition, anchoring cellular structures, and mediating signal transduction. These proteins often respond to specific stimuli, adjusting their function in response to environmental cues. Inspired by these dynamic biological systems, supramolecular chemists have developed synthetic membrane-interfacing systems that mimic such functions. Ion transport across membranes involves overcoming enthalpic and entropic penalties from dehydration and bilayer insertion. Synthetic ionophores overcome these barriers through precise coordination and non-covalent interactions such as electrostatics and hydrogen bonding. The process is further

influenced by dynamic bilayer rearrangements and transporter conformational flexibility, dictating ion selectivity and transport efficiency.

### 1.10 Strategies for identifying and measuring ion transport

The accuracy in measuring the ion transporter activity is essential for understanding their ability to alter solute concentrations across biological membranes. Two very widely used experimental approaches are the liposome-based fluorometric assay and black lipid membrane (BLM) conductance measurements. Liposome-based techniques are particularly favoured in supramolecular chemistry for the study of synthetic ion carriers. Large unilamellar vesicles (LUVs) serve as robust cell-mimetic platforms, providing a controlled environment to evaluate transporter function. These vesicles allow precise regulation of internal and external ion compositions, enabling the initiation of concentration gradients through techniques such as dialysis or size-exclusion chromatography. Ion transport events across the vesicle membrane can be quantitatively monitored using fluorescence-based probes (e.g., pH-sensitive or ion-sensitive dyes), ion-selective electrodes (ISE), or NMR spectroscopy.

BLM is a powerful tool to study channel mechanisms of a synthetic ion transporter by recreating a simplified version of the cellular membrane. In this setup, a lipid monolayer (DPhPC lipid) is painted across a smaller aperture (150–250 μm) in a Teflon partition separating two electrolyte-filled chambers. The lipid self-assembles into a bilayer, which is electrically insulating unless an ion channel or transporter is present. When a voltage is applied across the membrane via electrodes, any ion movement through the bilayer generates a current, which is measured by a high-sensitivity amplifier capable of detecting picoampere-level signals. These current measurements reflect the ion-conductance properties of the incorporated transporter and allow analysis of ion selectivity, gating behaviour, and transport rates under controlled conditions.

Commercially available ion-selective electrodes are another alternative to fluorescence, in which vesicle-encapsulated specific ions are invisible to the electrode but can be detected if released by a transporter. ISE is an analytical sensor that measures the activity of specific ions in solution by converting ionic activity into an electrical potential. They consist of a membrane that is selective to a particular ion, allowing only that ion to interact with the electrode surface. This interaction generates a potential difference relative to a reference electrode, governed by the Nernst equation. The measured voltage is directly related to the logarithm of the ion concentration in the solution. Commonly available electrodes are: $Cl^-$, $F^-$, $Br^-$, $I^-$, $K^+$ etc.

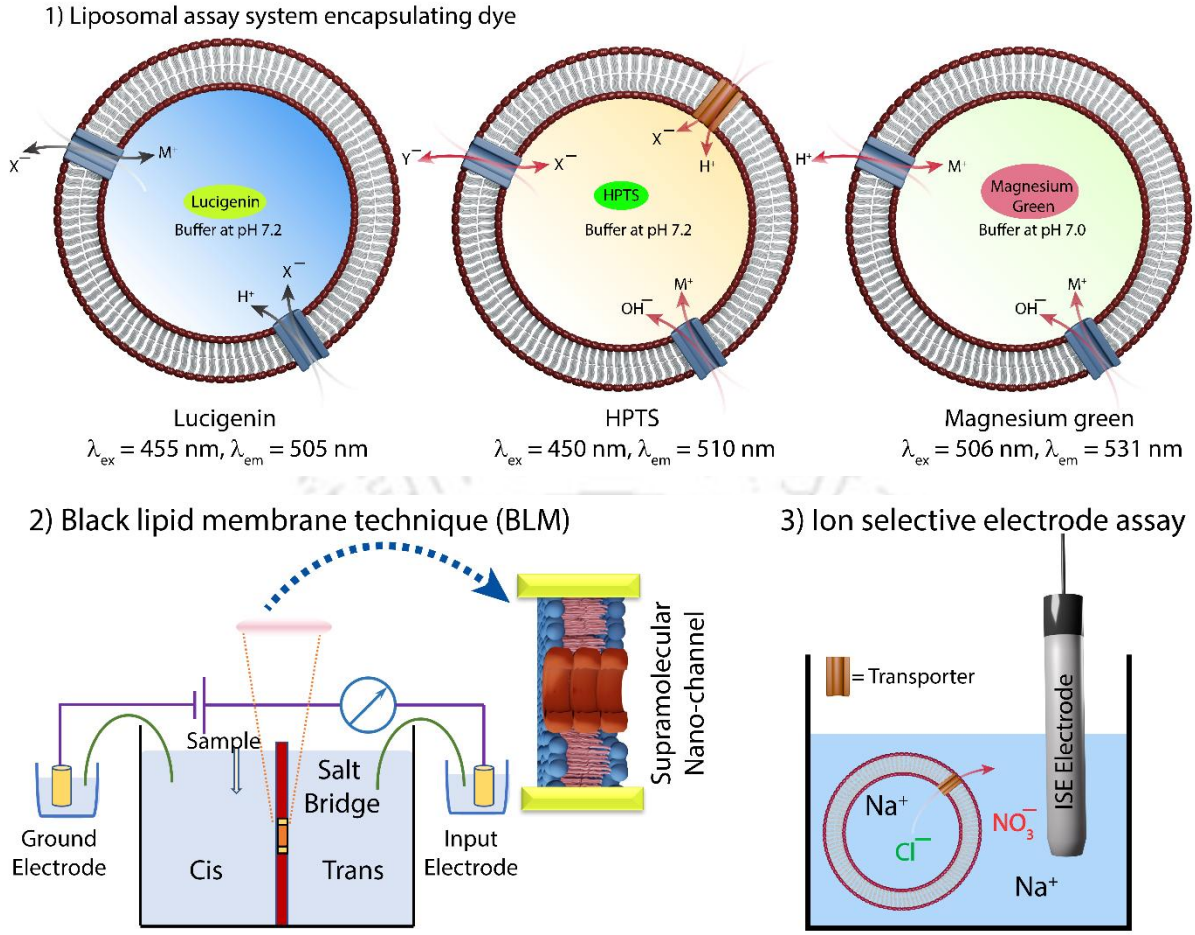


**Figure 1.13.** Illustration of various methods for measuring ion transport pathway and mechanism.

In vesicle-based methodology, the fluorescent probes that have been utilised are:

(1) 8-Hydroxy pyrene-1,3,6-trisulfonic acid (HPTS): Pyrene-based dye, used for detecting proton gradient change or $H^+$ transport across the membrane. Its fluorescence intensity decreases in an acidic environment and increases under basic conditions.

(2) Bis-N-methyl acridinium nitrate (Lucigenin): This dye senses halide exchange across the membrane. Its fluorescence intensity decreases in the presence of halide.

(3) Safranin (O): It is a phenazine-based dye that shows fluorescence intensity change upon generation of membrane potential due to the ion movement.

(4) Magnesium green pentapotassium salt (MgG): A fluorescein-based dye, which shows enhanced fluorescence intensity in the presence of transition metals at very low concentrations (nM).

(5) Calcein: A xanthene ring containing dye, which is self-quenching at higher concentration (50 mM). It is used for detecting pore formation in the vesicle in the presence of a synthesized ion transporter.

(6) Carboxyfluorescein (CF): This self-quenching fluorescein-based dye also helps in the vesicle leakage assay.

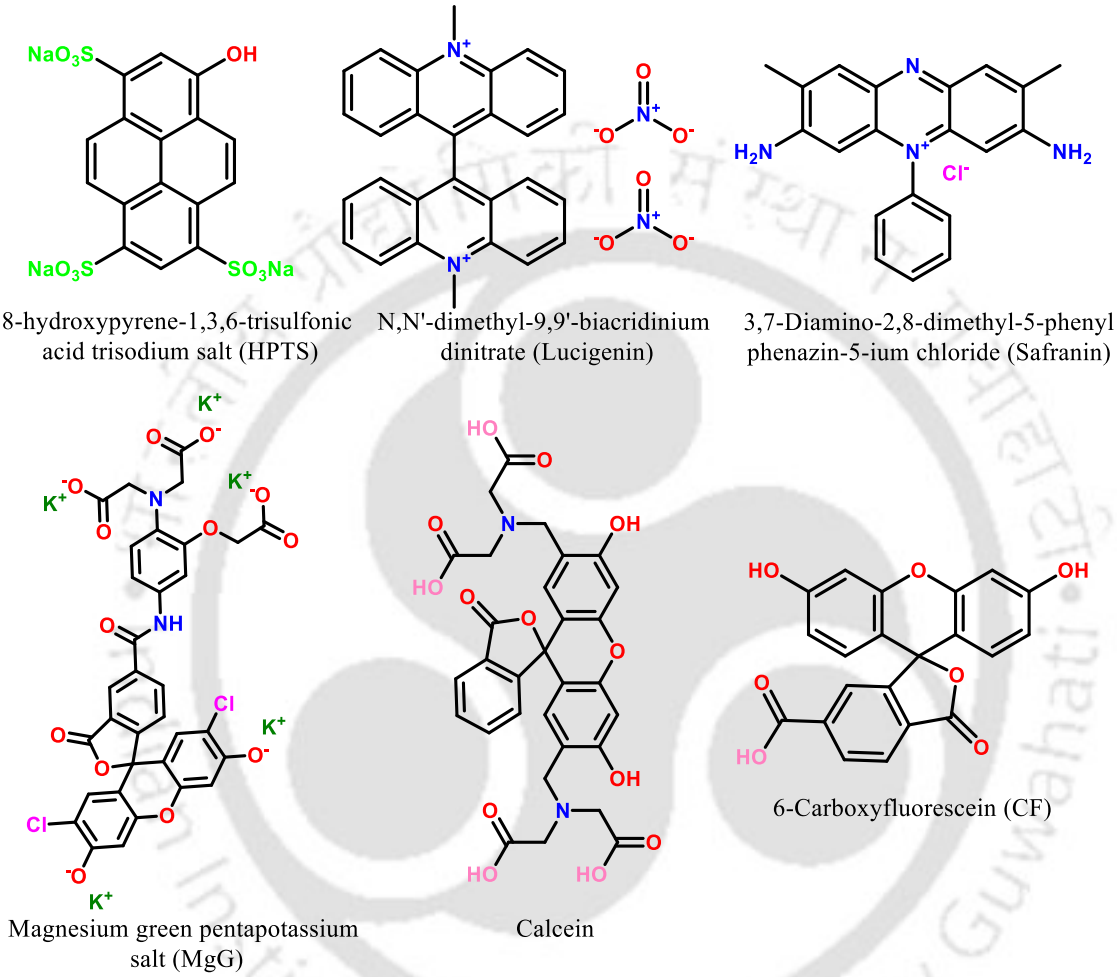


**Figure 1.14.** structural representation of various dyes utilised in ion transport liposomal studies.

### 1.11 Summary:

Synthetic ion channels and transporters represent a rapidly evolving frontier at the intersection of supramolecular chemistry and biology. By modulating or mimicking natural ion flux, these systems enable specific control over cellular processes and hold significant therapeutic potential, particularly for treating ion channel disorders. Recent advances in stimuli-responsive designs activated by light, pH, redox cues, or biomolecular triggers offer unprecedented spatiotemporal regulation and functional versatility. Beyond therapeutics, these dynamic transport systems provide innovative tools for molecular communication, paving the way for

the construction of artificial cells and smart, responsive materials. Collectively, the development of synthetic ion transporters and channels not only clarifies our understanding of fundamental membrane transport phenomena but also gives a compelling path toward next-generation biomedical technologies and molecular devices. Looking ahead, integrating these synthetic systems with biological components such as proteins, nucleic acids, or cellular membranes could further enhance selectivity and functionality. Combining rational design with computational modelling and high-resolution structural studies will accelerate discovery, enabling the development of tailored systems for specific biomedical challenges. This multidisciplinary approach highlights synthetic ion transporters and channels as both fundamental scientific tools and transformative platforms for therapeutic innovation and molecular engineering.

**1.12 State of the Art, Current Challenges, and Scope of the Thesis:**

Recent advances in ionophore research have led to the development of stimuli-responsive, carrier-based systems that enable spatiotemporal control over ion transport, offering promising avenues for next-generation anticancer and antibacterial therapeutics. In parallel, increasing attention has been directed toward supramolecular ion channels, which often exhibit enhanced transport efficiency and hold greater potential for therapeutic translation. Despite this rapid progress, several conventional and non-conventional design strategies remain underexplored. In the context of chloride ionophores, although various stimuli-responsive systems have been reported, selective targeting of cancer-specific biomarkers remains limited. To address this, we developed an RGD-peptide linked proionophore that is activated within the cancer microenvironment, enabling targeted ion transport and improved therapeutic precision.

Beyond conventional approaches, limited efforts have been devoted to $Zn^{2+}$-based supramolecular ion channels. In this thesis, we explore this non-conventional direction by demonstrating $Zn^{2+}$ transport-mediated catalytic activity within liposomal systems. Specifically, we establish $Zn^{2+}$-triggered esterase-like activity, highlighting the potential of ion transport to initiate functional transformations in confined environments. Building on this concept, we further demonstrate dual-controlled oxidative catalysis regulated by both $Zn^{2+}$ transport and photoirradiation, introducing an additional layer of external spatiotemporal control. Collectively, the studies in this thesis push the frontiers of ionophore research by refining conventional design principles and introducing non-conventional approaches that broaden functional capabilities and mechanistic insight.

**1.13 Reference**

1. Davis, J. T.; Gale, P. A.; Quesada, R. Advances in Anion Transport and Supramolecular Medicinal Chemistry. *Chem. Soc. Rev.* **2020**, *49* (16), 6056−6086.

2. Gokel, G. W.; Carasel, I. A. Biologically Active, Synthetic Ion Transporters. *Chem. Soc. Rev.* **2007**, *36* (2), 378−389.

3. Mura, S.; Nicolas, J.; Couvreur, P. Stimuli-Responsive Nanocarriers for *Drug Delivery. Nat. Mater.* **2013**, *12* (11), 991−1003.

4. Lang, F.; Föller, M.; Lang, K.; Lang, P.; Ritter, M.; Gulbins, E.; Vereninov, A.; Huber, S. Ion Channels in Cell Proliferation and Apoptotic Cell Death. *J. Membr. Biol.* **2005**, *205* (3), 147−157.

5. Goodman, S. R. *Medical Cell Biology*, 3rd ed.; Academic Press: San Diego, CA, **2007**.

6. Metzler, D. E. *Biochemistry: The Chemical Reactions of Living Cells*, 2nd ed.; Elsevier Academic Press: San Diego, CA, **2003**.

7. Lodish, H.; Berk, A.; Matsudaira, P.; Kaiser, C. A.; Krieger, M.; Scott, M. P.; Zipursky, S. L.; Darnell, J. *Molecular Cell Biology*, 6th ed.; W. H. Freeman: New York, **2008**.

8. Alberts, B.; Johnson, A.; Lewis, J.; Raff, M.; Roberts, K.; Walter, P. *Molecular Biology of the Cell*, 4th ed.; Garland Science: New York, **2002**; Chapter 11.

9. Kulbacka, J.; Choromańska, A.; Rossowska, J.; Wężgowiec, J.; Saczko, J.; Rols, M.-P. Cell Membrane Transport Mechanisms: Ion Channels and Electrical Properties of Cell Membranes. In *Advances in Anatomy, Embryology and Cell Biology*; Paulsen, F., Waschke, J., Eds.; Springer: Cham, **2017**; Vol. 227, pp 39−58.

10. Fyles, T. M. Synthetic Ion Channels in Bilayer Membranes. *Chem. Soc. Rev.* **2007**, *36* (2), 335−347.

11. Gouaux, E.; MacKinnon, R. Principles of Selective Ion Transport in Channels and Pumps. *Science* **2005**, *310* (5753), 1461−1465.

12. Voet, D.; Voet, J. G.; Pratt, C. W. *Fundamentals of Biochemistry: Life at the Molecular Level*, 5th ed.; John Wiley & Sons: Hoboken, NJ, **2016**.

13. Imbrici, P.; Altamura, C.; Pessia, M.; Mantegazza, R.; Desaphy, J.-F.; Camerino, D. C. ClC-1 Chloride Channels: State-of-the-Art Research and Future Challenges. *Front. Cell. Neurosci.* **2015**, *9*, 156.

14. Hanssens, L. S.; Duchateau, J.; Casimir, G. J. CFTR Protein: Not Just a Chloride Channel? *Cells* **2021**, *10* (11), 2844.

15. Artigas, P.; Gadsby, D. C., Ion channel—Like properties of the $Na^+/K^+$ pump. *Ann N Y Acad Sci.* **2002,** *976* (1), 31-40.

16. Bafaro, E.; Liu, Y.; Xu, Y.; Dempski, R. E. The Emerging Role of Zinc Transporters in Cellular Homeostasis and Cancer. *Semin. Thromb. Hemost.* **2017**, *43* (7), 736−746.

17. Taweechat, P.; Boonamnaj, P.; Samsó, M.; Sompornpisut, P. Significance of $Zn^{2+}$ in RyR1 for Structural Integrity and Ligand Binding: Insight from Molecular Dynamics. *J. Phys. Chem. B* **2024**, *128* (19), 4670−4684.

18. Jowett, L. A.; Howe, E. N.; Soto-Cerrato, V.; Van Rossom, W.; Pérez-Tomás, R.; Gale, P. A. Indole-Based Perenosins as Highly Potent HCl Transporters and Potential Anti-Cancer Agents. *Sci. Rep.* **2017**, *7* (1), 9397.

19. Harrell, W. A., Jr.; Bergmeyer, M. L.; Zavalij, P. Y.; Davis, J. T. Ceramide-Mediated Transport of Chloride and Bicarbonate across Phospholipid Membranes. *Chem. Commun.* **2010**, *46* (22), 3950−3952.

20. Rose, M. C.; Henkens, R. W. Stability of Sodium and Potassium Complexes of Valinomycin. *Biochim. Biophys. Acta* **1974**, *372* (2), 426−435.

21. Karunakar, K. K.; Cheriyan, B. V.; Velmurugan, R.; Gopalakrishnan, M.; Karthikha VS Mechanistic insights and therapeutic applications of hinokitiol in inflammation, antimicrobial therapy, and cancer *Pharmacol. Res. Mod. Chin. Med.* **2024**, 13, 100527.

22. Yasumoto, E.; Nakano, K.; Nakayachi, T.; Morshed, S. R. M.; Hashimoto, K.; Kikuchi, H.; Nishikawa, H.; Kawase, M.; Sakagami, H. Cytotoxic activity of deferiprone, maltol and related hydroxyketones against human tumor cell lines *Anticancer Res.* **2004**, 24 (2B), 755−762.

23. Mondal, A.; Barik, G. K.; Sarkar, S.; Shivpuje, U.; Mondal, J.; Santra, M. K.; Talukdar, P. Apoptosis-inducing activity of a 2-hydroxyphenyl benzamide-based self-assembled anion channel *Chem. Eur. J.* **2025**, 31 (3), e202403252.

24. Moore, S. J.; Wenzel, M.; Light, M. E.; Morley, R.; Bradberry, S. J.; Gomez-Iglesias, P.; Soto-Cerrato, V.; Perez-Tomas, R.; Gale, P. A. Towards "drug-like" indole-based transmembrane anion transporters *Chem. Sci.* **2012**, 3 (8), 2501−2509.

25. Akhtar, N.; Saha, A.; Kumar, V.; Pradhan, N.; Panda, S.; Morla, S.; Kumar, S.; Manna, D. Diphenylethylenediamine-based potent anionophores: Transmembrane chloride ion transport and apoptosis inducing activities *ACS Appl. Mater. Interfaces* **2018**, 10 (40), 33803−33813.

26. Biswas, O.; Akhtar, N.; Vashi, Y.; Saha, A.; Kumar, V.; Pal, S.; Kumar, S.; Manna, D. Chloride ion transport by PITENINs across the phospholipid bilayers of vesicles and cells *ACS Appl. Bio Mater.* **2020**, 3 (2), 935−944.

27. Akhtar, N.; Pradhan, N.; Barik, G. K.; Chatterjee, S.; Ghosh, S.; Saha, A.; Satpati, P.; Bhattacharyya, A.; Santra, M. K.; Manna, D. Quinine-based semisynthetic ion transporters with potential antiproliferative activities *ACS Appl. Mater. Interfaces* **2020**, 12 (23), 25521−25533.

28. Hong, X.-Q.; Yu, X.-H.; Zhang, K.; Chen, W.-H. Synthesis and properties of a lysosome-targeting fluorescent ionophore based on coumarins and squaramides *Org. Biomol. Chem.* **2018**, 16 (43), 8025−8029.

29. Zhi, H.-T.; Lu, Z.; Chen, L.; Wu, J.-Q.; Li, L.; Hu, J.; Chen, W.-H. Anticancer efficacy triggered by synergistically modulating the homeostasis of anions and iron: Design, synthesis and biological evaluation of dual-functional squaramide-hydroxamic acid conjugates *Bioorg. Chem.* **2024**, 147, 107421.

30. Zhang, S.; Wang, Y.; Xie, W.; Howe, E. N.; Busschaert, N.; Sauvat, A.; Leduc, M.; Gomes-da-Silva, L. C.; Chen, G.; Martins, I. Squaramide-based synthetic chloride transporters activate TFEB but block autophagic flux *Cell Death Dis.* **2019**, 10 (3), 242.

31. Li, X.; Shen, B.; Yao, X.-Q.; Yang, D. A small synthetic molecule forms chloride channels to mediate chloride transport across cell membranes *J. Am. Chem. Soc.* **2007**, 129 (23), 7264−7265.

32. Yu, X.-H.; Hong, X.-Q.; Chen, W.-H. Fluorinated bisbenzimidazoles: A new class of drug-like anion transporters with chloride-mediated, cell apoptosis-inducing activity *Org. Biomol. Chem.* **2019**, 17 (6), 1558−1571.

33. Saha, A.; Akhtar, N.; Kumar, V.; Kumar, S.; Srivastava, H. K.; Kumar, S.; Manna, D. pH-regulated anion transport activities of bis(iminourea) derivatives across the cell and vesicle membrane *Org. Biomol. Chem.* **2019**, 17 (23), 5779−5788.

34. Mondal, A.; Malla, J. A.; Paithankar, H.; Sharma, S.; Chugh, J.; Talukdar, P. A pyridyl-linked benzimidazolyl tautomer facilitates prodigious $H^+/Cl^-$ symport through a cooperative protonation and chloride ion recognition *Org. Lett.* **2021**, 23 (15), 6131−6136.

35. Davis, J. T.; Gale, P. A.; Okunola, O. A.; Prados, P.; Iglesias-Sánchez, J. C.; Torroba, T.; Quesada, R. Using small molecules to facilitate exchange of bicarbonate and chloride anions across liposomal membranes *Nat. Chem.* **2009**, 1 (2), 138−144.

36. Martínez-Crespo, L.; Valkenier, H. Transmembrane transport of bicarbonate by anion receptors *ChemPlusChem* **2022**, 87 (11), e202200266.

37. Wu, X.; Judd, L. W.; Howe, E. N.; Withecombe, A. M.; Soto-Cerrato, V.; Li, H.; Busschaert, N.; Valkenier, H.; Perez-Tomas, R.; Sheppard, D. N. Nonprotonophoric electrogenic $Cl^-$ transport mediated by valinomycin-like carriers *Chem.* **2016**, 1 (1), 127−146.

38. Zhang, Q.; Liang, Q.; Wang, G.; Xie, X.; Cao, Y.; Sheng, N.; Zeng, Z.; Ren, C. Highly selective artificial $K^+$ transporters reverse liver fibrosis in vivo *JACS Au* **2024**, 4 (10), 3869−3883.

39. Shen, F.-F.; Dai, S.-Y.; Wong, N.-K.; Deng, S.; Wong, A. S.-T.; Yang, D. Mediating $K^+/H^+$ transport on organelle membranes to selectively eradicate cancer stem cells with a small molecule *J. Am. Chem. Soc.* **2020**, 142 (24), 10769−10779.

40. Magda, D.; Lecane, P.; Wang, Z.; Hu, W.; Thiemann, P.; Ma, X.; Dranchak, P. K.; Wang, X.; Lynch, V.; Wei, W. Synthesis and anticancer properties of water-soluble zinc ionophores *Cancer Res.* **2008**, 68 (13), 5318−5325.

41. Yamada, K.; Deb, A.; Shoba, V. M.; Lim, D.; Maji, B.; Modell, A. E.; Choudhary, A., Rational design of silicon-based zinc ionophores *Angew. Chem. Int. Ed.* **2022**, 61 (23), e202201698.

42. Dey, S.; Patel, A.; Haloi, N.; Srimayee, S.; Paul, S.; Barik, G. K.; Akhtar, N.; Shaw, D.; Hazarika, G.; Prusty, B. M., Quinoline thiourea-based zinc ionophores with antibacterial activity. *J. Med. Chem.* **2023,** *66* (16), 11078-11093.

43. Wang, J.; Xia, C.; Xia, Z.; Shen, J., Disruption of zinc homeostasis reverses tigecycline resistance in Klebsiella pneumoniae. *Front. Cell. Infect. Microbiol.* **2025,** *15*, 1458945.

44. Dabbagh-Bazarbachi, H.; Clergeaud, G.; Quesada, I. M.; Ortiz, M.; O'Sullivan, C. K.; Fernández-Larrea, J. B., Zinc ionophore activity of quercetin and epigallocatechin-gallate: from Hepa 1-6 cells to a liposome model. *J. Agric. Food Chem.* **2014,** *62* (32), 8085-8093.

45. Guo, Z.; Chen, D.; Yao, L.; Sun, Y.; Li, D.; Le, J.; Dian, Y.; Zeng, F.; Chen, X.; Deng, G., The molecular mechanism and therapeutic landscape of copper and cuproptosis in cancer *Signal Transduct. Target. Ther.* **2025**, 10 (1), 149.

46. Saha, P.; Kumari Agarwala, P.; Dadhich, R.; Adhyapak, P.; Kapoor, S.; Madhavan, N., Ligand induced $Cu^{II}$ transport restricts cancer and mycobacterial growth: Towards a plug-and-select ion channel scaffold *ChemBioChem* **2021**, 22 (8), 1424-1429.

47. Pain, P. K.; Palit, D.; Shegane, M.; Singh, R. P.; Manna, D., Optochemical control of Cu(I) homeostasis in mammalian cells *Chem. Commun.* **2023**, 59 (16), 2315-2318.

48. Fikes, A. G.; Aggarwal, K.; Que, E. L., Glutathione-mediated activation of a disulfide containing $Fe^{3+}$ complex *Inorg. Chim. Acta.* **2019**, 490, 139-143.

49. Simms, B. A.; Zamponi, G. W., Neuronal voltage-gated calcium channels: structure, function, and dysfunction. *Neuron* **2014,** *82* (1), 24-45.

50. Wasserman, R.; Fullmer, C., Calcium transport proteins, calcium absorption, and vitamin D. *Annu. Rev. Physiol.* **1983,** *45* (1), 375-390.

51. Saha, P.; Basak, D.; Biswas, S.; More, P. A.; Madhavan, N., Small peptidic ionophore for calcium transport. *Bioconjugate Chemistry* **2022,** *33* (11), 2143-2148.

52. Li, X.; Shen, B.; Yao, X.-Q.; Yang, D., Synthetic chloride channel regulates cell membrane potentials and voltage-gated calcium channels *J. Am. Chem. Soc.* **2009**, 131 (38), 13676-13680.

53. Huang, W. L.; Wang, X. D.; Ao, Y. F.; Wang, Q. Q.; Wang, D. X., An artificial single molecular channel showing high chloride transport selectivity and pH-responsive conductance *Angew. Chem. Int. Ed.* **2023**, 62 (23), e202302198.

54. Das, S.; Karn, R.; Kumar, M.; Srimayee, S.; Manna, D., A chloride-responsive molecular switch: driving ion transport and empowering antibacterial properties. *Org. Biomol. Chem.* **2024,** *22* (1), 114-119.

55. Bickerton, L. E.; Langton, M. J., Controlling transmembrane ion transport via photo-regulated carrier mobility. *Chem. Sci.* **2022,** *13* (33), 9531-9536.

56. Chao, X.; Johnson, T. G.; Temian, M.-C.; Docker, A.; Wallabregue, A. L.; Scott, A.; Conway, S. J.; Langton, M. J., Coupling Photoresponsive Transmembrane Ion Transport with Transition Metal Catalysis. *J. Am. Chem. Soc.* **2024,** *146* (7), 4351-4356.

57. Ahmad, M.; Flerin, M.; Tay, H. M.; Thompson, A. L.; Duarte, F.; Langton, M. J., Stimuli-responsive anion transport utilising caged hydrazone-based anionophores. *Nanoscale* **2024,** *16* (46), 21545-21553.

58. Kar, M. K.; Mahata, R.; Srimayee, S.; Haloi, N.; Kumar, R.; Lindahl, E.; Santra, M. K.; Manna, D. β-Carboline-Based Light and pH Dual Stimuli-Responsive Ion Transporters Induce Cancer Cell Death. *Chem. Commun.* **2024**, *60* (64), 8419−8422.

59. Yang, J.; Johnson, C. H., Bioluminescent sensors for Ca++ flux imaging and the introduction of a new intensity-based Ca++ sensor. *Front. Bioeng. Biotechnol.* **2021,** *9*, 773353.

60. Colee, C. M.; Oberlag, N. M.; Simon, M.; Chapman, O. S.; Flanagan, L. C.; Reid-McLaughlin, E. S.; Gewing-Mullins, J. A.; Maiche, S.; Patel, D. F.; Cavalcanti, A. R., Discovery of red-shifting mutations in firefly luciferase using high-throughput biochemistry. *Biochemistry* **2024,** *63* (6), 733-742.

61. Bernitzki, K.; Schrader, T. Entirely Artificial Signal Transduction with a Primary Messenger. *Angew. Chem., Int. Ed.* **2009**, *48* (43), 8001−8005.

62. Bickerton, L. E.; Johnson, T. G.; Kerckhoffs, A.; Langton, M. J. Supramolecular Chemistry in Lipid Bilayer Membranes. *Chem. Sci.* **2021**, *12* (34), 11252−11274.

63. Langton, M. J.; Keymeulen, F.; Ciaccia, M.; Williams, N. H.; Hunter, C. A. Controlled Membrane Translocation Provides a Mechanism for Signal Transduction and Amplification. *Nat. Chem.* **2017**, *9* (5), 426−430.

64. Ding, Y.; Williams, N. H.; Hunter, C. A. A Synthetic Vesicle-to-Vesicle Communication System. *J. Am. Chem. Soc.* **2019**, *141* (44), 17847−17853.

65. Langton, M. J.; Williams, N. H.; Hunter, C. A. Recognition-Controlled Membrane Translocation for Signal Transduction across Lipid Bilayers. *J. Am. Chem. Soc.* **2017**, *139* (18), 6461−6466.

66. Gartland, S. A.; Johnson, T. G.; Walkley, E.; Langton, M. J. Inter-Vesicle Signal Transduction Using a Photo-Responsive Zinc Ionophore. *Angew. Chem., Int. Ed.* **2023**, *62* (38), e202309080.

67. Bickerton, L. E.; Sterling, A. J.; Beer, P. D.; Duarte, F.; Langton, M. J. Transmembrane Anion Transport Mediated by Halogen Bonding and Hydrogen Bonding Triazole Anionophores. *Chem. Sci.* **2020**, *11* (18), 4722−4729.

68. Cossu, C.; Fiore, M.; Baroni, D.; Capurro, V.; Caci, E.; Garcia-Valverde, M.; Quesada, R.; Moran, O. Anion-Transport Mechanism of a Triazole-Bearing Derivative of Prodigiosine: A Candidate for Cystic Fibrosis Therapy. *Front. Pharmacol.* **2018**, *9*, 852.

69. Busschaert, N.; Kirby, I. L.; Young, S.; Coles, S. J.; Horton, P. N.; Light, M. E.; Gale, P. A. Squaramides as Potent Transmembrane Anion Transporters. *Angew. Chem., Int. Ed.* **2012**, *51* (18), 4426−4430.

70. Marques, I.; Costa, P. M. R.; Miranda, M. Q.; Busschaert, N.; Howe, E. N. W.; Clarke, H. J.; Haynes, C. J. E.; Kirby, I. L.; Rodilla, A. M.; Pérez-Tomás, R.; Gale, P. A.; Matile, S. Full Elucidation of the Transmembrane Anion Transport Mechanism of Squaramides Using *In Silico* Investigations. *Phys. Chem. Chem. Phys.* **2018**, *20* (32), 20796−20811.

71. Patra, A. K.; Srimayee, S.; Halder, D.; Roy, A.; Mukherjee, S.; Kundu, S.; Hossain, M.; Saha, R.; Lee, C.-H.; Manna, D. Transmembrane Fluoride Anion Transport by meso-3,5-Bis(trifluoromethyl)phenyl Picket Calix[4]pyrrole. *Chem. Commun.* **2023**, *59* (48), 7407−7410.

72. Singh, A.; Torres-Huerta, A.; Vanderlinden, T.; Renier, N.; Martínez-Crespo, L.; Tumanov, N.; Wouters, J.; Bartik, K.; Jabin, I.; Valkenier, H. Calix[6]arenes with Halogen Bond Donor Groups as Selective and Efficient Anion Transporters. *Chem. Commun.* **2022**, *58* (42), 6255−6258.

73. Cater, M. A.; Pearson, H. B.; Wolyniec, K.; Klaver, P.; Bilandzic, M.; Paterson, B. M.; Bush, A. I.; Humbert, P. O.; La Fontaine, S.; Donnelly, P. S. Increasing Intracellular

Bioavailable Copper Selectively Targets Prostate Cancer Cells. *ACS Chem. Biol.* **2013**, 8 (7), 1621−1631. DOI: 10.1021/cb4002403.

74. Tardito, S.; Bassanetti, I.; Bignardi, C.; Elviri, L.; Tegoni, M.; Mucchino, C.; Bussolati, O.; Franchi-Gazzola, R.; Marchiò, L. Copper Binding Agents Acting as Copper Ionophores Lead to Caspase Inhibition and Paraptotic Cell Death in Human Cancer Cells. *J. Am. Chem. Soc.* **2011**, *133* (16), 6235−6242.

75. Saha, P.; Kumari Agarwala, P.; Dadhich, R.; Adhyapak, P.; Kapoor, S.; Madhavan, N. Ligand Induced $Cu^{II}$ Transport Restricts Cancer and Mycobacterial Growth: Towards a Plug-and-Select Ion Channel Scaffold. *ChemBioChem* **2021**, *22* (8), 1424−1429.

76. Prusty, B. M.; Srimayee, S.; Karn, R.; Haloi, N.; Singh, S. K.; Winterhalter, M.; Manna, D. Supramolecular Nanochannels: Suprasome-Mediated Delivery of Ionophore to Regulate Transmembrane $Zn^{2+}$ Ion Transport. *Chem. Eur. J.* **2025**, *31* (31), e202501013.

77. Zhao, Z.; Tang, B.; Yan, X.; Wu, X.; Li, Z.; Gale, P. A.; Jiang, Y.-B. Crown Ether-Thiourea Conjugates as Ion Transporters. *Front. Chem. Sci. Eng.* **2022**, *16* (1), 81−91.

78. Chattopadhyay, S.; Ghosh, A.; Kumar Mukhopadhyay, T.; Sharma, R.; Datta, A.; Talukdar, P. Supramolecular Barrel-Rosette Ion Channel Based on 3,5-Diaminobenzoic Acid for Cation-Anion Symport. *Angew. Chem., Int. Ed.* **2023**, *62* (46), e202313712.

# *Chapter 2*

## *Development of Stimuli-responsive release of active anionophore from RGD-peptide-linked proanionophore*

## 2.1 Background and objective of current work:

According to our literature survey in the previous chapter on synthetic bioactive anionophores exhibit significant therapeutic potential across a range of pathological conditions. It is well established that the controlled transport of ions such as $Na^+$, $K^+$, $Ca^{2+}$, and $Cl^-$ , which are present in abundance (~ 10-100 mM), is essential for maintaining ion and pH homeostasis. These ions are fundamental for regulating intracellular signalling, cell proliferation, and other vital physiological functions. Among them, chloride is one of the most abundant anions under physiological conditions, and its selective transmembrane conductance (typically within a 30–60 mV potential gradient in eukaryotic membranes) is crucial for biological activities like blood pressure regulation, chloride reabsorption, electrolyte balance, and neuronal signalling. Often due to genetic mutations in chloride channel proteins, dysfunction in $Cl^-$ homeostasis is linked to several disorders, including Bartter's syndrome, epilepsy, cystic fibrosis, and cancer. In order to overcome these challenges, researchers have developed synthetic anion transporters as a promising alternative to restore ion flux, offering new possibilities for therapeutic intervention in conditions caused by defective natural chloride ion channels.[1, 2]

In recent years, a variety of synthetic $Cl^-$ ion transporters have emerged, enhancing three key features: water solubility, ion transport efficiency, and responsiveness to specific stimuli. Several reported examples of molecules, such as sulfonium salts, Au(III)-imidazole complexes, and nitrobenzene sulfonyl derivatives, exhibit potent GSH-responsive $Cl^-$ transport, offering a promising strategy for inducing cancer cell death. These systems exploit the elevated intracellular glutathione concentrations found in cancer cells to trigger ionophore activation. However, many still suffer from a lack of selectivity, often harming healthy cells due to their limited targeting capability. [3-5]

To address this, researchers are exploring "targeted proionophore" designs that remain inactive during circulation but are activated specifically within cancerous environments. For example, GSH-cleavable protecting groups or acid-sensitive linkers have been employed to mask active ionophores until they reach tumor sites. Such stimulus-triggered delivery can promote $Cl^-$ imbalance in malignant cells, triggering apoptosis while minimizing off-target toxicity. This modular approach opens up exciting opportunities for more selective and safer therapeutic agents based on synthetic ion transporters. Earlier, Manna and co-workers reported a GSH-based pro-ionophore where 10 mM GSH efficiently cleaved the sulfonium moiety of the

proanionophore, regenerating the active thiourea-based anionophore and enhancing $Cl^-$ transport by over 80% in lipid bilayers. Cellular assays confirmed successful uptake of the ionophore and minimal cytotoxicity, which validates GSH as an effective biomarker for targeted ionophore activation.[3] Talukdar and his colleagues highlighted the development of a GSH-responsive proionophore that generates a potent synthetic ion channel capable of $M^+/Cl^-$ symport upon intracellular trigger. The activated ionophore transports ions and disrupts redox balance and mitochondrial integrity, initiating caspase-dependent apoptosis, thereby demonstrating the therapeutic promise of redox-activated ion transporters for targeting cancer cells.[4] Later on, Gale et al. developed Au(III)-based switchable anion transporters, which, upon intracellular GSH activation, showed slow release of bis-imidazole-based carriers for $Cl^-$ and $NO_3^-$ transport. GSH-mediated reduction of Au(III) results in efficient anion transport across the bilayer and selective inhibition of cancer cell lines through localised activation.[5] In this work, we demonstrated the design and synthesis of GSH-responsive RGD peptide-linked thiourea derivatives of 1,3-phenylenedimethanamine. Thiourea-functionalized 1,3-phenylenediamine scaffold was conjugated to an RGD peptide via a GSH-cleavable disulfide and carbonate linker. The RGD moiety enables integrin receptor-mediated uptake into cancer cells, where elevated intracellular GSH triggers linker cleavage, releasing the active ionophore. The regenerated thiourea-based compound is designed to recognize and transport $Cl^-$ ions across membranes, promoting selective inhibition in cancer cells. The carbonate linker acts as a ROS-sensitive species, enabling more controlled spatiotemporal release at the site. A thorough investigation was conducted using fluorescence and HPLC to assess anionophore activation by a proionophore in the presence of 10 mM GSH in PBS buffer. Also, the selective cytotoxicity of the proionophore towards tumor cells (A375) over normal cells (HEK293T) was studied in vitro.

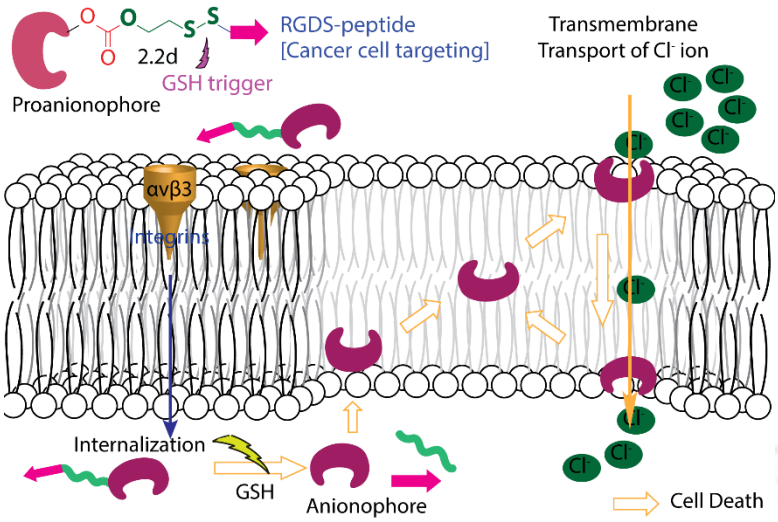


**Figure 2.1.** Schematic representation of pro-ionophore to ionophore release causing apoptotic cell death.

## 2.2 Results and discussion:

### 2.2.1 Synthesis of ionophore and pro-ionophore:

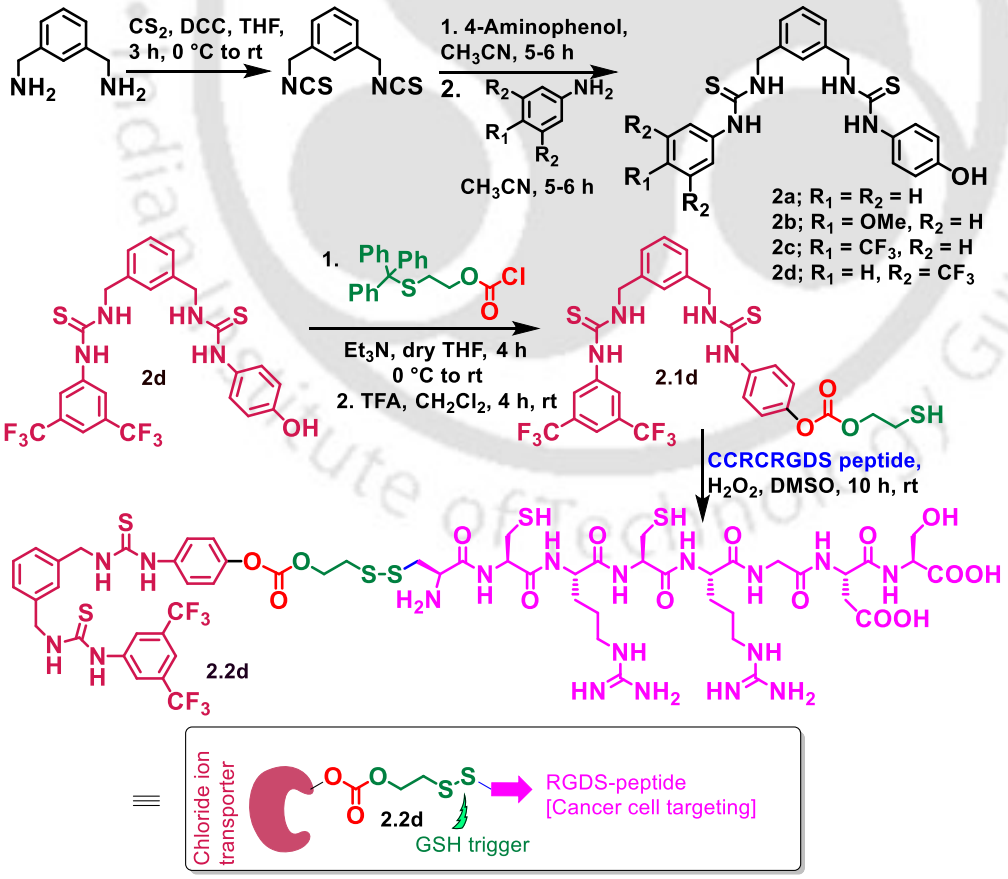


**Scheme 2.1.** Synthetic route of anionophore and proionophore.

The ionophores were synthesized from 1,3-bis(isothiocyanatomethyl)benzene, which was prepared from 1,3-phenylenedimethanamine following a literature protocol.[3] The reaction of 1,3-bis(isothiocyanatomethyl)benzene with 4-amino phenol led to the formation of a mono-thiourea derivative, which, upon further reaction with the substituted arylamines, resulted in the desired ionophores, **2a-d**. To append the GSH-responsive RGD-linker to the anionophore, first, 2-(tritylthio) ethyl carbonochloridate was synthesized from 2-mercaptoethanol. Reaction of compound **2d** with 2-(tritylthio)ethyl carbonochloridate yielded a carbonate-linked product. Finally, the coupling of carbonate-linked anionophore with CCRCRGDS (or RGD)-peptide via disulfide linkage provided the desired proionophore **2.2d** in moderate yield. There are three cysteine residues, but only one ionophore could be attached to the CCRCRGDS peptide, possibly due to the formation of a precipitate of proionophore **2.2d** under the reaction conditions.

### 2.2.2 Transport studies of Ionophore:

The transmembrane transport efficacy of these compounds was investigated using a model membrane of large unilamellar vesicles (LUVs). The LUVs were prepared from egg-yolk phosphatidylcholine (EYPC) and cholesterol (CHOL) (8:2 molar ratios) by encapsulating bis-N-methyl acridinium nitrate (lucigenin) in 20 mM HEPES buffer, 100 mM $NaNO_3$, pH 7.2. The LUVs were dispersed in 20 mM HEPES buffer, 100 mM NaCl, pH 7.2. The fluorescence kinetics measurement was initiated upon addition of the compound (Figure 2.2A). The reduction in lucigenin fluorescence intensity upon addition of the compounds indicated $Cl^-$ transport. The initial screening revealed that compound **2d**, with a di-trifluoromethyl-substituted aryl moiety, had the highest $Cl^-$ transport activity among the tested compounds, including the proionophore **2.2d** (Figure 2.2B and 2.9). The fluorescence concentration-dependent study (EYPC/CHOL-LUVs⊃lucigenin) showed that compound **2d** ($EC_{50}$ = 4.15 ± 0.81 μM or 0.01 mol% with respect to lipid) had moderated $Cl^-$ transport activity (Figure 2.2 C and 2.10A). The calculated Hill coefficient (n) of 0.78 indicates that a single molecule could form the active transport complex. The transport of $Cl^-$ by compound **2d** was also investigated by the chloride-ion selective electrode (Cl-ISE)-based assay. The time-dependent increase in the extent of the efflux confirmed the $Cl^-$ transport properties of compound **2d** (Figure 2.2 D and 2.10 B). The Cl-ISE-based concentration-dependent study showed that compound **2d** ($EC'_{50}$ = 5.24 ± 1.29 μM or 0.02 mol% with respect to lipid; n′ = 0.82) also had moderated $Cl^-$ transport activity. The confocal microscopic images of the time-dependent lucigenin

fluorescence quenching assay of giant unilamellar vesicles (GUV) after treatments also proved $Cl^-$ transport properties of compound **2d** (Figure 2.18).

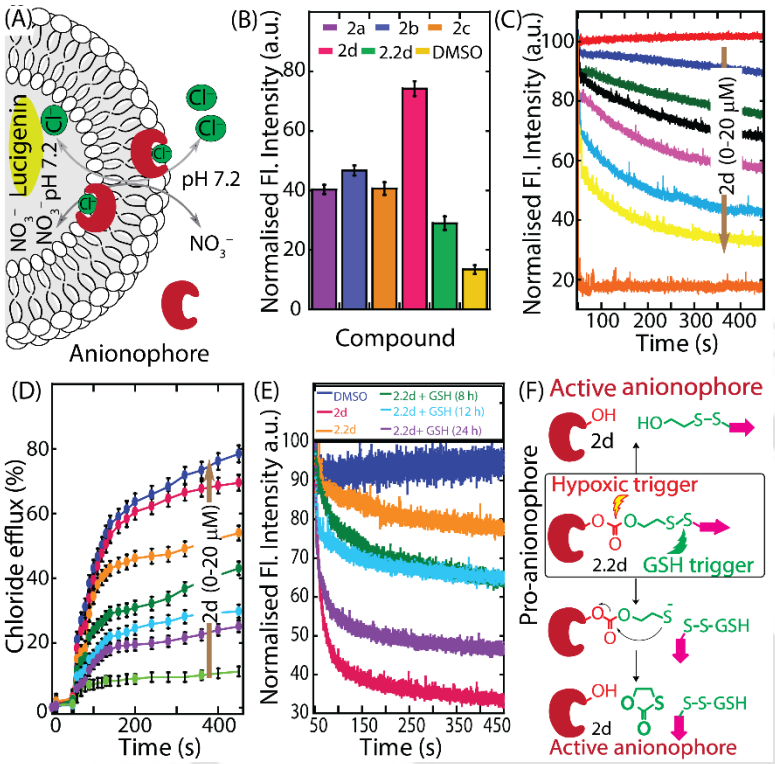


**Figure 2.2.** Schematic representation of the lucigenin assay for $Cl^-$ transport (A). Comparative $Cl^-$ transport activities of the compounds (B). Concentration-dependent $Cl^-$ transport activities of compound **2d** across the lipid bilayers of EYPC/CHOL-LUVs⊃lucigenin (C). The extent of $Cl^-$ efflux ability of compound **2d** across the EYPC/CHOL-LUV (D). The $Cl^-$ transport property of proionophore **2.2d** upon GSH (10 mM) treatment was studied through the lucigenin-based fluorescence method (E). Schematic representation of the GSH-mediated regeneration of active ionophore from its proionophore (F).

### 2.2.3 Ion binding studies of ionophore:

Inspired by the $Cl^-$ transport activity, we assessed the $Cl^-$ recognition mode of compound **2d** by $^1H$ NMR titration and UV based titration against tetrabutylammonium chloride (TBACl) concentrations in DMSO-$d_6$. The $^1H$ NMR titration data confirmed downfield shifts of the thiourea N-H (Ha, Hb, Hc, and Hd) protons, indicating their interaction with $Cl^-$. The analysis in the bindfit program v0.5 shows changes in the chemical shifts of the N-H protons with varying concentrations of TBACl.

It confirmed the host-guest stoichiometry of 1:1 with a binding constant of 14.63 $M^{-1}$ ± 5.98% (Figure 2.3 A and B). Together, these results support the $Cl^-$ recognition and transport properties of **2d**. The UV Vis titration studies were performed in 1:1 DMSO:$H_2O$ condition which also confirmed the host guest stoichiometry of 1:1 with a binding constant of 8957.67 $M^{-1}$± 9.56% (Figure 2.3 C and D).

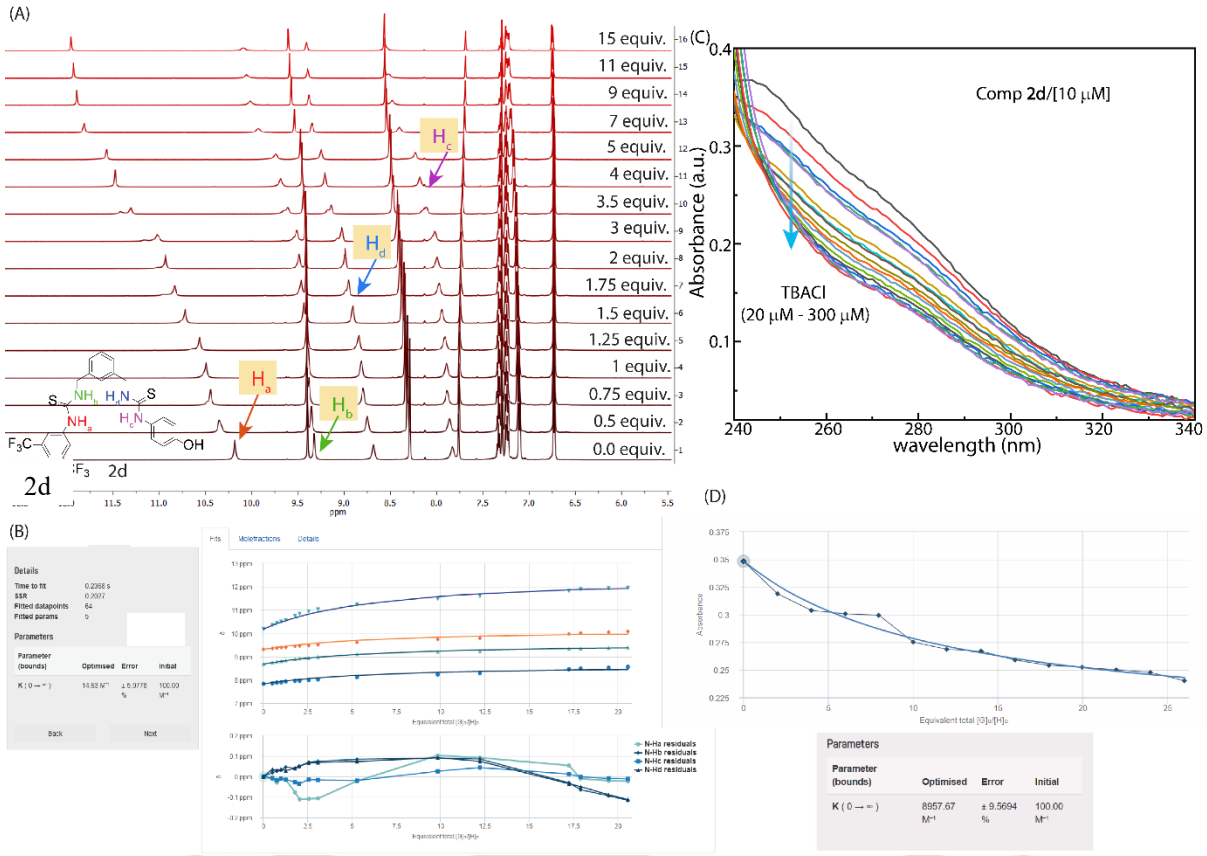


**Figure 2.3.** $^1$H NMR binding study of compound **2d** with TBACl in DMSO-$d_6$.

### 2.2.4 Ion selectivity studies of ionophore:

The cation selectivity studies were performed with EYPC/CHOL-LUV⊃HPTS (prepared in 20 mM HEPES buffer, 100 mM NaCl, pH 7.2) dispersed in 100 mM of MCl salt ($M^+$ = $Li^+$, $Na^+$, $K^+$, $Rb^+$, and $Cs^+$) in 20 mM HEPES buffer, pH 7.2 (Figure 2.13 A). The cation selectivity studies with EYPC/CHOL-LUVs⊃lucigenin (prepared in 20 mM HEPES buffer, 100 mM $NaNO_3$, pH 7.2) were also performed (Figure 2.4C and 2.4D). Both experiments suggest insignificant involvement of $M^+/Cl^-$ (and $M^+/OH^-$) in the transport process.[6] The anion selectivity studies were performed with EYPC/CHOL-LUV⊃HPTS (prepared in 20 mM HEPES buffer, 100 mM NaCl, pH 7.2) dispersed in an isotonic solution of $Na_xA_y$ ($Na_xA_y$ = NaCl, NaBr, NaI, $NaNO_3$, and $Na_2SO_4$) in 20 mM HEPES buffer, pH 7.2. The study showed

acidification of the intravesicular medium, suggesting $H^+/X^-$ influx.[7] (Figure 2.13 C). Meanwhile, the use of highly hydrophilic $SO_4^{2-}$ in an extravesicular medium showed increased HPTS fluorescence intensity, confirming $H^+/X^-$ co-influx.[8] Further ion selectivity studies with pH gradient (intravesicular solution of 20 mM HEPES buffer, 100 mM NaCl, pH 7.2 and extravesicular solution of 20 mM HEPES buffer, 100 mM NaX, pH 8.0; where $X^- = Cl^-, NO_3^-, I^-, F^-, Br^-$) suggested highest selectivity for $Cl^-$ over other anions (Figure 2.4 A and B). Hence, $Cl^-/H^+$ is the primary transport process of **2d**.

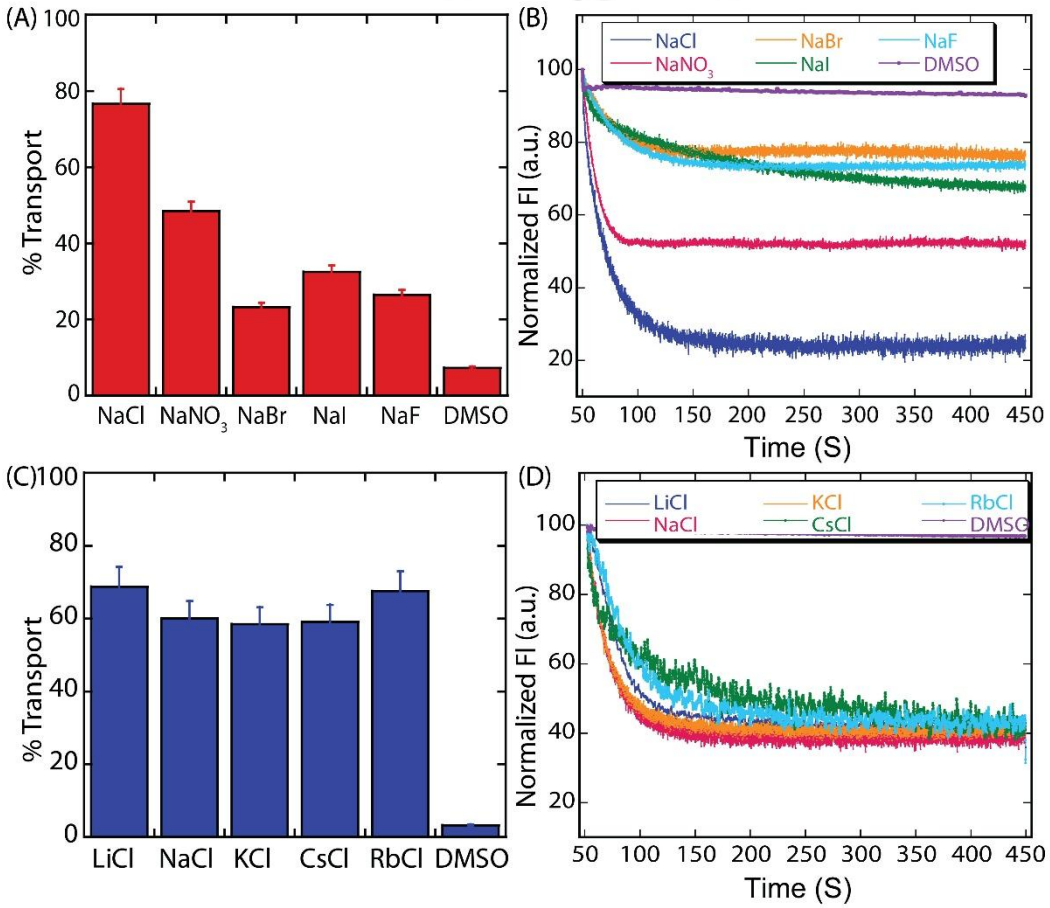


**Figure 2.4.** (A), (C) Bar plot and (B), (D) spectral representation of anion selectivity and cation selectivity studies, respectively, of compound **2d** in EYPC/CHOL-LUVs⊃lucigenin.

### 2.2.5 Transport mechanism of ionophore:

Lucigenin-based transport studies in the presence and absence of carbonyl cyanide-p-trifluoromethoxy phenylhydrazone (FCCP, $H^+$ carrier) showed no significant change in the transport activity of **2d**, suggesting the involvement of $H^+$ during the transport process (Figure 2.5 A).[9] In addition, no substantial alteration in the transport activity of compound **2d** in the absence and presence of valinomycin ($K^+$ carrier) suggests preferential transport of $Cl^-$ over

$OH^-$ (Figure 2.5 B and 2.14). Hence, compound **2d** follows the $H^+/Cl^-$ symport instead of the $Cl^-/OH^-$ antiport process. The presence of a phenolic moiety would be a source of $H^+$ during transport.

To probe the mode of $Cl^-$ transportation by compound **2d**, a temperature-dependent transport activity was performed using the model lipid bilayers of DPPC (DPPC-LUV⊃lucigenin) (Figure 2.15). A sharp increase in the $Cl^-$ transport rate with temperature-dependent membrane fluidity suggests that carrier-mediated $Cl^-$ transport could be the operating pathway. In addition, the classical U-tube assay was performed to investigate whether compound **2d** forms a self-assembled channel or acts as an anion carrier (Figure 2.5 C). An increase in the extent of Cl− efflux in the right arm of the U-tube (as measured by the Cl-ISE) across the CHCl3 layer directly confirmed the Cl− transport mechanism in compound **2d** via the mobile-carrier mechanism. A steady decrease in the pH in the right arm of the U-tube (as measured by the pH meter) confirmed the $H^+/Cl^-$ transport mechanism. The involvement of $H^+$ during the transport of $Cl^-$ prompted us to investigate the pH-dependent $Cl^-$ transport properties of compound **2d**. Meanwhile, the carboxyfluorescein-based leakage assay showed no pore, channel formation, or other deformation of the LUVs during the measurements (Figure 2.16).

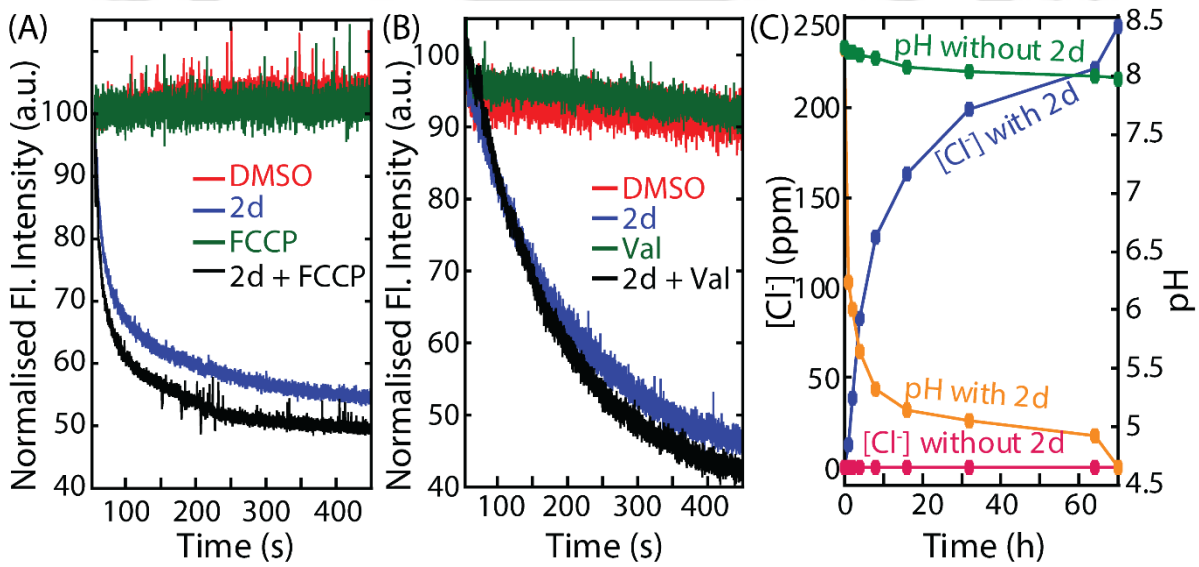


**Figure 2.5.** (A) Assessment of $Cl^-$ transport properties of **2d** in the absence and presence of FCCP. (B) Investigation of the $Cl^-$ transport activities of **2d** in the absence and presence of valinomycin (Val). (C) Measure of $H^+$ and $Cl^-$ transport efficacy of **2d** (2 mM) across the U-tube, using chloride-ISE and pH meter.

### 2.2.6 Regeneration of ionophore from pro-ionophore:

The intracellular GSH concentration (1-10 mM) is about 1000 times higher than the extracellular concentration (2-20 μM) in cancer cells. Hence, before performing the cellular assay, an in vitro assay was conducted to determine whether GSH-mediated cleavage of proionophore **2.2d** could regenerate the active ionophore **2d**. In this assay, for 10 μM proionophore, 10 mM GSH was used to release the active ion transporter. This additional GSH was used to accelerate the reduction procedure and to obtain detectable signals for better analysis. The addition of GSH to the proionophore **2.2d** showed an efficient transmembrane transport of $Cl^-$, which is comparable to that observed for **2d** (Figure 2.6 C). These results suggest the GSH-mediated cleavage of the disulfide linker followed by the carbonate moiety to regenerate the active ionophore **2d** from proionophore **2.2d** (Figure 2.6 C). HPLC traces of proionophore **2.2d** in the presence and absence of GSH showed the regeneration of the active ionophore **2d** (Figure 2.6 A and B). The HRMS analysis also confirmed the in situ generation of the active ionophore from the proionophore (Figures 2.11 and 2.12).

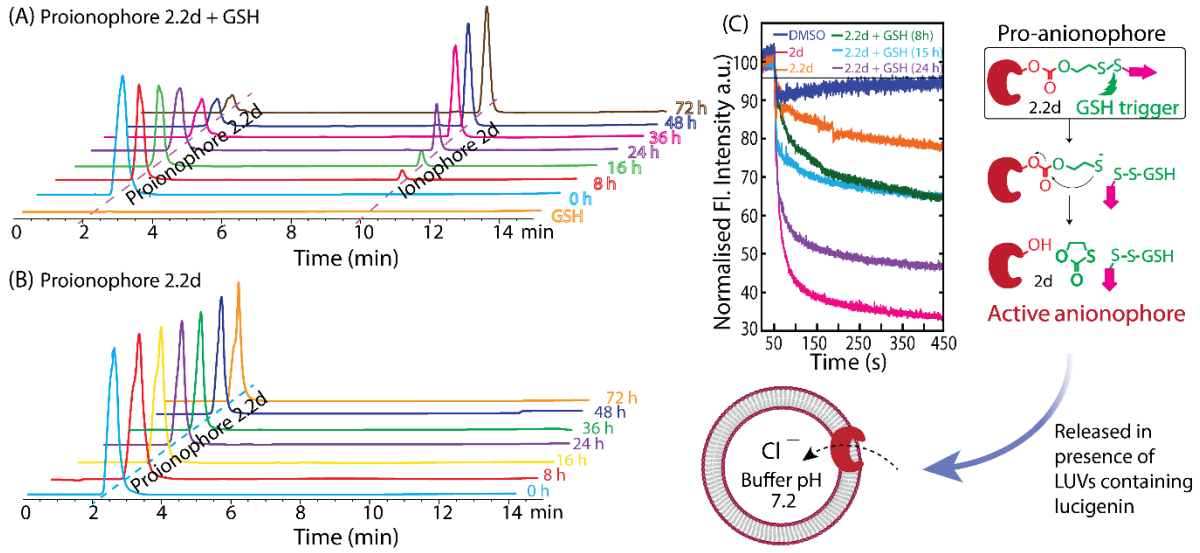


**Figure 2.6.** (A) Pro-ionophore to ionophore **2d** release study in HPLC post-GSH treatment for 72 h. (B) Stability checking of the pro-ionophore for 72 h. (C) Fluorescence-based spectral study of released ionophore **2d** in EYPC/CHOL-LUV⊃lucigenin and schematic representation of the process.

### 2.2.7 In-vitro studies of ionophore in cellular environment:

We performed cell viability experiments to investigate whether compound **2d** has an antiproliferative effect on the model cancer cells (A375; melanoma; procured from ATCC, USA) and normal cells (HEK293T kidney epithelial; procured from NCCS, Pune, India). A

similar pattern of dose-dependent reduction in the viability of A375 ($IC_{50}$ = 19.9 ± 4.05 μM) and HEK293T (IC50 = 21.0 ± 1.68 μM) cells was observed upon treatment with compound **2d** (Figure 2.7A), indicating its non-specificity towards mammalian cells. Among the tested compounds, **2d** showed higher cytotoxicity against A375 cells (Figure 2.19). The intracellular environment of cancer cells is also known to be more acidic than their extracellular environment.[10] Therefore, ionophore-assisted transport of $H^+/Cl^-$ across the membrane could be one of the reasons for the reduced viability of A375 cells. Additional cell viability analysis in the absence of chloride–containing and chloride-free HBSS buffers containing 10% FBS was performed using A375 cells.[11] (Figure 2.7 D) The MTT results demonstrated that the enhanced uptake of $Cl^-$ to the intracellular environment could be one of the reasons for the cytotoxicity of **2d**. We hypothesize that the proionophore **2.2d** could have more cancer cell-specific effects due to the preferential RGD-peptide-mediated internalization and subsequent regeneration of the active ionophore (Figure 2.7 B and C). Interestingly, our cell viability assay results clearly showed that proionophore **2.2d** has greater cytotoxicity against A375 cancer cells ($IC_{50}$ = 28.21 ± 1.73 μM) than against HEK293T cells ($IC_{50}$ = 38.43 ± 2.57 μM) in 10% FBS-supplemented DMEM. However, cancer cells modulate their intracellular metabolism to survive chemotherapeutic insults. The cancer cells also utilize ROS-induced mechanisms to promote metastasis and acquire drug resistance within the tumor microenvironment, thereby distinguishing them from their surrounding stromal cells.[12]

Hence, we used the serum starvation condition, which is a widely used method to induce ROS.[12] Interestingly, proionophore **2.2d** showed a significantly increased antiproliferative effect on A375 cells in a serum starvation condition (1% FBS), where the $IC_{50}$ value was 12.30 ± 2.33 μM. However, the $IC_{50}$ of proionophore **2.2d** in HEK293T cells was around 35.80 ± 3.05 μM. This difference (3-fold) in the cell viability of proionophore **2.2d** among A375 and HEK293T cells could also be due to a higher abundance of ROS in cancer cells, which might also induce the cleavage of the carbonate linker. We also prepared a control proanionophore **2.3**, which contains both disulfide and carbonate linkers but lacks the targeting RGD peptide. The HPLC assay showed its active anionophore regeneration capability. (Figure 2.22) The MTT assay showed that the control proanionophore **2.3** exhibited increased antiproliferative activity in HEK293T cells compared to A375 cancer cells. The cancer cell specificity of proionophore **2.2d** could also depend on various other factors, including (1) selection of suitable cancer cell line models, (2) strength of interaction of the selected RGD-peptide with the surface-exposed $\alpha_v\beta_3$ integrin protein, (3) flexibility of RGD-peptide-linker, and (4)

abundance of GSH and ROS concentrations. Further investigation of these parameters could improve the efficacy of such stimuli-responsive targeted-proionophore strategy. Overall, the above results suggest that proionophore **2.2d** has a more cancer-cell-specific effect, which could be due to its preferential RGD-peptide-mediated internalization and subsequent regeneration (owing to higher GSH and ROS levels in cancer cells) of the active ionophore **2d**.

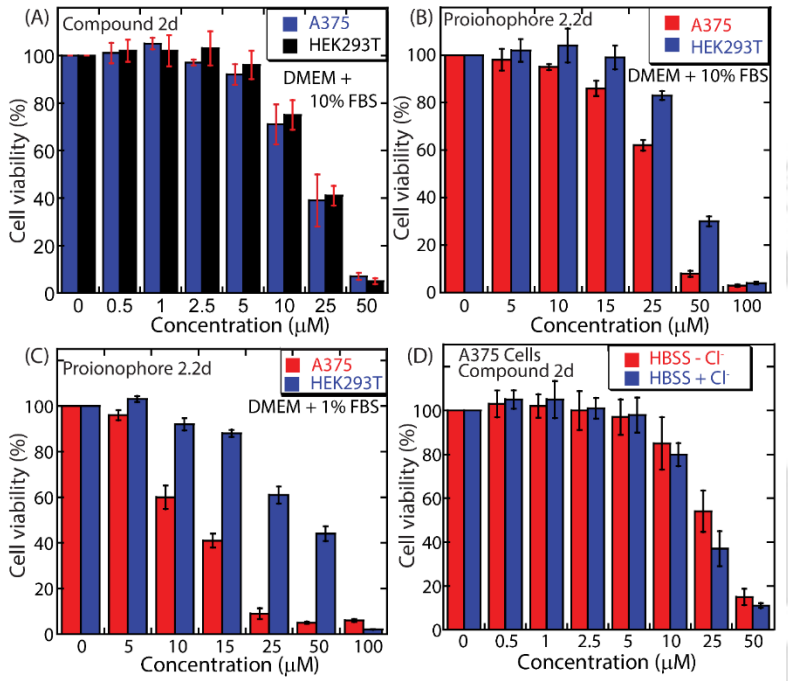


**Figure 2.7.** (A)The viability of **2d** in A375 and HEK293T cell lines. (B)Viability of A375 and HEK293T cells treated (24 h) with different concentrations of proionophore **2.2d** in the presence of 10% FBS. (C)Viability of A375 cells in DMEM containing 10% FBS or 1% FBS. (D) Viability of A375 cells in HBSS buffer with or without $Cl^-$ at different concentrations of compound **2d**.

### 2.3 Summary:

In this study, the bis-thiourea-based ion transporter was designed and synthesized for anion transport and modified as a proanionophore, incorporating a glutathione (GSH)-responsive disulfide linker and a tumor-targeting RGD peptide motif. The appended RGD peptide facilitates selective internalization into cancer cells via $\alpha_v\beta_3$ integrin-mediated endocytosis, a process that is highly active in malignant cells. Once inside the reductive intracellular environment of cancer cells, the higher GSH concentration cleaves the disulfide linker, releasing the active thiourea-based ionophore. The released ion carrier efficiently transports $Cl^-$ ion with $H^+/Cl^-$ symport mechanism across lipid membranes, disrupting ionic homeostasis

and triggering apoptosis selectively in cancer cells. The system demonstrated significantly greater cytotoxicity against A375 melanoma cells than against noncancerous HEK293T cells, supporting its targeted action. The transport ability was further confirmed through liposome-based assays (utilising lucigenin dye) and cell viability studies, validating the symport mechanism and GSH-triggered activation. This approach highlights the therapeutic promise of stimuli-responsive, tumor-targeting proionophore, enabling spatiotemporal control over ion transport activity.

## 2.4 Experimental section:

### 2.4.1 General information:

All chemical reactions were performed under an inert atmosphere. All reagents and solvents for synthesis were purchased from commercial sources (Sigma-Aldrich, TCI) and used without further purification. The column chromatography was carried out using silica (100−200 mesh size). The thin-layer chromatography was performed on silica gel 60−F254 plates. Egg yolk phosphatidylcholine (EYPC) as a solution of chloroform (25 mg/ mL), mini extruder, and polycarbonate membranes of 100 nm and 200 nm were purchased from Avanti Polar Lipid. Cholesterol, HEPES, HPTS, lucigenin, Triton X-100, valinomycin, DMSO, and all inorganic salts were obtained as molecular biology-grade from Sigma-Aldrich. The $^{1}H$ NMR spectra were recorded at 500 MHz, whereas the $^{13}C$ NMR spectra were recorded at 500 MHz. The residual solvent signals were considered as an internal reference ($^{1}H$ NMR $CDCl_3$: $\delta_{ppm}$ 7.26 ppm; $^{13}C$ NMR $CDCl_3$: $\delta_{ppm}$ 77.2 ppm; $^{1}H$ NMR DMSO-$d_6$: $\delta_{ppm}$ 2.54 ppm; $^{13}C$ NMR DMSO-$d_6$: $\delta_{ppm}$ 39.5 ppm) to calibrate spectra. The chemical shifts were reported in ppm. The following abbreviations were used to indicate multiplicity patterns m: multiplet, s: singlet, d: doublet, t: triplet, q: quartet, dd: doublet of doublet, ddd: doublet of doublet of doublet, td: triplet of doublet, dt: doublet of triplet. Coupling constants were measured in Hz. High−resolution mass spectra (HRMS) were recorded on electrospray ionization time−of−flight (ESI−TOF). Fluorescence experiments were recorded on Fluoromax−4 from HORIBA equipped with an injector port and magnetic stirrer in a micro fluorescence cuvette. All buffer solutions were prepared from autoclaved water. The pH of buffer solutions was adjusted using the Helmer pH meter. The extravesicular dye was removed by performing gel chromatography using Sephadex G-50. The fluorescence studies were conducted using Origin 9.0.

### 2.4.2 Estimation of $pK_a$ and logP values:

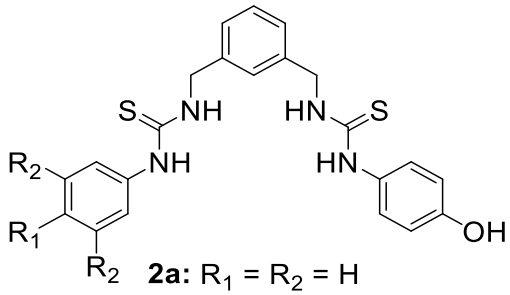


**2a:** $R_1 = R_2 = H$
**2b:** $R_1 = OMe$, $R_2 = H$
**2c:** $R_1 = CF_3$, $R_2 = H$
**2d:** $R_1 = H$, $R_2 = CF_3$

**Figure 2.8.** Structure of the synthesized ionophores **2a-2d**.

**Table 2.1**. $pK_a$ and logP of compounds **2a-2d**.

| compound | $R_1$ | $R_2$ | $pK_a$ | clogP |
|---|---|---|---|---|
| **2a** | H | H | 9.606 | 2.489 |
| **2b** | OMe | H | 9.606 | 2.592 |
| **2c** | $CF_3$ | H | 9.606 | 3.901 |
| **2d** | H | $CF_3$ | 9.606 | 4.969 |

### 2.4.3 Synthesis and characterization of the compounds:


**Scheme 2.2.** Synthesis of 1,3-bis(isothiocyanatomethyl)benzene.

**2.4.3.1** ***Synthesis of 1,3-bis(isothiocyanatomethyl)benzene*** **—** To the stirring solution of 1,3-phenylenedimethanamine (2.93 mmol) and *N*, *N*′-dicyclohexylcarbodiimide (29.3 mmol) in dry $CH_2Cl_2$, $CS_2$ (5.87 mmol) was added (dropwise) under the continuous stirring condition at 0 °C. Then the reaction mixture was stirred at room temperature until the maximum consumption of the starting material. The progress of the reaction was monitored by the TLC method (14% ethyl acetate/hexane). The residue was filtered out and concentrated under reduced pressure, which was further purified by a silica-gel-based column chromatographic technique using a 0-8% ethyl acetate/hexane system to obtain a yellowish liquid product with a 70% yield. The compound was characterized with $^1H$ and $^{13}C$ NMR, and the characteristic peaks are in accordance with the reported ones.[13]

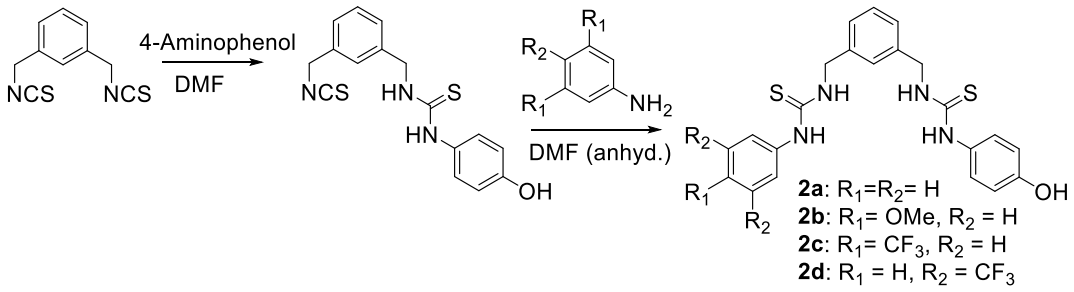


**Scheme 2.3.** Synthetic scheme of compounds **2a-2d**.

**2.4.3.2** ***General method for preparation of bis-thiourea compound*** — To the stirring solution of 1,3-bis(isothiocyanatomethyl)benzene (0.6 mmol) in DMF, 4-aminophenol (0.48 mmol) was added and stirred for 4h at room temperature. Then, the respective amines (0.6 mmol) in DMF were added to the mixture and stirred until complete consumption of the starting materials. Then it was extracted using ethyl acetate and chilled ice water (3 × 15 mL); layers were combined, passed over anhydrous sodium sulphate, and concentrated under reduced pressure.

**2.4.3.3** ***Synthesis of 1-(3-((3-(4-hydroxyphenyl) thioureido) methyl) benzyl)-3-phenylthiourea (2a)*** —

To the stirring solution of 1,3-bis(isothiocyanatomethyl)benzene (0.6 mmol) in DMF, 4-aminophenol (0.48 mmol) was added and stirred for 4h at room temperature to obtain 1-(4-hydroxyphenyl)-3-(3-(isothiocyanatomethyl)benzyl)thiourea. Then, aniline (0.6 mmol) was added to it, and the general protocol was followed as mentioned above. The crude reaction mixture was purified through column chromatography with a solvent gradient system of $CH_2Cl_2$/MeOH (0-5%) to obtain a white solid compound with a 66% yield. Characterization: **$^1$H NMR** (500 MHz, DMSO $d_6$) $\delta_{ppm}$ 9.58 (s, 1H), 9.38 (s, 1H), 9.29 (s, 1H), 8.13 (s, 1H), 7.80 (s, 1H), 7.44 (d, $J$ = 7.6 Hz, 2H), 7.31 (m, 3H), 7.27 (s, 1H), 7.21 (t, $J$ = 7.8 Hz, 2H), 7.11 (t, $J$ = 9.3 Hz, 3H), 6.73 (d, $J$ = 8.2 Hz, 2H), 4.75 – 4.70 (m, 4H). **$^{13}$C NMR** (125 MHz, DMSO-$d_6$) $\delta_{ppm}$ 181.6, 181.2, 155.5, 139.9, 139.6, 139.4, 129.1, 128.6, 127.0, 126.6, 126.3, 124.7, 123.8, 115.8, 47.7. **HRMS**: ESI calc. for $C_{22}H_{22}N_4OS_2$ $[M+H]^+$: 423.1314, found: 423.1316.

**2.4.3.4** ***Synthesis of 1-(3-((3-(4-hydroxyphenyl) thioureido) methyl) benzyl)-3-(4-methoxyphenyl) thiourea (2b)*** —

To the stirring solution of 1,3-bis(isothiocyanatomethyl)benzene (0.6 mmol) in DMF, 4-aminophenol (0.48 mmol) was added and stirred for 4h at room temperature to obtain 1-(4-hydroxyphenyl)-3-(3-(isothiocyanatomethyl)benzyl)thiourea. Then, to it, 4-methoxyaniline

(0.6 mmol) was added to the reaction following the general protocol described above. The crude reaction mixture was purified through column chromatography with a solvent gradient system of $CH_2Cl_2$/MeOH (0-5%) to give a solid white product with a 90% yield. Characterization: **$^1$H NMR** (600 MHz, DMSO- *$d_6$*) $\delta_{ppm}$ 9.43 (s, 1H), 9.41 (s, 1H), 9.32 (s, 1H), 7.92 (s, 1H), 7.81 (s, 1H), 7.28 (t, *J* = 7.6 Hz, 1H), 7.26 (s, 1H), 7.24 (d, *J* = 4.8 Hz, 2H), 7.18 (s, 2H), 7.10 (d, *J* = 8.5 Hz, 2H), 6.91 (d, *J* = 8.8 Hz, 2H), 6.73 (d, *J* = 8.6 Hz, 2H), 4.71 (d, *J* = 3.4 Hz, 4H), 3.73 (s, 3H). **$^{13}$C NMR** (150 MHz, DMSO- *$d_6$*) $\delta_{ppm}$ 181.5, 157.1, 155.5, 139.8, 131.9, 128.5, 127.1, 126.4, 126.2, 115.8, 114.5, 55.6, 47.7. **HRMS**: ESI calc. for $C_{23}H_{24}N_4O_2S_2$ $[M+H]^+$: 453.1418, found 453.1421.

**2.4.3.5** ***Synthesis of 1-(3-((3-(4-hydroxyphenyl) thioureido) methyl) benzyl)-3-(4-(trifluoromethyl) phenyl) thiourea (2c)*** — To the stirring solution of 1,3-bis(isothiocyanatomethyl)benzene (0.6 mmol) in DMF, 4-aminophenol (0.48 mmol) was added and stirred for 4h at room temperature to obtain 1-(4-hydroxyphenyl)-3-(3-(isothiocyanatomethyl)benzyl)thiourea. Then, to it, 4-trifluoromethyl aniline (0.6 mmol) was added to the reaction following the general protocol mentioned above. The crude reaction mixture was purified by column chromatography using a solvent gradient from 0 to 5% CH2Cl2/MeOH, yielding a white solid with 78% yield. Characterization: **$^1$H NMR** (600 MHz, DMSO- *$d_6$*) $\delta_{ppm}$ 9.94 (s, 1H), 9.47 (s, 1H), 9.31 (s, 1H), 8.45 (s, 1H), 7.81 (s, 1H), 7.73 (s, 1H), 7.71 (s, 1H), 7.65 (s, 1H), 7.64 (s, 1H), 7.30 (t, *J* = 7.6 Hz, 1H), 7.26 (s, 1H), 7.20 (dd, *J* = 12.0, 7.9 Hz, 2H), 7.08 (d, *J* = 8.1 Hz, 2H), 6.71 (d, *J* = 8.3 Hz, 2H), 4.72 (d, *J* = 20.4 Hz, 4H). **$^{13}$C NMR** (150 MHz, DMSO-
*$d_6$*) $\delta_{ppm}$ 179.84, 179.41, 153.85, 141.98, 138.31, 137.27, 126.99, 125.43, 124.93, 124.68, 124.46, 121.00, 114.16, 45.95. **HRMS**: ESI calc. for $C_{23}H_{21}F_3N_4OS_2$ $[M+H]^+$: 491.1184, found 491.1186.

**2.4.3.6** ***Synthesis of 1-(3,5-bis(trifluoromethyl) phenyl)-3-(3-((3- (4-hydroxyphenyl) thioureido) methyl) benzyl) thiourea (2d)*** — To the stirring solution of 1,3-bis(isothiocyanatomethyl)benzene (0.6 mmol) in DMF, 4-aminophenol (0.48 mmol) was added and stirred for 4h at room temperature to obtain 1-(4-hydroxyphenyl)-3-(3-(isothiocyanatomethyl)benzyl)thiourea. Then, to it, 3,5-bis(trifluoromethyl)aniline (0.6 mmol) was added to the reaction following the general protocol described above. The crude reaction mixture was purified by column chromatography using a solvent gradient from 0 to 5% $CH_2Cl_2$/MeOH, yielding a white solid with a 75% yield. Characterization: **$^1$H NMR** (500 MHz,

DMSO- $d_6$) $\delta_{ppm}$ 10.17 (s, 1H), 9.38 (s, 1H), 9.31 (s, 1H), 8.67 (s, 1H), 8.28 (s, 2H), 7.82 (s, 1H), 7.75 (s, 1H), 7.32 (t, $J$ = 7.5 Hz, 1H), 7.28 (s, 1H), 7.23 (t, $J$ = 8.2 Hz, 2H), 7.10 (d, $J$ = 7.0 Hz, 2H), 6.72 (d, $J$ = 7.5 Hz, 2H), 4.75 (d, $J$ = 24.1 Hz, 4H).**$^{13}$C NMR** (125 MHz, DMSO- $d_6$) $\delta_{ppm}$ 181.43, 181.26, 155.60, 142.30, 140.12, 138.75, 130.67, 130.45, 128.73, 127.12, 126.76, 126.42, 126.36, 124.61, 122.81, 122.60, 116.72, 115.85, 47.61. **HRMS**: ESI calc. for $C_{24}H_{20}F_6N_4OS_2$ $[M+H]^+$: 559.1046, found 559.1052.

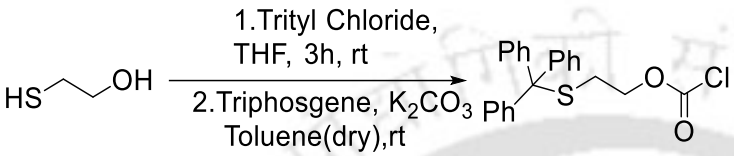


**Scheme 2.4.** Synthesis of 2-(tritylthio)ethyl carbonochloridate.

**2.4.3.7** ***Synthesis of 2-(tritylthio)ethyl carbonochloridate*** — Compound 2-(tritylthio)ethyl carbonochloridate was synthesized according to the previously reported protocol. Compound 2-(tritylthio)ethyl carbonochloridate was obtained with around 88% yield. The compound was characterized with $^1$H and $^{13}$C NMR, and the characteristic peaks are in accordance with the reported ones.[14]

**2.4.3.8** ***Synthesis of 4-(3-(3-((3-(3,5-bis(trifluoromethyl)phenyl) thioureido) methyl) benzyl) thioureido) phenyl(2-mercaptoethyl) carbonate*** —To the stirring solution of compound **2d** (0.179 mmol) in dry THF, $K_2CO_3$ (0.239 mmol) was added and stirred for 1 h. Then 2-(tritylthio)ethyl carbonochloridate (0.239 mmol) was added to it dropwise under ice conditions. The reaction mixture was stirred at room temperature for 4 h till completion (monitored by TLC). Purified using preparative TLC (30% Ethyl acetate/hexane). Characterization: **$^1$H NMR** (600 MHz, $CDCl_3$) $\delta_{ppm}$ 8.75 (s, 1H), 8.22 (s, 2H), 7.87 (s, 4H), 7.61 (s, 2H), 7.46 (d, $J$ = 7.7 Hz, 13H), 7.32 (t, $J$ = 7.4 Hz, 12H), 7.27 – 7.24 (m, 8H), 7.12 (d, $J$ = 16.2 Hz, 10H), 4.79 (d, $J$ = 42.0 Hz, 4H), 4.13 – 3.77 (m, 5H), 2.69 – 2.50 (m, 5H), 1.45 – 1.14 (m, 6H). **$^{13}$C NMR** (150 MHz, $CDCl_3$) $\delta_{ppm}$ 181.15, 181.08, 153.15, 149.49, 144.41, 139.63, 132.18, 131.96, 129.56, 128.06, 126.93, 126.28, 123.83, 123.06, 122.52, 122.02, 118.58, 67.17, 67.11, 48.63, 48.43, 30.42. **HRMS**: ESI calc. for $C_{46}H_{38}F_6N_4O_3S_3$ $[M+Na]^+$: 927.1902, found: 927.1904.

**2.4.3.9** ***Synthesis of 4-(3-(3-((3-(3,5-bis(trifluoromethyl)phenyl) thiourea) methyl) benzyl) thiourea) phenyl(2-mercaptoethyl) carbonate-CCRCRGDS (2.2d)*** — The deprotection of

trityl group was carried out under in $CH_2Cl_2$ by the addition of 30% TFA mixture and the reaction was monitored in every 30 min. When the maximum of compound 4-(3-(3-((3-(3,5-bis(trifluoromethyl)phenyl) thioureido) methyl) benzyl) thioureido) phenyl(2-mercaptoethyl) carbonate (0.039 mmol) got deprotected, $CH_2Cl_2$, TFA was evaporated out under high vacuum. To the same pot, acetonitrile/$H_2O$ mixture (4:1), CCRCRGDS peptide (0.013 mmol) of 4-(3-(3-((3-(3,5-bis(trifluoromethyl)phenyl) thioureido) methyl) benzyl) thioureido) phenyl(2-mercaptoethyl) carbonate) was added and, $H_2O_2$ (20 µL) was added dropwise under ice condition, and then it was stirred for 10 hours at room temperature. The reaction was monitored by TLC till starting material get consumed. The solvent was evaporated under a high vacuum, and a solid precipitate gets accumulated. After that, the crude mixture was washed with different solvents (water, $CH_2Cl_2$, and diethyl ether). Characterization: **$^1$H NMR** (600 MHz, DMSO- $d_6$) $\delta_{ppm}$ 9.81 (s, 1H), 8.75 (s, 1H), 8.25 (s, 1H), 7.71 (s, 4H), 7.36 (s, 1H), 7.17 (s, 3H), 7.03 (s, 1H), 6.76 (t, $J$ = 7.6 Hz, 4H), 6.72 (s, 4H), 6.65 (dd, $J$ = 14.2, 7.6 Hz, 7H), 6.54 (d, $J$ = 8.3 Hz, 4H), 6.17 (d, $J$ = 8.3 Hz, 5H), 6.04 (m, 1H), 4.74 (s, 1H), 4.19 (d, $J$ = 36.7 Hz, 4H), 3.98 (d, $J$ = 7.1 Hz, 2H), 3.92 (t, $J$ = 6.3 Hz, 2H), 3.85 (t, $J$ = 6.0 Hz, 2H), 3.72 (d, $J$ = 7.3 Hz, 2H), 3.11 (t, $J$ = 5.6 Hz, 4H), 2.42 (s, 1H), 2.35 (s, 3H), 2.30 (d, $J$ = 8.4 Hz, 2H), 2.19 (s, 2H), 2.07 (t, $J$ = 6.3 Hz, 1H), 1.99 (s, 4H), 1.28 (s, 2H), 1.14 – 0.86 (m, 5H).**$^{13}$C NMR** (150 MHz, DMSO- $d_6$) $\delta_{ppm}$ 181.37, 181.21, 172.93, 172.16, 171.22, 170.43, 170.20, 169.60, 163.47, 159.83, 159.62, 159.41, 157.00, 155.30, 142.04, 139.80, 138.75, 131.02, 130.80, 130.58, 130.36, 128.83, 127.22, 126.36, 126.35, 126.28, 124.47, 122.67, 122.62, 120.86, 120.22, 118.25, 116.84, 116.28, 116.09, 115.84, 114.32, 62.08, 54.18, 54.13, 47.44, 47.23, 42.63, 40.72, 40.60, 36.50, 31.39, 29.25, 26.10, 25.79, 25.18, 25.03. **MALDI-TOF** for $[C_{57}H_{76}F_6N_{18}O_{15}S_6]$:1559.7012, found $[M/2]^+$: 779.357.

**NOTE 1:** The RGD-peptide sequence (CCRCRGDS) containing three cysteine residues was designed for targeted cargo delivery. Three cysteine residues could install more cargo; however, only one cysteine residue could form a disulfide bond with compound 4-(3-(3-((3-(3,5-bis(trifluoromethyl)phenyl) thioureido) methyl) benzyl) thioureido) phenyl(2-mercaptoethyl) carbonate**.** The reaction of the CCRCRGDS peptide with compound 4-(3-(3-((3-(3,5-bis(trifluoromethyl)phenyl) thioureido) methyl) benzyl) thioureido) phenyl(2-mercaptoethyl) carbonate only provided compound **2.2d** with the formation of one disulfide bond. Compound **2.2d** precipitated out of the reaction conditions.

**NOTE 2:** $^1$H NMR characterisation of compound **2.2d** shows spectral changes consistent with selective modification of a single cysteine residue, including the disappearance of one free thiol

environment while the remaining cysteine signals remain largely unperturbed. Importantly, the spectra do not indicate the presence of multiple regio-isomeric conjugates, suggesting that a single dominant product is formed rather than a statistical mixture.

Further support for the assigned structure comes from our glutathione (GSH) treatment studies, which demonstrate predictable thiol-exchange behaviour consistent with conjugation to a more solvent-accessible, less sterically hindered cysteine residue. Such reactivity would be significantly attenuated if the anionophore were attached at a more sterically congested cysteine site within the peptide sequence. In addition, analytical HPLC analysis reveals a single, well-resolved peak, indicating product homogeneity and further supporting the absence of multiple cysteine-linked isomers.

**HPLC trace for compound 2d and 2.2d:**

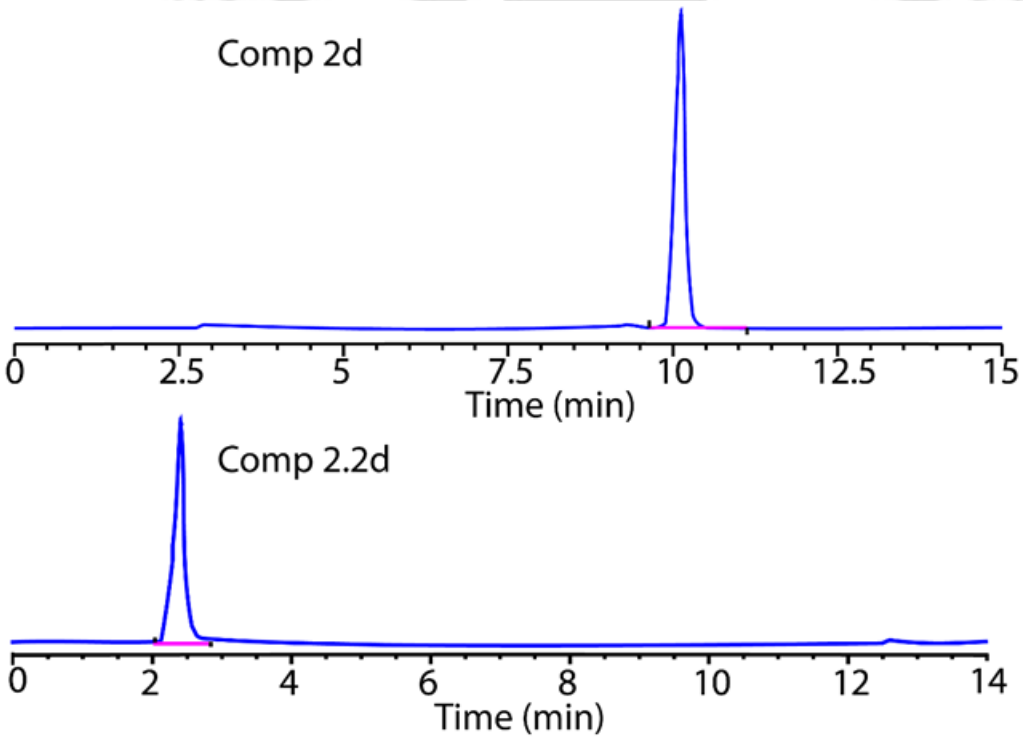


**2.4.3.10** ***Synthesis of 4-(3-(3-((3-(3,5-bis (trifluoromethyl) phenyl) thioureido) methyl) benzyl) thioureido) phenyl (2-(phenyldisulfaneyl) ethyl) carbonate (2.3)*** — To the stirring solution of 2-mercaptoethanol (4.5 mmol) in $CH_3CN/H_2O$ (3:2) mixture, thiophenol (4.5 mmol) was added dropwise. To the above mixture, $H_2O_2$ (45 mmol) was added, and the mixture was stirred at room temperature for 4 hours (monitored by TLC until completion). The crude mixture 2-(phenyldisulfanyl)ethan-1-ol was evaporated under reduced pressure and purified by column chromatography (10-20% EA/Hex system). Again, to the stirring solution of $K_2CO_3$

(3.23 mmol) and triphosgene (1.61 mmol), in anhydrous toluene, 2-(phenyldisulfaneyl) ethan-1-ol was added dropwise in 0 °C. Stirred for another 45 mins, and 2-(phenyldisulfaneyl) ethylcarbonochloridate was obtained in moderate yield (55%). Characterization: **$^1$H NMR (600 MHz, Chloroform-*d*) δ:** 7.57 (d, *J* = 7.2 Hz, 2H), 7.38 (t, *J* = 7.7 Hz, 2H), 7.30 (t, *J* = 7.4 Hz, 1H), 4.54 (t, *J* = 6.7 Hz, 2H), 3.03 (t, *J* = 6.7 Hz, 2H). **$^{13}$C NMR (151 MHz, $CDCl_3$) δ:** 150.57, 136.39, 129.26, 128.14, 127.54, 68.93, 35.97.

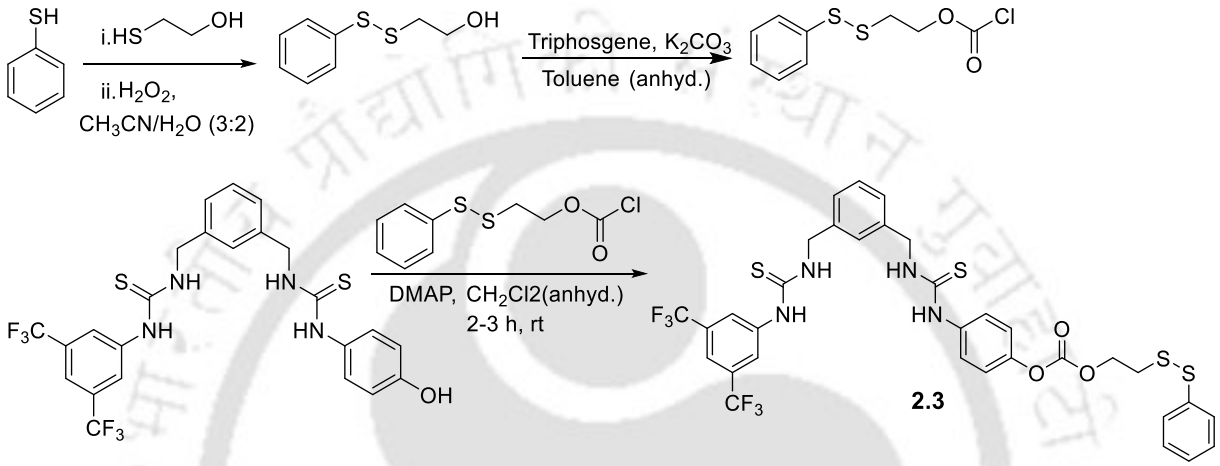


**Scheme 2.5.** Synthesis of control proionophore **2.3**.

To the stirring solution of **2d**, DMAP was added in anhydrous $CH_2Cl_2$. Then, to the above solution, 2-(phenyldisulfaneyl)ethylcarbonochloridate was added under 0 °C and stirred at room temperature for 2-3 hrs (monitored through TLC). The solvent was evaporated under a rotary evaporator and purified in a column (20-25% EA/Hex system). **$^1$H NMR (600 MHz, Chloroform-*d*) δ:** 8.65 (s, 1H), 8.09 (s, 1H), 7.88 (s, 2H), 7.62 (s, 1H), 7.59 – 7.55 (m, 2H), 7.36 (t, *J* = 7.7 Hz, 2H), 7.28 (d, *J* = 7.6 Hz, 3H), 7.21 – 7.12 (m, 7H), 6.81 (s, 1H), 4.84 (d, *J* = 5.8 Hz, 2H), 4.78 (d, *J* = 5.3 Hz, 2H), 4.49 (t, *J* = 6.6 Hz, 2H), 3.05 (t, *J* = 6.6 Hz, 2H). **$^{13}$C NMR (151 MHz, $CDCl_3$) δ:** 181.25, 153.27, 149.55, 139.63, 136.54, 132.29, 132.07, 129.30, 129.19, 128.04, 127.39, 127.20, 126.87, 126.54, 125.28, 123.82, 123.23, 122.63, 122.01, 118.67, 66.28, 48.70, 48.48, 36.44. **HRMS**: ESI calculated for $C_{33}H_{28}F_6N_4O_3S_4$, $[M+Na]^+$:793.0841, found 793.0831, , $[M+K]^+$: 809.058, found 809.0574.

(P.S: In the final prepared compound **7**, **$^1$H NMR**: grease peak appeared at – 0.86 ppm and 1.27 ppm. **$^{13}$C NMR**: grease peak appeared at – 29.7 ppm.)

**2.4.4 Ion transport studies:**

**2.4.4.1 Buffer and stock solution preparation —** Required buffer solution was prepared by dissolving HEPES and salt (LiCl, NaCl, KCl, RbCl, CsCl, NaCl, NaBr, NaI, $NaNO_3$) in Milli-Q water to obtain a buffer composition of 20 mM HEPES buffer, pH 7.2, containing 100 mM of the respective salt (MCl or $Na_xA$). The stock solutions of the compounds were prepared in molecular biology-grade DMSO. The concentration of the DMSO stock solution used in our experiment is 0.26% for both the ionophore and the proionophore.

**2.4.4.2 Preparation of EYPC/CHOL-LUVs⊃lucigenin —** For conducting the lucigenin-based ion transport studies, egg yolk phosphatidylcholine (EYPC, 50 mg/mL in deacidified $CHCl_3$) and CHOL (25 mg/mL in deacidified $CHCl_3$) was taken in a clean sample vial in the molar ratio of 8:2. The solution was evaporated by continuous rotation for 6 h under reduced pressure to form a thin lipid film. The thin lipid film was rehydrated by adding 800 µL of 20 mM HEPES buffer containing 1 mM lucigenin and 100 mM $NaNO_3$ solution, pH 7.2. The resultant suspension was vortexed 6-7 times for 1 h, followed by 17-19 freeze-thaw cycles and, finally, 15 minutes of constant vortexing to incorporate lucigenin within the lipid bilayer. The lipid suspension was extruded using a mini extruder (a polycarbonate membrane from Avanti Polar Lipids) with a 200 nm pore size 19-21 times (must be an odd number). The unencapsulated lucigenin dye was removed by size exclusion column chromatography (Sephadex G-50) and 20 mM HEPES buffer containing 1 mM lucigenin and 100 mM $NaNO_3$ solution, pH 7.2 as the eluting solution to get the final lipid concentration of 25 mM (assuming 100% lipid regeneration).

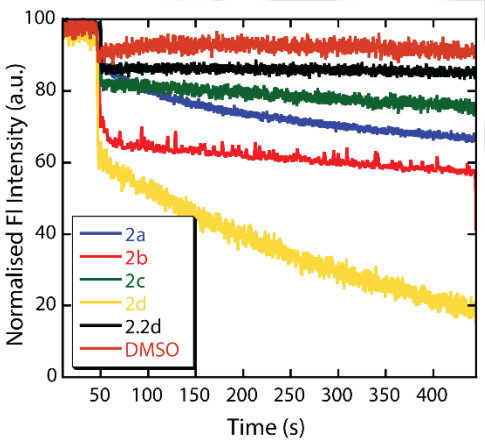


**Figure 2.9.** The $Cl^-$ transport activities of the compounds.

[NOTE: The procedure used to prepare lucigenin-loaded vesicles and establish the desired internal/external ion gradient follows a well-established and widely used protocol for

lucigenin-based chloride transport assays, and we regret that this was not made sufficiently explicit to your understanding in the experimental section.

Briefly, multilamellar vesicles were first prepared by hydration of a dry lipid film with an internal solution containing 20 mM HEPES, 1 mM lucigenin, and 100 mM $NaNO_3$, followed by freeze-thaw cycling and extrusion to afford unilamellar vesicles. At this stage, as correctly inferred by the reviewer, the vesicles are indeed suspended in the same $NaNO_3$-containing buffer used for hydration.

Subsequently, and this is the key step that may not have been stated explicitly, the external buffer was exchanged to generate the final suspension medium. This was achieved by passing the vesicle suspension through a size-exclusion column (e.g., Sephadex G-25) or by repeated centrifugation, resuspension steps, and replacing the external medium with 20 mM HEPES containing 100 mM NaCl, while retaining the original intravesicular composition (HEPES/lucigenin/$NaNO_3$). This buffer-exchange step is a routine and essential part of lucigenin transport assays and is standard practice in the literature.

The resulting vesicles therefore contain $NaNO_3$ and lucigenin encapsulated, while being suspended in a NaCl-containing buffer, thereby establishing the chloride gradient required to monitor transport via fluorescence quenching of lucigenin. The transport experiment itself then proceeds by addition of the transporter to this final vesicle suspension, as described.]

**2.4.4.3** ***Quantitative measurement of transport activity from lucigenin assay*** — The fluorescence emission intensities of the lucigenin dye were normalized, and the intensities appearing at t = 0 and t = 500 s were taken as 0 and 100 units, respectively. The normalized fluorescent intensities (FI) at t = 450 s (before the addition of Triton X-100) were used to measure the transport activity of the compounds.

*i.e.* $Transport\ activity$,

$$T_{HPTS} = \frac{F_t - F_0}{F_\infty - F_0} \times 100\% \quad \text{..... Eq (2.1)}$$

Where, $F_t$ = fluorescence intensity at t = 450 s (before the addition of Triton X-100 solution), $F_0$ = fluorescence intensity immediately before the addition of the transporter (t = 0 s), and $F_\infty$ = fluorescence intensity after the addition of Triton X-100 solution (i.e., at saturation after complete leakage at t = 500 s).

[ NOTE: Regarding the time point used for comparison, the normalized fluorescence intensities were analysed over the time window clearly indicated on the x-axis of Figure 2.2 (50–450 s), after establishment of a stable baseline and upon initiation of chloride transport. This time range

is explicitly shown in the figure and corresponds to the standard analysis window used to evaluate transport kinetics in such assays. For the concentration-dependent studies, a wide range of transporter concentrations was intentionally examined to reliably estimate $EC_{50}$ values. Displaying each individual concentration explicitly in the kinetic trace legend would significantly reduce the readability of the figure. Instead, concentration ranges are indicated in Figure 2.2, while specific concentrations and their quantitative comparison are presented in the corresponding $EC_{50}$ plots, where they can be more clearly and accurately assessed. ]

**2.4.4.4 Chloride ion efflux studies using chloride ion-selective electrode (chloride-ISE) —** The $Cl^-$ ion transport activities of the compounds were measured by monitoring the $Cl^-$ ion concentration outside the liposomes using a chloride ion-selective electrode (chloride-ISE) (Thermo Scientific™ Orion™). Before each experiment, the ISE was calibrated with 1 ppm, 10 ppm, and 100 ppm standard chloride solutions containing an ionic strength adjuster. A filling solution was poured into the electrode up to the mark before each experimental session. The chloride concentration (ppm) displayed by the ion meter was set to continuous mode for the time-dependent measurements.

**2.4.4.5 Preparation of EYPC/CHOL-LUV —** The LUVs were prepared according to the reported procedure using EYPC and CHOL, as mentioned in the earlier section.[3] The dry film was hydrated with 800 µL of 5 mM Phosphate buffer and 100 mM NaCl. The unilamellar vesicles were dialyzed against 5 mM phosphate buffer, pH 7.2, containing 100 mM NaNO3 to remove extravesicular NaCl. Finally, the LUVs were collected, and the volume was adjusted to 800 µL using phosphate buffer (5 mM) and $NaNO_3$ (100 mM) solution. The final lipid concentration was 25 mM (assuming 100% lipid regeneration).

**2.4.4.6 Chloride efflux study across EYPC/CHOL-LUV —** To measure the extent of efflux of $Cl^-$ in the absence and presence of the compound, the EYPC/CHOL-LUVs (50 µL) and 5 mM phosphate buffer, pH 7.2, containing 100 mM $NaNO_3$ (3940 µL) were taken in a clean and dry glass vial and kept under mild stirring conditions. The glass electrode was immersed in the solution under mild stirring conditions. To initiate the $Cl^-$ transport kinetics at t = 50 s, 10 µL of the respective compound (from DMSO stock solution) was added into the stirring solution, and the readings were noted from the ion meter. After 5 minutes, the vesicles were lysed with 50 µL of 20% Triton X-100. The total $Cl^-$ efflux reading was taken at 7 minutes (allowing

complete disruption of the LUVs). The initial reading was considered 0% Cl─ efflux, and the final reading at 7 min was considered 100% $Cl^-$ efflux.

**2.4.4.7 Quantitative measurement of transport activity from chloride ISE assay —** To find out the $EC_{50}$ value of all the compounds, the chloride-ISE-based $Cl^-/NO_3^-$ exchange assay was performed at varying concentrations. From these experiments, the chloride efflux (%) at 500 s was plotted as a function of the carrier concentration (μM). The data points were fitted to the modified Hill equation using the Origin program 6.0.

$$y = Start + (End - Start) * x\hat{}n/(k^n + x\hat{}n) \quad \ldots\ldots (Eq.2.2)$$

In this equation, a = START = control value (DMSO), b = END = 100, y is the chloride efflux efficiency at 500 s (%), and x is the carrier concentration (μM). Where n is the Hill coefficient, $EC_{50}$ values at 500 s can be obtained directly from this modified Hill plot.

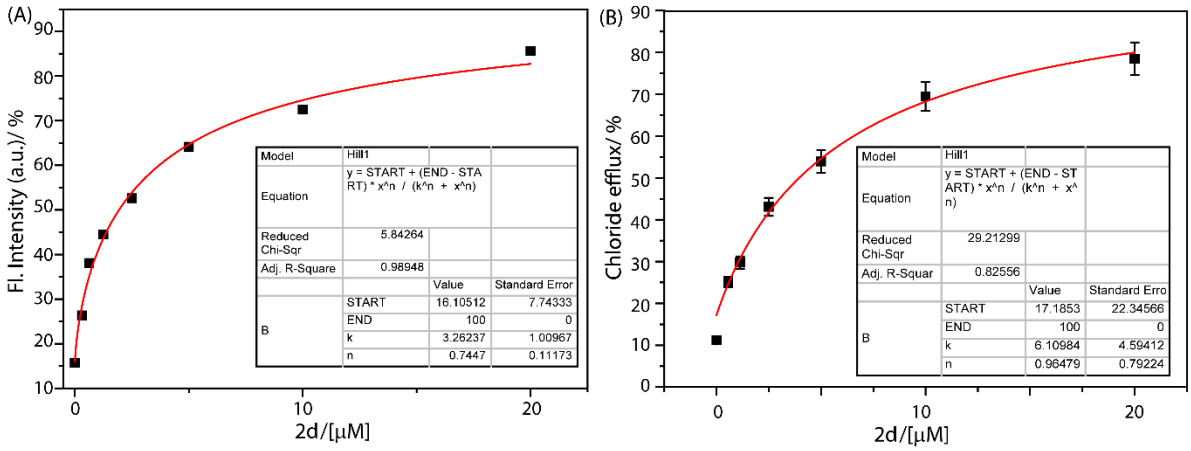


**Figure 2.10.** Concentration-dependent transmembrane transport of $Cl^-$ in the presence of compound **3d** across the LUVs. The ion transport activity was measured using a lucigenin-based fluorescence assay (A) and a Cl-ISE assay (B). The $EC_{50}$ value was calculated using the modified Hill equation.

**Note:** The standard deviation calculated based on at least 3 experiments is like the following:

FFluorescence-based$EC_{50}$ value: 4.15 ± 0.82 μM (Hill coefficient, n = 0.78)

ISE based $EC_{50}$ value: 5.2423 ± 1.29 μM (Hill coefficient, n = 0.82)

### 2.4.5 Anionophore regeneration study

**2.4.5.1 Liposomal-based fluorescence study of GSH pretreated proanionophore (2.2d) —** The lucigenin-encapsulated LUVs were prepared as described in the earlier section. To measure the regeneration aptitude, 2940 μL of 20 mM HEPES buffer, pH 7.2, containing 100 mM

$NaNO_3$, and 50 µL of EYPC/CHOL-LUV⊃lucigenin was placed in a fluorescence cuvette. Then,

it was placed in the fluorescence spectrophotometer at room temperature under a slow stirring condition. The lucigenin fluorescence intensity of the solution was monitored. After 50 s, 10 µL of compound **2.2d** (10 mM GSH pre-incubated for 8h, 15h, and 24h) was added to initiate the anion transport kinetics. At 450 s, the vesicles were lysed by adding 20 µL of 20% Triton X-100 solution, and the fluorescence measurement was continued up to t = 500 s.

**2.4.5.2 HPLC-based study of GSH pretreated proionophore (2.2d) —** HPLC method: In order to confirm the regeneration of active ionophore **2d** from proanionophore **2.2d**, HPLC analysis was performed. Proionophore (10 µM) was incubated in the PBS buffer system with 10 mM GSH in 37 °C. At time intervals of 8h, 16h, 24 h, 36 h, 48 h, and 72h incubated samples were recorded. Time-dependent study confirms successful release of 3d from proionophore. However, in the absence of GSH, compound 6 integrity remained for 72 hours. Column used: Ascentis® express C18, 2.7 µm HPLC column, flow rate: 0.5 mL/min, mobile phase used: Optimized gradient of PBS buffer/acetonitrile. The gradient used: 0-5 min- 20% buffer:80% $CH_3CN$, 5-10 min- 10% buffer:90% $CH_3CN$, 10-14 min- 5% buffer:95% $CH_3CN$, 14-16 min- 30% buffer:70% $CH_3CN$.

**2.4.5.3 Characterization of regeneration of active anionophore by HRMS analysis —** The HRMS analysis was performed to confirm the in-situ generation of the active anionophore **2d** from the proionophore **2.2d** after treatment with GSH. MALDI-TOF analysis of compound **2.2d** showed a peak at 779.357 ($[M/2]^+$). The HRMS of compound **2d**, found 559.1052 ($[M+1]^+$) and 1,3-oxathiolan-2-one, found at 103.9556 ($[M]^+$).

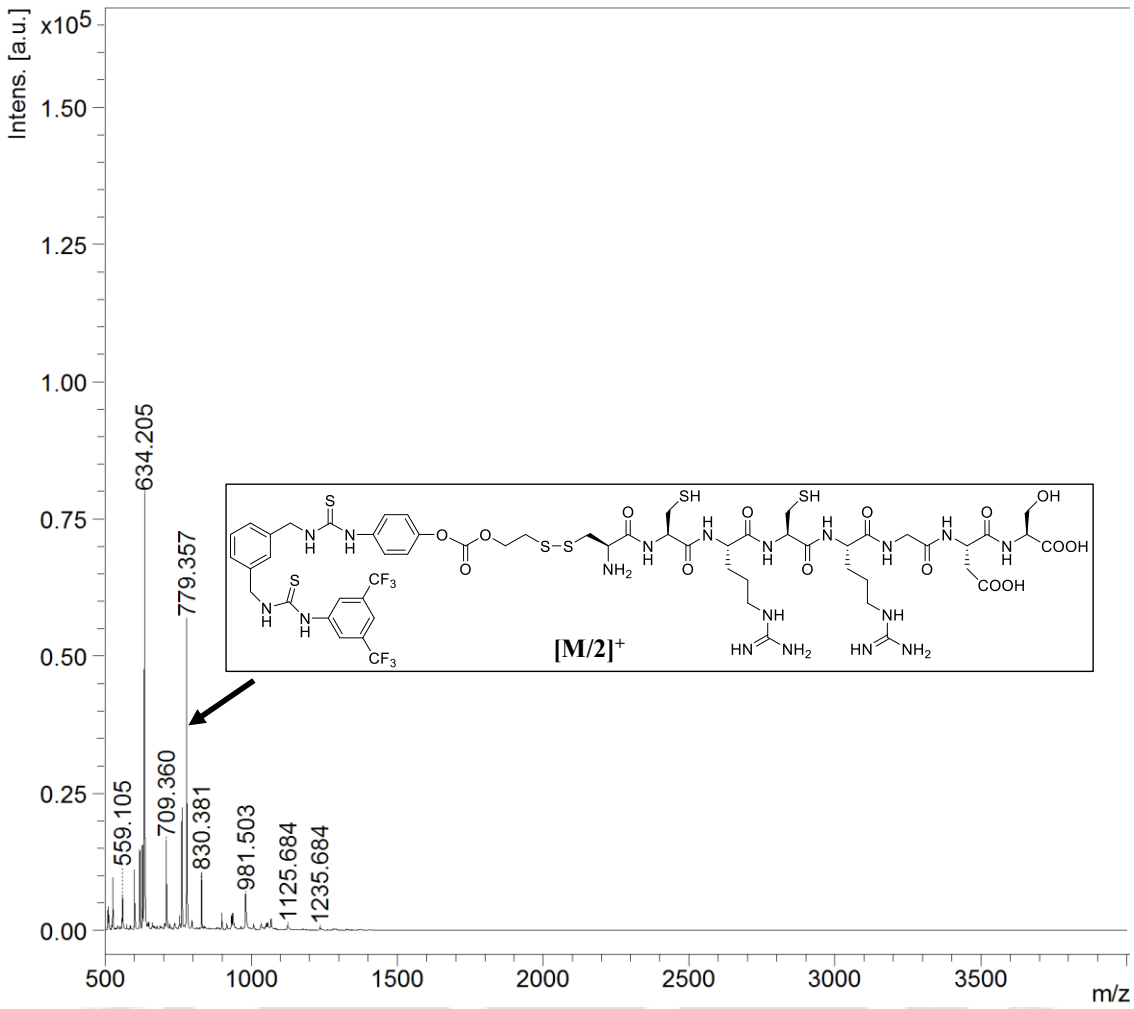


**Figure 2.11.** MALDI-TOF analysis (m/Z above 500) of the proionophore **2.2d** treated.

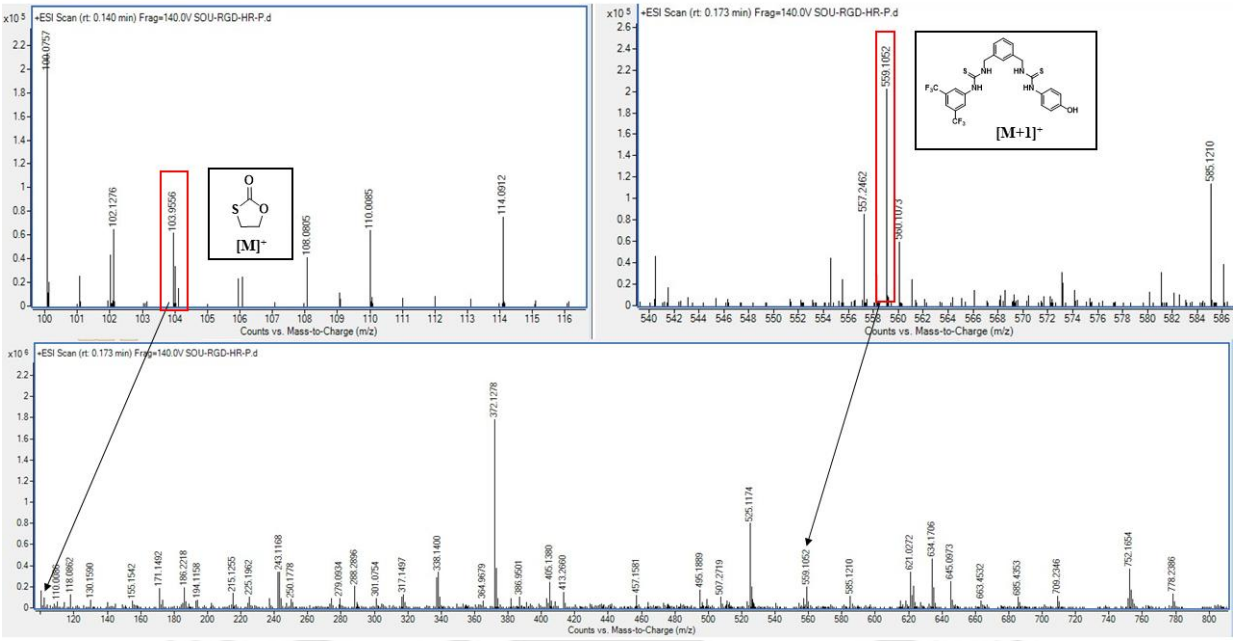


**Figure 2.12.** HRMS analysis of the reaction mixture of proionophore **2.2d** treated with GSH.

### 2.4.6 $^1$H NMR titration studies

Stock solutions of compound **2d** (2 mM) and tetrabutylammonium chloride (TBACl; 200 mM) were prepared in DMSO-d6. The $^1$H NMR spectra were recorded on a Bruker Ascend 600 spectrometer and calibrated with respect to the residual solvent peak in DMSO-$d_6$. $^1$H NMR titrations were performed by stepwise addition of TBACl to the solution of the compounds in DMSO-$d_6$. Upon addition of TBACl, changes in the amide N−H chemical shifts were used to calculate binding constant values. The $^1$H NMR stacked plots were processed using MestReNova 6 software. The association constant was obtained by fitting the data in the 1:1 binding model of the Bindfit v0.5 program.

### 2.4.7 Mechanistic studies for chloride ion transportation

**2.4.7.1 Cation Selectivity studies across EYPC/CHOL-LUV⊃HPTS —** The cation selectivity studies were performed according to the reported procedure.[16, 17] Briefly, in a clean fluorescence cuvette, 2940 µL of buffer solution (100 mM MCl, 20 mM HEPES, pH 7.2; where $M^+ = Li^+$, $Na^+$, $K^+$, $Rb^+$, and $Cs^+$), 50 µL of EYPC/CHOL-LUV⊃HPTS (prepared in 20 mM HEPES buffer containing 100 mM NaCl, pH 7.2) and fluorescence cuvette was placed in a fluorescence instrument equipped with a magnetic stirrer at t = 0 s. The fluorescence emission intensity of the HPTS dye was measured at $\lambda_{em}$ = 510 nm ($\lambda_{ex}$ = 450 nm) over a time course of 0 to 500 s. At t = 50 s, between the intra- and extra-vesicular medium, which leads to

the increase in the fluorescence intensity. Triton X-100 (20 µL of 20% solution in water) was added at t = 450 s to destroy all the vesicles.

**2.4.7.2 Cation Selectivity studies across EYPC/CHOL-LUV⊃lucigenin —** The cation selectivity studies were performed according to the reported procedure.(section 4.1.2).[17] Briefly, in a clean fluorescence cuvette, 2940 µL of buffer solution (100 mM MCl, 20 mM HEPES, pH 7.2; where $M^+$ = $Li^+$, $Na^+$, $K^+$, $Rb^+$, and $Cs^+$), 50 µL of above-prepared vesicles solution were taken, and fluorescence cuvette was placed in a fluorescence instrument equipped with a magnetic stirrer at t = 0 s. The fluorescence emission intensity of the lucigenin dye was measured at $\lambda_{em}$ = 505 nm (where $\lambda_{ex}$ = 455 nm) for the time course of 0 to 500 s. At t = 50 s, between the intra- and extra-vesicular medium, which leads to the increase in the fluorescence intensity. Triton X-100 (20 µL of 20% solution in water) was added at t = 450 s to destroy all the vesicles.

**2.4.7.3 Anion selectivity studies across EYPC/CHOL-LUV⊃HPTS —** The anion selectivity studies were performed according to the reported procedure.[16] Briefly, 2940 µL of 20 mM HEPES buffer, pH 7.2, containing 100 mM of the respective salt of $Na_xA_y$ (where $Na_xA_y$ = NaCl, NaBr, NaI, $NaNO_3$, and $Na_2SO_4$) and 50 µL of EYPC/CHOL-LUV⊃HPTS (prepared in 20 mM HEPES buffer containing 100 mM NaCl, pH 7.2) were taken in a fluorescence cuvette. Then, it was placed in the fluorescence spectrophotometer at room temperature under slow stirring conditions. The HPTS fluorescence intensity of the solution was monitored. After 50 s, 10 µL of the respective compound (from DMSO stock) was added to initiate the anion transport kinetics. For the pH gradient study, ΔpH = 0.8 was created by adding 10 µL of 1M NaOH to the extravesicular solution at t = 0 s. At 450 s, the vesicles were lysed by adding 20 µL of 20% Triton X-100, and fluorescence was measured for an additional 50 s.

**2.4.7.4 Quantitative measurement of transport activity from HPTS assay —** The fluorescence emission intensities of the HPTS dye were normalized, and the intensities appearing at t = 0 and t = 500 s were taken as 0 and 100 units, respectively.[13] The normalized fluorescent intensities (FI) at t = 450 s (before the addition of Triton X-100 solution) were considered to measure the transport activity of the compounds.

*i.e. Transport activity*,

$T_{HPTS} = \frac{F_t - F_0}{F_\infty - F_0} \times 100\%$ ..... Eq (S2)

Where, $F_t$ = fluorescence intensity at t = 450 s (prior to the addition of Triton X-100 solution), $F_0$ = fluorescence intensity immediately before the addition of the transporter (t = 0 s), and $F_\infty$ = fluorescence intensity after the addition of Triton X-100 solution (i.e., at saturation after complete leakage at t = 500 s).

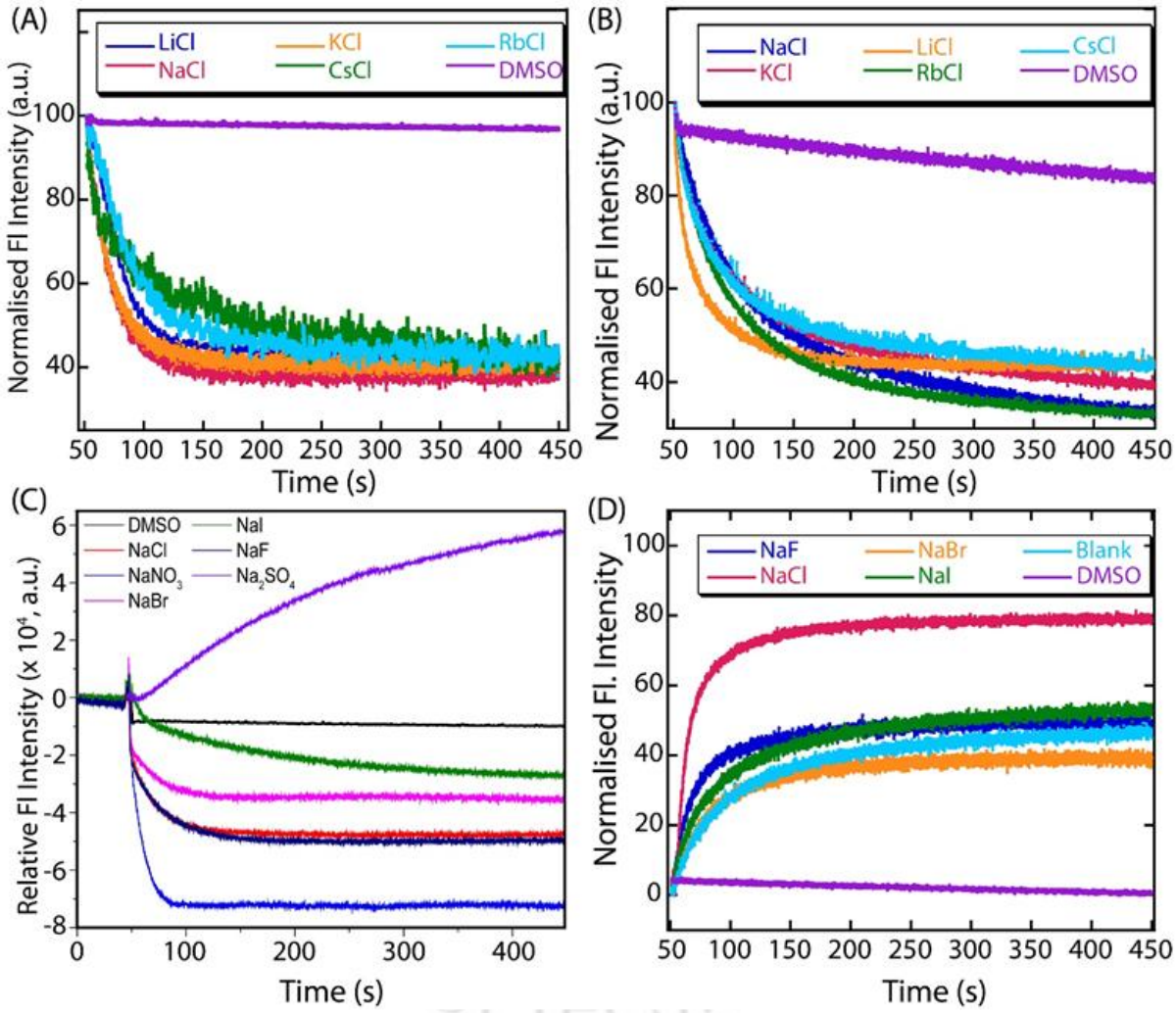


**Figure 2.13.** (A) Cation selectivity study for compound **2d** across EYPC/CHOL-LUVs⊃HPTS where intravesicular solution contains 20 mM HEPES buffers containing 100 mM NaCl, HPTS (1 mM) at pH 7.2 and extravesicular solution contains 20 mM HEPES buffers, 100 mM MCl (where $M^+ = Li^+, Na^+, K^+, Cs^+, Rb^+$) at pH = 7.2. (B) Cation selectivity study for compound **2d** across EYPC/CHOL-LUVs⊃lucigenin where intravesicular solution contains 20 mM HEPES buffers, 100 mM $NaNO_3$, lucigenin (1 mM) at pH 7.2 and extravesicular solution contains 20 mM HEPES buffers, 100 mM MCl (where $M^+ = Li^+, Na^+, K^+, Cs^+, Rb^+$) at pH = 7.2. (C) Anion selectivity study compound **2d** using anion gradient assay across EYPC/CHOL-LUVs⊃HPTS

where intravesicular solution contains 20 mM HEPES buffers, 100 mM NaCl, HPTS (1 mM) at pH 7.2 and extravesicular solution contains 20 mM HEPES buffers, 100 mM NaX (where $X^- = Cl^-, NO_3^-, I^-, Br^-, SO_4^{2-}$) at pH = 7.2. (D) Anion selectivity study compound **2d** using dual gradient assay across EYPC/CHOL-LUVs⊃HPTS where intravesicular solution contains 20 mM HEPES buffers,100 mM NaCl, HPTS (1 mM) at pH 7.2 and extravesicular solution contains 20 mM HEPES buffers, 100 mM NaX (where $X^- = Cl^-, NO_3^-, I^-, Br^-, SO_4^{2-}$) at pH = 8.0.

**Note:** We performed the anion gradient assay where $NaCl^{in}$/ $NaX^{out}$ (pH 7.2) based on method reported by Gale and co-workers.[7] The outcome of this study showed that compound **2d** in the absence of pH gradient followed higher $H^+/X^-$ influx efficacy over $H^+/Cl^-$ efflux which causes the acidification of intravesicular medium. In the absence of initial pH gradient, a pH gradient is generated by the anion transporter which assist prevailing HX influx or HCl efflux depending on the $X^-$ vs. $Cl^-$ selectivity. The impetus for net $H^+$ transport is the membrane potential initiating from the permeability variance between $X^-$ and $Cl^-$. The faster transport of HX over HCl could lead to the acidification of intracellular vesicles.[7] In case of $Na_2SO_4$, since $SO_4^{2-}$ being highly hydrophilic anion, transporter could not allow it to cross the lipid bilayer causing only $H^+/Cl^-$ efflux. Hence, we saw basification of intravesicular media. (owing to the increased fluorescence intensity due to the formation of $HPTS^-$). We also performed anion selectivity studies with pH gradient (ΔpH = 0.8) mentioned in Figure 2.13 D, where highest transport rate was observed for $Cl^-$.[17, 18, 19]

**2.4.7.5 Transport activity in the presence of FCCP —** The vesicles were prepared by following the same procedure as discussed in the earlier section. The ion transport activity was measured in the absence and presence of FCCP ($H^+$ selective transporter).[17] First, 2920 µL of 20 mM HEPES buffer, pH 7.2, containing 100 mM NaCl and 50 µL of the EYPC/CHOL-LUV⊃lucigenin was taken in a 3 mL fluorescence cuvette, and the cuvette was placed in the fluorescence spectrophotometer at room temperature under mild stirring condition. After that, the compound (8 µL of the stock solution in DMSO) and 2 µL of FCCP solution in DMSO (1 µM) were added to the solution. The cuvette was then kept inside the fluorescence instrument under stirring conditions for 3 minutes to allow maximum incorporation of the compounds into the lipid bilayers. After that, the lucigenin fluorescence intensity was monitored (t = 0 sec) at 506 nm ($\lambda_{ex}$ = 455 nm). After 450 sec, the kinetic experiment was terminated by adding 20 µL of 20% Triton-X100 solution (to rupture the vesicular arrangements) into the cuvette, and the

fluorescent measurements were continued for another 50 sec (t = 500 sec). The control experiment was performed in the absence of FCCP also.

**2.4.7.6 Preferential ion transport activity in the presence of valinomycin (valinomycin assay) —** For the valinomycin assay, the EYPC/CHOLLUV⊃lucigenin was prepared by following a similar procedure as mentioned in the earlier section.[18] The extracellular buffer was replaced with 100 mM KCl with 100 mM $NaNO_3$. Here at 50 s, the performed as solution, the respective compound (from DMSO stock) and /or 2 µL valinomycin (12.0 pM) of 10 µL of was added to initiate the anion transport kinetics. The fluorescence emission intensity of the lucigenin dye was normalized at t = 50, and t = 500 s and transferred as 0 and 100 units, respectively.

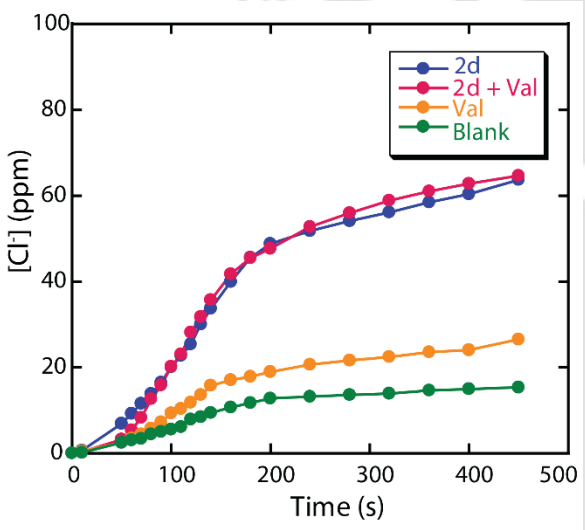


**Figure 2.14.** Chloride ion efflux activities of compound **2d** in the presence and absence of valinomycin. (Val = valinomycin.)

**2.4.7.7 Evidence for the carrier mechanism —** Lucigenin assay using 1,2-dipalmitoylphosphatidylcholine (DPPC) was employed to determine the transport mechanism of the compounds.[21] DPPC-LUV⊃lucigenin was prepared in 20 mM HEPES buffer pH 7.2, containing 100 mM $NaNO_3$. For the preparation of DPPC-LUV⊃lucigenin, first 50 µL of DPPC (100 mg/mL stock in de-acidified $CHCl_3$) was taken in a clean and dry glass vial, and the organic solvent was removed under reduced pressure (for 5-6 h) at room temperature. The dry, thin film was then hydrated with 600 µL of 20 mM HEPES buffer, pH 7.2, containing 1 mM lucigenin and 100 mM $NaNO_3$. The solution was then sonicated for 30 min at 50 °C and vortexed intermittently for 15-20 min. After that, the solution was subjected to a freeze-thaw cycle 12-13 times and again was sonicated 10 times (40-sec sonication followed by 20-sec

incubations in ice water). The LUVs were prepared by extrusion using an Avanti Mini-Extruder (Avanti Polar Lipids, Alabaster, AL) through 200-nm pore-size polycarbonate membranes according to the manufacturer's protocol. The unencapsulated dye was removed using a gel filtration (Sephadex G-50) column with 20 mM HEPES buffer, pH 7.2, containing 100 mM $NaNO_3$. The final volume of the collected vesicle solution was adjusted to 500 µL with 20 mM HEPES buffer, pH 7.2, containing 100 mM $NaNO_3$. The final lipid concentration was 13.62 mM (assuming 100 % lipid regeneration). For the transport activity assay, the first 2920 µL of 20 mM HEPES buffer, pH 7.2, containing 100 mM $NaNO_3$, 50 µL of the DPPC-LUV⊃lucigenin (concentration of stock solution = 13.62 mM), and 20 µL of 5M NaCl was taken in a 3 mL fluorescence cuvette, and the cuvette was placed in the fluorescence spectrophotometer under slow stirring conditions. After that, compounds (10 µL from a 5 µM stock solution in DMSO) were added to the solution to achieve a concentration ratio of 1 25,000 for the compound and lipids. The lucigenin fluorescence-based kinetic measurements were performed as mentioned above.

**2.4.7.8 Transport Activity across DPPC-LUV⊃lucigenin (DPPC Assay) —** DPPC assay was performed using a Fluoromax-4 spectrofluorometer (Horiba Scientific, Singapore) connected with a refrigerated system for temperature control (where the temperature was regulated using a temperature controller).[17] In this assay, 2920 µL of 20 mM HEPES buffer, pH 7.2 containing 100 mM $NaNO_3$, and 50 µL of the DPPC-LUV⊃lucigenin was taken in a 3 mL fluorescence cuvette. 10 µL of DMSO stock solution of the compounds 1e and 1f was added to the cuvette (to make the anionophore and lipid ratio of 1: 25,000).[3] The kinetic experiment was started (at t = 0 s), and lucigenin fluorescence emission was monitored, as mentioned above. The cuvette was then kept under stirring conditions, and the chamber temperature was set to 25 ºC. After 50 sec, NaCl (20 µL, 5 M) was added to initiate the $Cl^-$ influx kinetics. Finally, to terminate the kinetic experiment, the vesicles were lysed by adding 20% Triton X-100 (20 µL) in the cuvette at t = 450 sec, and fluorescent measurements were continued for another 50 sec (i.e., up to t = 500 sec).

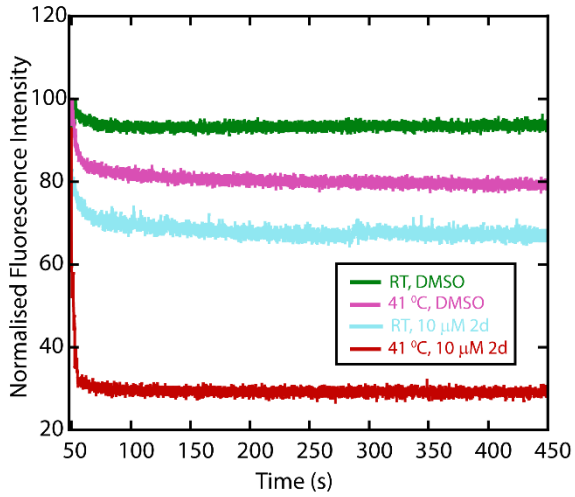


**Figure 2.15.** Temperature-dependent lucigenin assay to demonstrate the carrier-mechanistic pathway of $Cl^-$ transport activity of compound **2d** across DPPC-LUV⊃lucigenin at 25 °C and 41 °C.

**2.4.7.9 U-tube experiment —** The Classical U-tube experiment was performed according to the reported procedure to confirm the mechanistic pathway for $Cl^-$ transport by the compounds. The lipid bilayer was mimicked by using chloroform (12 mL) as the organic layer. The compound (2 mM) in chloroform was placed at the bottom of the U-tube under mild stirring. The left arm of the tube was filled with 0.1 M aqueous HCl (10 mL), and the right arm with 0.1 M aqueous $NaNO_3$ (10 mL). The $Cl^-$ concentration of the receiver end was monitored using a chloride-ISE. In the meantime, the pH of the receiver end was monitored using a pH meter. $H^+/Cl^-$ cotransport by the compound was observed by monitoring the right arm of the tube using both a pH meter and an ISE.

**2.4.7.10 Preparation of EYPC−LUV⊃carboxyfluorescein —** A thin lipid film was prepared by evaporating a solution of 154 μL EYPC (50 mg/mL stock in chloroform), and 39 μL cholesterol (25 mg/mL stock in chloroform) in vacuo for 4 h.[19] After that lipid film was hydrated with 800 $\mu$L buffer (10 mM HEPES, 10 mM NaCl, 50 mM carboxyfluorescein (CF), pH 7.2) for 1 h with occasional vortexing of 4−5 times and then subjected to freeze-thaw cycle (≥ 15 times). The vesicle solution was extruded through a polycarbonate membrane with 200 nm pores 19 times (has to be an odd number) to give vesicles with a mean diameter of ~ 200 nm. The extracellular dye was removed by size-exclusion chromatography (Sephadex G-50) using 10 mM HEPES buffer (100 mM NaCl, pH 7.2). Final concentration: ~25 mM EYPC-

CHOL lipid; intravesicular solution: 10 mM HEPES, 10 mM NaCl, 50 mM CF, pH 7.2; extravesicular solution: 10 mM HEPES, 100 mM NaCl, pH 7.2.

**2.4.7.11 Carboxyfluorescein leakage assay —** To clean and dry the fluorescence cuvette, 50 µL of the lipid solution and 2940 µL of 10 mM HEPES buffer, 100 mM NaCl, pH 7.2, were taken and kept in a slowly stirring condition by a magnetic stirrer equipped with the fluorescence instrument (at $t$ = 0 s). The CF fluorescence emission intensity time course, $F_t$, was observed at $\lambda_{em}$ = 517 nm ($\lambda_{ex}$ = 492 nm). Compound **2d** was added at $t$ = 50 s, and at $t$ = 450 s, 20 µL of 20% Triton X-100 was added to lyse the vesicles and achieve 100% chloride influx. This study confirmed that the integrity of the bilayer membranes is intact in the presence of compound **2d**.

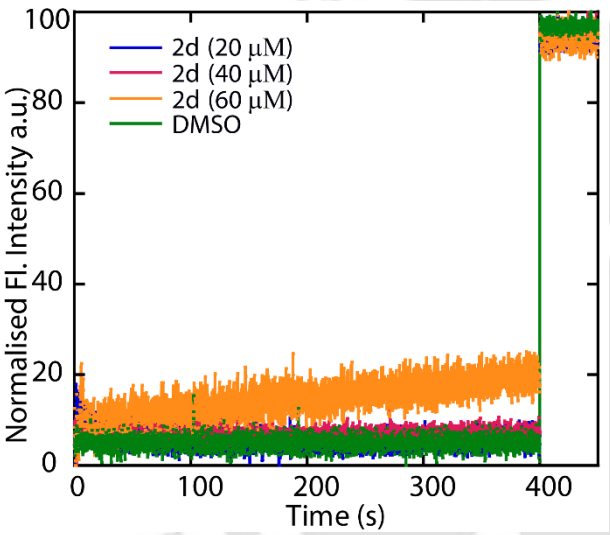


**Figure 2.16.** Carboxy fluorescein leakage assay of compound **2d** across EYPC-CHOL-LUVs.

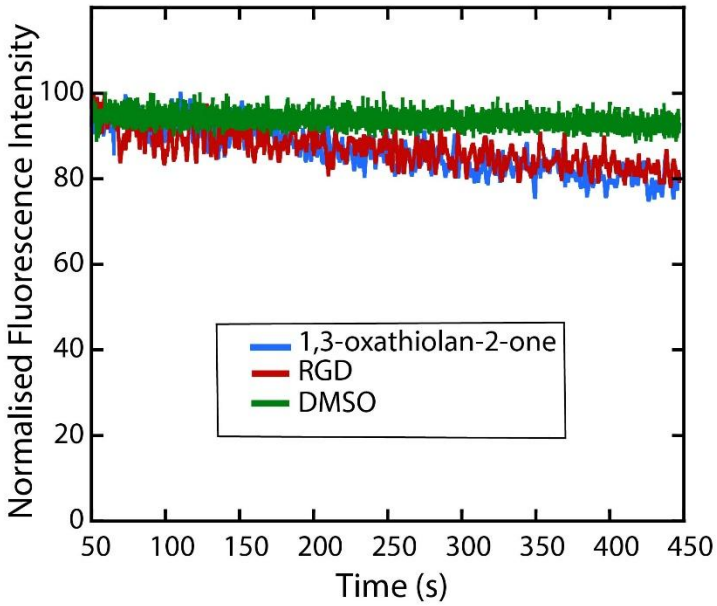


**Figure 2.17.** The $Cl^-$ transport activity of control compounds.

**2.4.8 Confocal Studies with GUV:**

**2.4.8.1 Ion transport measurements using GUVs-floated in the solution ─** In a clean and dry glass vial, EYPC, cholesterol, and DPPS (from the respective stock solution) were taken in the molar ratio of 6:3.5:0.5 and dried under vacuum for 6 hours. To that lipid film, 200 µL of light liquid paraffin oil was added and sonicated for 30 minutes until the lipid film gets completely dissolved in the oil. After that, 20 µL of the upper buffer (100 mM HEPES, 200 mM sucrose, 1 mM lucigenin in $H_2O$, pH = 7.4) was added, and the solution was mixed thoroughly to form an emulsion. The emulsion was then carefully added to 500 µL of the lower buffer (100 mM HEPES, 200 mM glucose in $H_2O$, pH = 7.4) in a centrifuge tube, and the mixture was thoroughly pipetted up and down to mix everything. The emulsion was centrifuged for 15 minutes at 10000 rpm to remove the oil and the extravehicular dye. This process was repeated for 4-5 times for maximum removal of paraffin oil from the solution. The final precipitate (GUVs) was mixed with 100 µL of lower buffer (final vesicle conc. of 15 mM). The microscopic images were collected, and/ or video was recorded using these floating GUVs.

**2.4.8.2 Ion transport measurements using GUVs coated on the glass surface ─** GUVs were prepared by following the reported methods with minor modifications. In an acid-washed glass vial, N-(3,4-dihydroxyphenethyl)palmitamide and DPPS solutions were taken in the molar ratio of 1:4 and dried under vacuum for 6 hours. The mixture was dissolved in 0.1 mL of tetrahydrofuran/water (9:1 v/v) mixture, and the solution was injected to 0.9 mL 5 mM PBS buffer of pH 5.6 (final conc. of 0.2 mM). The solution was then sonicated for 5 minutes. The prepared vesicle solution was directly used for the glass coating. The vesicle solution was drop-cast on the surface of a glass-bottom disk and incubated overnight at 37 °C. Finally, the substrate was washed by HEPES buffer thoroughly.

The prepared GUV solution (100 µL) mixed with compound **2d** (10 µM) was placed on a hydrophobic-coated glass-bottom dish. The GUVs were allowed to settle down for 5 hours. After that, a NaCl solution (100 mM) was added. At this stage, the image was captured (on a Nikon ECLIPSE Ts2R fluorescence microscope) before and after the addition of NaCl, in the green channel and in bright field, to confirm lucigenin fluorescence quenching. Here, the decay of the lucigenin fluorescence intensity is due to Cl─ influx and consequently H+ influx (as the compound follows the $H^+/Cl^-$ antiport mechanism for its chloride transport activity).

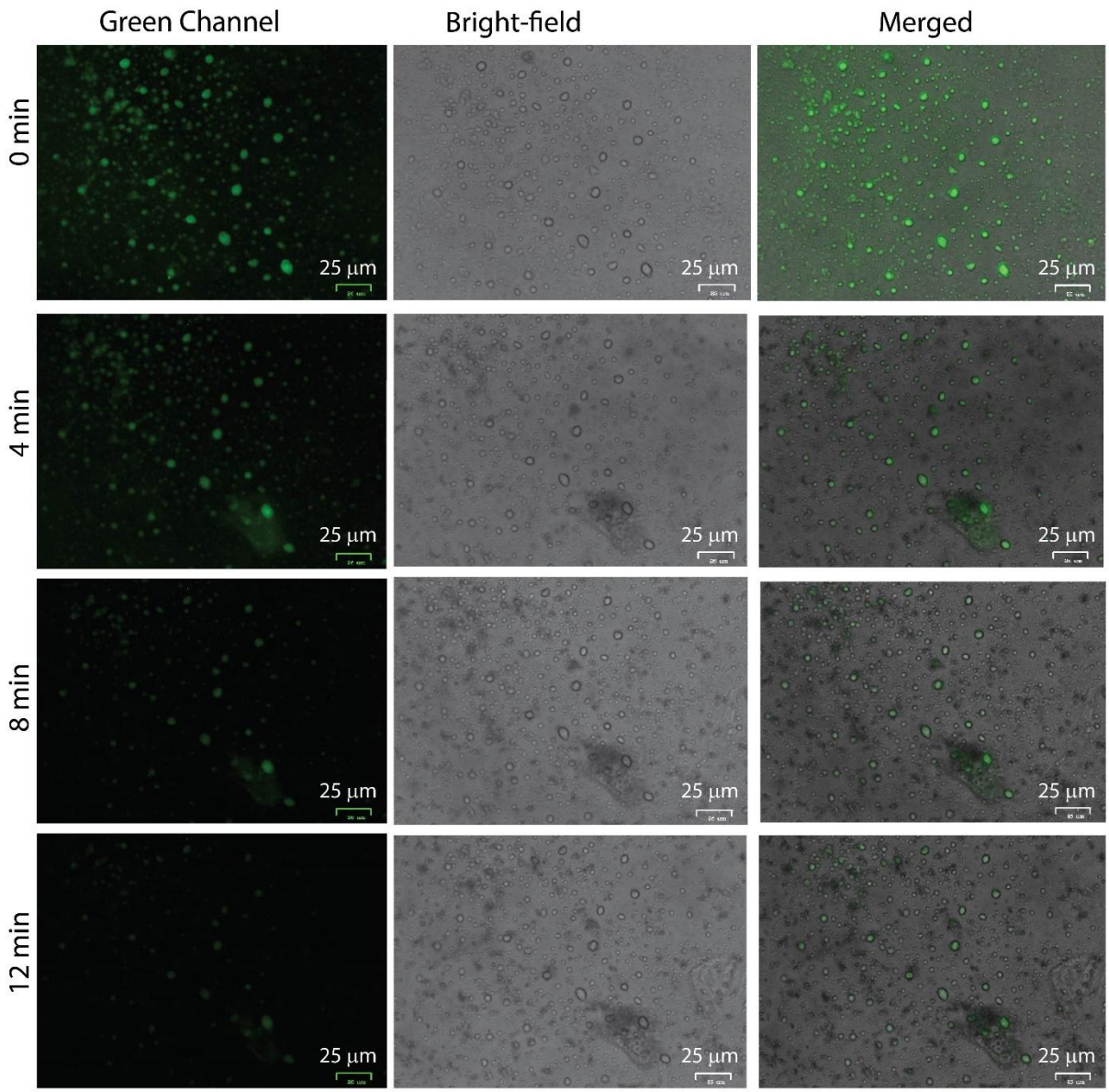


**Figure 2.18.** The time-dependent confocal microscopic images of the giant unilamellar vesicles (GUVs) after the addition of **2d**.

### 2.4.9 Cellular studies

**2.4.9.1 Cell culture —** HEK293T human kidney epithelial, A375 human melanoma cell lines, and HeLa cervical cancer, were cultured in DMEM medium. The culture medium for all the cell lines was supplemented with 10% FBS (Gibco, USA), antibiotics (Gibco, USA), and L-glutamine (Gibco, USA). They were maintained routinely at 37°C, in a humidified atmosphere with 5% $CO_2$ in an incubator (Eppendorf) in the cell culture laboratory. For each experiment, cells were first trypsinized, counted using a cell counter (Countess 3, Invitrogen, USA), and then seeded in multi-well cell culture plates as required.

**2.4.9.2 MTT-cell viability assay in DMEM cell culture media —** MTT cell viability assays were performed to assess the effect of the reported compound on the viability of the normal HEK293T or the cancer cell A375. Briefly, $1\times10^4$ cells of HEK293T or A375 were seeded in 96-well cell culture plates with 100 µL complete DMEM media and incubated overnight to allow attachment. After attaining confluency, cells were treated with different concentrations of compounds **2d** or **2.2d** under different conditions, including 10% and 1% FBS. After the treatment, MTT solution (10 µL of 5 mg MTT/mL of PBS) was added to each plate and incubated for 4 hours to allow the formation of formazan crystals. Next, formazan crystals were dissolved by using acidified IPA and incubated for 30 minutes at 37 °C. The absorbance was measured using a multimode microplate reader (EPOCH, BioTek, Agilent, USA) at 570 nm. All experiments were performed at least three times, and relative cell viability (%) was expressed as a percentage of untreated/control cells.

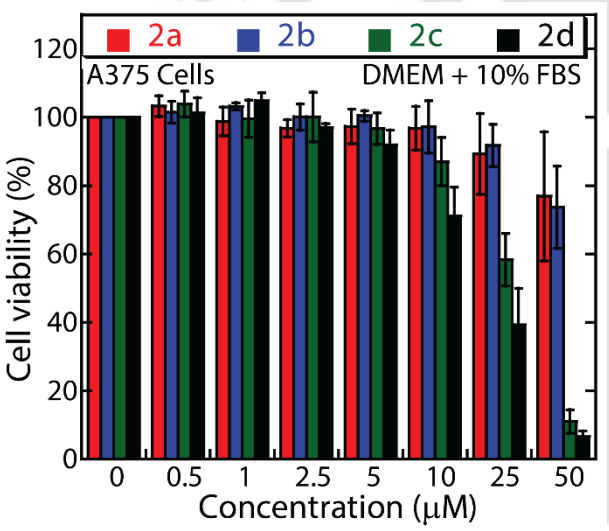


**Figure 2.19.** Viability of A375 cells treated (24 h) with selected compounds.

**2.4.9.3 MTT-cell viability assay in HBSS buffer —** MTT assays were repeated in the A375 cell line using HBSS (Hank's balanced salt solution) buffer in the presence and absence of $Cl^-$. Hank's balanced salt solution with $Cl^-$ has the following composition: 136.9 mM NaCl, 5.5 mM KCl, 0.34 mM $Na_2HPO_4$, 0.44 mM $KH_2PO_4$, 0.81 mM $MgSO_4$, 1.25 mM $CaCl_2$, 5.5 mM D-glucose, 4.2 mM $NaHCO_3$ and 10 mM HEPES (pH 7.4) Hank's balanced salt solution without $Cl^-$ was prepared using 136.9 mM Na-gluconate, 5.5 mM K-gluconate, 0.34 mM $Na_2HPO_4$, 0.44 mM $KH_2PO_4$, 0.81 mM $MgSO_4$, 1.25 mM Ca-gluconate, 5.5 mM D-glucose, 4.2 mM $NaHCO_3$ and 10 mM HEPES (pH 7.4). Briefly, $1x10^4$ numbers of A375 cells were seeded in 96-well cell culture plates with 100 µL complete DMEM media, and after overnight incubation, the media was replaced with HBSS buffer (with $Cl^-$ and without $Cl^-$) containing

10% FBS for drug treatment. Cells in HBSS buffers were exposed to different doses of compound **2d** and incubated for 24 h. After the treatment, MTT solution was added to each plate and incubated for 4 hours. Next, formazan crystals were dissolved in acidified IPA, and absorbance was measured using a multimode microplate reader (BioTek, Agilent, USA) at 570 nm. All experiments were performed at least three times, and relative cell viability (%) was expressed as a percentage of untreated/control cells.

#### 2.4.9.4 Statistical Analysis

For all the biological experiments, at least 3 different experiments were performed, and the data are presented as mean ± SD.

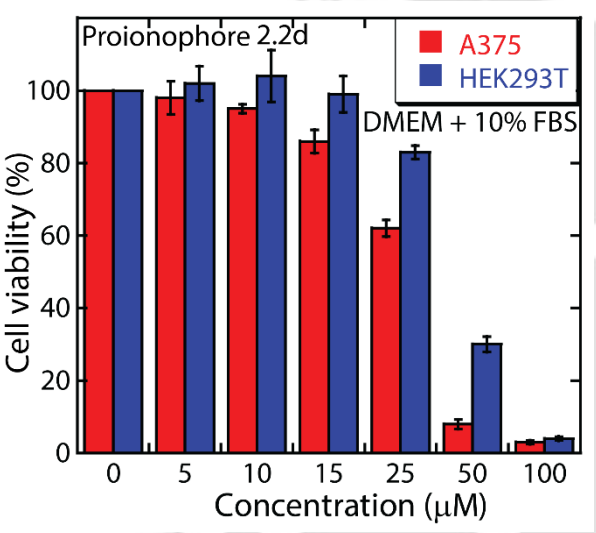


**Figure 2.20.** Viability of A375 and HEK293T cells treated (24 h) with different concentrations of proionophore **2.2d** in the presence of 10% FBS.

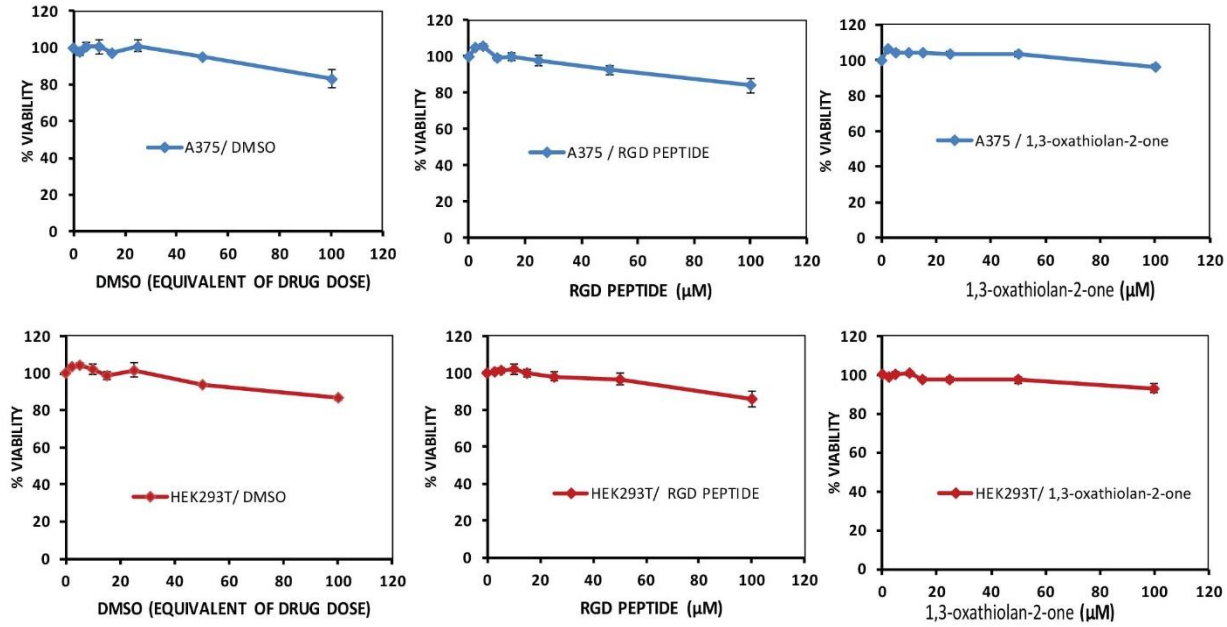


**Figure 2.21.** Viability of A375 and HEK293T cells treated (24 h) with different concentration of DMSO, RGD-peptide and 1,3-oxathiolan-2-one in the presence of 10% FBS.

**Note:** The compound reported by Gale and coworkers are bis-urea moieties (Chem. Sci., 2013, 4, 103-117), whereas we reported phenylene-based bisthiourea compounds with a free phenolic OH group. Gale and coworkers reported that molecules follow $Cl^-/NO_3^-$ antiport as well as $H^+/Cl^-$ symport pathway, but the carrier molecule **2d** has specifically $H^+/Cl^-$ transport activity. Also, our anionophore was attached to the RGD peptide via a carbonate and S-S linker, making it more interesting because anionophore **2.2d** showed 5.4-fold lower toxicity towards normal cells than cancer cell lines. The RGD-peptide helps selectively deliver the ion carriers to cancer cells rather than normal cells. We presume there is a significant difference in the structure and activity of the ionophores, as reported by Gale et al. and others (Chem. Sci., 2013, 4, 103-117).

**2.4.10 HPLC-based analysis of anionophore**

**e (2d) regeneration from control proanionophore (2.3)**

The HPLC analysis was performed to confirm the regeneration of active ionophore **2d** from the control proanionophore **7**. The control proanionophore **2.3** (10 μM) was incubated in PBS buffer containing 10 mM GSH at 37 °C. At 12 h, incubated samples were recorded. Time-dependent studies confirm the successful release of compound **2d** from the control proanionophore **2.3**. (Detector: UV light used at 250 nm). HPLC analysis was performed using Ascentis® express C18, 2.7 μm HPLC column. The optimized gradient mobile phase of PBS buffer/acetonitrile was used with a 0.5 mL/min flow rate. This study confirmed the successful

release of compound **2d** from the control proionophore **7**. (UV light used: 250 nm). The gradient used: 0-5 min- 40% buffer:60% $CH_3CN$; 5-10 min- 20% buffer:80% $CH_3CN$; 10-12 min- 5% buffer: 95% $CH_3CN$; 12-15 min- 50% buffer: 50% $CH_3CN$.

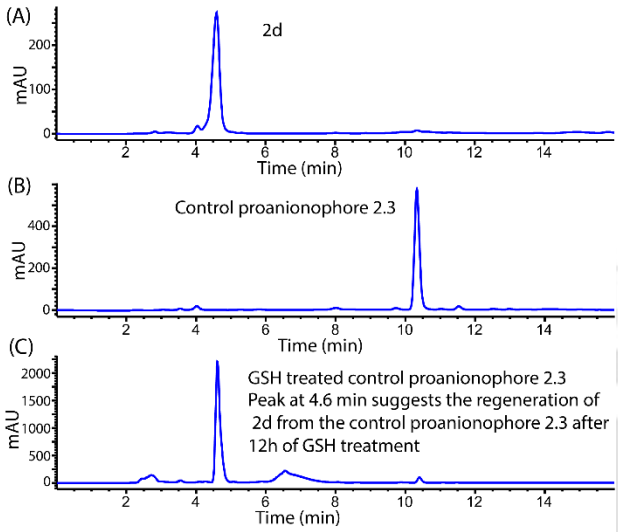


**Figure 2.22.** HPLC-based regeneration assay for control proanionophore **7**. HPLC traces of only anionophore **2d** (A), only control proanionophore **2.3** (B), and GSH-treated control proanionophore **2.3** for 12 h (C).

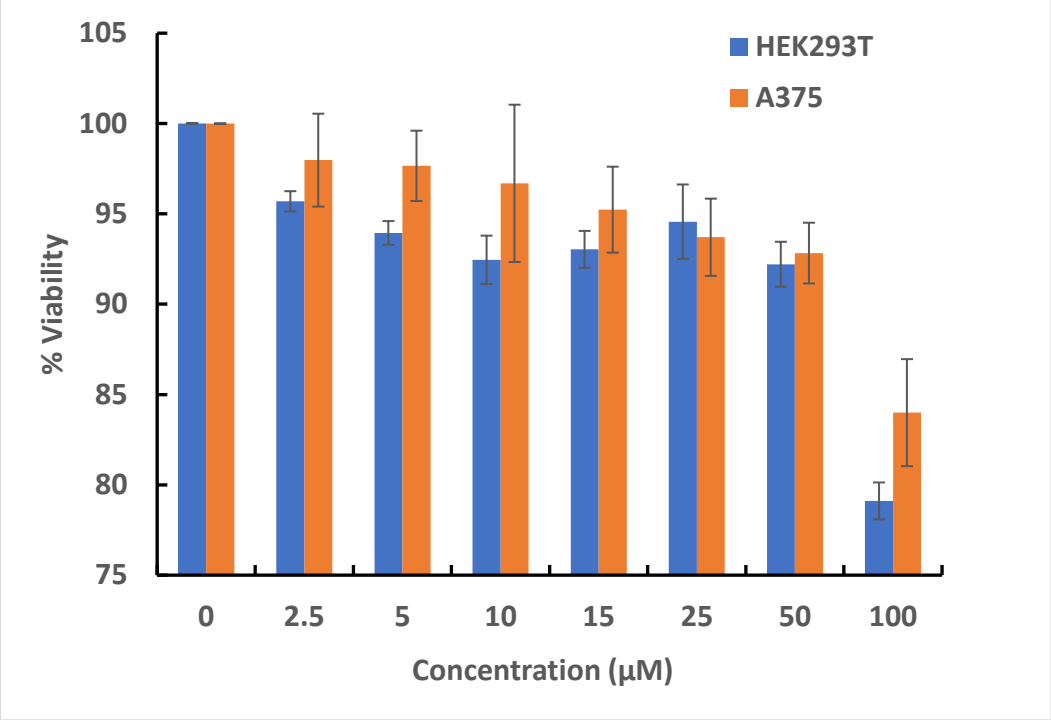


**Figure 2.23.** Viability of HEK293T and A375 cells treated (24 h) at different concentrations of control proanionophore **2.3.**

### 2.4.11 NMR Spectra of the synthesized compounds

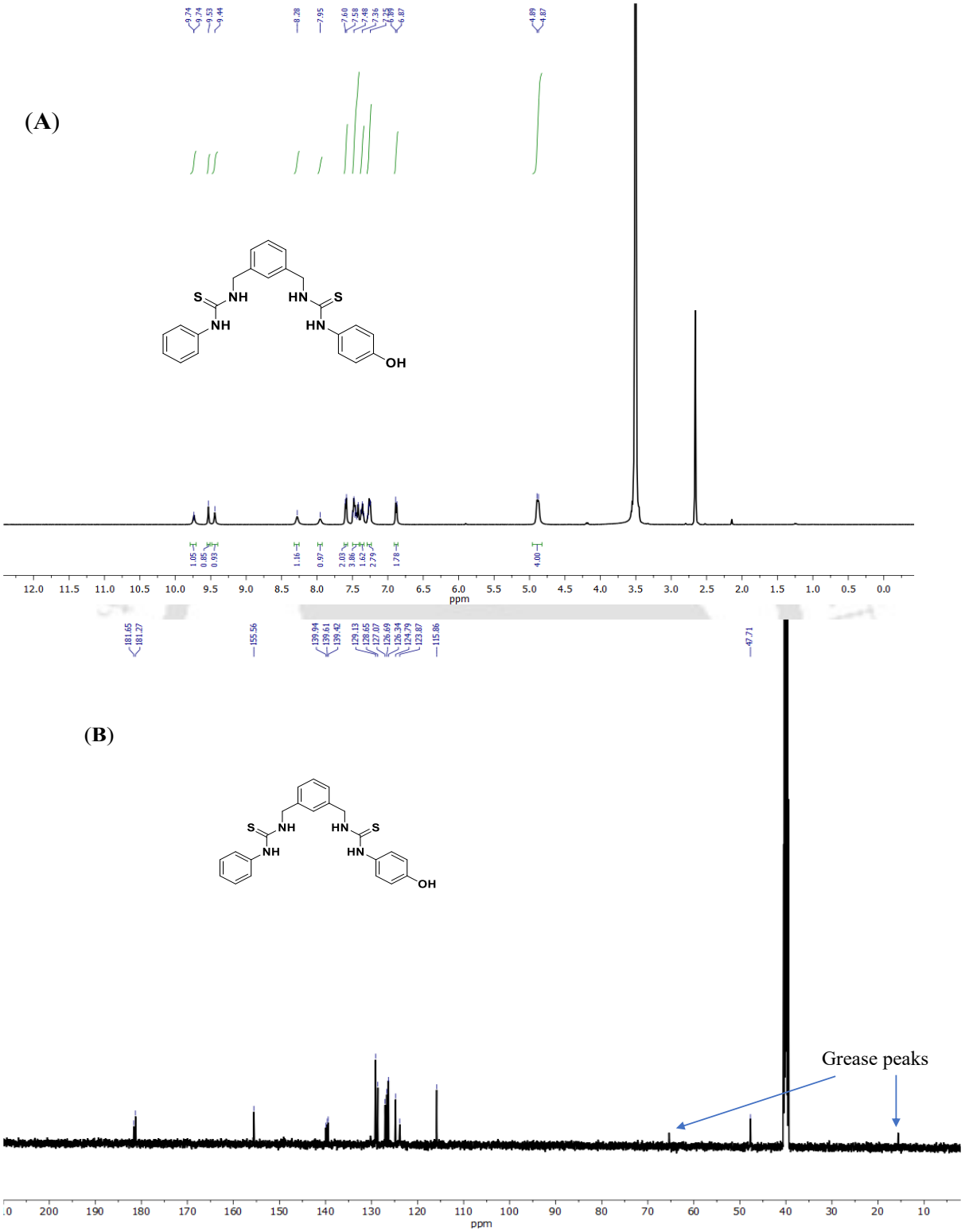


**Figure 2.24.** $^{1}H$ (A) and $^{13}C$ (B) NMR of **2a** in DMSO-$d_6$.

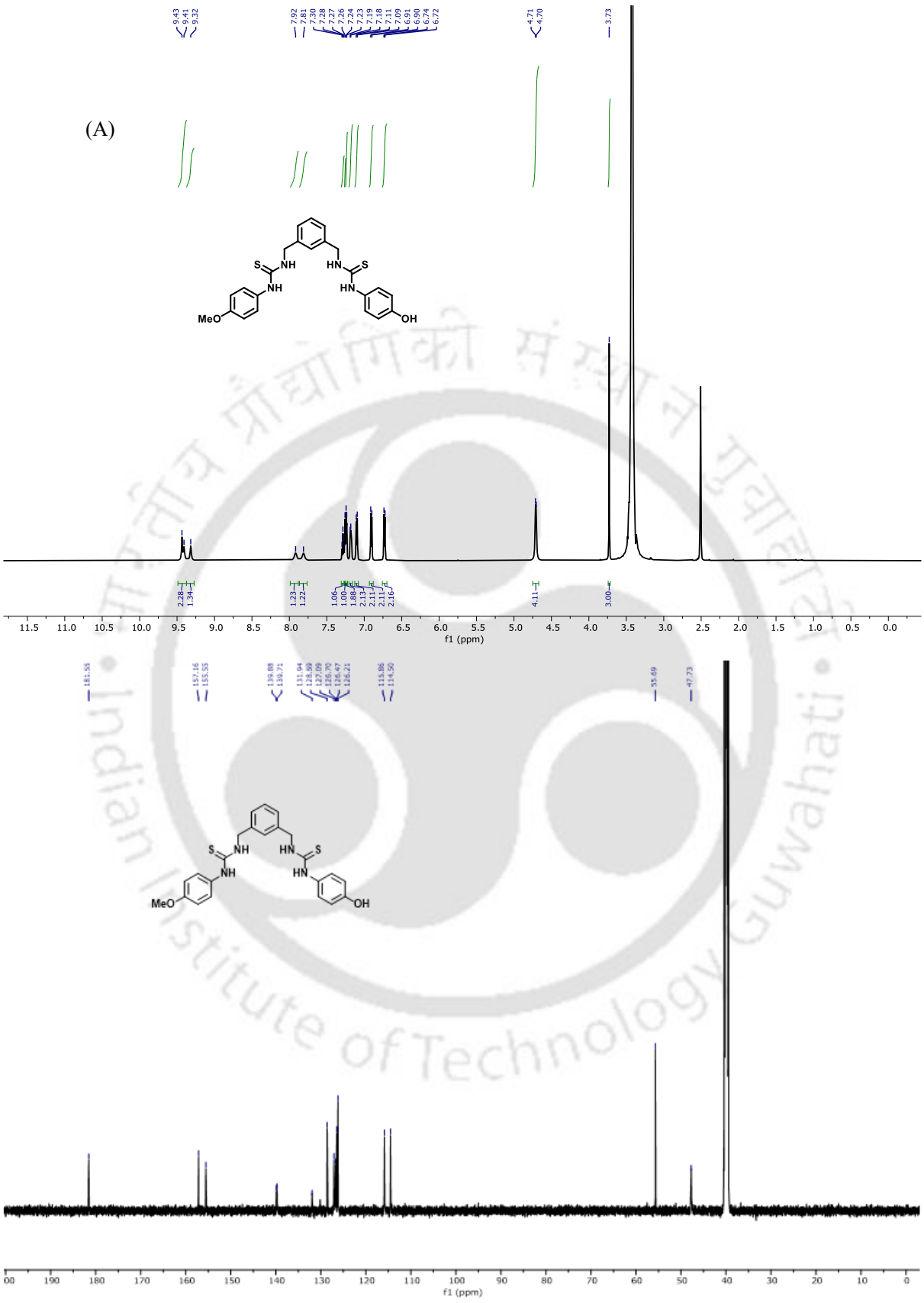


**Figure 2.25.** $^{1}H$ (A) and $^{13}C$ (B) NMR of **2b** in DMSO-$d_6$.

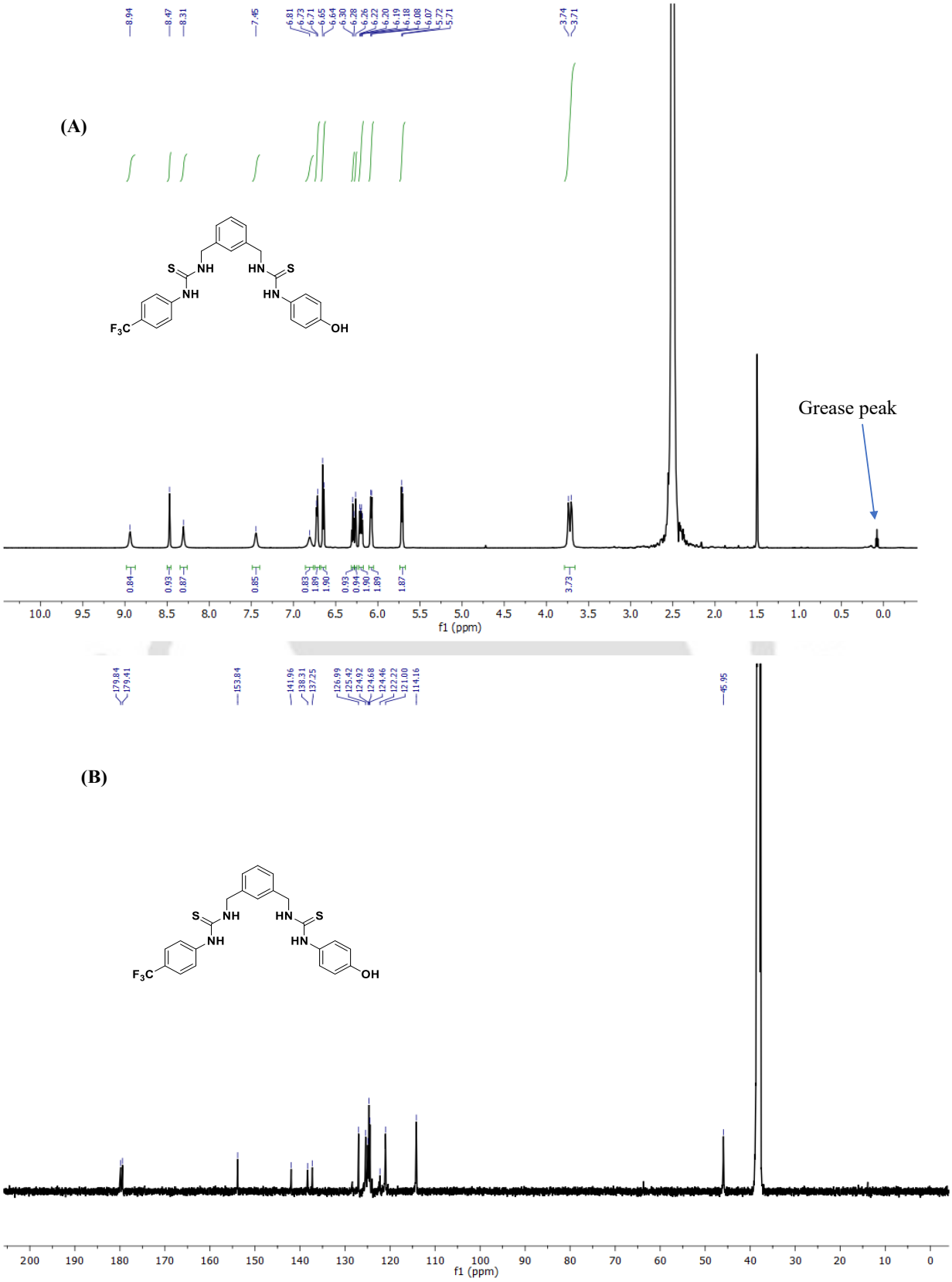


**Figure 2.26.** $^{1}H$ (A) and $^{13}C$ (B) NMR of **2c** in DMSO-$d_6$

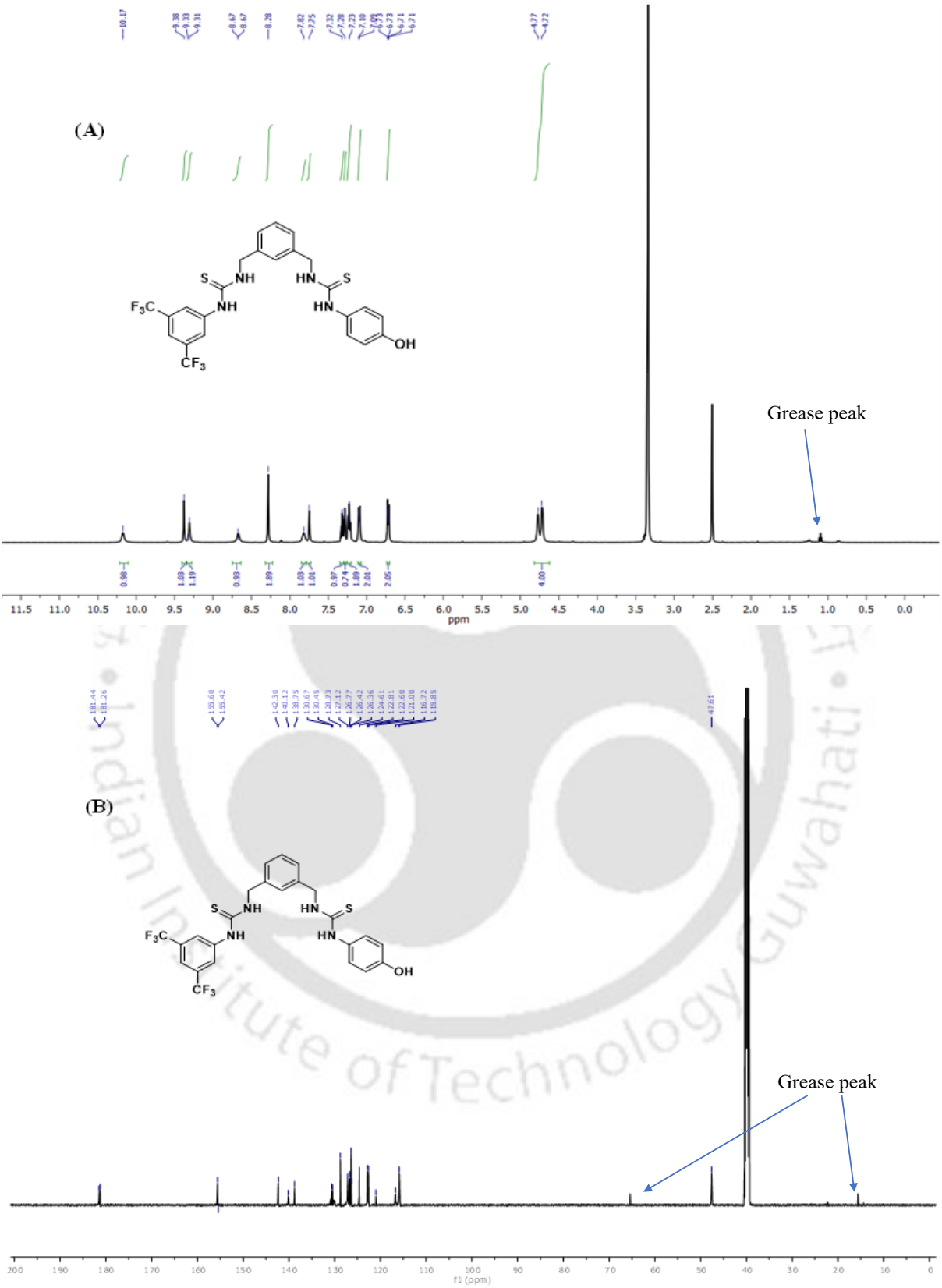


**Figure 2.27.** $^{1}$H (A) and $^{13}$C (B) NMR of compound **2d** in DMSO-$d_6$.

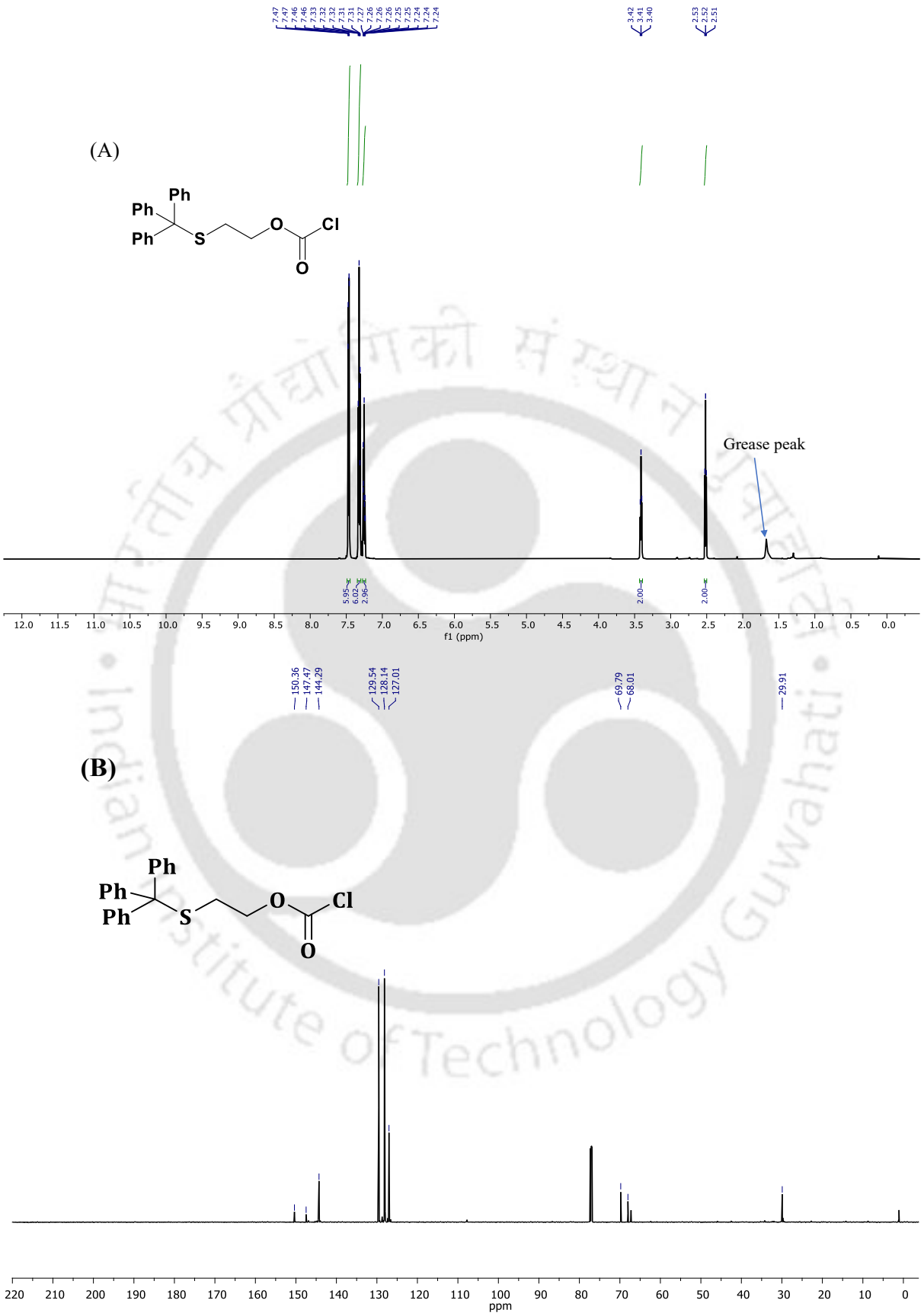


**Figure 2.28.** $^{1}H$ (A) and $^{13}C$ (B) NMR of 2-(tritylthio)ethyl carbonochloridate in $CDCl_3$.

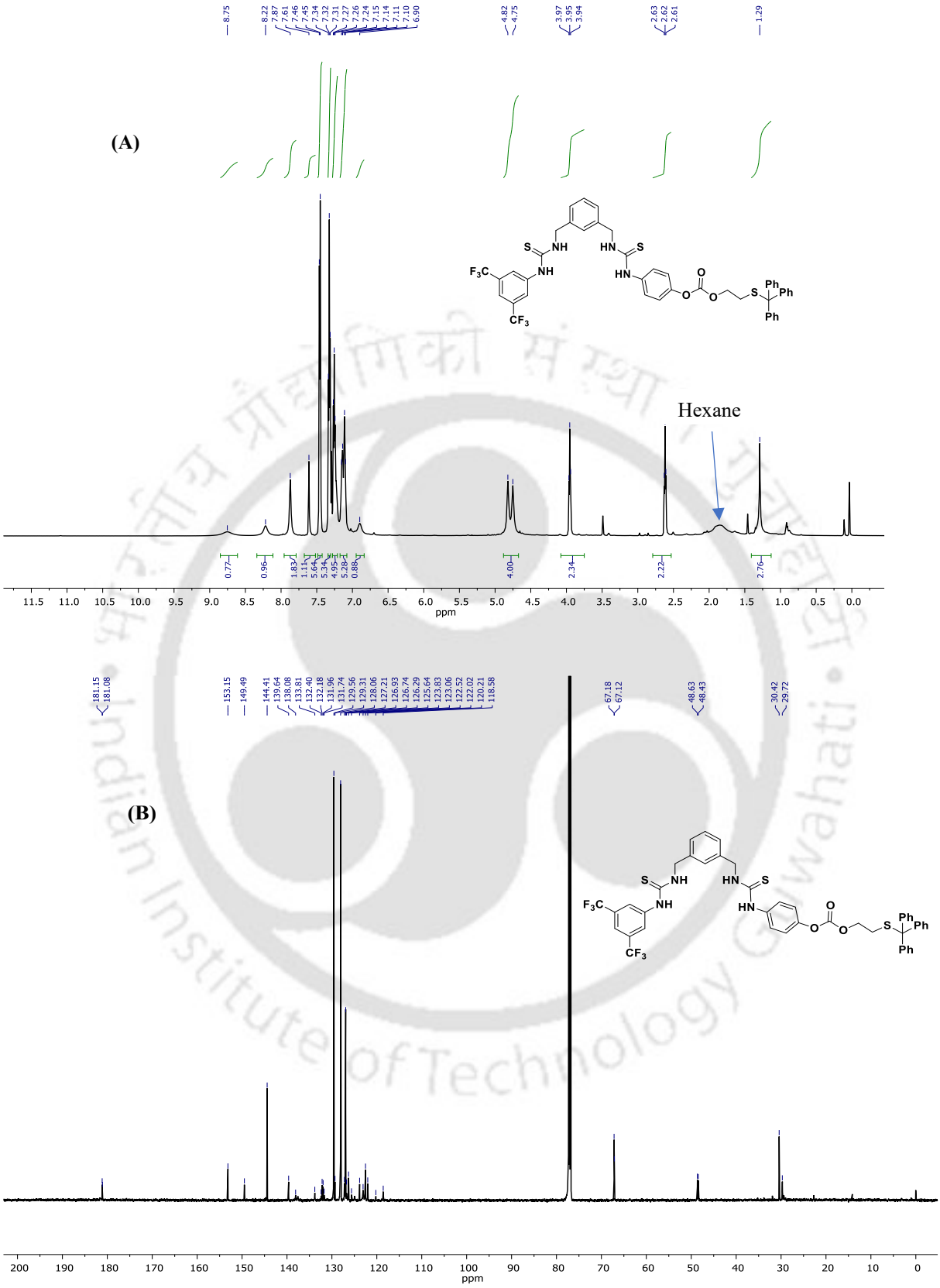


**Figure 2.29.** $^{1}H$ (A) and $^{13}C$ (B) NMR of 4-(3-(3-((3-(3,5-bis(trifluoromethyl)phenyl) thioureido) methyl) benzyl) thioureido) phenyl(2-mercaptoethyl) carbonate in $CDCl_3$.

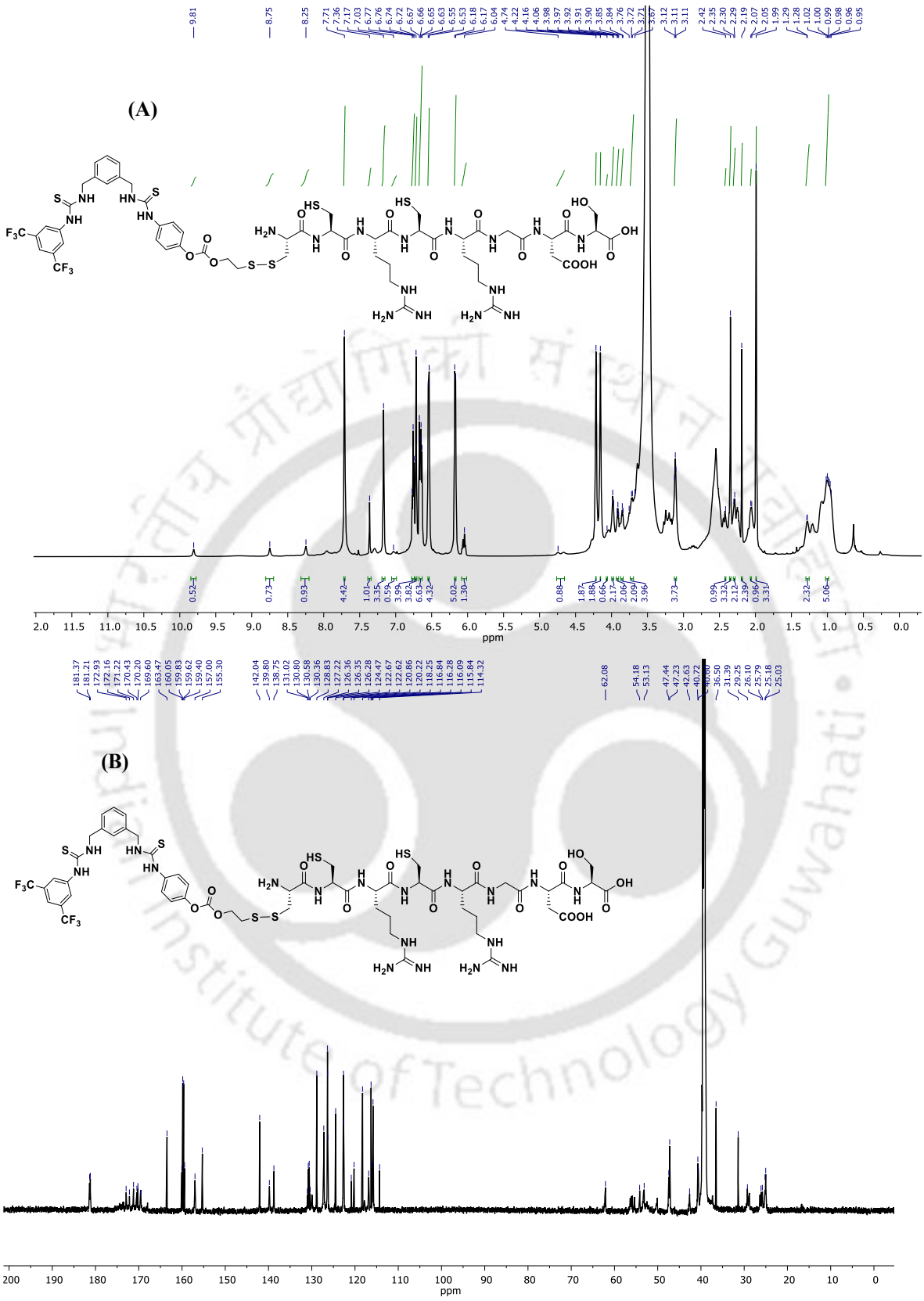


**Figure 2.30.** $^{1}H$ (A) and $^{13}C$ (B) NMR of **2.2d** in DMSO-$d_6$.

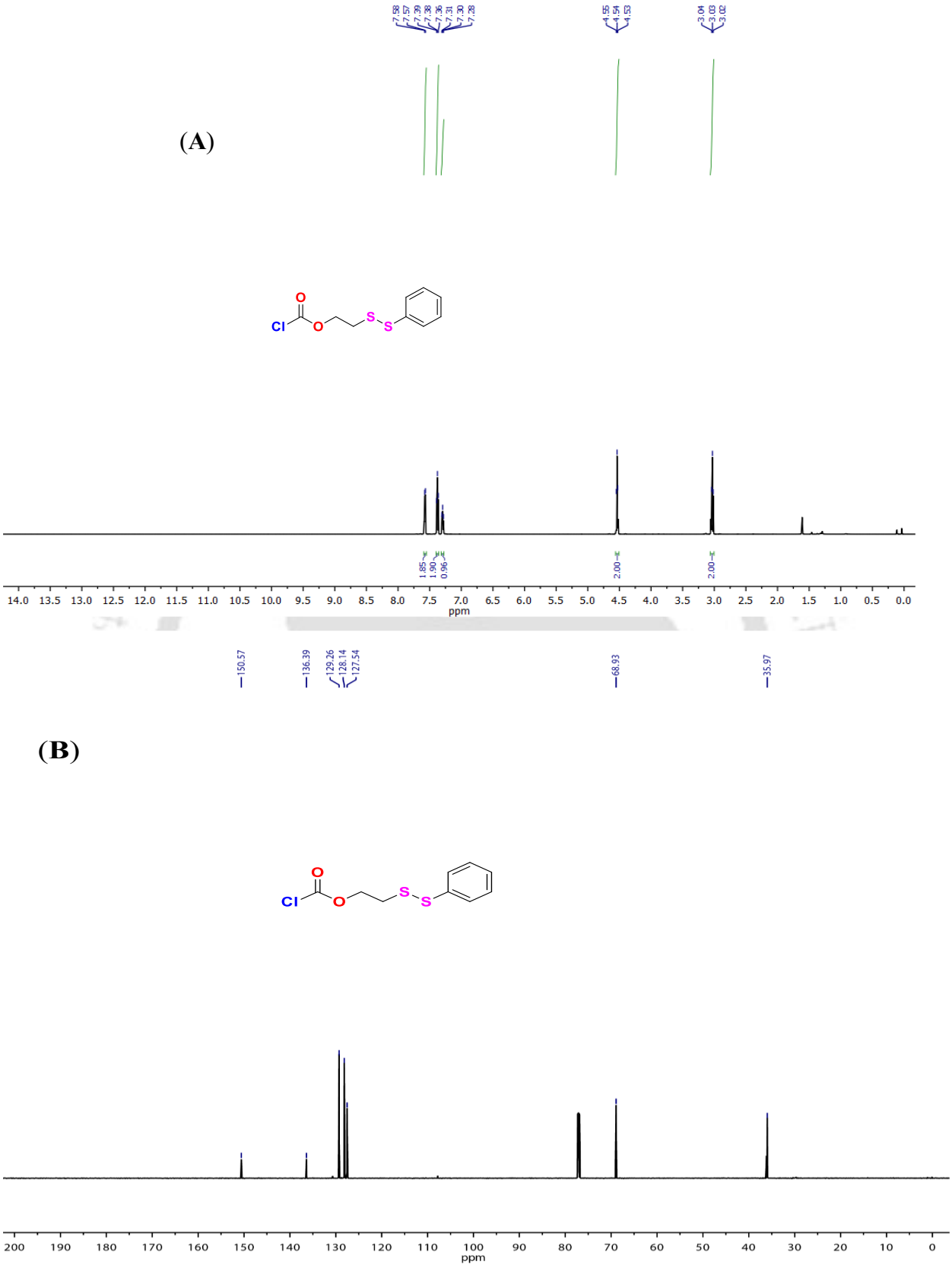


**Figure 2.31.** $^{1}H$ NMR (A) and $^{13}C$ NMR (B) of 2-(phenyldisulfaneyl)ethylcarbonochloridate in $CDCl_3$ solvent.

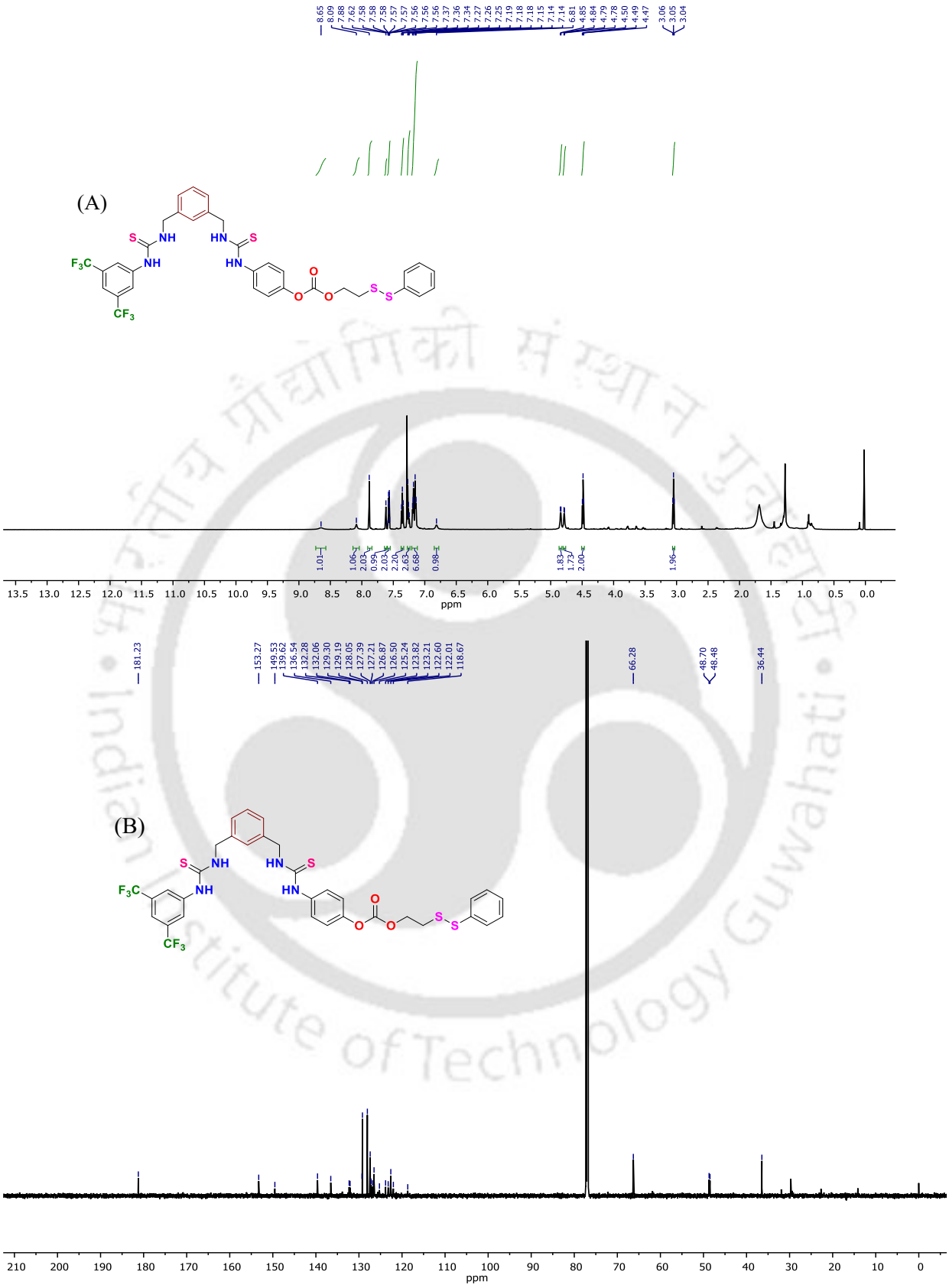


**Figure 2.32.** $^{1}H$ NMR (A) and $^{13}C$ NMR (B) of compound **2.3** in $CDCl_3$ solvent.

**2.5 HPLC trace of compound:**

HPLC analysis was performed using Ascentis® express C18, 2.7 µm HPLC column. The optimized gradient mobile phase of PBS buffer/acetonitrile was used with a 0.5 mL/min flow rate.

The gradient used: 0-5 min- 20% buffer:80% $CH_3CN$, 5-10 min- 10% buffer:90% $CH_3CN$, 10-13 min- 5% buffer:95% $CH_3CN$, 13-15 min- 30% buffer:70% $CH_3CN$.

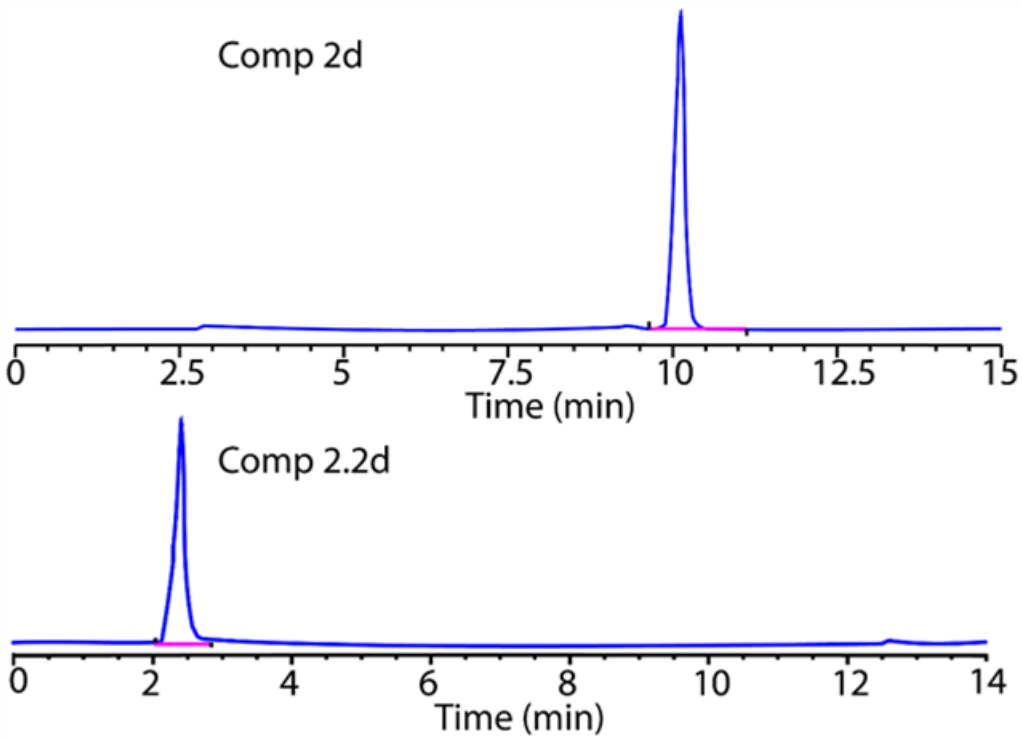


**Figure 2.35.** HPLC trace of compound **2d** and **2.2 d** ensuring more than 97% purity level.

## 2.6 Reference


1. Davis, J. T.; Gale, P. A.; Quesada, R., Advances in anion transport and supramolecular medicinal chemistry. *Chem. Soc. Rev.* **2020**, *49*, 6056−6086.
2. Akhtar, N.; Biswas, O.; Manna, D., Biological applications of synthetic anion transporters. *Chem. Commun.* **2020**, *56*, 14137−14153.
3. Akhtar, N.; Pradhan, N.; Saha, A.; Kumar, V.; Biswas, O.; Dey, S.; Shah, M.; Kumar, S.; Manna, D. Tuning the Solubility of Ionophores: Glutathione-Mediated Transport of Chloride Ions across Hydrophobic Membranes. *Chem. Commun.* **2019**, *55*, 8482−8485.
4. Malla, J. A.; Umesh, R. M.; Yousf, S.; Mane, S.; Sharma, S.; Lahiri, M.; Talukdar, P. A Glutathione Activatable Ion Channel Induces Apoptosis in Cancer Cells by Depleting Intracellular Glutathione Levels. *Angew. Chem., Int. Ed.* **2020**, *59*, 7944−7952.
5. Fares, M.; Wu, X.; Ramesh, D.; Lewis, W.; Keller, P. A.; Howe, E. N.; Pérez-Tomás, R.; Gale, P. A. Stimuli-Responsive Cycloaurated "OFF-ON" Switchable Anion Transporters. *Angew. Chem., Int. Ed.* **2020**, *59*, 17614−17621.
6. Sharma, S.; Roy, N. J.; Kuttanamkuzhi, A.; Save, S. N.; Lahiri, M.; Talukdar, P.; Abraham, B.; Sharma, V. K. NAD(P)H:Quinone Acceptor Oxidoreductase 1 (NQO1) Activatable Salicylamide $H^+/Cl^-$ Transporters. *Chem. Eur. J.* **2023**, *29*, e202301412.
7. Wu, X.; Gale, P. A. Measuring Anion Transport Selectivity: A Cautionary Tale. *Chem. Commun.* **2021**, *57*, 3979−3982.
8. Shinde, S. V.; Talukdar, P. An Anion Receptor That Facilitates Transmembrane Proton–Anion Symport by Deprotonating Its Sulfonamide N–H Proton. *Chem. Commun.* **2018**, *54*, 10351−10354.
9. Saha, A.; Akhtar, N.; Kumar, V.; Kumar, S.; Srivastava, H. K.; Kumar, S.; Manna, D. pH-Regulated Anion Transport Activities of Bis(iminourea) Derivatives across the Cell and Vesicle Membrane. *Org. Biomol. Chem.* **2019**, *17*, 5779−5788.
10. Okon, I. S.; Zou, M.-H. Mitochondrial ROS and Cancer Drug Resistance: Implications for Therapy. *Pharmacol. Res.* **2015**, *100*, 170−174.
11. Ahmadiankia, N. In Vitro and In Vivo Studies of Cancer Cell Behavior under Nutrient Deprivation. *Cell Biol. Int.* **2020**, *44* (8), 1588−1597.
12. Shen, R.; Zhang, B.; Liu, J.; Yi, M.; Chen, Y.; Fang, J. Palladium-Catalyzed In Vivo Bioorthogonal Activation of N,N-Dialkyl-α-hydroxymethyl Acrylamide for Efficient Payload Release. *J. Mater. Chem. B* **2025**, *13*, 4849−4860.

13. Das, S.; Biswas, O.; Akhtar, N.; Patel, A.; Manna, D. Multi-Stimuli Controlled Release of a Transmembrane Chloride Ion Carrier from a Sulfonium-Linked Procarrier. *Org. Biomol. Chem.* **2020**, *18* (45), 9246−9252.

14. Rocard, L.; Berezin, A.; De Leo, F.; Bonifazi, D. Templated Chromophore Assembly by Dynamic Covalent Bonds. *Angew. Chem., Int. Ed.* **2015**, *54* (52), 15739−15743.

15. Malla, J. A.; Upadhyay, A.; Ghosh, P.; Mondal, D.; Mondal, A.; Sharma, S.; Talukdar, P. Chloride Transport across Liposomes and Cells by Nontoxic 3-(1H-1,2,3-Triazol-1-yl)benzamides. *Org. Lett.* **2022**, *24* (23), 4124−4128.

16. Roy, N. J.; Save, S. N.; Sharma, V. K.; Abraham, B.; Kuttanamkuzhi, A.; Sharma, S.; Lahiri, M.; Talukdar, P. NAD(P)H:Quinone Acceptor Oxidoreductase 1 (NQO1) Activatable Salicylamide $H^+/Cl^-$ Transporters. *Chem. Eur. J.* **2023**, *29* (51), e202301412..

17. Shinde, S. V.; Talukdar, P. A Dimeric Bis(melamine)-Substituted Bispidine for Efficient Transmembrane $H^+/Cl^-$ Cotransport. *Angew. Chem., Int. Ed.* **2017**, *56* (15), 4238−4242..

18. Akhtar, N.; Pradhan, N.; Barik, G. K.; Chatterjee, S.; Ghosh, S.; Saha, A.; Satpati, P.; Bhattacharyya, A.; Santra, M. K.; Manna, D. Quinine-Based Semisynthetic Ion Transporters with Potential Antiproliferative Activities. *ACS Appl. Mater. Interfaces* **2020**, *12* (23), 25521−25533.

19. Biswas, O.; Akhtar, N.; Vashi, Y.; Saha, A.; Kumar, V.; Pal, S.; Kumar, S.; Manna, D. Chloride Ion Transport by PITENINs across the Phospholipid Bilayers of Vesicles and Cells. *ACS Appl. Bio Mater.* **2020**, *3* (2), 935−944.

# *Chapter 3*

## *Development of supramolecular ion channels to engineer $Zn^{2+}$ transport mediated chemical-to-optical signal transduction*

### 3.1 Background and objective of current work:

Metal ions are pivotal in enzymatic catalysis, functioning as tightly bound cofactors at the active sites of core of protein. They help in orienting substrates, stabilizing the transition states, and accelerate reaction rates, making them indispensable for a wide range of biochemical processes.[1] Driven by the essential roles metal ions play in human physiology, the development of synthetic metal ion transporters has emerged as a crucial frontier in supramolecular chemistry and chemical biology. Metal ions such as $Na^+$, $K^+$, $Ca^{2+}$, $Fe^{2+}$, $Cu^{2+}$, and $Zn^{2+}$ are vital cofactors in enzymatic catalysis, maintain osmotic and pH balance, and regulate neurotransmission, signal transduction, and cell proliferation.[2] Controlled ion transport movement of these ions underly critical processes like nerve impulse propagation, muscle contraction, and hormone release. Synthetic metalophore and channels are able to closely mimic the function of natural ion transport proteins, offering potential therapeutic strategies for diseases linked to ion imbalance, including neurodegenerative disorders, cardiovascular diseases, and cancers.[3] Hence, careful design for cation transporters is necessary for precise control over metal ion selectivity, binding affinity and membrane permeability while avoiding cytotoxicity. Structural components like hydrophobic framework, coordinating ligands, and stimuli responsive elements are further considered for precise regulation. Beyond therapeutics, these synthetic ion transporter systems are important tools in constructing artificial cells and molecular devices which can mimic natural biologically relevant processes.[4] By harnessing these systems, we can better explain complex biological ion transport mechanisms and develop new technologies which bridge living cells with artificial cells.

Synthetic metalophore has a prime aspect, that is incorporating metal-binding sites exhibiting selectivity and high affinity for the desired ion. Thus, designing synthetic metal ion transporters or chelators requires precise control over structural features to ensure selective binding, membrane permeability, and reversibility towards targeted cations. The core functional groups include amines, amides, carboxylates, phosphonates, and hydroxamates, each capable of forming coordinate bonds with metal centres by donating electron density. Macrocyclic ligands like cryptands and crown ethers are classic scaffolds, using oxygen donor atoms to selectively complex alkali and alkaline earth metal ions. Pincer ligands, recognised by a tridentate framework often containing nitrogen, phosphorus, or sulphur donors, offer rigid and preorganized chelation sites, enhancing both kinetic stability and binding strength. N-containing heteroaromatic systems like phenanthroline, bipyridine, and terpyridine provide planar, multidentate binding sites especially suited for transition metals, facilitating π-back

bonding and electronic stabilization. Schiff bases, formed from the condensation of aldehydes and amines, introduce imine nitrogen atoms that efficiently coordinate to metals, and can be further functionalized to tune lipophilicity and electronic properties. Catechols and hydroxypyridinones are notable for chelating hard metal ions such as $Fe^{3+}$ and $Al^{3+}$ through oxygen donors, often applied in medicinal chelation therapy. The spatial arrangement of donor groups is equally critical; rigid or semi-rigid backbones reduce entropic penalties upon binding, while flexible linkers may accommodate a range of ionic radii but risk reduced selectivity. Attaching hydrophobic tails or amphiphilic moieties promotes membrane association and transport, while stimuli-responsive linkers (e.g., disulfides cleaved by GSH) allow controlled release in targeted environments. Overall, successful metal ionophores must balance high binding affinity, selectivity, and suitable lipophilicity to achieve efficient transmembrane transport, making structural design a multidisciplinary challenge informed by coordination chemistry, supramolecular design, and biological context.[5]

By imitating these processes, scientist can develop systems that sense and transmit chemical signals, leading to smarter therapeutic strategies. For instance, stimuli-responsive nanochannels and ion transporters can be engineered to activate only inside targeted cells, guided by factors like low pH or high glutathione levels.[6] This targeted approach helps deliver therapy right where it's needed, limiting side effects on healthy cells something especially valuable in cancer treatment, where disturbing ionic balance can trigger cancer cell death. Beyond therapy, these molecular communication systems can act as amplifiers, turning subtle biochemical changes into clear optical or electrical signals.[7] This opens up exciting possibilities for highly sensitive biosensors and early disease detection. Embedding such systems in artificial cells or vesicles can even recreate natural cell-to-cell communication, allowing researchers to build synthetic tissues that respond adaptively to their environment. Cells are the fundamental functional and structural units of all living organisms, operating through intricate and highly regulated mechanisms. To investigate the underlying mechanism to decipher how these complex cellular systems sustain vital biological functions, simplified model cells are developed to unravel the processes governing natural cell behaviour.[8, 9] Living cells function as self-optimised units capable of executing complex processes within confined systems. While natural cells originated from non-living matter through evolutionary processes, reconstructing life from non-living components remains crucial for understanding the origins.[10] By merging nanotechnology, chemistry, and biology, molecular communication offers not just a deeper

understanding of cellular signaling but also innovative tools for precision medicine, diagnostics, and smart biomaterials.

Inspired by intriguing structural combinations for metalophore and unexplored aspect of its applicability in the direction of molecular communication, we have designed our current chapter where pincer cavity and salicylaldehyde-imine based arc shaped molecule utilised as a metal ion transporter. Further its prospect was explored in the direction of molecular communication where it generates optical signal from given chemical signal like natural signal transduction process.

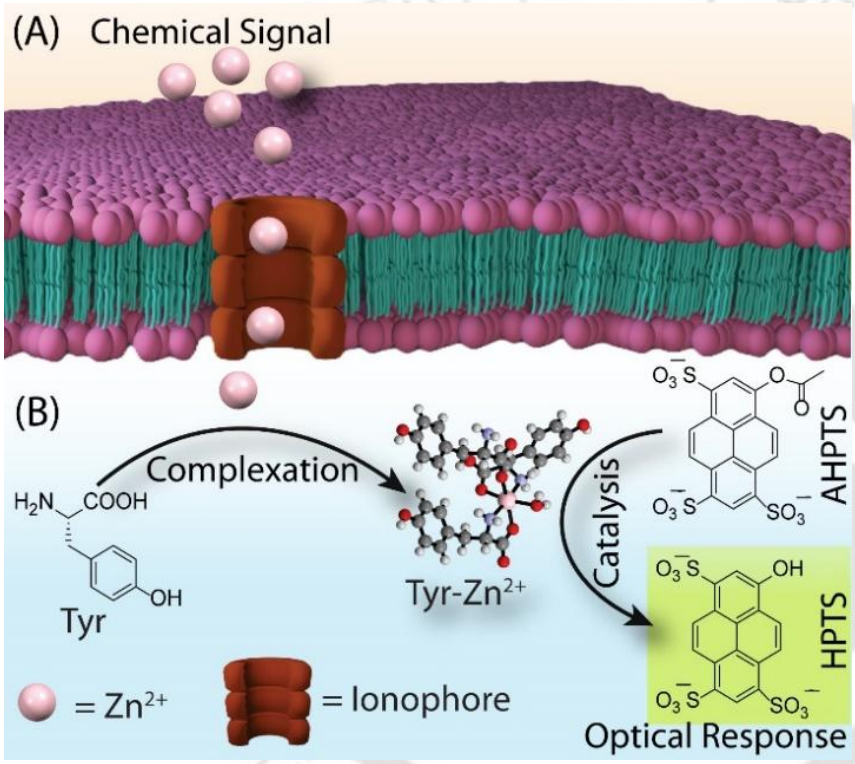


**Figure 3.1.** (A) Schematic representation of the formation of a supramolecular ion channel within the lipid bilayer that regulates the influx of $Zn^{2+}$ ions and (B) the in-situ complexation of $Zn^{2+}$ ions with tyrosine (Tyr) leads to catalysis, producing an optical response within the intravesicular environment.

### 3.2 Results and discussion:

#### 3.2.1 Design and synthesis of Synthetic $Zn^{2+}$ transporter:

We developed a molecular communication system where synthetic $Zn^{2+}$ ion transporters selectively deliver $Zn^{2+}$ across lipid bilayers, while $Zn^{2+}$-bound tyrosine (Tyr) acts as a catalytic site to convert non-fluorescent ester substrates into fluorescent products, enabling chemical-to-optical signal transduction. Salicylaldehyde-based imine derivative was shown to form

supramolecular channels validated by electrophysiological studies representing, to our knowledge, the first synthetic $Zn^{2+}$ ion channel. Translocated $Zn^{2+}$ ions complex with Tyr inside vesicles, catalysing the hydrolysis of substrates like AHPTS and CFDA-SE to produce fluorescence. Removing any component ($Zn^{2+}$ transporter, $Zn^{2+}$, or Tyr) stops signal generation, thus functioning as a three-input AND logic gate.

To develop potent transmembrane $Zn^{2+}$ transporters, we synthesized a series of salicylaldehyde-based imine derivatives of 2-(6-(6-amino-1H-benzo[d]imidazol-2-yl) pyridine-2-yl)-1H-benzo[d]imidazol-5-amine (**3.2a-d**) with comparable logP values (Table 3.1)[11]. The structure of 2,6-bis(2-benzimidazolyl) pyridine provides a conformationally restrained environment, while the salicylaldehyde-based imine moieties offer the necessary sites for $Zn^{2+}$ binding and membrane transport. Two probable metal binding sites are present in these arc-shaped molecules: the core moiety and the imine N and -OH group of the salicylaldehyde. The core moiety is a well-known complexation site for 3d-transition metals.[12] Compounds **3.1**, **3.3,** and **3.4** were synthesized to investigate the role of different moieties in transmembrane $Zn^{2+}$ transportation (Figure 3.2).

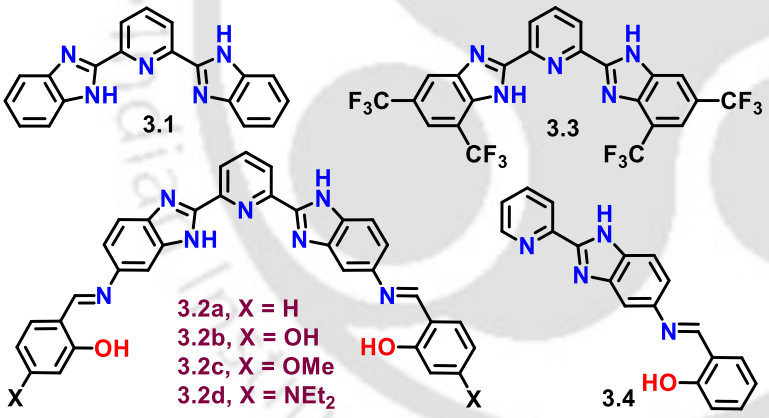


**Figure 3.2.** Structures of synthesized transporters

### 3.2.2 Morphological investigation of ion transporter:

Field emission scanning electron microscopy (FESEM) was used for investigating the morphology of compound **3.2a** in the aqueous and organic medium at the same sample concentration (1 mM) after slow evaporation from water and $CHCl_3$, respectively. The FESEM images of the samples prepared in an aqueous medium revealed the agglomeration property of the compound **3.2a**. However, the FESEM images of the samples prepared in the $CHCl_3$ medium revealed a tubular morphology of compound **3.2a**, suggesting its characteristic self-assembly pattern within the hydrophobic medium of the lipid bilayer (Figure 3.3).

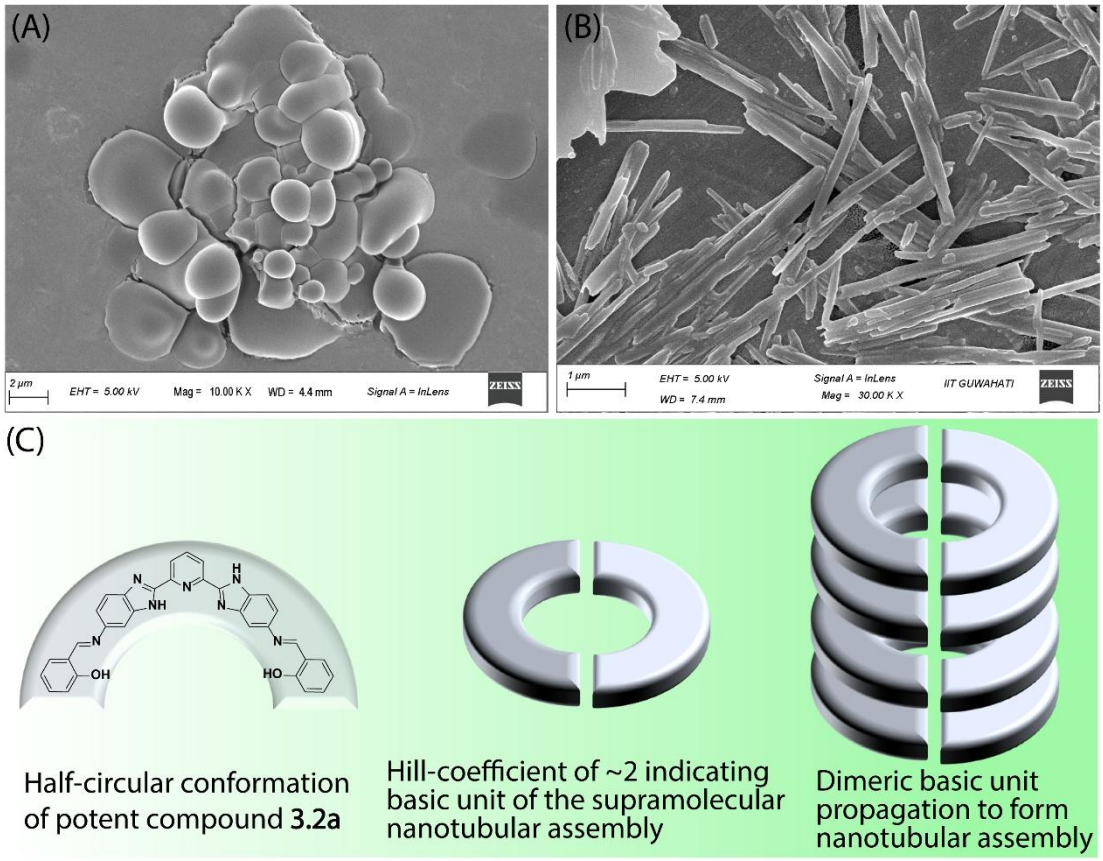


**Figure 3.3.** Representative FESEM images of compound **3.2a** in the (A) aqueous and (B) $CHCl_3$ medium. (C) Probable structural arrangement hypothesis for compound **3.2 a**.

### 3.2.3 Ion transport studies of synthesized transporter:

The effect of the synthesized compounds on the transmembrane ion transport was initially investigated by monitoring the fluorescence signal modulation of pentapotassium salt of magnesium green (MgG) using large unilamellar vesicles (LUVs) as model membranes. The LUVs were prepared from egg-yolk phosphatidylcholine (EYPC) and cholesterol (CHOL) (8:2 molar ratios) by encapsulating MgG in 10 mM HEPES buffer, 100 mM NaCl, 100 µM ethylenediaminetetraacetic acid (EDTA), pH 7.0. The LUVs were dispersed in 10 mM HEPES buffer, 100 mM NaCl, 100 µM EDTA, pH 7.0 (Figure 3.4 A). EDTA was used in low concentration to avoid interference from transition metal ions. The fluorescence kinetics measurement was initiated with the equilibration of $ZnCl_2$ (1 mM) at 0s and after the addition of the compound at 50s. The enhancement of MgG fluorescence intensity ($\lambda_{ex}$ = 506 nm, $\lambda_{em}$ = 531 nm) was attributed to the $Zn^{2+}$ ions transport activity of compounds.[4] The outcome of the compound screening studies revealed compound **3.2a** with the highest transport efficacy (78%) among its various derivatives (Figure 3.4 B). However, compound **3.3** (comparable logP value with **3.2a**) showed negligible transport efficacy for $ZnCl_2$. This suggests either its non-

involvement or a strong complexation ability of the core moiety, which may hinder its transport efficacy. To assess the significance of the imine bond and hydroxyl group, control compound **3.4** was synthesized, and its transport study revealed a transport efficacy of approximately 37% for $Zn^{2+}$ ions. The other salicylaldehyde derivatives (**3.2b-d**) showed lower $Zn^{2+}$ ions transport efficacy than compound **3.2a**. This comparative study concluded that the imine-N and hydroxyl –OH groups of salicylaldehyde are responsible for the reversible binding of $Zn^{2+}$ ions. The concentration-dependent MgG assay of compound **3.2a** (Figure 3.4C) showed an $EC_{50}$ value of 167.19 ± 10.32 nM (compound **3.2a**: lipid = 1: 1.48×105) and Hill coefficient (n) 1.92 ± 0.08. (Figure 3.4 D). The calculated Hill coefficient of ≈2 indicates that more than one molecule of compound **3.2a** (positive cooperativity) might form supramolecular ion channels for transporting $Zn^{2+}$ ions.[13]

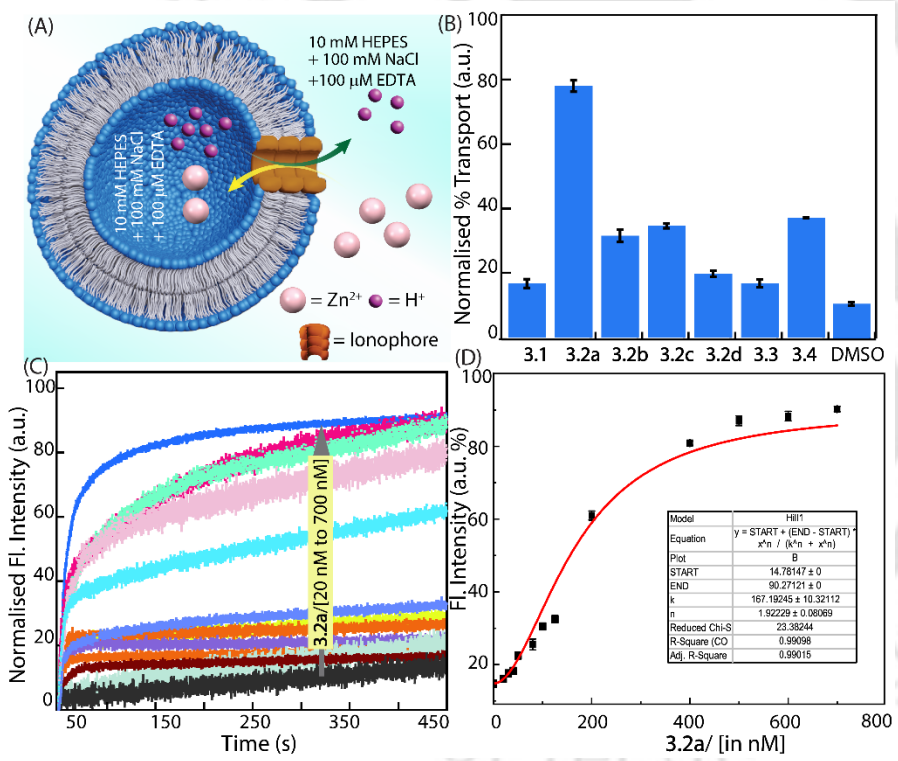


**Figure 3.4.** (A) Schematic representation of ion transport studies across EYPC/CHOL-LUVs⊃MgG vesicles. (B) Assessment of the $Zn^{2+}$ transport activity (at t = 450 s) of the synthesized compounds (300 nM) across EYPC/CHOL-LUVs⊃MgG prepared in 10 mM HEPES buffer, 100 mM NaCl, 100 µM EDTA, 50 µM MgG, pH 7.0, and dispersed in 10 mM HEPES buffer, 100 mM NaCl, 100 µM EDTA. The LUVs were equilibrated with $ZnCl_2$, and a pulse of compound **3.2a** (300 nM) was added to initiate the transport studies. (C) Concentration-dependent transmembrane $Zn^{2+}$ transport activities of compound **3.2a**. (D)

Concentration-dependent transmembrane $Zn^{2+}$ ions transport efficacy of compound **3.2a** across EYPC/CHOL-LUVs⊃MgG. The $EC_{50}$ value was calculated using the Hill equation.

[NOTE: The kinetic traces in Figure 3.4C do not indicate slow transport at low receptor concentrations. Instead, the initial steep increase in fluorescence reflects rapid $Zn^{2+}$ translocation across the membrane, consistent with a channel-mediated transport process. The subsequent plateau arises once the system approaches ion equilibration or probe saturation within the vesicle, rather than from a limitation in transport rate. Under these conditions, further increases in signal are constrained by the availability of transportable ions and the response range of the fluorescent reporter, not by the intrinsic transport efficiency of the ionophore.

Such kinetics characterised by a fast initial transport phase followed by signal saturation are well documented for supramolecular ion channels and are commonly interpreted as signatures of efficient membrane permeation rather than sluggish carrier-type behaviour. At higher receptor concentrations, the sustained increase in fluorescence reflects prolonged transport before equilibrium is reached, consistent with a higher number of active channels operating simultaneously.

Importantly, such kinetics are characteristic of channel-type transport, which typically displays a fast initial flux followed by early equilibration, whereas carrier-mediated transport generally shows a gradual, concentration-dependent increase without an early plateau due to the requirement for repeated carrier diffusion across the membrane.]

### 3.2.4 Binding and CAC studies of transporter:

The binding affinity of compound **3.2a** for $Zn^{2+}$ ions was examined through UV-vis titration of the water medium. In this experiment, a 20 μM solution of compound **3.2a** was titrated with $ZnCl_2$, gradually decreasing absorbance with each addition of $Zn^{2+}$ ions. The association constant ($K_a$) for the interaction was determined using the Bindfit v0.5 program by fitting the absorbance data to a 1:1 binding model. Under the experimental conditions, the calculated (average of three measurements) $K_a$ was $(3.13 \pm 0.17) \times 10^2\ M^{-1}$. (Figure 3.5 A) The specific concentration above which amphiphilic or self-assembling molecules spontaneously organize to form higher ordered structures like micelles, vesicles or supramolecular assemblies is known as critical aggregation constant (CAC). This parameter helps us in understanding cooperative self-assemblies, and functional properties like size and stability of the formed aggregates. We measured the CAC value of compound **3.2a** from the concentration-dependent transport study. A distinct inflection point was observed at approximately 40 nM concentration of compound

**3.2a** (Figure 3.5 B). This result suggests the initiation of supramolecular nanochannels of compound **3.2a** (> 40 nM) within the lipid bilayer of the vesicles.

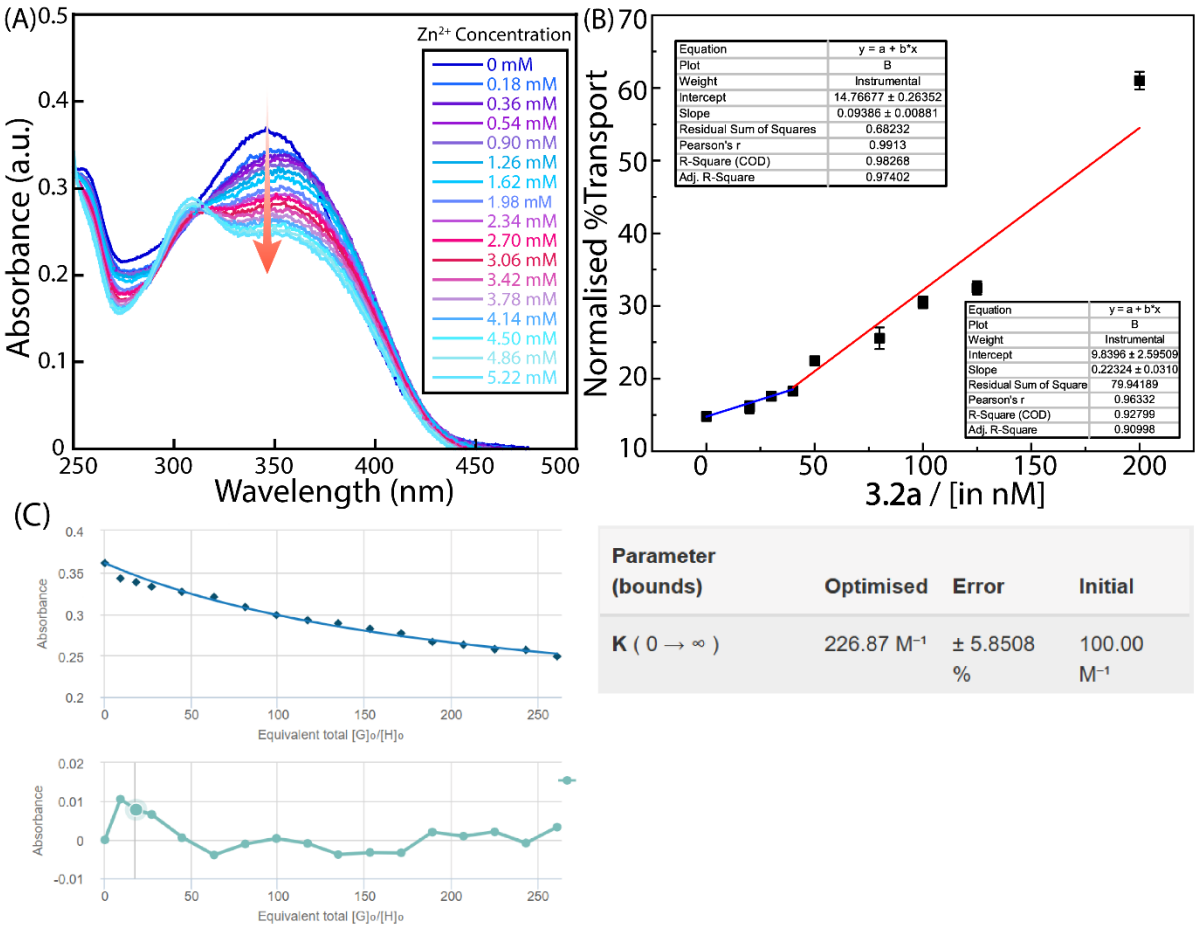


| Parameter (bounds) | Optimised | Error | Initial |
|---|---|---|---|
| K ( 0 → ∞ ) | 226.87 $M^{-1}$ | ± 5.8508 % | 100.00 $M^{-1}$ |

**Figure 3.5.** (A) Representative UV-Vis absorbance titration spectra of compound **3.2a** (20 µM) with varying concentrations of $Zn^{2+}$ ions (0-5.2 mM). (B) Measurement of critical aggregation concentration (CAC) of compound **3.2a** calculated from the concentration-dependent $Zn^{2+}$ ions transport properties across EYPC/CHOL-LUVs⊃MgG. (C) Fitting parameter obtained from bindfit v0.5.

[NOTE:

The UV vis titration of compound **3.2a** with $ZnCl_2$ shows a gradual and monotonic decrease in absorbance intensity upon incremental addition of $Zn^{2+}$ ions, consistent with the formation of a single dominant complex in solution. Although the spectra are presented as stacked plots to show the overall spectral evolution, the quantitative binding analysis was performed by extracting absorbance values at a selected wavelength and fitting them using the Bindfit v0.5 program. The experimental binding isotherm, together with the fitted curve and corresponding

residuals, confirms a good agreement between the experimental data and the calculated 1:1 binding model, with minimal and randomly distributed residuals.]

### 3.2.5 Ion selectivity studies of transporter:

By varying different ions, we get a clear picture about selectivity of the transporter molecule. Herein, we have performed cation selectivity with transition metal ions. The cation selectivity study performed for **3.2a** revealed the selectivity order to be $Zn^{2+} > Cu^{2+} > Ni^{2+} > Mn^{2+} > Fe^{3+} > Co^{2+}$ (Figure 3.6A, 3.11), and no significant changes were observed in anion selectivity studies for anion varying salts ($ZnCl_2$, $ZnBr_2$, $Zn(NO_3)_2$, $ZnSO_4$) (Figure3.6 B and 3.12). Moreover, lucigenin-based ion transport studies were performed across the bilayers of EYPC/CHOL-LUV⊃lucigenin for chloride selectivity in the absence and presence of compound **3.2a.** The assay suggested the inability of $Cl^-$ transport by compound **3.2a** under the experimental conditions (Figure 3.13).

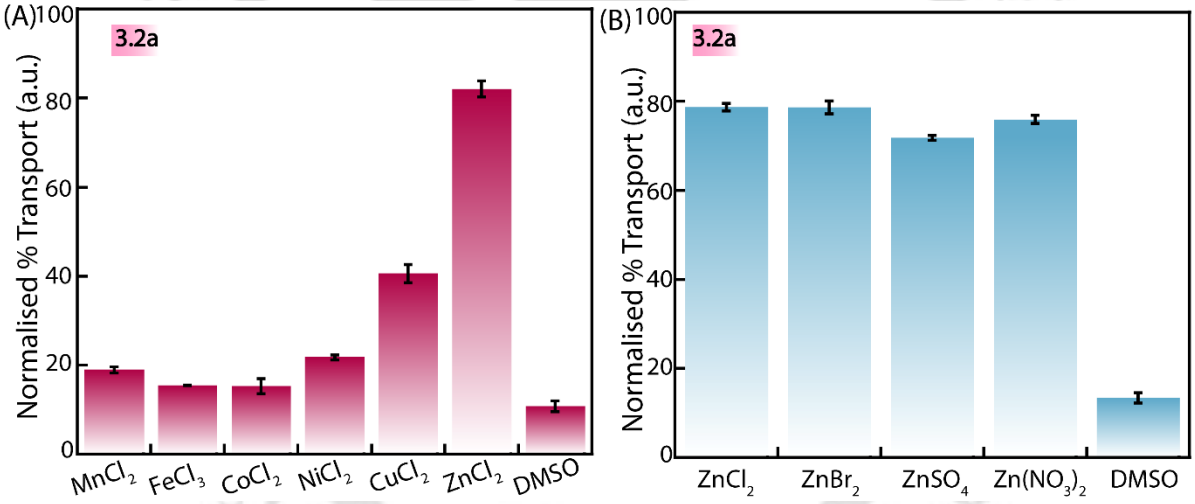


**Figure 3.6.** (A) Cation and (B) anion transport selectivity (at t = 450 s) of compound **3.2a** (300 nM) across EYPC/CHOL-LUVs⊃MgG.

### 3.2.6 Ion Transport Mechanism:

MgG-based fluorescence measurements were performed with the potent compound **3.2a** to elucidate the possible operative mechanism during the ion transport process. The ion transport studies were carried out in the presence of carbonyl cyanide-p-trifluoromethoxyphenylhydrazone (FCCP, natural $H^+$ carrier) and valinomycin (natural $K^+$ uniporter). The MgG-based transport study of compound **3.2a** in the absence and presence of FCCP showed no significant difference in the fluorescence intensity of MgG, indicating the involvement of $H^+$ ions in the transport mechanism along with $Zn^{2+}$ ions (Figure 3.7A). We

also performed ion transport studies of compound **3.2a** using fluorescein (pH-sensitive dye). An increase in fluorescence intensity of the encapsulated fluorescein suggests an efflux of $H^+$ ions by compound **3.2a** (Figure 3.14A). However, the fluorescence intensity of fluorescein was not affected by the presence of $Zn^{2+}$ ions (Figure 3.14B). Therefore, the FCCP assay and fluorescein-based ion transport studies concluded the involvement of $H^+$ ions in the transport mechanism of compound **3.2a,** along with $Zn^{2+}$ ions. The valinomycin-based ion transport studies showed an unvaried transport efficacy of compound **3.2a** with and without the uniporter, supporting no involvement of $OH^-$ ions in the mechanistic pathway (Figure 3.7B). Overall, the LUV-based transport study revealed that compound **3.2a** transports $Zn^{2+}$ and $H^+$ ions in an antiport manner. The carboxyfluorescein-based vesicle leakage assay showed no pore formation or destabilization of the vesicles in the presence of compound **3.2a** (Figure 3.15). A temperature-dependent ion transport assay was conducted using LUVs made of dipalmitoyl phosphatidylcholine (DPPC) lipids to investigate the type of ion transport pathway, whether it is via a carrier or a channel.[14] As the temperature increases, the fluidity of the membrane also increases, enhancing the efficacy of ion transport through the carrier pathway. In contrast, the efficacy of ion transport through supramolecular ion channels remains largely unchanged. Ion transport studies using DPPC-based LUVs in the presence of compound **3.2a** showed no difference in $Zn^{2+}$ transport efficacy at 30 °C and 45 °C (Figure 3.16), suggesting possible channel formation. The classical U-tube-based ion transport measurements of compound **3.2a** showed no significant increase in $Zn^{2+}$ concentration in the receiver arm, indicating compound **3.2a** could not act as a carrier through a nonpolar phase ($CHCl_3$). Meanwhile, the control U-tube-based transport study with clioquinol (a $Zn^{2+}$ carrier) showed an increase in $Zn^{2+}$ concentration over time in the receiver arm (Figure 3.17). Therefore, DPPC-based and U-tube-based ion-transport studies indicate that compound **3.2a** forms channels in a hydrophobic environment.

Real-time measurements of current across the diphytanoyl phosphatidylcholine (DPhPC) bilayer lipid membrane (BLM) were conducted to further investigate the channel-forming ability of compound **3.2a**. The lipid bilayer was prepared over the orifice in the Teflon foil connecting two electrolyte chambers containing $ZnCl_2$ (0.5 M) solution. Upon adding compound **3.2a** (4 μM), we observed rapid flickering events at different holding potentials, confirming the formation of an ion channel in the planar lipid bilayer (Figure 3.7C, 3.18). In a symmetrical solution of 0.5 M $ZnCl_2$, we measured a single-channel conductance (G) of 88 ± 7 pS, corresponding to a simple pore model with a pore diameter (d) of 1.9 Å. The change in

current with voltage (I–V plot) was further monitored with a symmetrical 0.5 M $ZnCl_2$ solution. A linear increase in current with increasing voltage was observed, confirming the ohmic behaviour of the ion channel (Figure 3.19). Additional ion conductance measurements in asymmetrical $ZnCl_2$ solution (GND:0.5 M; Active: 1 M) showed the formation of more ion channels within the planar lipid bilayer by compound **3.2a** (± 150 mV) at the same concentration (4 µM) (Figure 3.20). The ion conductance measurements in the presence of compound **3.2a** in an asymmetrical KCl solution or an asymmetrical $ZnCl_2$ solution without any compound showed no significant ion channel formation (Figure 3.21).

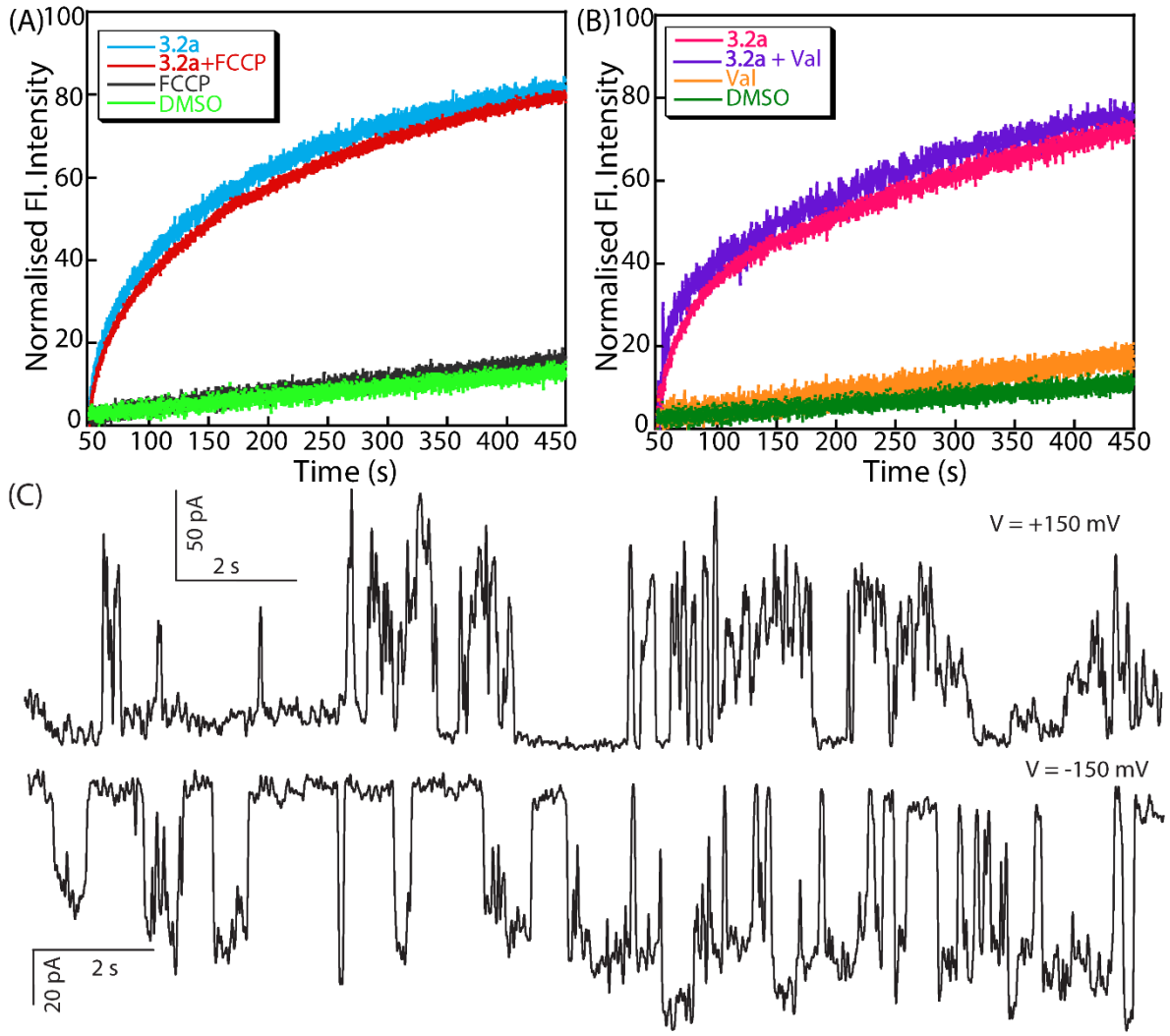


**Figure 3.7.** (A) Ion transport activity of compound **3.2a** (300 nM) in the absence and presence of FCCP (1 nM) across EYPC/CHOL-LUVs⊃MgG. (B) Ion transport activity of compound **3.2a** (300 nM) in the absence and presence of valinomycin (12 pM) across EYPC/CHOL-LUV⊃MgG prepared in 10 mM HEPES buffer containing 100 mM KCl and 100 µM EDTA, pH 7.0, and suspended in 10 mM HEPES buffer containing 100 mM NaCl and 100 µM EDTA,

pH 7.0. Val = valinomycin. DMSO (10 µL) was used as a control. (C) Ion conductance measurements of compound **3.2a** (4 µM) at +150 mV and −150 mV in symmetrical $ZnCl_2$ solution (0.5 M).

### 3.2.7 Development of $Zn^{2+}$ mediated catalytic system:

Metalloenzymes play a crucial role in biological systems. Several enzymes utilize $Zn^{2+}$ as a metal centre for their catalytic processes.[15] To mimic this natural enzyme catalysis, we attempted to develop a $Zn^{2+}$-based artificial catalytic system using natural amino acids. After experimenting with different amino acids, we identified that the $Zn^{2+}$ coordinated Tyr amino acid displayed significant esterase activity in the aqueous medium. The Tyr molecule formed a colourless co-crystal structure with a $Zn^{2+}$ in water. XRD studies revealed that the $NH_2$ and $COO^-$ groups of two Tyr molecules and the $COO^-$ group of a third amino acid molecule, along with a water molecule, interacted with a $Zn^{2+}$, resulting in an octahedral-shaped geometry (Table 3.2 and Figure 3.22). The exobidentate bridging coordination mode with the µ-carboxyl leads to a one-dimensional chain structure.[16] We hypothesized that the water binding site of $Zn^{2+}$ could be the possible site for the catalytic reaction. This artificial catalytic system effectively catalysed the conversion of non-fluorescent AHPTS to fluorescent HPTS. However, the absence of either Tyr or $Zn^{2+}$ failed to generate luminescent HPTS from AHPTS. Hence, the Tyr-$Zn^{2+}$ complex serves as the catalyst for hydrolysing the ester derivatives of HPTS (Figure 3.9A and 3.8).[17] Additional studies of AHPTS with Tyr and $Cu^{2+}$ ions in 50 mM HEPES, pH 7.0, failed to generate luminescent HPTS (Figure 3.23). To determine the reaction rate, we monitored the hydrolysis of AHPTS to HPTS via fluorometric measurements. The change in the reaction rate against the substrate concentrations was analysed using the Michaelis–Menten equation ($R^2$ = 0.99). The maximum catalytic rate ($V_{max}$) and Michaelis constant ($K_m$) values were found to be 91.57 ± 1.51 µM $min^{-1}$ and 106.06 ± 7.51 µM, respectively (Figure 3.24). The data analysis with the Michaelis–Menten equation indicated an enzyme-like first-order reaction of AHPTS hydrolysis. However, the actual $V_{max}$ and $K_m$ values could be more than the calculated ones due to the quenching of HPTS fluorescence by the free $Zn^{2+}$ ions in the solution (Figure 3.25 A).

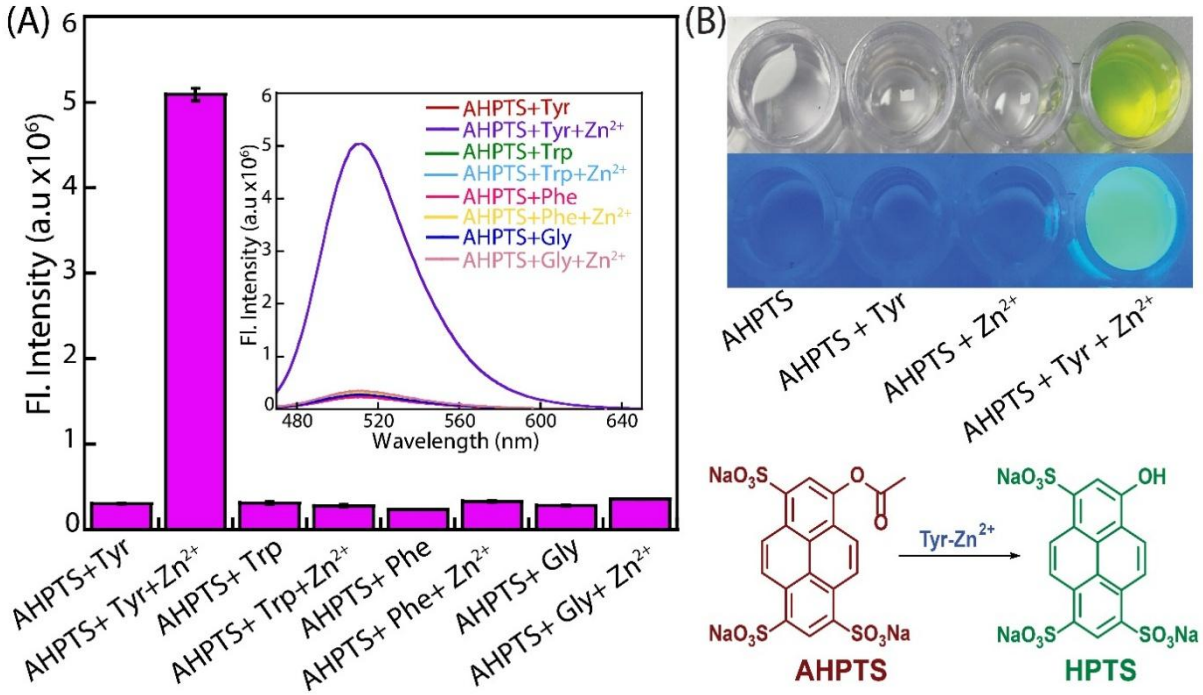


**Figure 3.8.** (A) The bar diagram represents the hydrolysis of AHPTS to HPTS with different amino acids (Phe, Gly, Trp, Tyr)/ $Zn^{2+}$ ions in 50 mM HEPES, pH 7.0. Inset shows the fluorescence spectral changes due to the hydrolysis of AHPTS to HPTS with different amino acids (Phe, Gly, Trp, Tyr)/ $Zn^{2+}$ ions in 50 mM HEPES, pH 7.0 (B) Representative images under UV-vis light (365 nm) demonstrating the hydrolysis of nonfluorescent AHPTS to fluorescent HPTS in the presence of Tyr-$Zn^{2+}$ complex and schematic presentation of the ester hydrolysis.

### 3.2.8 Zinc-mediated catalysis within vesicles:

To investigate the $Zn^{2+}$-mediated catalysis within the vesicular environment, **3.2a** was added to the extravesicular solution. The membrane penetration of **3.2a** would allow the transport of $Zn^{2+}$ into the intracellular system from the extravesicular system and promote $Zn^{2+}$-Tyr-mediated catalysis. Therefore, EYPC/CHOL-LUV⊃AHPTS/Tyr were prepared in 20 mM HEPES buffer containing 100 mM $NaNO_3$ at pH 7.0. Initially, no generation of HPTS was observed in the absence of transporter **3.2a**, revealing the negligible permeability of $Zn^{2+}$ ions. When transporter **3.2a** was incorporated into the membrane by introducing it to the extravesicular solution, no generation of HPTS was observed. However, after adding $Zn^{2+}$ ions into the extravesicular solution, rapid generation of HPTS was observed in the presence of transporter **3.2a**. This could be due to the transmembrane transport of $Zn^{2+}$ ions into the lumen

of vesicles and the in-situ generation of Tyr-$Zn^{2+}$ complex, leading to the hydrolysis of AHPTS into luminescent HPTS inside the vesicles. We performed a real-time catalytic activity assay using EYPC/CHOL-LUV⊃AHPTS/Tyr by varying the concentration of **3.2a**. As a result, we observed a gradual increase in catalytic activity with increasing compound concentration (Figure 3.9B). We also measured the AHPTS hydrolysis activity within the vesicles by varying the substrate (AHPTS) concentration and observed a gradual increase in HPTS fluorescence intensity (Figure 3.26). However, we were unable to accurately measure the catalytic activity parameters (rate, $V_{max}$ and $K_m$) within the vesicles, as it is difficult to measure the precise AHPTS concentration within the vesicles and AHPTS encapsulation efficacy of vesicles. Additionally, an induction period (>10 s) is required to introduce sufficient $Zn^{2+}$ ions into the vesicle before steady-state kinetics can be reliably observed. Hence, the Michaelis-Menten kinetics model was not applied to monitor the catalytic activity parameters within the vesicular environment. Additionally, we performed control experiments in the absence of transporter **3.2a** as well as $Zn^{2+}$ ions to confirm that the catalytic process occurs only when both the transporter (acting as an influx pump) and $Zn^{2+}$ (signal) are present (Figure 3.27). To further investigate the Tyr-$Zn^{2+}$ complex mediated catalytic process across EYPC/CHOL-LUV⊃AHPTS/Tyr, the fluorescence measurements were performed before and after the addition of EDTA in the extravesicular environment (Figure 3.9 C). EDTA is known to form a coordination complex with free $Zn^{2+}$ ions, which would limit the influx of $Zn^{2+}$ ions. The rapid reduction in the HPTS fluorescence signal after the addition of EDTA could be due to the formation of the EDTA-$Zn^{2+}$ complex and initial acidification in the extravesicular environment (Figure 3.28). This extravesicular EDTA-$Zn^{2+}$ complex is unlikely to cross the lipid bilayer due to its high aqueous solubility. However, a gradual increase in HPTS fluorescence indicates the Tyr-$Zn^{2+}$ complex-mediated catalysis within the vesicles. We also performed the catalytic activity using CFDA-SE. The catalytic activity across EYPC/CHOL-LUV⊃CFDA-SE/Tyr was measured by varying the concentration of **3.2a**. The enhancement of fluorescence intensity with the increase in the concentration of **3.2a** also suggests the ester hydrolysis of non-fluorescent CFDA-SE to fluorescent CFSE (Figure 3.9D and 3.29).[18]

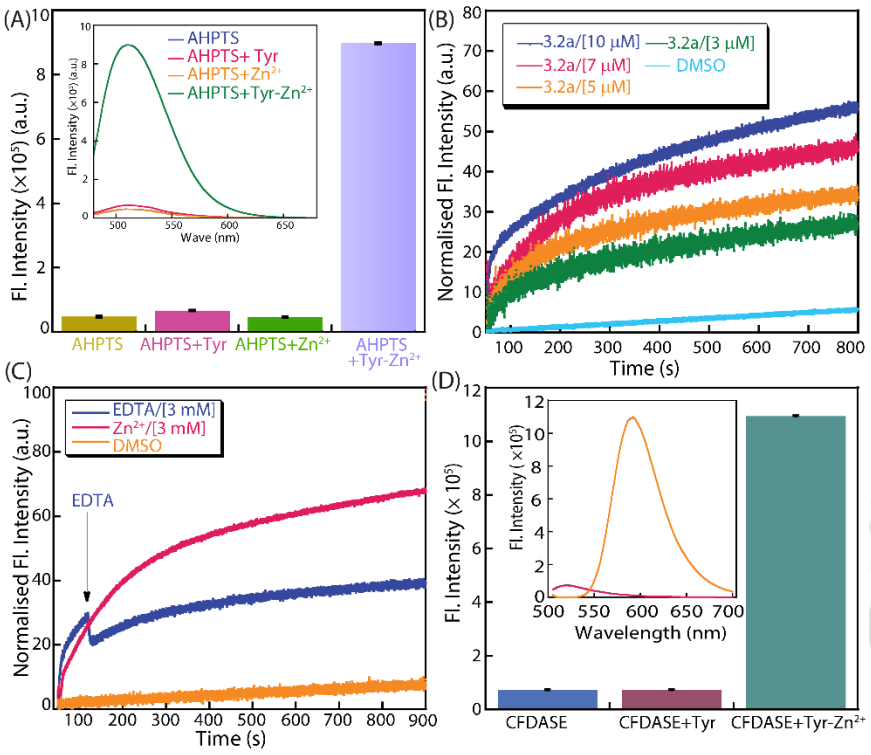


**Figure 3.9.** (A) Fluorescence intensity changes due to the hydrolysis of AHPTS to HPTS in 50 mM HEPES buffer pH 7.0. The inset depicts the fluorescence spectral change due to the hydrolysis of AHPTS. (B) Concentration-dependent (**3.2a**; 0-10 μM) hydrolysis of AHPTS to HPTS in the presence of $ZnCl_2$ (3 mM) across EYPC/CHOL-LUV⊃AHPTS/Tyr. (C) Spectral analysis of AHPTS hydrolysis in the presence of EDTA pulse (3 mM) and without EDTA pulse across EYPC/CHOL-LUVs⊃AHPTS/Tyr. (D) Fluorescence intensity changes due to the hydrolysis of CFDA-SE to CFSE in 50 mM HEPES buffer pH 7.0. The inset depicts the fluorescence spectral change due to the hydrolysis of CFDA-SE.

### 3.2.9 Chemical to optical signal transfer (formation of AND logic gate):

The chemical-to-optical signal transfer in this molecular communication system is driven by the coordinated interaction of three essential components: $Zn^{2+}$, transporter **3.2a**, and the Tyr-$Zn^{2+}$ catalytic complex. This suggests the formation of a three-input AND logic gate, where the absence of any one component disrupts the entire communication process across the lipid bilayers (Figure 3.10A).[19]The truth table representing % transport and normalized fluorescence signals indicates the ion transport in the presence of **3.2a** and $Zn^{2+}$ ions (Figure 3.10B). In contrast, the fluorescence signal is observed only in the presence of $Zn^{2+}$, transporter **3.2a** and Tyr (Figure 3.30). The images of giant unilamellar vesicles (GUVs) under UV light and fluorescence microscope also represent the successful ion transport-mediated intravesicular

catalytic process only where all three components are present (Figure 3.10C, 3.31). Herein, this artificial cell-like system can efficiently capture chemically encrypted data in the form of $Zn^{2+}$ (invisible to the naked eye) and translate it into an observable optical response, effectively decrypting the information. This process successfully constitutes the three-input AND logic gate demonstrating the ion transport mediated chemical conversion to optical signal within the vesicular system.

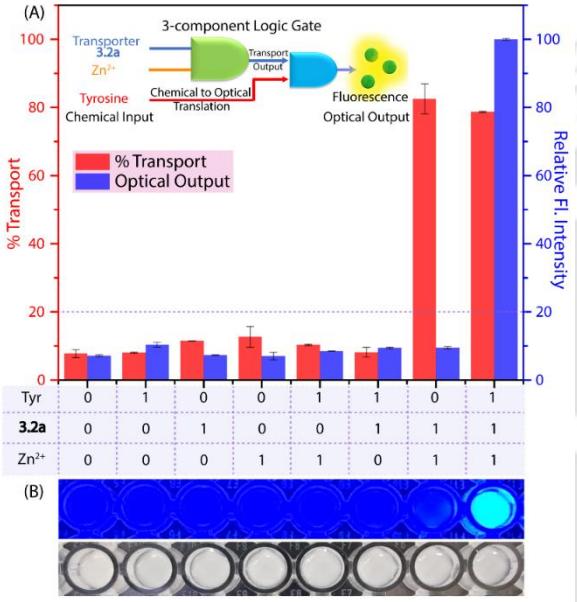


**Figure 3.10.** Transmembrane $Zn^{2+}$ transport efficacy and in-situ generated Tyr-$Zn^{2+}$ complex mediated AHPTS to HPTS hydrolysis efficacy under different conditions. The inset depicts the three-input mediated AND logic gate. The %T indicates the $Zn^{2+}$ transport efficacy (at t = 450 s). The fluorescence intensity is referred to as optical output. (B) The truth table demonstrates different conditions used for the chemical-to-optical signal transfer process under the vesicular environment. (C) Illustration of an optical response triggered by a chemical signal under UV light exposure in GUVs.

### 3.3 Summary:

We developed synthetic ion-channel-based molecular communication systems that selectively transport $Zn^{2+}$ ions across lipid bilayers. This transmembrane transport of $Zn^{2+}$ ions leads to catalytic activity involving Tyr within the intravesicular system and amplifies the chemical signal into an optical signal by generating fluorescent reporters via esterase-like activity. Among the synthesized salicylaldehyde-based imine derivatives of 2-(6-(6-amino-1H-benzo[d]imidazol-2-yl) pyridine-2-yl)-1H-benzo[d]imidazol-5-amine compound **3.2a** showed higher and selective $Zn^{2+}$ transport activity across the lipid bilayers. Further studies revealed

that the $Zn^{2+}/H^{+}$ antiport mechanism operates to transport ions across the bilayer. The electrophysiological measurements confirmed the formation of supramolecular ion channels with single channel conductance of 88 ± 7 pS, corresponding to a simple pore model with a pore diameter of 1.9 Å at 0.5 M $ZnCl_2$ symmetrical solution. The complexation of transported $Zn^{2+}$ ions with Tyr resulted in the formation of a Tyr-$Zn^{2+}$ catalytic system that stimulates the hydrolysis of non-fluorescent ester derivatives of reporters to generate fluorescent reporters. This molecular communication system was also tested with other luminescence reporters, such as CFDA-SE. The ion channel-mediated selective transport of $Zn^{2+}$ ions and in situ generated Tyr-$Zn^{2+}$ complex-mediated catalytic hydrolysis of non-fluorescent reporters to fluorescent reporters indicates the formation of a three-input AND logic gate. Therefore, this transmembrane $Zn^{2+}$ ions transport-mediated catalytic system offers a new approach for transferring encrypted chemical signals that could be amplified and decrypted by optical responses. Hence, we believe our findings would provide a new direction to ion transport-related research and underscore the potential for advanced molecular engineering to inspire future innovations in synthetic biology, paving the way for designing artificial cells capable of complex decision-making and environmental adaptation.

### 3.4 Experimental selection:

**3.4.1 General methods:** Mentioned in previous chapter.

### 3.4.2 Synthesis and characterisation of the compounds:

**3.4.2.1 Synthesis of 2,6-bis(1*H*-benzo[d]imidazol-2-yl)pyridine (3.1) —** The solution of 2,6-pyridine dicarboxylic acid (6 mmol) in 3 mL phosphoric acid was mixed with *o*-phenylene diamine (12 mmol) in a sealed tube, and the reaction was stirred at 150 ºC for 4 hours.[20] The reaction mixture was brought to room temperature before being transferred and added to ice-cold water. Neutralization was carried out using a concentrated NaOH solution, and the resulting precipitate was filtered using suction filtration. The precipitate was then washed with water to remove any remaining phosphoric acid. The off-white precipitate was dried and then used in the following reaction.

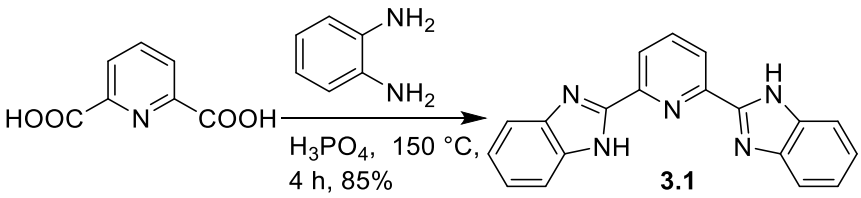


**Scheme 3.1**. Synthesis of 2,6-bis(1*H*-benzo[d]imidazol-2-yl)pyridine.

**3.4.2.2 Synthesis of 6-nitro-2-(6-(5-nitro-1*H*-benzo[d]imidazol-2-yl)pyridin-2-yl)-1*H*-benzo[d]imidazole —** The 2,6-bis(1H-benzo[d]imidazol-2-yl)pyridine (0.62 g, 2 mmol) in a round bottom flask was dissolved in 5 mL solution of $HNO_3$:$H_2SO_4$ (1:1 v/v ratio) on an ice bath and stirred for 4 hours at room temperature. The obtained solution was poured into ice-cold water to produce a pale-yellow precipitate. The precipitate was collected using suction filtration, washed with water, and dried in the oven to proceed with the following synthetic procedure.[21]

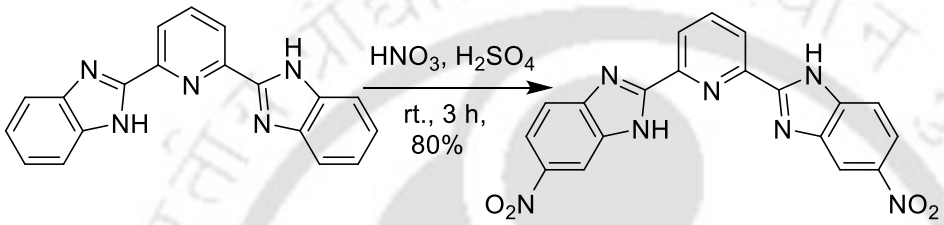


**Scheme 3.2.** Synthesis of compound 6-nitro-2-(6-(5-nitro-1*H*-benzo[d]imidazol-2-yl)pyridin-2-yl)-1*H*-benzimidazole.

**3.4.2.3 Synthesis of 2-(6-(6-amino-1*H*-benzo[d]imidazol-2-yl)pyridin-2-yl)-1*H*-benzo[d]imidazol-5-amine —** The solution of 6-nitro-2-(6-(5-nitro-1*H*-benzo[d]imidazol-2-yl)pyridin-2-yl)-1*H*-benzimidazole (0.56 g, 1.4 mmol) in 5 mL ethanol was mixed with a catalytic amount of 10% Pd/C under $N_2$ atmosphere. Subsequently, dropwise hydrazine hydrate (3 mL) was added to this mixture. The reaction was refluxed for 6 hours. It was then filtered over celite to separate the metal residue. The collected filtrate was added to cold water, resulting in the collection and drying of the precipitate. The obtained characterization is in accordance with the mentioned report.[21]

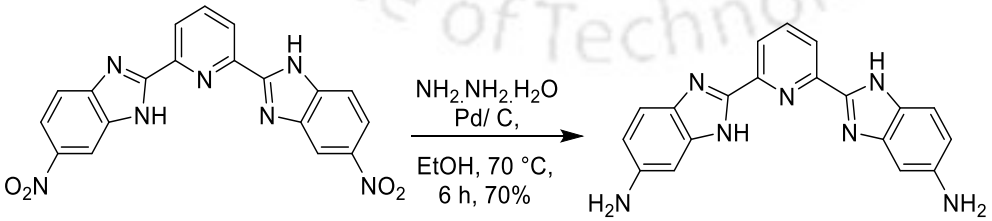


**Scheme 3.3.** Synthesis of 2-(6-(6-amino-1*H*-benzo[d]imidazol-2-yl)pyridin-2-yl)-1*H*-benzo[d]imidazol-5-amine.

**3.4.2.4 General procedure for the synthesis of imine derivatives —** The mixture of 2-(6-(6-amino-1*H*-benzo[d]imidazol-2-yl)pyridin-2-yl)-1*H*-benzo[d]imidazol-5-amine in methanol (5

mL) was heated, and respective salicylaldehyde derivatives were added. The mixture was refluxed until the starting material was consumed, which was monitored using TLC. The resulting precipitate was filtered and washed with cold methanol to remove any excess unreacted salicylaldehyde derivatives. The precipitate was then dried in an oven and used for further characterization and other biophysical studies.

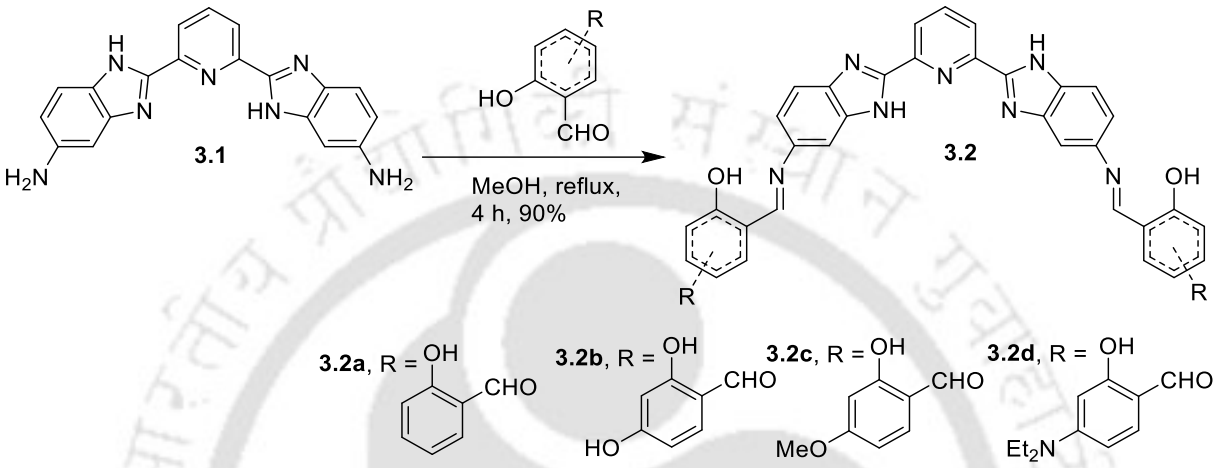


**Scheme 3.4.** Synthetic routes to various imine derivatives **3.2a-d.**

**3.4.2.4.1 Synthesis of 2-((E)-((2-(6-(6-(((E)-2-hydroxybenzylidene) amino)-1*H*-benzo[d]imidazol-2-yl) pyridin-2-yl)-1*H*-benzo[d]imidazol-5-yl) imino) methyl) phenol (3.2a) —** The 2-(6-(6-amino-1H-benzo[d]imidazol-2-yl)pyridin-2-yl)-1H-benzo[d]imidazol-5-amine (1.5 mmol) and salicylaldehyde (3.05 mmol) were used in the reaction by following the general protocol **2.4**. The product was washed with cold methanol and diethyl ether, and a yellow solid was obtained with a moderate yield. (yield: 64%). Characterisation: **$^{1}$H NMR**: (600 MHz, DMSO-$d_6$) $\delta_{ppm}$ 13.38 (s, 1H), 13.26 (s, 1H), 13.11 (dd, $J$ = 12.0, 5.0 Hz, 2H).), 9.10 (s, 1H), 9.08 (d, $J$ = 1.8 Hz, 1H), 8.38 (m, 2H), 8.22 (m, 1H), 7.89 (d, $J$ = 1.8 Hz, 1H), 7.86 (d, $J$ = 9.0 Hz, 1H), 7.81 (d, $J$ = 8.4 Hz, 1H), 7.71 (m, 3H), 7.50 (dd, $J$ = 8.4 Hz, 1.8 Hz, 1H), 7.44 (m, 3H), 7.02 (m, 4H). **$^{13}$C NMR**: (151 MHz, DMSO-$d_6$) $\delta_{ppm}$ 163.22, 162.75, 160.69, 152.20, 151.93, 151.91, 148.08, 148.04, 148.01, 145.34, 144.90, 143.91, 143.72, 139.76, 135.49, 134.16, 133.59, 133.56, 133.41, 133.03, 132.96, 122.12, 120.82, 119.95, 119.63, 119.57, 119.49, 117.18, 117.05, 117.02, 112.78, 111.73, 104.90. **HRMS**: ESI calc. for $C_{33}H_{23}N_7O_2$ [M+H] $^{+}$: 550.1986, found: 550.1987.

**3.4.2.4.2 Synthesis of 4-((E)-((2-(6-(6-(((E)-2,4-dihydroxybenzylidene)amino)-1H-benzo[d]imidazol-2-yl)pyridin-2-yl)-1H-benzo[d]imidazol-5-yl)imino)methyl)benzene-**

**1,3-diol (3.2b)** — The 2-(6-(6-amino-1*H*-benzo[d]imidazol-2-yl)pyridin-2-yl)-1*H*-benzo[d]imidazol-5-amine (1.5 mmol) and 2,4-dihydroxybenzaldehyde (3.05 mmol) were used in the reaction following the general protocol **2.4**. The obtained yellow precipitate was washed with cold methanol and proceeded for further studies. (yield: 58%) Characterisation: **$^{1}$H NMR**: (600 MHz, DMSO-$d_6$) $\delta_{ppm}$ 13.75 (s, 1H), 13.70 (s, 1 H), 13.07 (m, 2H), 10.26 (d, $J$ = 21.6 Hz, 2H), 8.92 (s, 2H), 8.36 (m, 2H), 8.20 (m, 1H), 7.80 (m, 3H), 7.63 (s, 1H), 7.48 (m, 2H), 7.41 (d, $J$ = 6.6 Hz, 1H), 7.36 (d, $J$ = 7.2 Hz, 1H), 6.43 (s, 2H), 6.33 (s, 2H). **$^{13}$C NMR**: (151 MHz, DMSO-$d_6$) $\delta_{ppm}$ 163.41, 162.79, 162.54, 162.23, 161.14, 151.82, 148.09, 139.69, 134.84, 133.41, 121.97, 112.68, 110.75, 108.68, 108.30, 102.93, 102.87. **HRMS**: ESI calc. for $C_{33}H_{23}N_7O_4$ $[M+H]^+$: 582.1884, found: 582.1897.

**3.4.2.4.3 Synthesis of 2-((E)-((2-(6-(6-(((E)-2-hydroxy-4-methoxybenzylidene)amino)-1H-benzo[d]imidazol-2-yl)pyridin-2-yl)-1H-benzo[d]imidazol-5-yl)imino)methyl)-5-methoxyphenol (3.2c)** — The 2-(6-(6-amino-1*H*-benzo[d]imidazol-2-yl)pyridin-2-yl)-1*H*-benzo[d]imidazol-5-amine (1.5 mmol) and 2-hydroxy-4-methoxybenzaldehyde (3.05 mmol) were used in reaction according to the general protocol **2.4**. The obtained product was washed with cold methanol to obtain a pale-yellow solid compound with a moderate yield. (Yield: 67%) Characterisation: **$^{1}$H NMR**: (600 MHz, DMSO-$d_6$) $\delta_{ppm}$ 13.92 (s, 1H), 13.82 (s, 1H), 13.07 (t, $J$ = 9.9 Hz, 2H), 8.98 (d, $J$ = 7.2 Hz, 2H), 8.36 (d, $J$ = 4.2 Hz, 2H), 8.20 (t, $J$ = 7.6 Hz, 1H), 7.84 (m, 2H), 7.78 (d, $J$ = 8.4 Hz, 1H), 7.66 (s, 1H), 7.59 (dd, $J$ = 15.9, 8.7 Hz, 2H), 7.44 (d, $J$ = 9.0 Hz, 1H), 7.38 (d, $J$ = 8.4 Hz, 1H), 6.59 (m, 2H), 6.52 (d, $J$ = 1.8 Hz, 2H), 3.83 (s, 6H). **$^{13}$C NMR**: (151 MHz, DMSO-$d_6$) $\delta_{ppm}$ 164.01, 163.88, 163.51, 162.45, 161.99, 144.82, 143.62, 135.55, 134.57, 134.45, 133.83, 122.04, 119.33, 113.67, 107.22, 107.14, 101.34, 55.97. **HRMS**: ESI calc. for $C_{35}H_{27}N_7O_4$ $[M+H]^+$: 610.2197, found: 610.2185.

**3.4.2.4.4 Synthesis of 5-(diethylamino)-2-((E)-((2-(6-(6-(((E)-4-(diethylamino)-2-hydroxybenzylidene)amino)-1H-benzo[d]imidazol-2-yl)pyridin-2-yl)-1H-benzo[d]imidazol-5-yl)imino)methyl)phenol (3.2d)** — The 2-(6-(6-amino-1*H*-benzo[d]imidazol-2-yl)pyridin-2-yl)-1*H*-benzo[d]imidazol-5-amine (1.5 mmol) and 4-(diethylamino)-2-hydroxybenzaldehyde (3.05 mmol) were used in the reaction by following the general protocol **2.4**. The product was washed with cold methanol to obtain a dark yellow solid compound with a moderate yield (Yield: 60%). Characterisation: **$^{1}$H NMR**: (600 MHz, DMSO-$d_6$) $\delta_{ppm}$ 13.80 (s, 1H), 13.73 (s, 1H), 13.01 (dd, $J$ = 18.6, 9.0 Hz, 2H), 8.79 (d, $J$ = 6.6 Hz, 2H), 8.35 (m, 2H), 8.19 (m, 1H), 7.79 (d, $J$ = 8.4 Hz, 1H), 7.74 (d, $J$ = 9.0 Hz, 2H), 7.56

(t, J = 3.0 Hz, 1H), 7.37 (m, 3H), 7.31 (dd, *J* = 8.7, 2.1 Hz, 1H), 6.35 (m, 2H), 6.11 (dd, *J* = 5.1, 2.1 Hz, 2H), 3.41 (q, *J* = 3.4 Hz, 8H), 1.14 (t, *J* = 6.9 Hz, 12H). **$^{13}$C NMR**: (151 MHz, DMSO-*d*$_6$) $\delta_{ppm}$ 163.62, 161.53, 161.16, 151.89, 148.18, 145.52, 143.06, 135.65, 134.64, 134.50, 120.72, 119.28, 117.08, 109.23, 104.28, 104.17, 97.35, 44.41, 13.04. **HRMS**: ESI calc. for $C_{41}H_{41}N_9O_2$ $[M+H]^+$: 692.3456, found 692.3459.

**3.4.2.5 Synthesis of 2-(6-(4,6-bis(trifluoromethyl)-1*H*-benzo[d]imidazol-2-yl)pyridin-2-yl)-5,7-bis(trifluoromethyl)-1*H*-benzo[d]imidazole (3.3) —** In a sealed tube, pyridine-2,6-dicarboxylic (1.5 mmol), 3,5-bis(trifluoromethyl)benzene-1,2-diamine (3.1 mmol) and $POCl_3$ (2 ml) were added and stirred for 2 hours. Then, the reaction mixture was cooled to room temperature and neutralized in ice-cold water using a bicarbonate solution. The reaction mixture was extracted with EtOAc (20×3 mL), and the targeted compound was purified by column chromatography using a solvent system of 70:30 Hex/EtOAc (Yield: 68%). Characterisation: **$^1$H NMR**: (400 MHz, DMSO-*d*$_6$) $\delta_{ppm}$ 14.02 (s, 2H), 8.70 (d, *J* = 8.0 Hz, 3H), 8.49 (s, 1H), 8.46 (d, *J* = 7.6 Hz, 1H), 8.08 (s, 2H). **$^{13}$C NMR**: (151 MHz, DMSO-*d*$_6$) $\delta_{ppm}$ 162.55, 154.90, 147.32, 143.16, 139.83, 135.78, 125.29, 124.19, 123.49, 116.44, 114.06. **HRMS**: ESI calc. for $C_{23}H_9F_{12}N_5$ $[M+H]^+$: 584.0739, found: 584.0739.

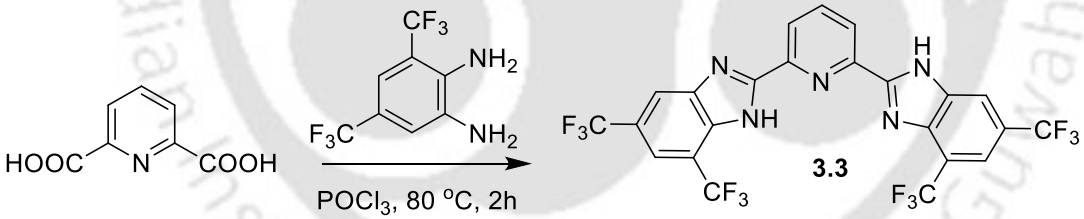


**Scheme 3.5.** Synthetic procedure of 2-(6-(4,6-bis(trifluoromethyl)-1*H*-benzo[d]imidazol-2-yl)pyridin-2-yl)-5,7-bis(trifluoromethyl)-1*H*-benzo[d]imidazole.

**3.4.2.6 *Synthesis of* (E)-2-(((2-(pyridin-2-yl)-1*H*-benzo[d]imidazol-5-yl)imino)methyl)phenol (3.4) —** In a round bottom flask 2-(pyridin-2-yl)-1*H*-benzo[d]imidazol-5-amine and MeOH (5 mL) were added and then salicylaldehyde was added to the mixture dropwise and stirred at room temperature. The reaction was monitored through TLC till the starting material was consumed. The solvent was evaporated and extracted with DCM (20×3 mL). The mixture was reduced under pressure and purified through the column. (50:50 Hex/EtOAc) (yield: 82%). Characterisation: **$^1$H NMR**: (600 MHz, $CDCl_3$) $\delta_{ppm}$ 13.48 (s, 1H), 13.39 (s, 1H), 10.79 (s, 1H), 8.73 (d, *J* = 8.4 Hz, 1H), 8.66 (d, *J* = 4.8 Hz, 1H), 8.44

(dd, *J* = 8.1, 3.3 Hz, 1H), 7.89 (m, 1H), 7.43 (d, J = 9.0 Hz, 2H), 7.40 (dd, J = 12.0, 5.4 Hz, 2H), 7.32 (t, J = 10.5 Hz, 1H), 7.05 (d, J = 8.4 Hz, 1H), 6.97 (t, J = 7.5 Hz, 1H). **$^{13}$C NMR**: (151 MHz, $CDCl_3$) $\delta_{ppm}$ 161.94, 161.68, 161.07, 149.24, 147.97, 137.39, 133.04, 132.23, 124.76, 121.74, 121.65, 120.73, 119.13, 119.06, 117.26, 116.76, 111.70, 111.08, 104.01. **HRMS**: ESI calc. for $C_{19}H_{14}N_4O$ $[M+H]^+$: 315.124, found: 315.1245.

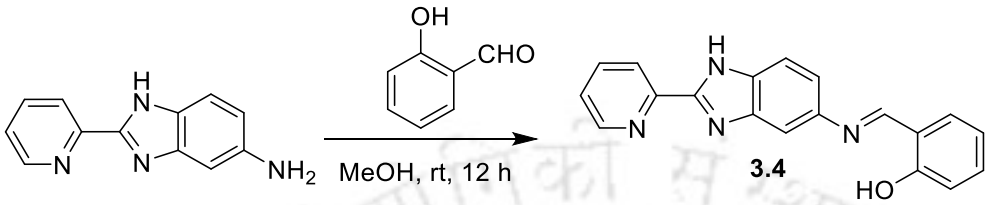


**Scheme 3.6.** Synthetic procedure of (E)-2-(((2-(pyridin-2-yl)-1*H*-benzo[d]imidazol-5-yl)imino)methyl)phenol.

**3.4.2.7 Synthetic of sodium 8-acetoxypyrene-1,3,6-trisulfonate —** The sodium 8-acetoxypyrene-1,3,6-trisulfonate (AHPTS) salt was synthesized using the method mentioned in previous reports.[22] The 8-hydroxypyrene-1,3,6-trisulfonate (HPTS) trisodium salt (100 mg, 0.19 mmol) and sodium acetate (1.87 mg, 0.02 mmol) were taken in a two-neck round bottom flask and dissolved in acetic anhydride (4 mL). The mixture was stirred at reflux for 48 h. Then, the mixture was left to cool to room temperature and diluted with 4 mL of tetrahydrofuran containing 10% (v/v) acetic acid. The solid was then collected using vacuum filtration and washed sequentially with cold acetone and diethyl ether to get the desired product (80% yield).

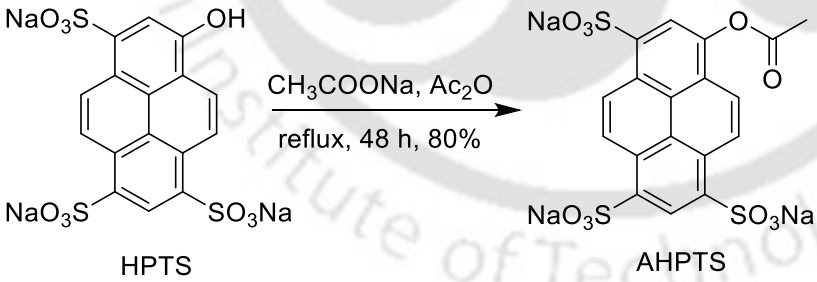


**Scheme 3.7.** Synthetic procedure of sodium 8-acetoxypyrene-1,3,6-trisulfonate (AHPTS) salt.

### 3.4.3 Estimation of $pK_a$ and logP values

The logP and $pK_a$ values of the compounds were calculated using Chemdraw 23.0.1 software.

**Table 3.1** Estimated $pK_a$ & logP of synthesised compounds.

| Compound | logP | $pK_a$ |
|---|---|---|
| **3.1** | 3.15 | - |
| **3.2a** | 6.16 | 8.95 |

| | | |
|---|---|---|
| **3.2b** | 5.38 | 12.37 |
| **3.2c** | 5.91 | 8.79 |
| **3.2d** | 8.08 | 9.18 |
| **3.3** | 6.89 | - |
| **3.4** | 3.43 | 8.96 |

### 3.4.4 Field emission scanning electron microscopy (FESEM) analysis

To apprehend the effect of solvent polarity on the self-assembly property of the compound, we conducted a morphological study through FESEM analysis. Compound **3.2a** (1 mM) solutions in water and $CHCl_3$ were prepared and then drop-casted for the FESEM experiment and dried at room temperature. Before analysis, the samples were stacked onto the FESEM grid and coated with gold solution.[23]

[NOTE: For hypothesis regarding structural assembly by the molecule or channel formation the following description is given below:

The design of the ionophores was guided by the need to balance selective $Zn^{2+}$ recognition with the ability to self-assemble within a lipid bilayer. The 2,6-bis(benzimidazolyl)pyridine unit was selected as the central scaffold because it is a well-established, preorganized chelating motif for 3d transition metals, including $Zn^{2+}$. Its rigid and slightly curved geometry provides a conformationally restrained environment that favours metal binding while also promoting directional intermolecular interactions when embedded in membranes.

The salicylaldehyde-based imine units were incorporated intentionally to introduce a second, complementary $Zn^{2+}$ binding site. The imine nitrogen and phenolic oxygen together provide a soft–hard donor set that matches well with the coordination preferences of $Zn^{2+}$. In addition to metal recognition, these aromatic imine moieties increase hydrophobic surface area and facilitate π–π stacking and hydrogen-bonding interactions, both of which are known to promote supramolecular aggregation in lipid bilayers. The presence of two spatially distinct $Zn^{2+}$ binding sites was therefore not incidental. Rather, we anticipated that $Zn^{2+}$ coordination could act as a structural organizing element, promoting intermolecular association through metal-mediated interactions and stabilizing extended assemblies across the membrane.]

### 3.4.5 Methodology of Ion Transport Studies

**3.4.5.1 Preparation of EYPC/CHOL-LUVs⊃MgG vesicles —** Phosphatidylcholine (PC) and cholesterol (CHOL) are the two most abundant lipids in mammalian cell membranes;

hence, both these lipids were used to prepare model large unilamellar vesicles (LUVs). To conduct the pentapotassium salt of magnesium green (MgG) fluorescence-based ion-transport studies, we took EYPC (50 mg/mL in deacidified $CHCl_3$) and cholesterol (CHOL; 25 mg/mL in deacidified $CHCl_3$) in a clean, dry glass vial in a molar ratio of 8:2.[24] The solution was evaporated for 6 hours under reduced pressure to form a thin lipid film. After that, we rehydrated the film with 10 mM HEPES buffer containing 100 mM NaCl, 100 µM EDTA, and 50 µM MgG dye at pH 7.0. The resulting suspension was vortexed six to seven times over 1 hour. Next, we performed 6-7 freeze-thaw cycles followed by 10 minutes of constant vortexing. We then extruded the lipid suspension 19–21 times using a mini extruder with a 200 nm pore size to achieve a uniform vesicle size of 200 nm. Finally, we removed the unencapsulated MgG dye using gel filtration (Sephadex G-50) with 10 mM HEPES buffer containing 100 mM NaCl at pH 7.0 as the eluent. This process yielded a final lipid concentration of 25 mM (assuming 100% lipid regeneration).

**3.4.5.2 Ion transport studies using EYPC/CHOL-LUVs⊃MgG vesicles —** For the MgG-based ion transport assay, in a clean and dry fluorescence cuvette (3 mL), 10 mM HEPES buffer containing 100 mM NaCl and 100 µM EDTA, pH 7.0 (1930 µL), EYPC/CHOL-LUV⊃MgG (40 µL), and $ZnCl_2$ (final concentration 1 mM) were added.[24] The cuvette was placed under slow stirring conditions in a fluorescence spectrophotometer for about 3 minutes to equilibrate. The fluorescence was evaluated as a function of time ($\lambda_{em}$ = 531 nm, $\lambda_{ex}$ = 506 nm). At 50 s, the compound (stock solution of DMSO) was added to the cuvette solution to initiate the transport studies. Finally, the vesicles were completely lysed at 450 s by adding 20 µL of 20% Triton X-100. The transport studies for the compounds were performed in repetition at various compound concentrations (20 - 700 nM). The fluorescence intensity measurement was continued for a further 50 s. The normalized % transport efficiency (%EE) at t = 450 s was considered for the particular transport efficiency of the compounds.

Transport activity, $T_{MgG} = (\frac{F_t - F_0}{F_\infty - F_0} \times 100)$ %

[NOTE:

Compound **3.2a**, which contains two salicylaldehyde-derived imine-phenol units, exhibits the highest $Zn^{2+}$ transport efficiency (78%). In contrast, compound 3.3, which retains the same central pincer-like core but lacks the peripheral imine-phenol functionality, shows negligible $Zn^{2+}$ transport despite having a comparable logP value. This observation indicates that the core tridentate motif, although well known for strong 3d metal complexation, likely binds $Zn^{2+}$ too

strongly, resulting in kinetically trapped complexes that are un-favourable for transmembrane transport.

Further insight is provided by the control compound 3.4, which contains only one imine–phenol unit. The significantly reduced transport efficiency of 3.4 (~37%) compared to **3.2a** demonstrates that both the number and spatial arrangement of these imine-OH sites are critical. The presence of two such motifs in **3.2a** enables cooperative yet labile coordination of $Zn^{2+}$ ions, consistent with reversible binding required for effective ion transport.

Taken together, these results establish a clear structure-transport relationship: strong, multidentate coordination by the pincer-like core alone is detrimental to transport, whereas the imine-N and phenolic -OH groups provide weaker, reversible $Zn^{2+}$ binding that facilitates uptake and release across the lipid bilayer.]

**3.4.5.3 Critical aggregation concentration measurements —** The critical aggregation concentration (CAC) of compound **3.2a** was determined using its concentration-dependent $Zn^{2+}$ ions transport properties. A distinct inflection point was observed through the linear fitting after analysing the %transport ($Zn^{2+}$ ions) in the lower concentration range. Below 40 nM, the slope of the linear fit was 0.09 ± 0.008, while above 40 nM, the slope increased to 0.22 ± 0.03. The change in slope at the inflection point suggests the initiation of supramolecular nanochannels (> 40 nM) within the bilayer of vesicles.

**3.4.5.4 Cation selectivity studies across EYPC/CHOL-LUV⊃MgG vesicles —** As mentioned in the previous section, a similar procedure was followed for vesicle preparation and ionophore activity studies for the cation-selectivity studies.[24] For the fluorescence-based ion transport assay, 10 mM HEPES buffer containing 100 mM NaCl and 100 µM EDTA at pH 7.0 (1930 µL), EYPC/CHOL-LUV⊃MgG (40 µL), and $M_xCl_y$ salt (1 mM final concentration) ($MnCl_2$, $FeCl_3$, $CoCl_2$, $NiCl_2$, $CuCl_2$, $ZnCl_2$) were taken in a clean fluorescence cuvette (3 mL). The cuvette was placed in the spectrofluorometer under a slow stirring condition for ~3 minutes. The MgG fluorescence intensity was recorded as a function of time ($\lambda_{em}$ = 531 nm, $\lambda_{ex}$ = 506 nm). At 50 s, compound **3.2a** (stock solution of DMSO) was added to the cuvette solution (final concentration of 300 nM) to initiate the transport studies. Finally, the vesicles were lysed entirely by adding 20 µL of 20% Triton X-100 at 450 s, and the fluorescence intensity measurement was continued for a further 50 s. The studies on cation selectivity were conducted multiple times.

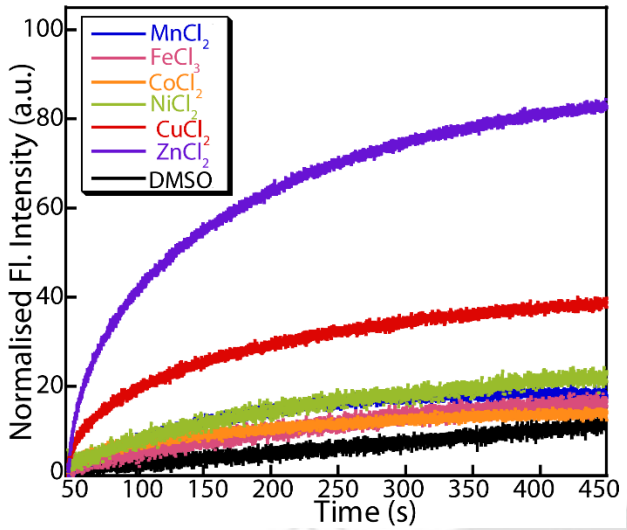


**Figure 3.11.** Comparison of cation transport activity of compound **3.2a** (300 nM) across the bilayers of EYPC/CHOL-LUV⊃MgG. The intravesicular solution was 10 mM HEPES buffer containing 100 mM NaCl, 100 μM EDTA and MgG dye at pH 7.0, and the extravesicular solution was 10 mM HEPES buffer containing 100 mM NaCl and 100 μM EDTA at pH 7.0 and 1 mM $M_xCl_y$ (where M = $Mn^{2+}$, $Fe^{3+}$, $Co^{2+}$, $Ni^{2+}$, $Cu^{2+}$ and $Zn^{2+}$). DMSO (10 μL) was used as a control.

**3.4.5.5 Anion selectivity studies across EYPC/CHOL-LUV⊃MgG vesicles —** For the MgG-based anion selectivity studies, vesicles were prepared similarly to those mentioned in the earlier section.[24] For the fluorescence assay, 10 mM HEPES buffer containing 100 mM NaCl and 100 μM EDTA at pH 7.0 (1930 μL), EYPC/CHOL-LUV⊃MgG (40 μL), and $Zn_xB_y$ (1 mM final concentration, $ZnCl_2$, $ZnBr_2$, $ZnSO_4$, and $Zn(NO_3)_2$ ) were taken in a clean fluorescence cuvette (3 mL). The cuvette was placed in a spectrofluorometer under a slow stirring condition for ~3 minutes. The MgG fluorescence intensity was monitored as a function of time ($\lambda_{em}$ = 531 nm, $\lambda_{ex}$ = 506 nm). At 50 s, compound **3.2a** (stock solution of DMSO) was added to the cuvette solution (final concentration of 300 nM) to initiate the transport studies. Finally, the vesicles were lysed by adding 20 μL of 20% Triton X-100 at 450 s, and the fluorescence intensity measurement was continued for a further 50 s. The studies on anion selectivity were conducted multiple times.

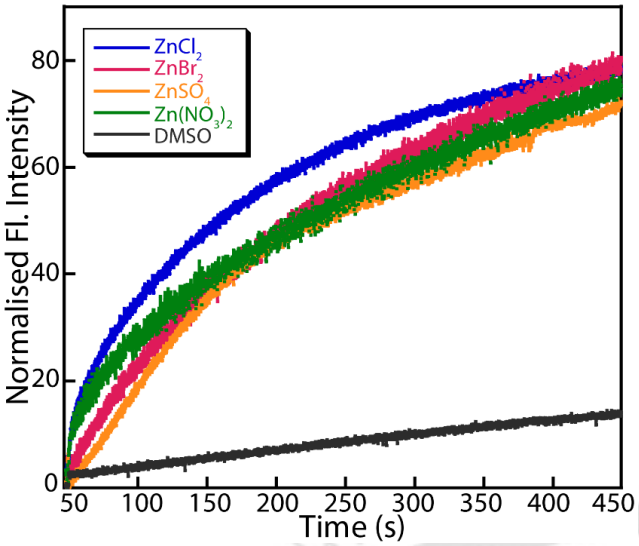


**Figure 3.12.** Comparison of anion transport activity of compound **3.2a** (300 nM) across the bilayers of EYPC/CHOL-LUV⊃MgG in the presence of different zinc salts. Normalized fluorescence spectra of MgG in the presence of compound **3.2a** (300 nM). The intravesicular solution was 10 mM HEPES buffer containing 100 mM NaCl, 100 μM EDTA and MgG dye at pH 7.0, and the extravesicular solution was 10 mM HEPES buffer containing 100 mM NaCl and 100 μM EDTA at pH 7.0 and 1 mM $Zn_xB_y$ ($ZnCl_2$, $ZnBr_2$, $ZnSO_4$, and $Zn(NO_3)_2$). DMSO (10 μL) was used as a control.

**3.4.5.6 Investigation of $Cl^-$ ion transport ability of the compound:**

**Ion transport studies across the EYPC/CHOL-LUVs⊃lucigenin —** To study ion transport using lucigenin fluorescence, large unilamellar vesicles (LUVs) composed of egg yolk phosphatidylcholine (EYPC) and cholesterol (CHOL) were prepared. EYPC (50 mg/mL in deacidified $CHCl_3$) and CHOL (25 mg/mL in deacidified $CHCl_3$) were mixed in a clean glass vial in an 8:2 molar ratio. The organic solvent was evaporated under reduced pressure for 6 hours, forming a uniform thin lipid film. The lipid film was hydrated by adding 800 μL of 20 mM HEPES buffer containing 1 mM lucigenin and 100 mM $NaNO_3$ (pH 7.0). The resulting suspension was subjected to six to seven vortex cycles over one hour to ensure homogeneity, followed by 17–19 freeze-thaw cycles. Subsequently, the suspension underwent constant vortexing for 10 minutes to encapsulate lucigenin within the lipid bilayer. Using a mini extruder, the lipid suspension was extruded through a 200 nm polycarbonate membrane (Avanti Polar Lipids). This extrusion process was repeated 19–21 times (ensuring an odd number of passes) to obtain uniformly sized LUVs. Unencapsulated lucigenin dye was removed by size-exclusion chromatography using a Sephadex G-50 column equilibrated with 20 mM HEPES buffer containing 100 mM $NaNO_3$ (pH 7.0) to get the final lipid concentration of 25 mM

(assuming 100% lipid regeneration). For the fluorescence-based transport assay, 1940 µL of 20 mM HEPES buffer containing 100 mM NaCl (pH 7.0) and 50 µL of the EYPC/CHOL⊃lucigenin suspension was transferred to a quartz fluorescence cuvette. The sample was maintained at room temperature under slow stirring. Fluorescence emission was monitored using a spectrophotometer at an excitation wavelength of 455 nm and an emission wavelength of 505 nm. After recording the baseline fluorescence for 50 seconds, 10 µL of compound **3.2a** (from a DMSO stock solution) was added to initiate ion transport. At 450 seconds, the vesicles were lysed by adding 20 µL of 20% Triton X-100 solution, and fluorescence was recorded until 500 seconds to determine the endpoint.

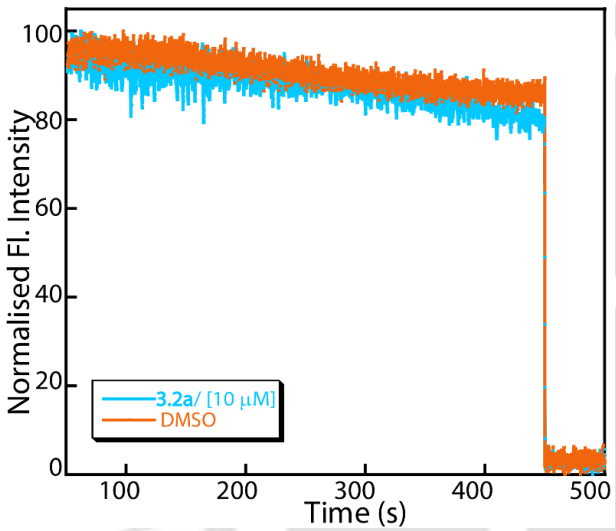


**Figure 3.13.** Chloride ion transport activity of compound **3.2a** (10 µM) across EYPC/CHOL-LUVs⊃lucigenin, with DMSO (10 µL) as the control.

**Note:** The lucigenin-based ion transport studies across the bilayers of EYPC/CHOL-LUVs⊃lucigenin in the absence and presence of compound **3.2a** clearly suggest the inability of $Cl^-$ transport by compound **3.2a** under the experimental conditions.

**3.4.5.7 Binding affinity of compound 3.2a with $Zn^{2+}$ —** The binding affinity of compound **3.2a** for $Zn^{2+}$ ions was examined through UV-Vis titration of the water medium. In this experiment, a 20 µM solution of compound **3.2a** was titrated with $ZnCl_2$, gradually decreasing absorbance with each addition of $Zn^{2+}$ ions. The association constant ($K_a$) for the interaction was determined using the Bindfit v0.5 program by fitting the absorbance data to a 1:1 binding model. Under the experimental conditions, the calculated (average of three measurements) $K_a$ was 313.29 ± 5.4 $M^{-1}$.

**3.4.5.8. Mechanism of ion transport activities**

**3.4.5.8.1. Ion transport study across EYPC/CHOL-LUV⊃MgG in the presence of FCCP** — For the FCCP assay, the vesicles were prepared similarly as mentioned in the earlier section using 10 mM HEPES, 100 mM NaCl, 100 μM EDTA buffer pH 7.0.[24] In a clean fluorescence cuvette (3 mL), 10 mM HEPES buffer containing 100 mM NaCl and 100 μM EDTA, pH 7.0 (1930 μL), EYPC/CHOL-LUV⊃MgG (40 μL), $Zn^{2+}$ (final concentration 1 mM), and FCCP (1.0 nM) were taken. The cuvette was placed in the spectrofluorometer under a slow stirring condition for ~3 minutes. The fluorescence intensity was recorded as a function of time ($\lambda_{em}$ = 531 nm, $\lambda_{ex}$ = 506 nm). At 50 s, compound **3.2a** (stock solution of DMSO) was added to the cuvette solution (final concentration 300 nM) to initiate the transport studies. Finally, the vesicles were lysed entirely by adding 20 μL of 20% Triton X-100 at 450 s, and the fluorescence intensity measurement continued for a further 50 s. The control experiment was performed in the presence of DMSO and only FCCP. The FCCP assay was performed in multiple.

**3.4.5.8.2. Fluorescein-based assay to monitor pH modulation along with $Zn^{2+}$ transportation across EYPC/CHOL-LUVs⊃fluorescein vesicles** — To conduct the fluorescein-based ion transport measurements for monitoring pH changes along with $Zn^{2+}$ transport process within the vesicles, LUVs were prepared similarly as mentioned in the earlier section using 10 mM fluorescein dye in 10 mM HEPES buffer containing 100 mM NaCl at pH 6.0. In a clean fluorescence cuvette (3 mL), 10 mM HEPES buffer containing 100 mM NaCl, pH 6.0 (1930 μL), EYPC/CHOL-LUV⊃fluorescein (40 μL), and $ZnCl_2$ (final concentration 3 mM) were added. The cuvette was placed under slow stirring conditions in a fluorescence spectrophotometer for about 3 min to equilibrate. The fluorescence was evaluated as a function of time ($\lambda_{em}$ = 520 nm, $\lambda_{ex}$ = 495 nm). At 50 s, compound **3.2a** (1 μM) was added to the cuvette solution to initiate the transport studies. Similarly, the transport studies were also performed with various extravesicular buffers of different pH (pH 6.5 and 7.0). The normalized fluorescence intensity was determined by using the equation below,

$$I_{rel} = \frac{I_t}{I_{min}}$$

where $I_t$ is fluorescence intensity at time t, and $I_{min}$ is the fluorescence minima of the particular kinetics.

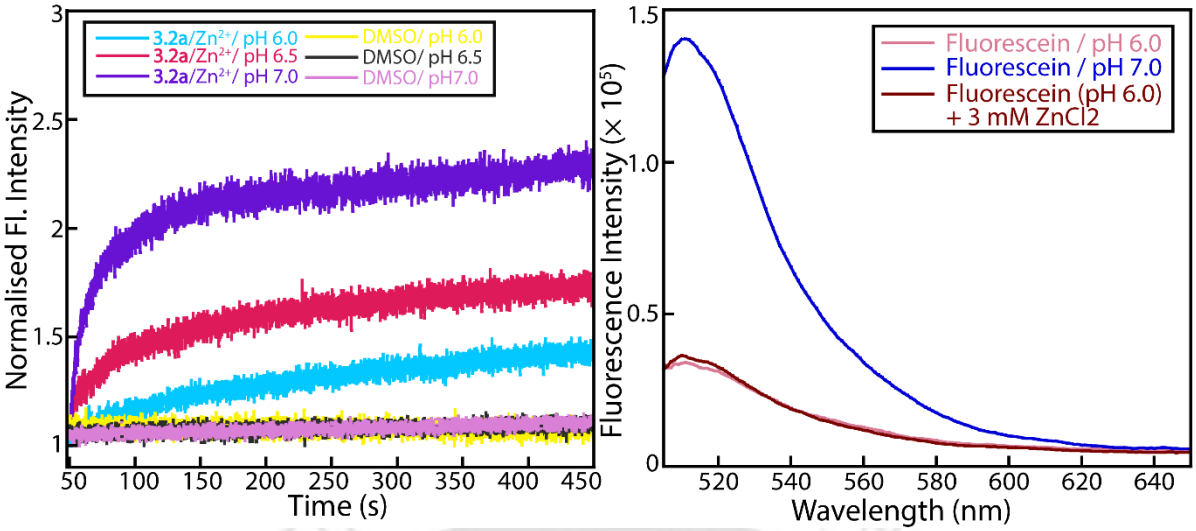


**Figure 3.14.** (A) Measurement of intravesicular pH modulation upon addition of compound **3.2a** across EYPC/CHOL LUV⊃fluorescein suspended in 10 mM HEPES buffer containing 100 mM NaCl at pH 6.0/6.5/7.0 after the addition of 3 mM $ZnCl_2$ and 1 μM compound **3.2a** in the extravesicular environment. Intervesicular solution was 10 mM HEPES buffer containing 100 mM NaCl at pH 6.0. (B) Effect of $Zn^{2+}$ on the fluorescence intensity of fluorescein dye.

**3.4.5.8.3. Ion transport study across EYPC/CHOL-LUV⊃MgG in the presence of valinomycin —** For the valinomycin assay, the vesicles were prepared similarly as mentioned in the earlier section using 10 mM HEPES, 100 mM KCl, 100 μM EDTA pH 7.0.[24] In a clean fluorescence cuvette (3 mL), 10 mM HEPES buffer containing 100 mM NaCl and 100 μM EDTA, pH 7.0 (1930 μL), EYPC/CHOL-LUV⊃MgG (40 μL), $Zn^{2+}$ (final concentration 1 mM), and valinomycin (12 pM) were taken. The cuvette was placed in the spectrofluorometer under a slow stirring condition for ~3 minutes. The fluorescence intensity was recorded as a function of time ($\lambda_{em}$ = 531 nm, $\lambda_{ex}$ = 506 nm). At 50 s, compound **3.2a** (stock solution of DMSO) was added to the cuvette solution (final concentration 300 nM) to initiate the transport studies. Finally, the vesicles were lysed entirely by adding 20 μL of 20% Triton X-100 at 450 s, and the fluorescence intensity measurement continued for a further 50 s. The control experiment was performed in the presence of DMSO and only valinomycin. The valinomycin assay was performed in multiple.

**3.4.5.9. Vesicle leakage assay**

**3.4.5.9.1 Preparation of EYPC−LUV⊃carboxyfluorescein —** A thin lipid film was prepared by evaporating a solution of 154 μL of EYPC (50 mg/mL stock in chloroform) and 39 μL cholesterol (25 mg/mL stock in chloroform) in vacuo for 6 h.[25] After that, the lipid film was

hydrated with 500 µL buffer (10 mM HEPES, 10 mM NaNO3, 50 mM carboxyfluorescein (CF), pH 7.0) for 1 h with occasional vortexing of 4−5 times and then subjected to a freeze-thaw cycle (≥ 15 times). The vesicle solution was extruded through a polycarbonate membrane with 200 nm pores 19 times (an odd number) to give vesicles with a mean diameter of ~200 nm. The extracellular dye was removed with size exclusion chromatography (Sephadex G-50) with 10 mM HEPES buffer (100 mM NaCl, pH 7.0.) Final concentration: ~25 mM EYPC-CHOL lipid; intravesicular solution: 10 mM HEPES, 10 mM $NaNO_3$, 50 mM CF, pH 7.0; extravesicular solution: 10 mM HEPES, 100 mM NaCl, pH 7.0.

**3.4.5.9.2. Carboxyfluorescein leakage assay —** In a clean and dry fluorescence cuvette, 50 µL of the above lipid solution and 1930 µL of 10 mM HEPES buffer 100 mM NaCl, pH 7.0 were taken and kept in slowly stirring condition by a magnetic stirrer equipped with the fluorescence instrument (at t = 0 s). The CF fluorescence emission intensity time course, $F_t$, was observed at $\lambda_{em}$ = 517 nm ($\lambda_{ex}$ = 492 nm). Compound **3.2a** was added at t = 50 s, and at t = 450 s, 20 µL of 20% Triton X-100 was added to lyse the vesicles and achieve 100% CF release. This study confirmed that the integrity of the bilayer membranes is intact in the presence of compound **3.2a**.

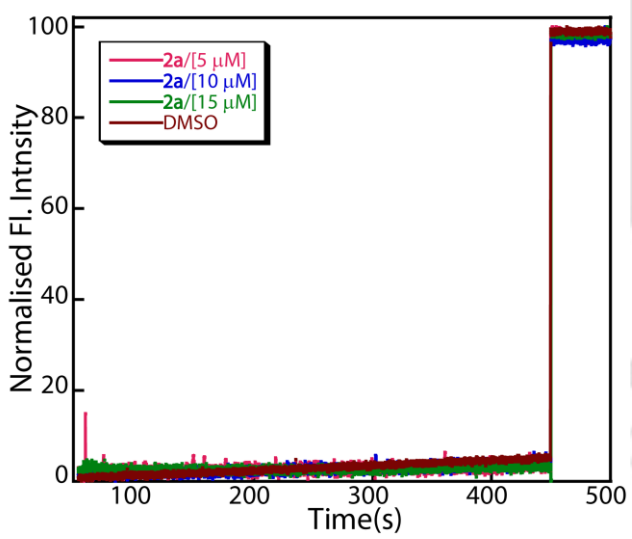


**Figure 3.15.** Vesicle leakage assay of compound **3.2a** across EYPC/CHOL-LUV⊃CF. DMSO (10 µL) was used as a control.

**3.4.5.10 Preparation of DPPC-LUV⊃MgG vesicles —** The MgG-based fluorescence assay using synthetically pure 1,2-dipalmitoylphosphatidylcholine (DPPC) was employed to determine the transport mechanism of the compounds above and below its phase transition temperature (41 °C).[24, 26] The MgG fluorescence-based temperature-dependent ion transport activities of compound **3.2a** were measured using 1,2-dipalmitoylphosphatidylcholine (DPPC).

DPPC-LUV⊃MgG vesicles were prepared in 10 mM HEPES buffer containing 100 mM NaCl and 100 µM EDTA, pH 7.0. For the preparation, 50 µL of DPPC (100 mg/mL stock in de-acidified $CHCl_3$) was taken in a clean, dry glass vial, and the organic solvent was removed under reduced pressure (5-6 h) at room temperature. The dry, thin film was then hydrated with 500 µL of 10 mM HEPES buffer, pH 7.0, containing 100 mM NaCl and 100 µM EDTA with 50 µM MgG dye. The solution was then sonicated for 20 min at 50 °C and vortexed intermittently for 15-20 min. After that, the solution was subjected to a freeze-thaw cycle 12-13 times and was again sonicated 10 times (40 s sonication followed by 20 s incubation in ice water). The LUVs were prepared by extrusion at 45 °C using Avanti Mini-Extruder (Avanti Polar Lipids, Alabaster, AL) through 200 nm pore-size polycarbonate membranes according to the protocol of the manufacturer. The unencapsulated dye was removed using a size exclusion column (Sephadex G-50) with 10 mM HEPES buffer, pH 7.0, containing 100 mM NaCl and 100 µM EDTA. The final volume of the collected vesicle solution was adjusted to 500 µL with 10 mM HEPES buffer pH 7.0 containing 100 mM NaCl and 100 µM EDTA. The final lipid concentration was 14 mM (assuming 100 % lipid regeneration).

**3.4.5.11 Temperature-dependent ion transport studies across DPPC-LUV⊃MgG —** The DPPC assay was performed using a Fluoromax-4 spectrofluorometer (Horiba Scientific, Singapore) connected to a temperature controller. In this assay, 1930 µL of 10 mM HEPES buffer, pH 7.0 containing 100 mM NaCl, 100 mM EDTA, and 40 µL of the DPPC-LUV⊃MgG, $Zn^{2+}$ ions (1 mM final concentration) were taken in a 3 mL fluorescence cuvette. The kinetic experiment was started (at t = 0 s), and MgG fluorescence emission was monitored, as mentioned in an earlier section. The cuvette was then kept under stirring conditions, and the chamber temperature was set to 30 ºC. After 50 s, compound **3.2a** (final concentration 500 nM) was added to initiate the transport studies. Finally, to terminate the kinetic experiment, the vesicles were lysed by adding 20% Triton X-100 (20 µL) to the cuvette at t = 450 sec, and fluorescent measurements were continued for an additional 50 s (i.e., up to t = 500 s). Following the same procedure, kinetics in DPPC-LUV⊃MgG was measured at 45 ºC.

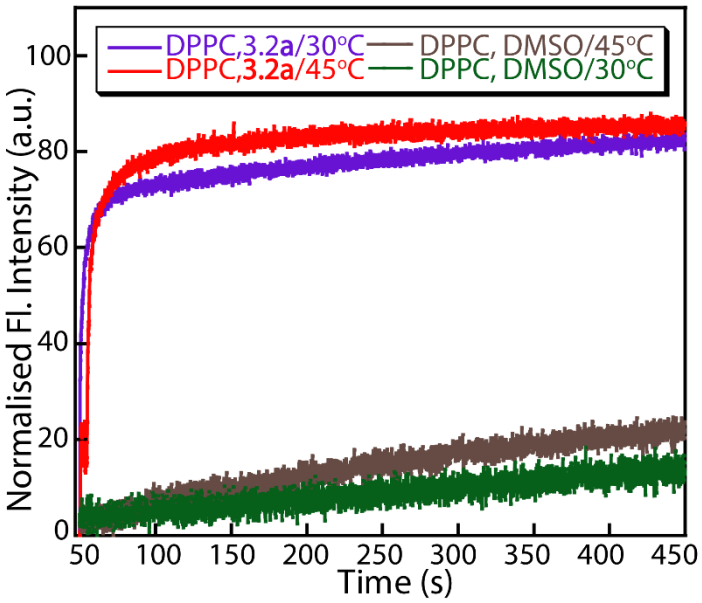


**Figure 3.16.** Temperature-dependent transmembrane $Zn^{2+}$ transport activities of compound **2a** across DPPC-LUV⊃MgG.

[NOTE: DPPC bilayers are well known to undergo a sharp gel-to–liquid crystalline phase transition ($T_m$ ~ 41 °C), below which the membrane exists in a rigid, gel-like state with markedly reduced lateral mobility and permeability. In the present study, transport measurements were deliberately carried out at 30 °C (below $T_m$) and 45 °C (above $T_m$) to probe whether $Zn^{2+}$ transport mediated by compound **3.2a** is sensitive to membrane fluidity. In carrier-mediated transport processes, ion flux is typically suppressed in the gel phase due to limited diffusion of the carrier across the bilayer, whereas supramolecular ion channels are comparatively insensitive to such changes in the membrane phase.

The observation that $Zn^{2+}$ transport efficiencies at 30 °C and 45 °C are essentially identical strongly indicates that the transport process does not rely on diffusive carrier motion but instead proceeds via a channel-like pathway. Thus, while the thesis states more generally that increased temperature enhances membrane fluidity and favours carrier transport, the DPPC system was specifically chosen to exploit its well-defined phase transition and to distinguish between carrier- and channel-mediated mechanisms.]

**3.4.5.12 U-Tube assay for compound 3.2a –** The classical U-tube experiment was performed according to the reported procedure to confirm the mechanistic pathway for the $Zn^{2+}$ transport by compound **3.2a**.[26] The lipid bilayer was mimicked using chloroform (12 mL) as the organic layer. The compound **3.2a** (2 mM) in chloroform was placed at the bottom of the U-tube with

a mild stirring condition. The left arm of the tube was filled with 20 mM HEPES and 0.1 M $ZnCl_2$ solution (12 mL), and the right arm was filled with 20 mM HEPES and 0.1 M aqueous $NaNO_3$ solution (12 mL). Arsenazo-III, a metal ion-sensing dye (20 µM), was added to the receiver arm for sensing $Zn^{2+}$ ions. The $Zn^{2+}$ binding to arsenazo-III dye (20 uM; $\lambda_{max}$ = 545 nm) showed a significant shift in UV-Vis spectra ($\lambda_{max}$ = 600 nm). The $Zn^{2+}$ concentration at the receiver end was monitored using a UV-Vis spectrophotometer after 72 h. The obtained spectra suggested that after 72 h, no significant amount of $Zn^{2+}$ was carried to the receiver end of the U tube. Hence, compound **3.2a** could not act as a carrier through a nonpolar phase ($CHCl_3$). A similar study was performed in the presence of clioquinol (CQ, 2 mM), a $Zn^{2+}$ carrier.

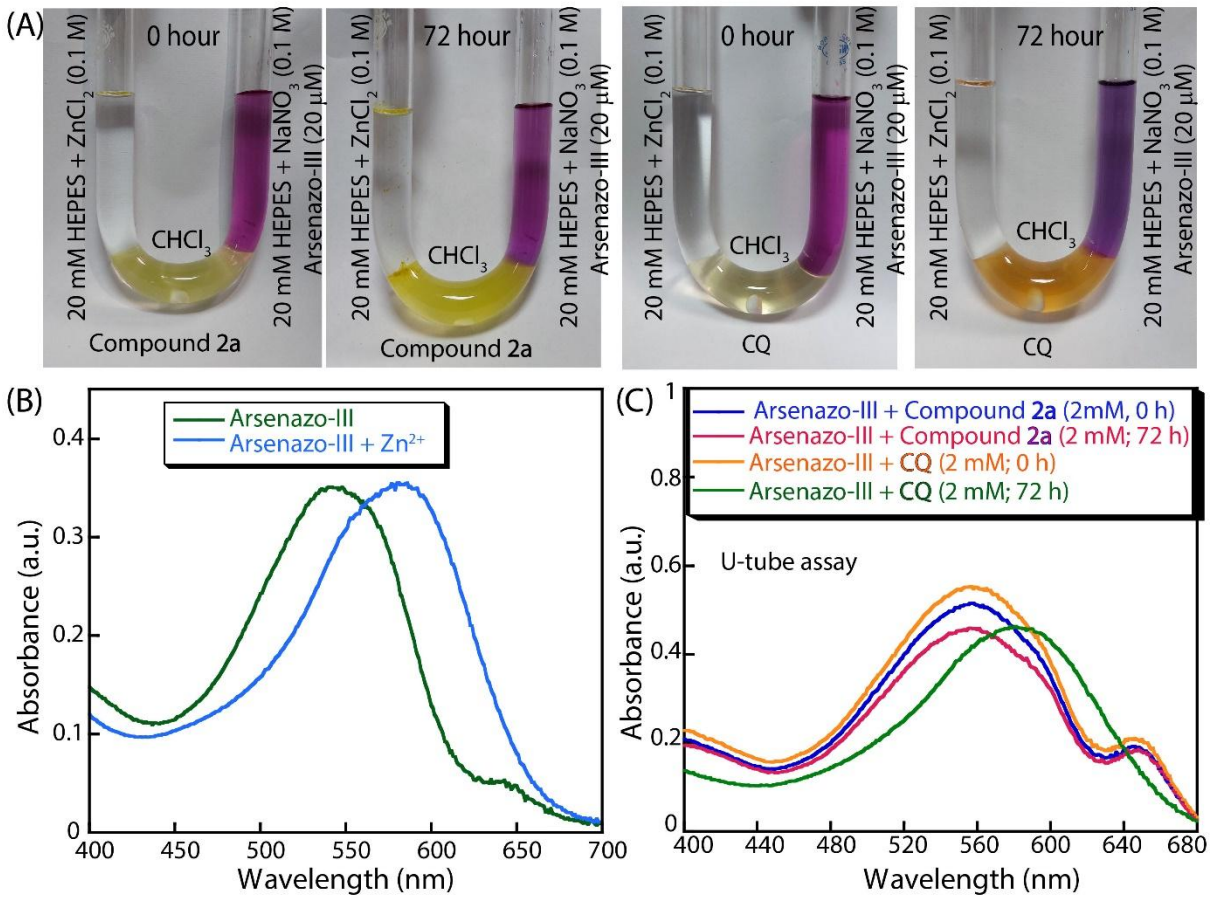


**Figure 3.17.** (A) U-tube assay of compound **3.2a** and clioquinol (CQ; control). (B) UV-Vis absorbance spectra of arsenazo-III dye (20 µM) in the absence and presence of $Zn^{2+}$ ion. (C) UV-Vis absorbance spectra of arsenazo-III dye-containing solution from the receiver end of the U-tube in the presence of compound **3.2a** and clioquinol (CQ) at 0 and 72 h.

### 3.4.6 Black lipid membrane conductance measurements

A solvent-free black lipid membrane (BLM) was formed, as mentioned previously.[27] Briefly, a 20 µm thick Teflon foil (Goodfellow) containing a 50-100 µm orifice was sandwiched between two homemade Delrine half-cells. The orifice in the Teflon foil was carefully pre-painted with 3 µL of hexane/hexadecane on both sides, dried for 20 min, and filled with 2.5 mL of aqueous solution of $ZnCl_2$ on each side. No other salt, acid, or bases were added to avoid their interference with ion conductance measurements. Before forming the lipid bilayer, about 10 µL (size of the surface around 1×1 $cm^2$) of a 1 v% 1,2-diphytanoyl-sn-glycero-3-phosphocholine (diPhyPC) in pentane was introduced on the buffer surface. DPhyPC is generally used in BLM studies to form stable bilayers.[14] After 5-10 min drying, the bilayer was formed by lowering and raising the buffer level. Measurements were performed with Ag-AgCl electrodes. One electrode (GND) was connected to the ground, and the other electrode (Active) was connected to the head stage of an $eONE^{HS}$ amplifier (Elements, Italy) that was used for the conductance measurements in the voltage clamp mode. Signals were recorded with a sampling rate (SR) of 1.25 kHz, final bandwidth-SR/10, and current range of 0-20 nA. The conductance was obtained from the averaged ion current for a series of voltage steps. All measurements were taken from at least three independent measurements. Compound **3.2a** (1 mM) was prepared in DMSO and diluted accordingly. Compound **3.2a** (4 µM) was incorporated into both (GND and Active) chambers with equimolar concentrations (equilibrated for 1 h) to avoid strong asymmetry of the compound. When compound **3.2a** was only added to the Active chamber, it slowly permeated through the bilayer, and a very long time was required for equilibration. Channel formation in the presence of compound **3.2a** was confirmed by the distinctive channel opening and closing events after applying voltages. All data were analysed using the software pClamp 9. The complete data traces were recorded over a long period, and from a large trace, a small portion is presented in the manuscript and supporting information.

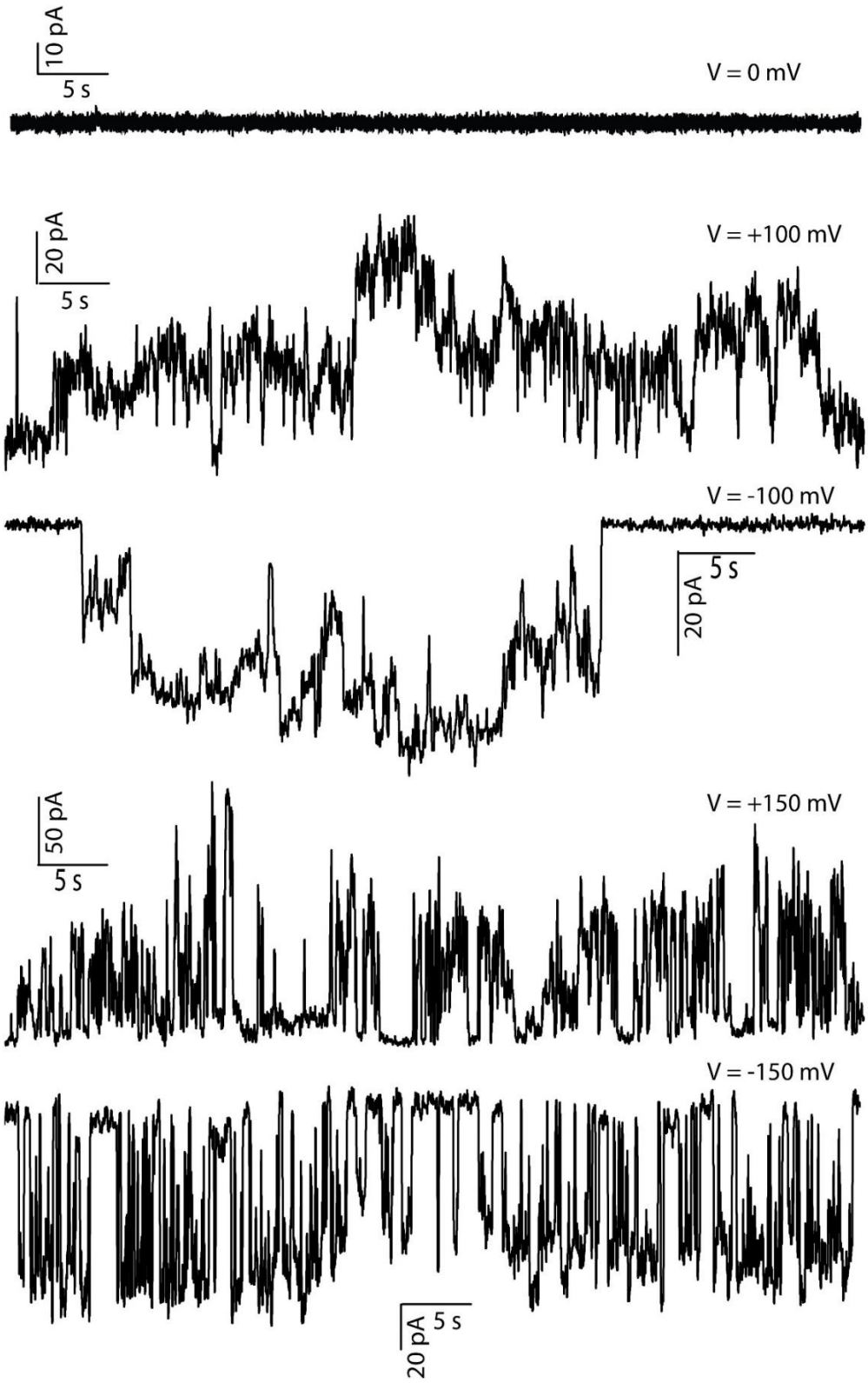


**Figure 3.18.** Ion conductance measurements of compound **3.2a** (4 μM) were recorded at 0 mV, +100 mV, -100 mV, +150 mV, and -150 mV in a symmetrical $ZnCl_2$ solution (0.5 M).

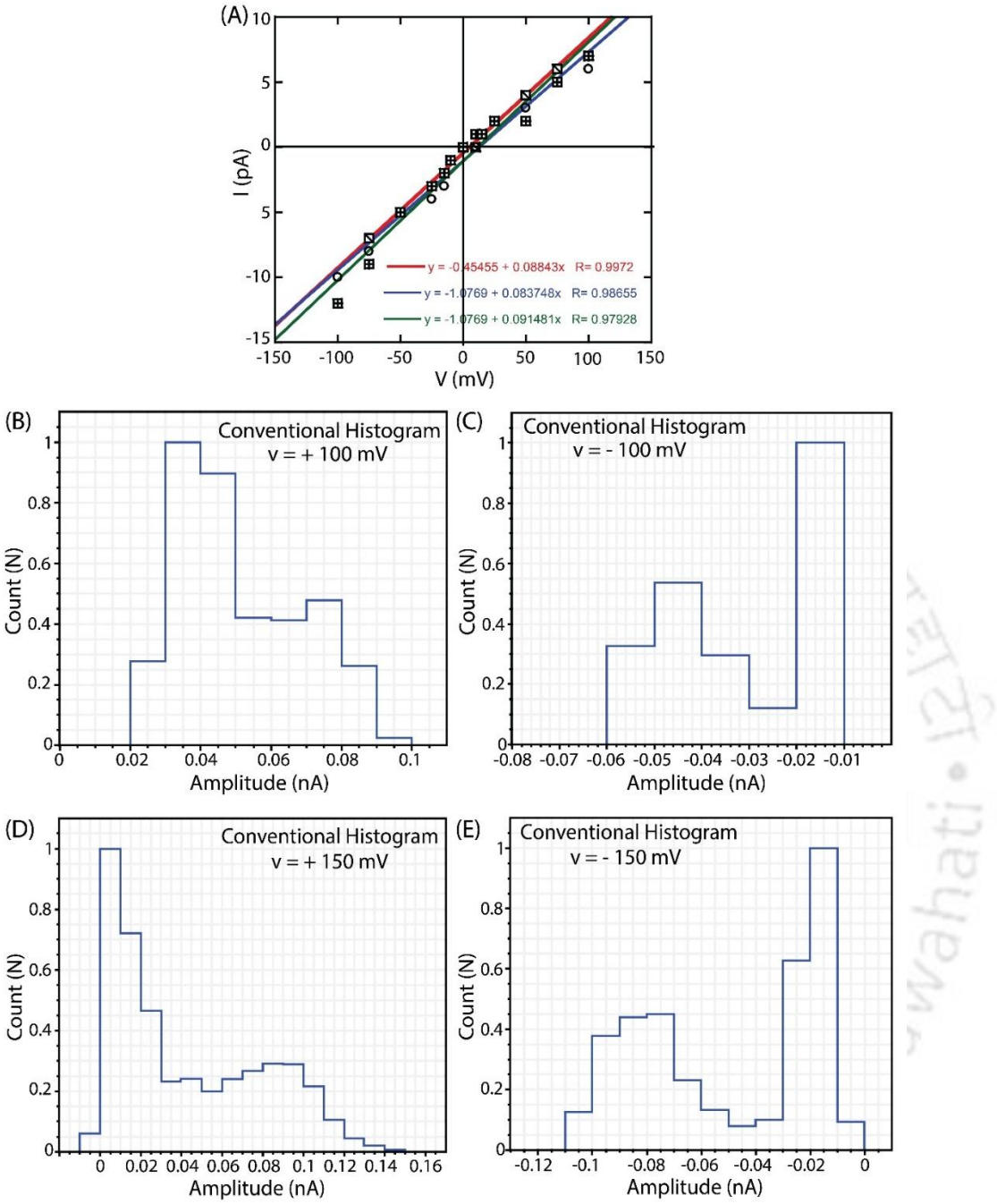


**Figure 3.19.** (A) I–V plots of compound **3.2a** in symmetrical $ZnCl_2$ solution (0.5 M). This curve presents the average of a highly fluctuating ion current. Histograms of the fluctuating ion current for (B) +100 mV, (C) -100 mV, (D) +150 mV, and (E) -150 mV in a symmetrical $ZnCl_2$ solution (0.5 M). The pronounced peak was observed at around 0.02 nA in both cases. This peak we identified as a stable single channel. Less pronounced are multiple of it.

The pore size is estimated from the measured single-channel pore conductance G and is proportional in first order to the bulk conductivity kappa to the pore area $S = \frac{\pi d^2}{4}$ and inversely proportional to the pore length L.[14, 28]

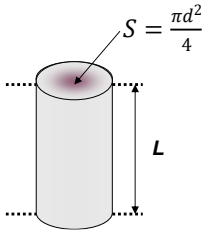


$$G = \kappa \frac{\pi d^2}{4L}; \qquad \kappa = \sum_{i=1}^{N} c_i \rho_i$$

Where our experimentally measured (from I-V plot, Figure S10A) conductance G = 88 pS, d = diameter of the pore, L = length of the channel = 40 Å, $c_i$ = concentration of the ion *i,* [mol/m$^3$] and $\rho_i$ = specific conductance of the ion *i*, [S·m$^2$/mol]. Using published values for $\rho_{Zn(II)}$ = specific conductance of the $Zn^{2+}$ = 52.8 × 10$^{-4}$ [S·m$^2$/mol] and $\rho_{Cl(I)}$ = specific conductance of the $Cl^-$ ion = 76.31 ×10$^{-4}$ [S·m$^2$/mol].[29] We obtained for a concentration of $ZnCl_2$ = 0.5 M the κ = bulk conductivity = 12.9 S/m. Inverting the equation yields the pore diameter (d) = 1.9 Å.

From the histogram analysis (for +150 mV and -150 mV; Figure S10B and S10C), we identified conductance G = 0.02 nA/150 mV = 133 pS. Hence, the pore diameter (d) = 2.3 Å.

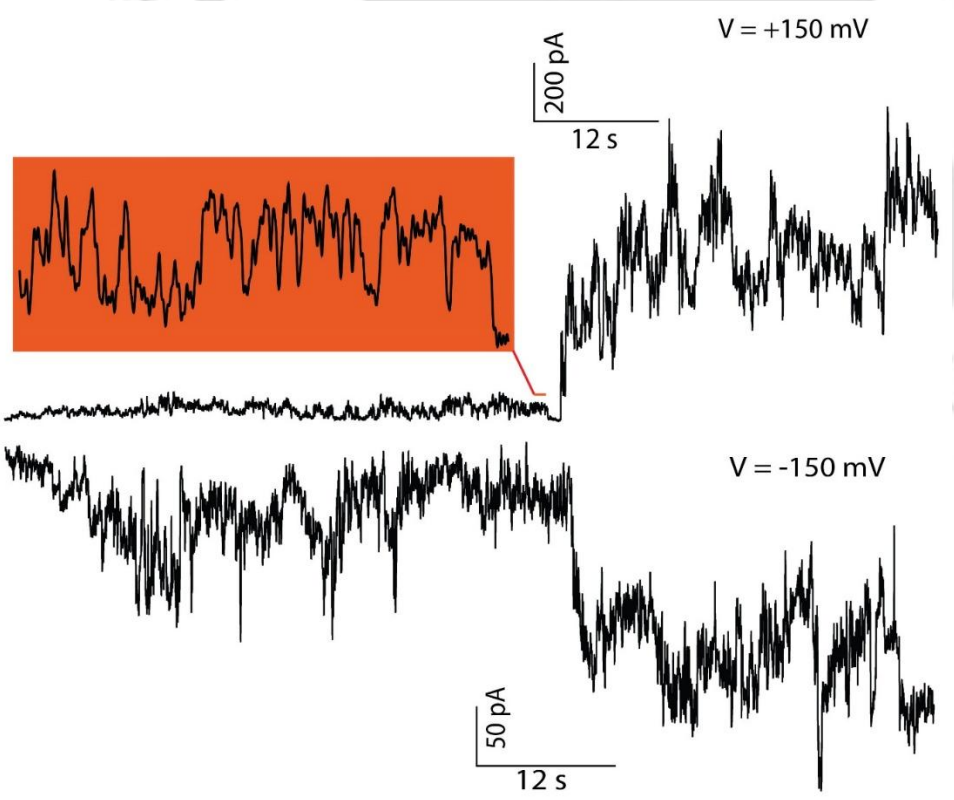


**Figure 3.20.** Ion conductance measurements of compound **3.2a** (4 μM) were recorded at +150 mV and -150 mV in an asymmetrical $ZnCl_2$ solution (GND:0.5 M; Active: 1 M).

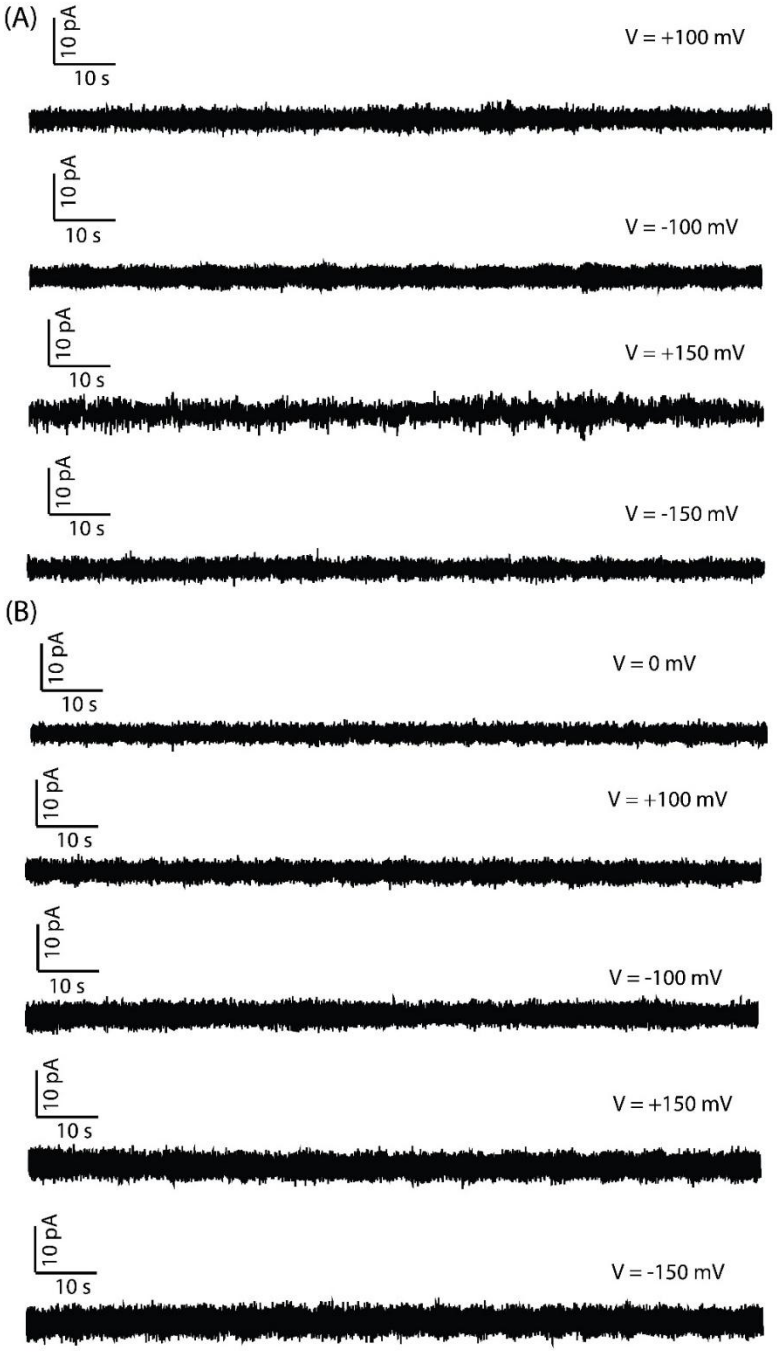


**Figure 3.21.** (A) Ion conductance measurements in the presence of compound **3.2a** (4 μM) in an asymmetrical KCl solution (GND:0.5 M; Active: 1 M) by applying +100 mV, -100 mV, +150 mV, and -150 mV. (B) Ion conductance measurements (no compound added) in an asymmetrical $ZnCl_2$ solution (GND:0.5 M; Active: 1 M) by applying 0 mV, +100 mV, -100 mV, +150 mV, and -150 mV.

### 3.4.7 Crystallographic Study

The crystallographic data were collected using SMART software from the Bruker APEX-II CCD diffractometer equipped with a graphite monochromator and Apex CCD camera. A single

crystal was mounted at the end of the loop, and all crystallographic data were refined using the SHELXL-2018/3 and S-20 Olex2 1.2-alpha. Tyr was solubilised in a DMSO/Water (1:9) mixture with 1 equivalent NaOH for neutralisation, and then $ZnCl_2$ was used as the $Zn^{2+}$ source for co-crystallisation. The obtained data found an octahedral arrangement of Tyr and $Zn^{2+}$ ions in a monoclinic crystal system. Each zinc i78on was coordinated with two Tyr residues through amine (–$NH_2$) and carboxylate (–OOC). One of the axial positions was filled by the carboxylate residue of another Tyr molecule, and a water molecule adjusted the other axial position. The aromatic ring of Tyr provided the π- π stacking energy to hold and form an order in the assembly.

**Table 3.2. Crystallographic analysis of Tyr-$Zn^{2+}$ complex.**

| **Parameter** | **Tyr-$Zn^{2+}$** |
|---|---|
| Empirical formula | C18 H24 N2 O8 Zn |
| Formula weight | 461.76 |
| Temperature (K) | 293 K |
| Crystal system | monoclinic |
| Space group | P 21 |
| a (Aº) | 6.0302(4) |
| b (Aº) | 8.0563(6) |
| c (Aº) | 20.3763(17) |
| α (deg) | 90 |
| β (deg) | 95.479(7) |
| γ (deg) | 90 |
| V (Aº3) | 985.38(13) |
| Z | 2 |
| λ | 0.71073 |
| μ (mm-1) | 1.295 |
| Theta (max) | 28.788 |
| h, k, l max | 8,10,25 |
| F000 | 480.0 |
| Density (g/cm-3) | 1.556 |
| R1, I > 2σ(I) | 0.0582 (3116) |
| wR2 | 0.1415 (3606) |

| | |
|---|---|
| GooF | 1.025 |
| CCDC | 2367108 |

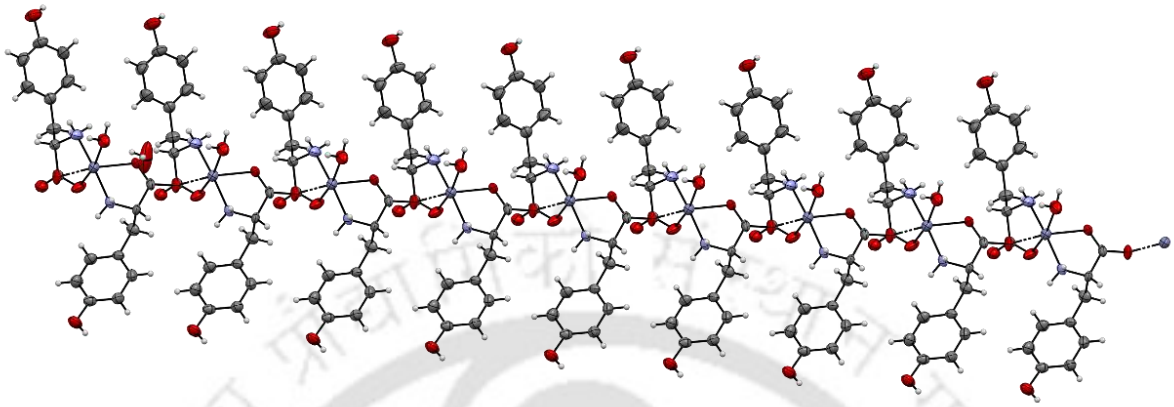

**Figure 3.22.** The XRD structure of Tyr-$Zn^{2+}$ complex (CCDC ID: 2367108).

### 3.4.8 Tyrosine and $Zn^{2+}$-mediated catalytic activities of AHPTS

**3.4.8.1 Tyrosine and $Zn^{2+}$-mediated catalytic activities in HEPES buffer —** The esterase-like activity of artificially synthesized metal complexes is a unique and intriguing property. This phenomenon imparts apoenzyme-like behaviour to natural amino acids, initiating ester hydrolysis in the presence of $Zn^{2+}$ ions.[30] To observe this phenomenon, we treated acylated HPTS (AHPTS) in 50 mM HEPES, pH 7.0, with a solution of tyrosine (Tyr) mixed with $Zn^{2+}$ ions, resulting in a green colour visible to the naked eye, as well as green fluorescence under UV light. This observation suggested the release of HPTS from AHPTS, indicating successful ester hydrolysis mediated by the Tyr-$Zn^{2+}$ complex formed in the solution. Control studies using only Tyr, only $Zn^{2+}$, or lacking both the ligand and metal showed no colour change or fluorescence, indicating the absence of ester hydrolysis and subsequent HPTS release. In addition to visual observation, fluorescence measurements confirmed the release of HPTS, verifying the interaction between Tyr and $Zn^{2+}$ ions to form the active Tyr-$Zn^{2+}$ complex responsible for ester hydrolysis. The AHPTS hydrolysis activity in solution was also investigated in the presence of other amino acids, including phenylalanine (Phe), glycine (Gly), and tryptophan (Trp). Among these tested amino acids, AHPTS hydrolysis activity was observed in the presence of Tyr, while no activity was detected with Phe, Gly, or Trp. The AHPTS hydrolysis in solution was also investigated in the presence of $Cu^{2+}$ ions using AHPTS and Tyr in 50 mM HEPES, pH 7.0. However, no significant hydrolysis of AHPTS to HPTS was observed in the presence of $Cu^{2+}$ ions.

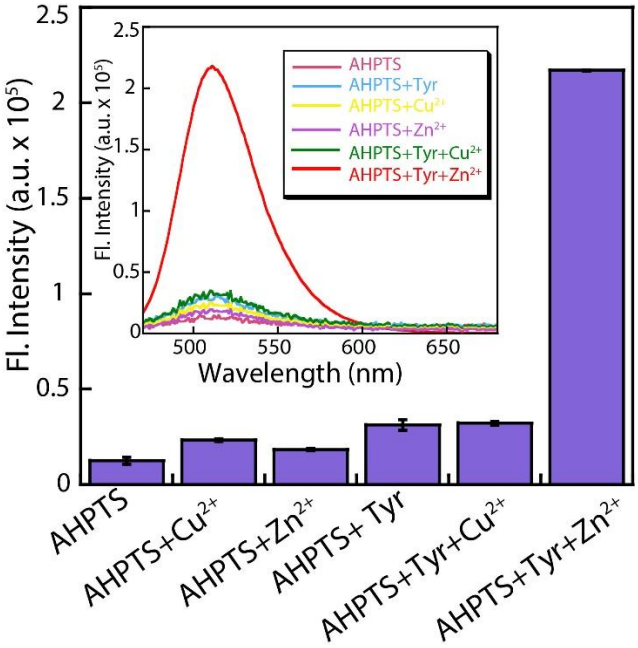


**Figure 3.23.** Bar diagram and fluorescence spectral representation of the hydrolysis of AHPTS to HPTS with Tyr and $Cu^{2+}$/ $Zn^{2+}$ ions in 50 mM HEPES, pH 7.0.

**3.4.8.2 Rate and order of the Tyrosine and $Zn^{2+}$-mediated catalytic activities of AHPTS in the HEPES buffer —** To determine the reaction rate, we conducted a fluorescence-based ester hydrolysis reaction using AHPTS as the substrate and HPTS as the final product in 20 mM HEPES buffer, pH 7.0. We measured the product concentration formed in the reaction vessel at various substrate concentrations using a fluorescence-based calibration plot for HPTS. When the rate of the reaction v/s product concentration was fitted in the model enzymatic catalysis equation, i.e. in Michaelis–Menten curve fitting ($R^2 = 0.999$), the maximum catalytic rate $V_{max}$ and Michaelis constant $K_m$ values were found to be 91.57 ± 1.51 μM $min^{-1}$ and 106.06 ± 7.51 μM respectively. Hence, it proves that the reaction follows first-order enzyme kinetics similar to the other biological catalytic systems.[31] The calculated catalytic efficiency (using $V_{max}$ and $K_m$ values) was 719 $M^{-1}$ $s^{-1}$.

The compound concentration = 20 μM.

$V_{max}$ = 91.57 μM $min^{-1}$ = 1.52 μM $s^{-1}$.

$K_m$ = 106.06 μM.

$K_{cat}$ = 0.0763 $s^{-1}$.

Catalytic efficiency = ($K_{cat}/K_m$) = [ 0.0763 $s^{-1}$]/ [106.06 μM] = 719 $M^{-1}$ $s^{-1}$.

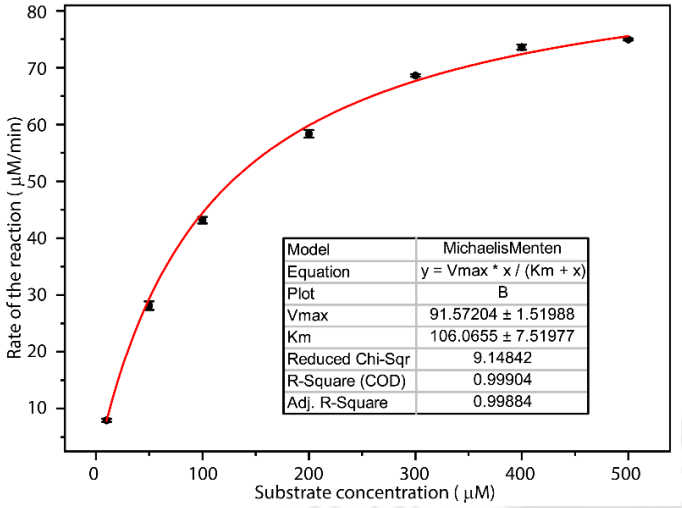


**Figure 3.24.** Michaelis–Menten curve fitting for catalytic system Tyr-$Zn^{2+}$ performed in 20 mM HEPES buffer, pH 7.0, with AHPTS as substrate.

**Note:** However, the catalytic activities of the Tyr-$Zn^{2+}$ complex under the experimental condition could be underestimated. Our additional studies revealed that the Tyr-$Zn^{2+}$ complex does not significantly alter the fluorescence signal of generated HPTS from AHPTS. Meanwhile, free $Zn^{2+}$ ions significantly quench the fluorescence signal of HPTS. Therefore, the actual fluoresce signal could be more than the recorded one due to its quenching by free $Zn^{2+}$ ions in solution.

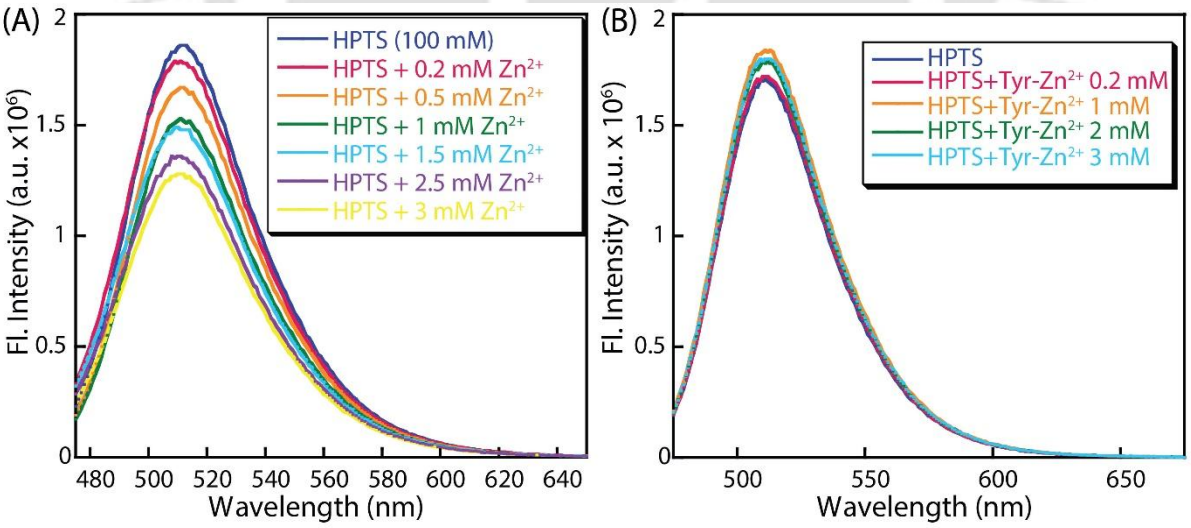


**Figure 3.25.** Variation of HPTS fluorescence intensity in the presence of (A) free $Zn^{2+}$ ions and (B) Tyr-$Zn^{2+}$ complex in 20 mM HEPES buffer, pH 7.0.

### 3.4.9 Tyrosine and $Zn^{2+}$-mediated catalytic activities under the vesicular environment

**3.4.9.1 Preparation of EYPC/CHOL-LUVs⊃AHPTS/Tyr —** For the ion transport mediated catalysis activity studies, (50 mg/mL in deacidified $CHCl_3$) and CHOL (25 mg/mL in deacidified $CHCl_3$) were taken in a clean and dry sample vial in a molar ratio of 8:2. The solution was evaporated for 6 h under reduced pressure to form a thin lipid film. This film was rehydrated with 20 mM HEPES buffer containing 100 mM $NaNO_3$ and 2 mM AHPTS (sodium 8-acetoxypyrene-1,3,6-trisulfonate) and 500 μM Tyrosine (Tyr), pH 7.0, and the resultant suspension was vortexed six to seven times for a period of 1 h.[30] The suspension was then frozen–thawed 7–9 times, followed by 10 min of constant vortexing. The lipid suspension was then extruded 19–21 times using a mini extruder (200 nm pore size) to obtain a uniform vesicle size of 200 nm. Finally, the unencapsulated dye was removed using the size exclusion column (Sephadex G-50) and 20 mM HEPES buffer containing 100 mM $NaNO_3$, pH 7.0, as the eluting solution. The final lipid concentration was 25 mM (assuming 100% lipid regeneration). Other vesicles encapsulating a lower concentration of precatalyst (100 μM Tyrosine) was also prepared following the same procedure.

**3.4.9.2 Ion transport mediated catalytic activity studies across EYPC/CHOL-LUV⊃AHPTS/Tyr —** For the catalysis-based fluorescence assay, in a clean and dry fluorescence cuvette (3 mL), 20 mM HEPES buffer containing 100 mM $NaNO_3$, pH 7.0 (1920 μL), EYPC/CHOL-LUV⊃AHPTS/Tyr (50 μL), and $ZnCl_2$ (final concentration 3 mM) were added. The cuvette was placed under slow stirring conditions in a fluorescence spectrophotometer for about 3 min to equilibrate the compound with the LUVs. The fluorescence was evaluated over time ($\lambda_{em}$ = 510 nm, $\lambda_{ex}$ = 450 nm). At 50 s, 10 μL of the compound (from the DMSO stock) was added to the cuvette solution to initiate transport. Finally, the vesicles were completely lysed at 800 s by adding 20 μL of 20% Triton X-100. As AHPTS hydrolysed to generate HPTS, the fluorescence intensity increased. Transport studies for the compounds were performed in triplicate at various concentrations (10 μM, 7 μM, 5 μM, 3 μM). The control experiment was performed under similar assay conditions, with spectral measurements taken in the absence of **3.2a** or $Zn^{2+}$ ions. Similarly, another experiment was performed where 2920 μL of buffer, EYPC/CHOL-LUV⊃AHPTS/Tyr (50 μL), and 10 μL of compound (from DMSO stock to make the final concentration 10 μM) were stirred for 3 min, and at t = 50 s, a zinc pulse (3 mM) was applied to the cuvette to start the influx kinetics. Subsequent $Zn^{2+}$ pulses at 350 s and 650 s led to a stepwise $Zn^{2+}$ influx, resulting in a gradual increase in catalysis. Then, 20 μL of 20% Triton X-100 was added at t = 950 s for lysing the vesicles. The fluorescence intensity measurement was continued for a further 100 s. Similarly,

another experiment was performed to check the catalytic process occurring in a lower concentration of $Zn^{2+}$ and tyrosine, for which LUVs encapsulating 100 μM tyrosine were taken, and measurements were done as mentioned above by changing the $ZnCl_2$ pulse to 1 mM and 500 μM (final concentration).

**3.4.9.3 Ion transport mediated catalytic activity studies across EYPC/CHOL-LUV⊃AHPTS/Tyr —** Vesicles were prepared following a previously mentioned method, with the encapsulated AHPTS concentration varied across different measurements (0.5 mM, 0.75 mM, 1 mM, 2 mM, 3 mM, and 5 mM). For the fluorescence-based kinetics measurements, in a clean and dry fluorescence cuvette (3 mL), 20 mM HEPES buffer containing 100 mM $NaNO_3$, pH 7.0 (1920 μL), EYPC/CHOL-LUV⊃AHPTS/Tyr (50 μL), and $ZnCl_2$ (final concentration 3 mM) were added. The cuvette was placed under slow stirring conditions in a fluorescence spectrophotometer for about 3 min to equilibrate the compound with the LUVs. The fluorescence was evaluated as a function of time ($\lambda_{em}$ = 510 nm, $\lambda_{ex}$ = 450 nm). At 50 s, 10 μL of compound (10 mM final concentration) was added to the cuvette solution to initiate the transport. Finally, the vesicles were completely lysed at 800 s by adding 20 μL of 20% Triton X-100. As AHPTS hydrolysed to generate HPTS, the fluorescence intensity increased.

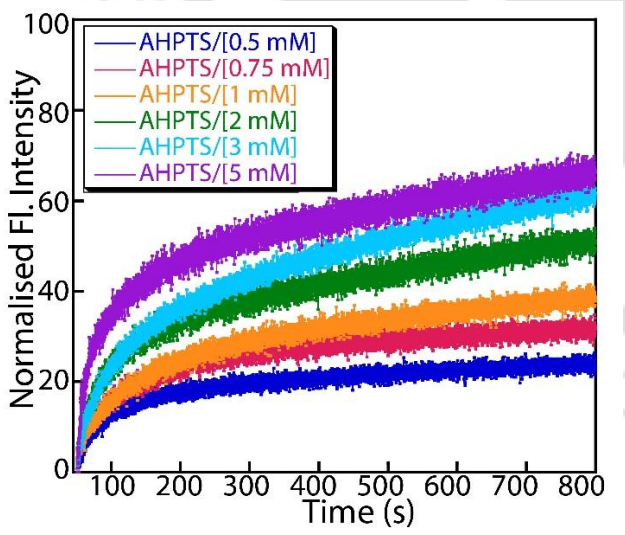


**Figure 3.26.** Kinetics measurement of the conversion from AHPTS to HPTS in EYPC/CHOL LUVs⊃AHPTS/Tyr with varying AHPTS concentrations (0.5 mM, 0.75 mM, 1 mM, 2 mM, 3 mM, and 5 mM).

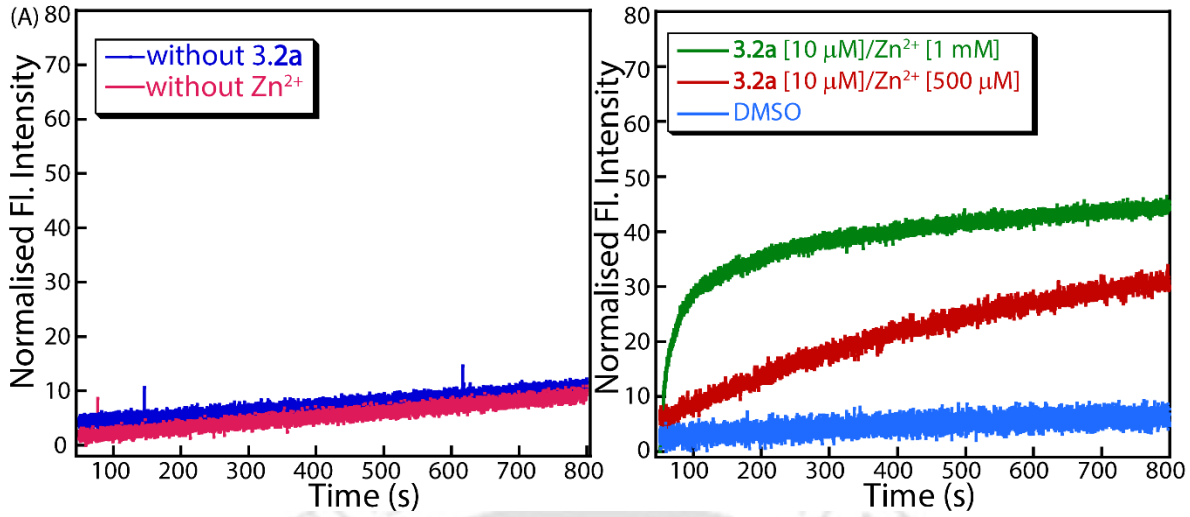


**Figure 3.27.** (A) Control study for the hydrolysis of AHPTS to HPTS in the absence of transporter 2a and $Zn^{2+}$ ions using LUVs. (B) Control study for the hydrolysis of AHPTS to HPTS in the presence of a lower concentration of Tyr (100 µM) encapsulated and 1 mM $ZnCl_2$ pulse.

**Note:** We also measured Tyr- and $Zn^{2+}$-mediated catalytic activities under vesicular conditions at lower concentrations of $Zn^{2+}$ (1 mM and 500 µM) and pre-catalyst Tyr (100 µM) to demonstrate that this catalytic system is sensitive to low-concentration counterparts.

**3.4.9.4 EDTA-based catalysis study in EYPC/CHOL-LUVs⊃AHPTS/Tyr —** For the EDTA-based catalytic study, LUVs were prepared according to the previously mentioned procedure. For the fluorescence assay, in a clean and dry fluorescence cuvette, 20 mM HEPES buffer pH 7.0 (1920 µL), EYPC/CHOL-LUV⊃AHPTS/Tyr (50 µL), and **3.2a** (final concentration 10 µM) were added. The cuvette was placed under slow stirring conditions in a fluorescence spectrophotometer for about 3 min to equilibrate the compound with the LUVs. The fluorescence was evaluated as a function of time ($\lambda_{em}$ = 510 nm, $\lambda_{ex}$ = 450 nm). At 50 s, 20 µL of $ZnCl_2$ (final concentration 3 mM) was added to the cuvette solution to initiate the transport. At 120s, EDTA (3mM pulse) was added to the solution, and similar amounts of EDTA were added at 350s, 450s, and 750s to observe the change in the catalytic process. Finally, the vesicles were completely lysed at 900 s by adding 20 µL of 20% Triton X-100.

**3.4.9.5 Effect of EDTA on the fluorescence intensity of HPTS —** For the EDTA control experiment, a lipid mixture consisting of egg yolk phosphatidylcholine (EYPC, 50 mg/mL in deacidified $CHCl_3$) and cholesterol (CHOL, 25 mg/mL in deacidified $CHCl_3$) in an 8:2 molar

ratio was placed in a clean, dry sample vial. The solution was evaporated under reduced pressure for 6 hours to form a thin lipid film. This film was then rehydrated with 20 mM HEPES buffer containing 100 mM $NaNO_3$, 1 mM HPTS (sodium 8-acetoxypyrene-1,3,6-trisulfonate), and 500 µM tyrosine (Tyr), pH 7.0. The resulting suspension was vortexed 6-7 times for 1 hour, then subjected to 7-9 freeze-thaw cycles and 10 minutes of constant vortexing. The lipid suspension was extruded 19-21 times through a mini extruder with a 200 nm pore size to obtain uniformly sized vesicles (~200 nm). Unencapsulated dye was removed by size-exclusion chromatography (Sephadex G-50) using 20 mM HEPES buffer containing 100 mM $NaNO_3$, pH 7.0, as the elution buffer. The final lipid concentration was 25 mM, assuming complete lipid regeneration. For the transport experiment, 1910 µL of 20 mM HEPES buffer with 100 mM $NaNO_3$ (pH 7.0) was mixed with 50 µL of the EYPC/CHOL LUVs containing HPTS/Tyr, and 20 µL $Zn^{2+}$ (final working concentration 3 mM) in a fluorescence cuvette. The solution was placed in a fluorescence spectrophotometer at room temperature under slow stirring. The fluorescence intensity of the HPTS dye was monitored at $\lambda_{ex}$ = 450 nm and $\lambda_{em}$ = 510 nm. At 50 s, 20 µL of EDTA (final working concentration 3 mM) was added to the stirring vesicle solution. After 900 s, the vesicles were lysed with 20 µL of 20% Triton X-100 solution, and fluorescence measurements were continued until 1000 s.

**Note:** Interestingly, rapid initial acidification (decrease in HPTS fluorescence) was observed upon the addition of EDTA in the presence of $Zn^{2+}$ ions. However, only EDTA (without $Zn^{2+}$ ion) addition showed no significant change in HPTS fluorescence. These observations suggest that the complexation of the $Zn^{2+}$ ion with EDTA (an EDTA-$Zn^{2+}$ complex unlikely to cross the lipid bilayer) leads to the release of protons into the extravesicular environment, creating a proton gradient across the lipid bilayer.

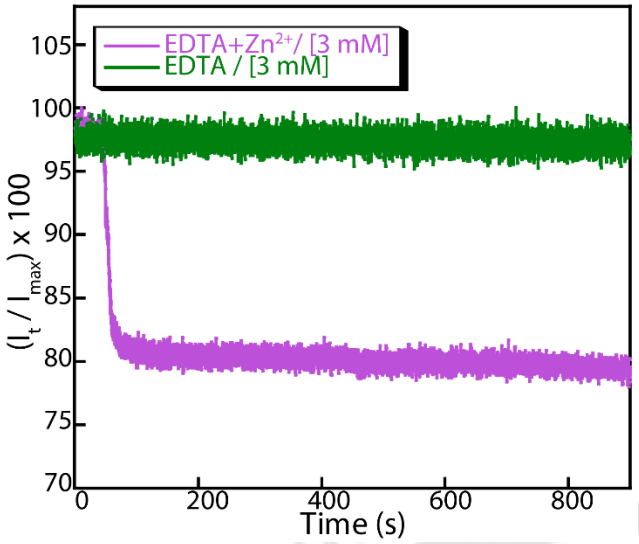


**Figure 3.28.** Effect of EDTA addition to the fluorescence intensity of HPTS in $Zn^{2+}$ ion-equilibrated EYPC/CHOL-LUV⊃AHPTS/Tyr.

**3.4.9.6 Catalysis verification across EYPC/CHOL-LUV⊃CFDA-SE/Tyr —** For the CFDA-SE assay, vesicles were prepared, as mentioned in the earlier section. Briefly, EYPC/CHOL were taken in an 8:2 molar ratio, and to it, 20 mM HEPES, 100 mM $NaNO_3$, 2 mM CFDA-SE, and 500 µM Tyr, pH 7.0, were added for hydration. The resultant solution was vortexed, and a freeze-thaw cycle was performed 6-7 times, followed by 10 min of constant vortexing. Then, the lipid solution was extruded 19-21 times using a mini extruder with a 200 nm polycarbonate membrane from Avanti Polar Lipids. Finally, the unencapsulated dye was removed using a size-exclusion chromatography column (Sephadex G-50) with 20 mM HEPES buffer containing 100 mM NaNO3, pH 7.0, as the eluent. The final lipid concentration was 25 mM (assuming 100% lipid regeneration).

**3.4.9.7 Ion-transport mediated catalytic activity studies across EYPC/CHOL-LUV⊃CFDA-SE/Tyr —** For the catalysis-based fluorescence assay, in a clean and dry fluorescence cuvette (3 mL), 20 mM HEPES buffer containing 100 mM $NaNO_3$, pH 7.0 (1920 µL), EYPC/CHOL-LUV⊃CFDA-SE/Tyr (50 µM), and $ZnCl_2$ (20 µL from a stock solution of 1.5 M) was added. The cuvette was then placed under slow stirring conditions in a fluorescence spectrophotometer for about 3 min to equilibrate the compound with the LUVs. The fluorescence was evaluated as a function of time ($\lambda_{em}$ = 590 nm, $\lambda_{ex}$ = 490 nm). At 50 s, 10 µL of compound (from DMSO stock) was added to the cuvette solution to initiate the transport. Finally, the vesicles were completely lysed at 800 s by adding 20 µL of 20% Triton X-100. As

CFDA-SE hydrolysed to give CFSE, the fluorescence intensity increased. The transport studies for the compounds were performed in repetition and at various concentrations (10 μM, 5 μM, 2.5 μM). The fluorescence intensity measurement was continued for a further 200 s.

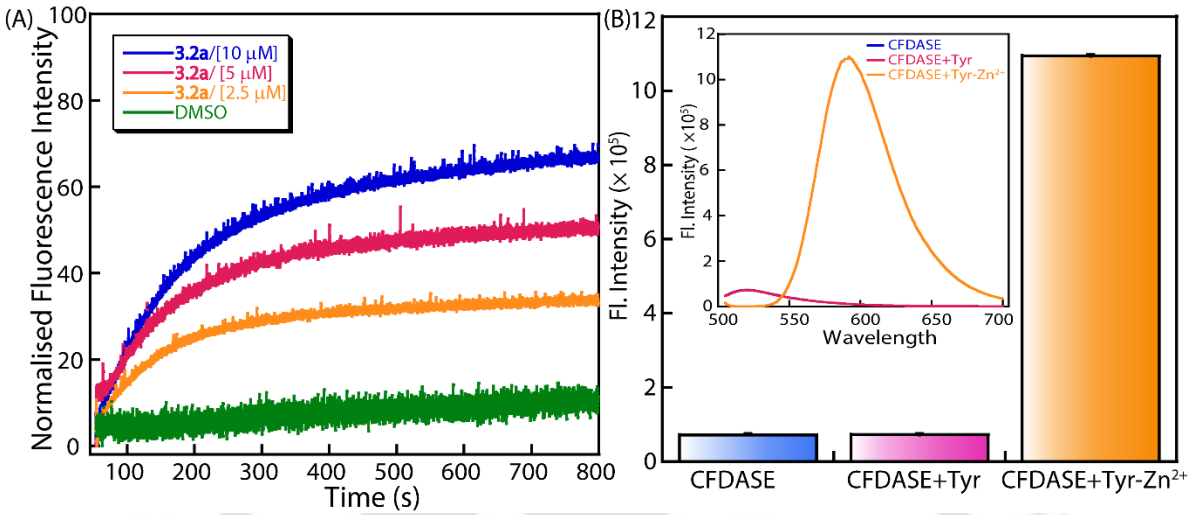


**Figure 3.29.** (A) Fluorescence spectra of CFSE in the presence of Tyr-$Zn^{2+}$ complex and different concentrations of compound **3.2a** using EYPC/CHOL-LUV⊃CFDA-SE/Tyr. (B) The extent of CFDA-SE hydrolysis in the presence of Tyr-$Zn^{2+}$ in 20 mM HEPES buffer, pH 7.0. Inset: Fluorescence spectral change for the hydrolysis of CFDA-SE in the presence of Tyr-$Zn^{2+}$ in 20 mM HEPES buffer, pH 7.0.

### 3.4.10 Chemical-to-optical signal transduction study

**3.4.10.1 Ion transport and catalysis-mediated fluorescence measurements across EYPC/CHOL-LUV⊃AHPTS/Tyr —** For the fluorescence spectral study, we have taken a combination of **3.2a**, $Zn^{2+}$ ions and Tyr in 20 mM HEPES buffer where various eight combinations were recorded ($\lambda_{em}$ = 510 nm, $\lambda_{ex}$ = 450 nm) according to truth table input. For transport studies, two different kinds of vesicles were prepared, as mentioned in the earlier section, wherein one system, Tyr, was absent; in the second, Tyr, was kept inside, but **3.2a**, $Zn^{2+,}$ ions were added according to the truth table. Transport studies were performed as mentioned in the earlier section.

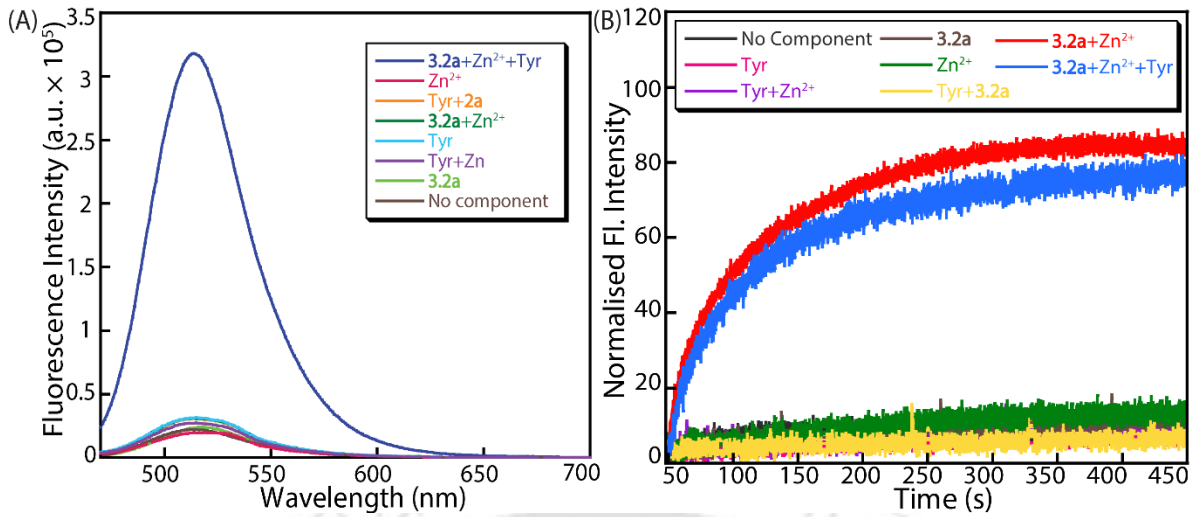


**Figure 3.30.** (A) Fluorescence spectra of AHPTS in the presence and absence of various additives. (B) MgG-based ion transport studies in the presence and absence of different additives. All these measurements were performed using EYPC/CHOL-LUV⊃MgG encapsulating either Tyr, $Zn^{2+}$ ions or both in the presence and absence of compound **3.2a**. All measurements were conducted using EYPC/CHOL-LUV⊃MgG, with or without Tyr encapsulation, while the other two inputs-$Zn^{2+}$ and compound **3.2a,** were adjusted according to the truth table.

**3.4.10.2 Chemical-to-optical signal transduction study in giant unilamellar vesicles (GUVs) —** In a clean and dry glass vial, EYPC, cholesterol and DPPS (from the respective stock solution) were taken in the molar ratio of 6:3.5:0.5 and dried under vacuum for 6 hours. To that lipid film, 200 µL of light liquid paraffin oil was added and sonicated for 30 minutes until the lipid film was completely dissolved in the oil. After that, 20 µL of the upper buffer (100 mM HEPES, 200 mM sucrose, 1 mM Tyr, 2 mM AHPTS, pH = 7.4) was added, and the solution was mixed thoroughly to form an emulsion. The emulsion was then carefully added to 500 µL of lower buffer (100 mM HEPES, 200 mM glucose in $H_2O$, pH = 7.4) in a centrifuge tube, and the whole mixture was pipetted up and down thoroughly to mix everything. The emulsion was centrifuged for 15 minutes at 10000 rpm to remove the oil and the extravesicular components. This process was repeated 4-5 times for maximum removal of paraffin oil from the solution. The final precipitate (GUVs) was mixed with 100 µL of lower buffer (final vesicle conc. of 15 mM). The experiment was performed under a fluorescence microscope using these floating GUVs.

(A)

| | Tyrosine | Transporter **3.2a** | $Zn^{2+}$ | % Transport | Relative Fl. Intensity |
|---|---|---|---|---|---|
| a | 0 | 0 | 0 | 7.7 | 7.1 |
| b | 1 | 0 | 0 | 8.0 | 10.3 |
| c | 0 | 1 | 0 | 11.5 | 7.3 |
| d | 0 | 0 | 1 | 12.7 | 7.0 |
| e | 1 | 0 | 1 | 10.3 | 8.4 |
| f | 1 | 1 | 0 | 8.1 | 9.4 |
| g | 0 | 1 | 1 | 82.5 | 9.5 |
| h | 1 | 1 | 1 | 78.7 | 100 |

(B)

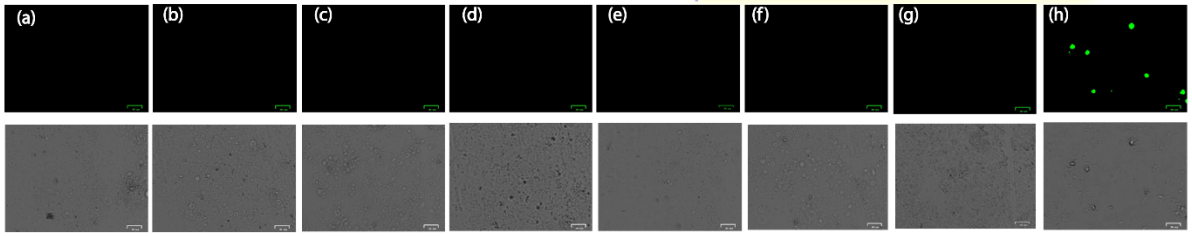


**Figure 3.31.** (A) Truth table with %T and relative fluorescence intensity data with respect to the algorithm of 1 and 0. (B) Representative fluorescence microscopic images of GUVs with respect to the truth table. The GUVs were suspended in 100 mM HEPES, 200 mM glucose in $H_2O$, pH = 7.4, under different conditions mentioned in the truth table (a-h).

### 3.4.11 NMR spectra of the synthesized compound

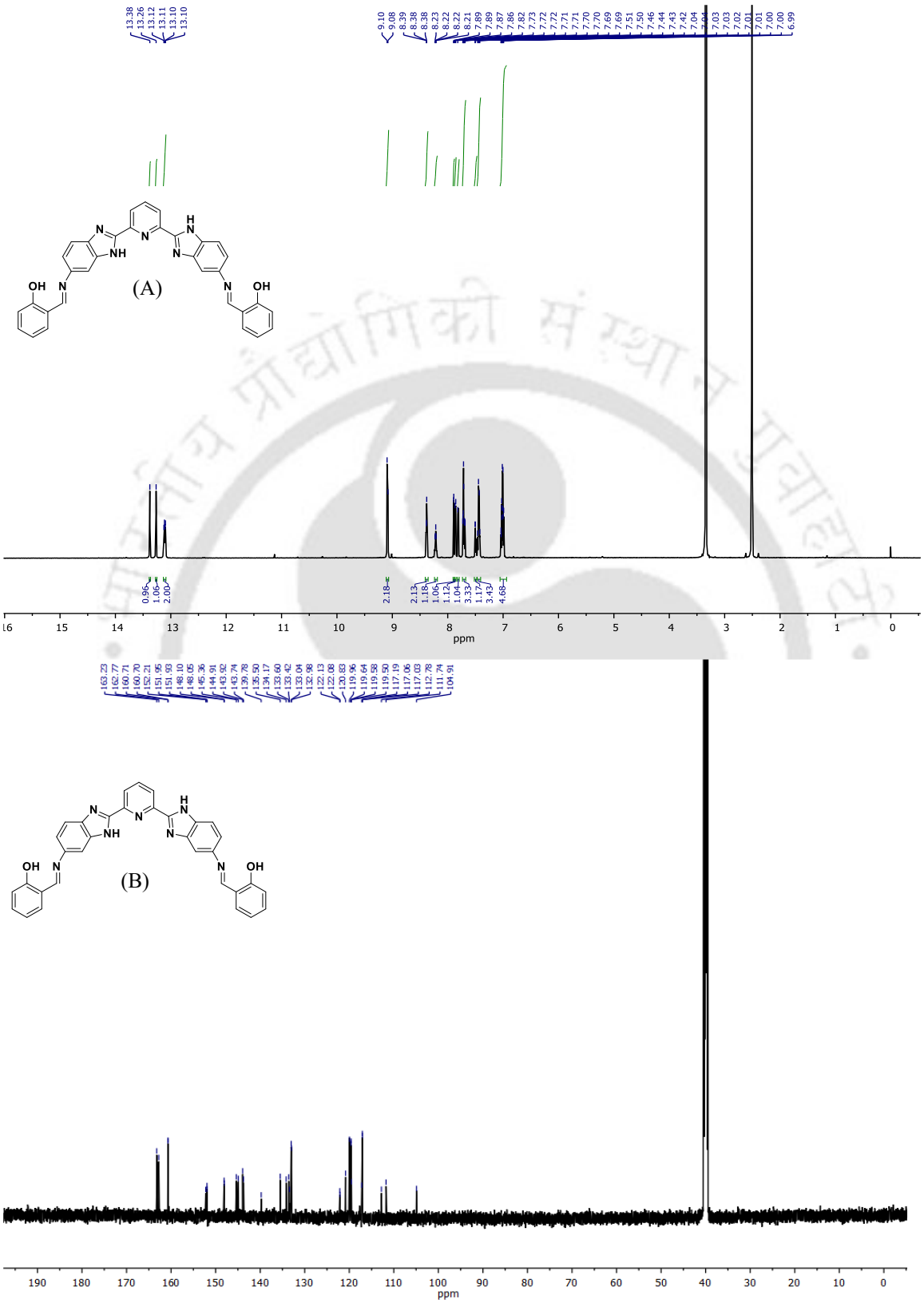


**Figure 3.32.** (A) $^{1}H$ and (B) $^{13}C$ (B) NMR of compound **3.2a**.

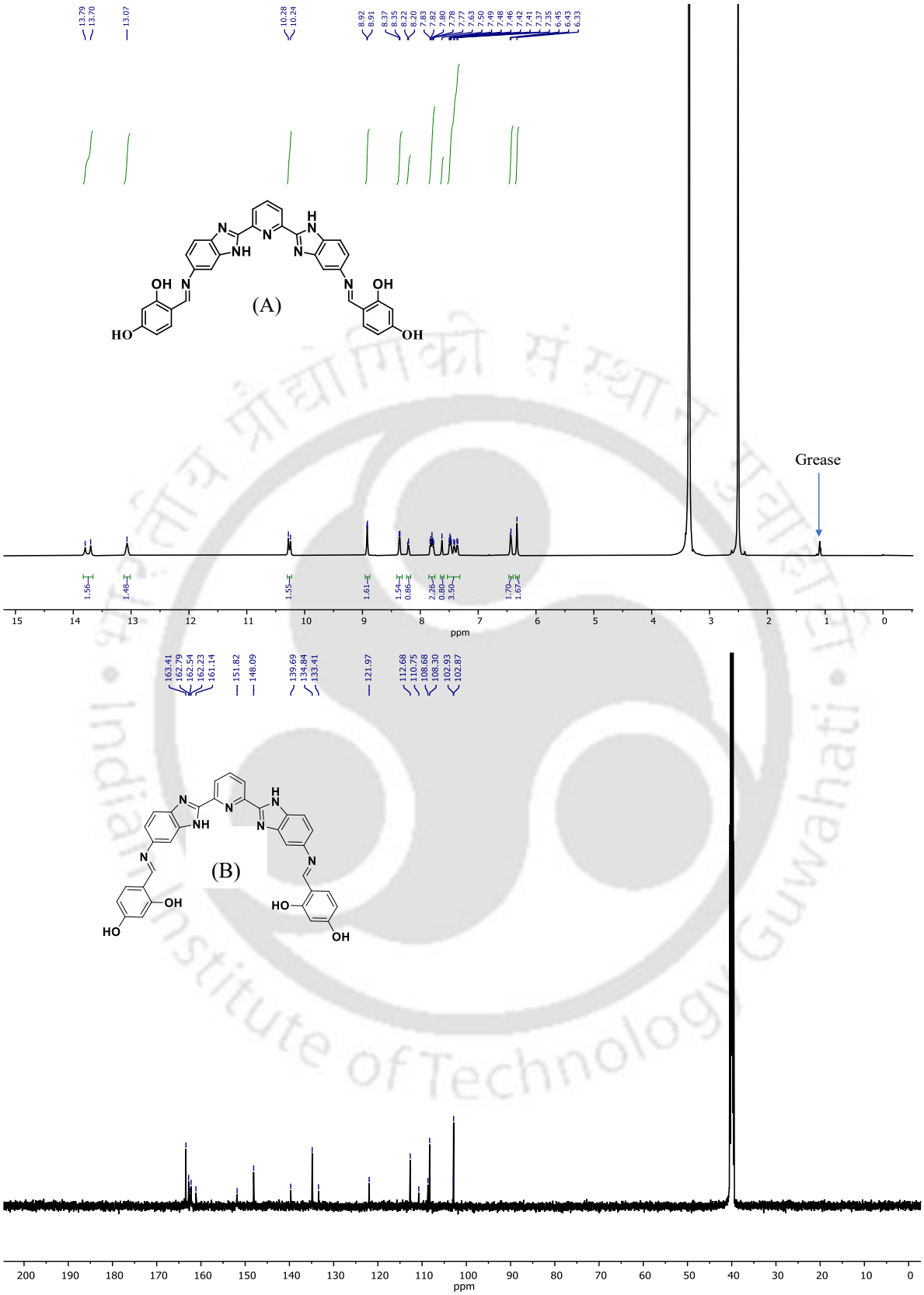


**Figure 3.33.** (A) $^{1}H$ and (B) $^{13}C$ (B) NMR of compound **3.2b**.

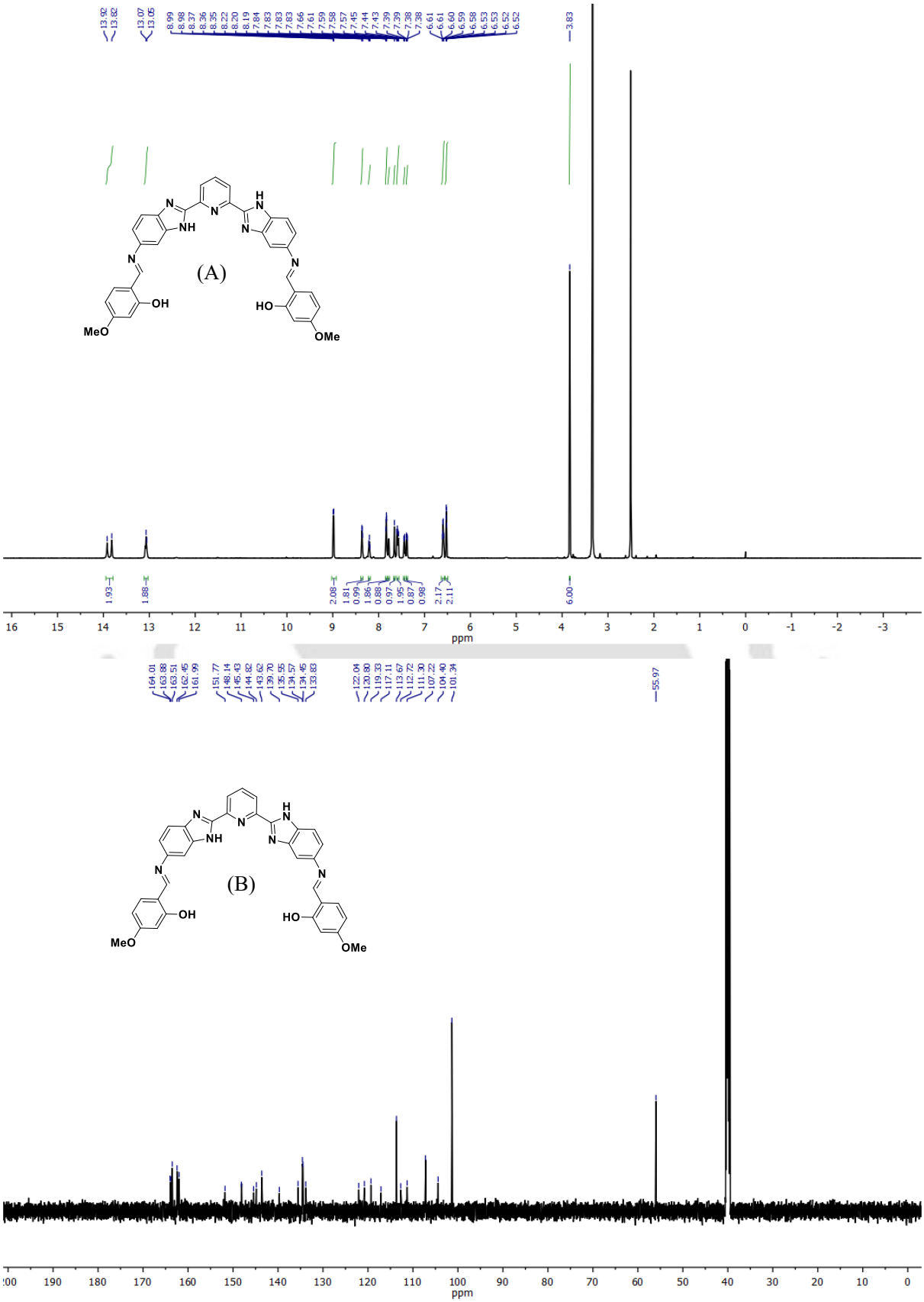


**Figure 3.34.** (A) $^{1}H$ and (B) $^{13}C$ (B) NMR of compound **3.2c**.

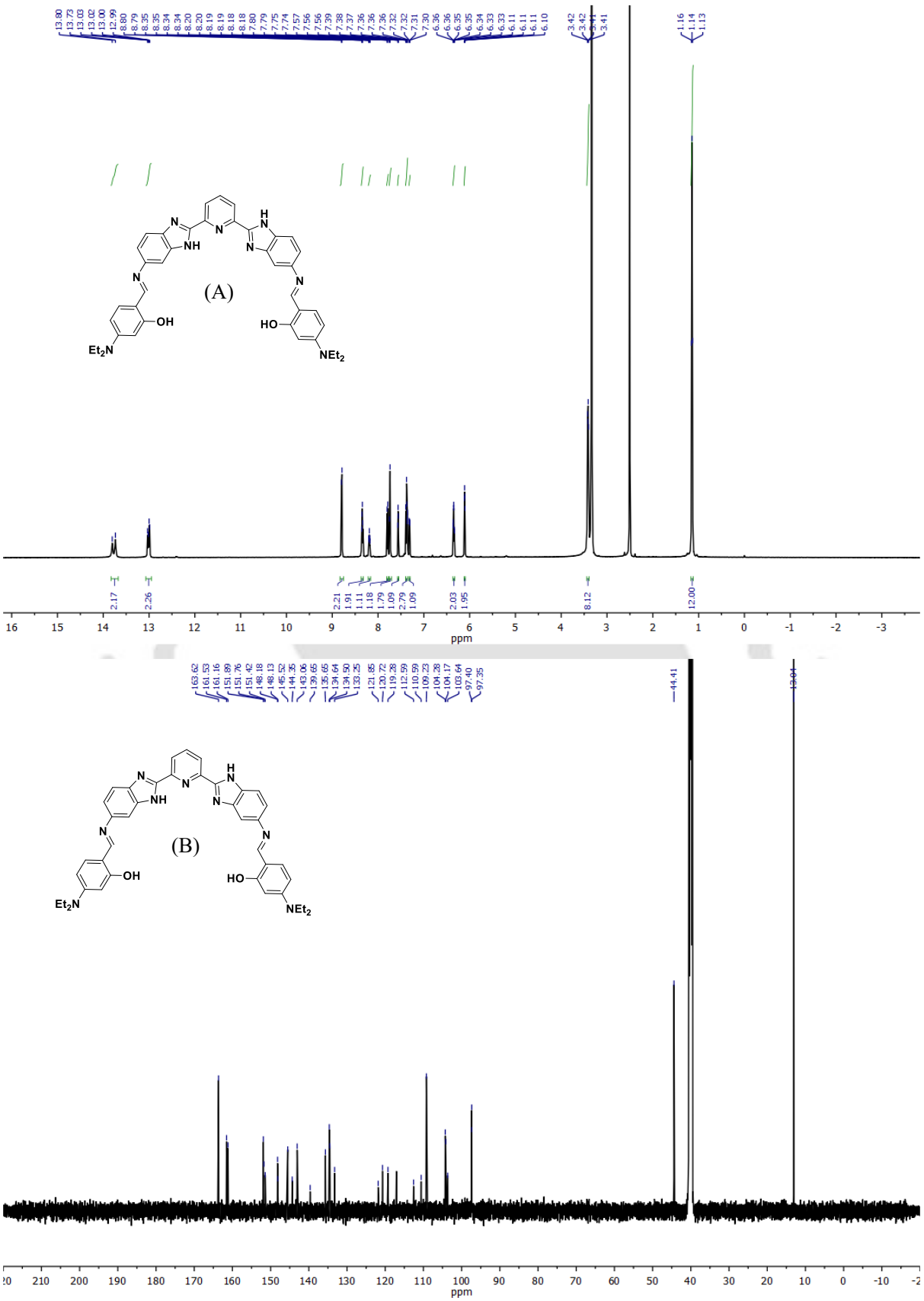


**Figure 3.35.** (A) $^{1}H$ and (B) $^{13}C$ (B) NMR of compound **3.2d**.

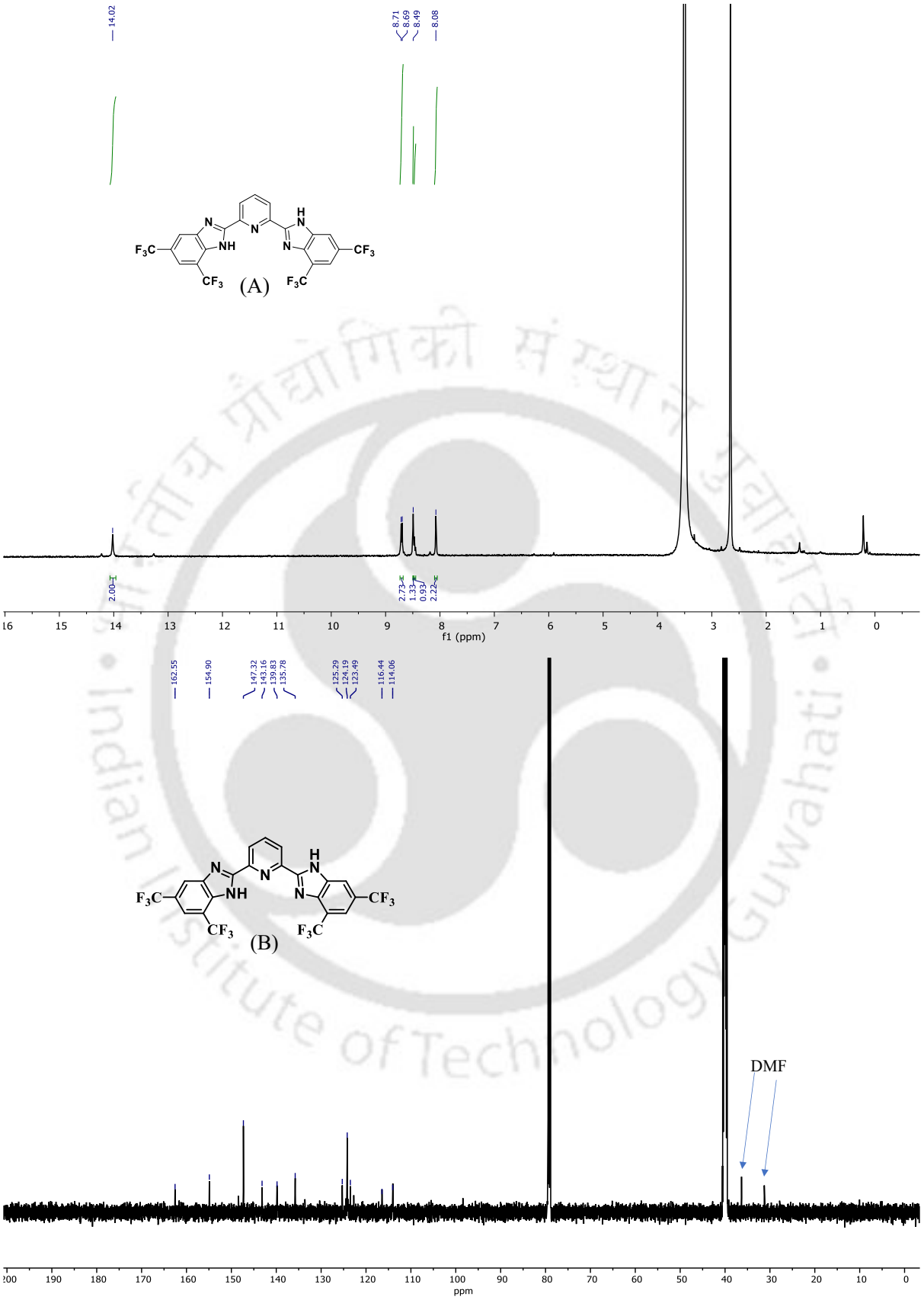


**Figure 3.36.** (A) $^{1}H$ and (B) $^{13}C$ (B) NMR of compound **3.3**.

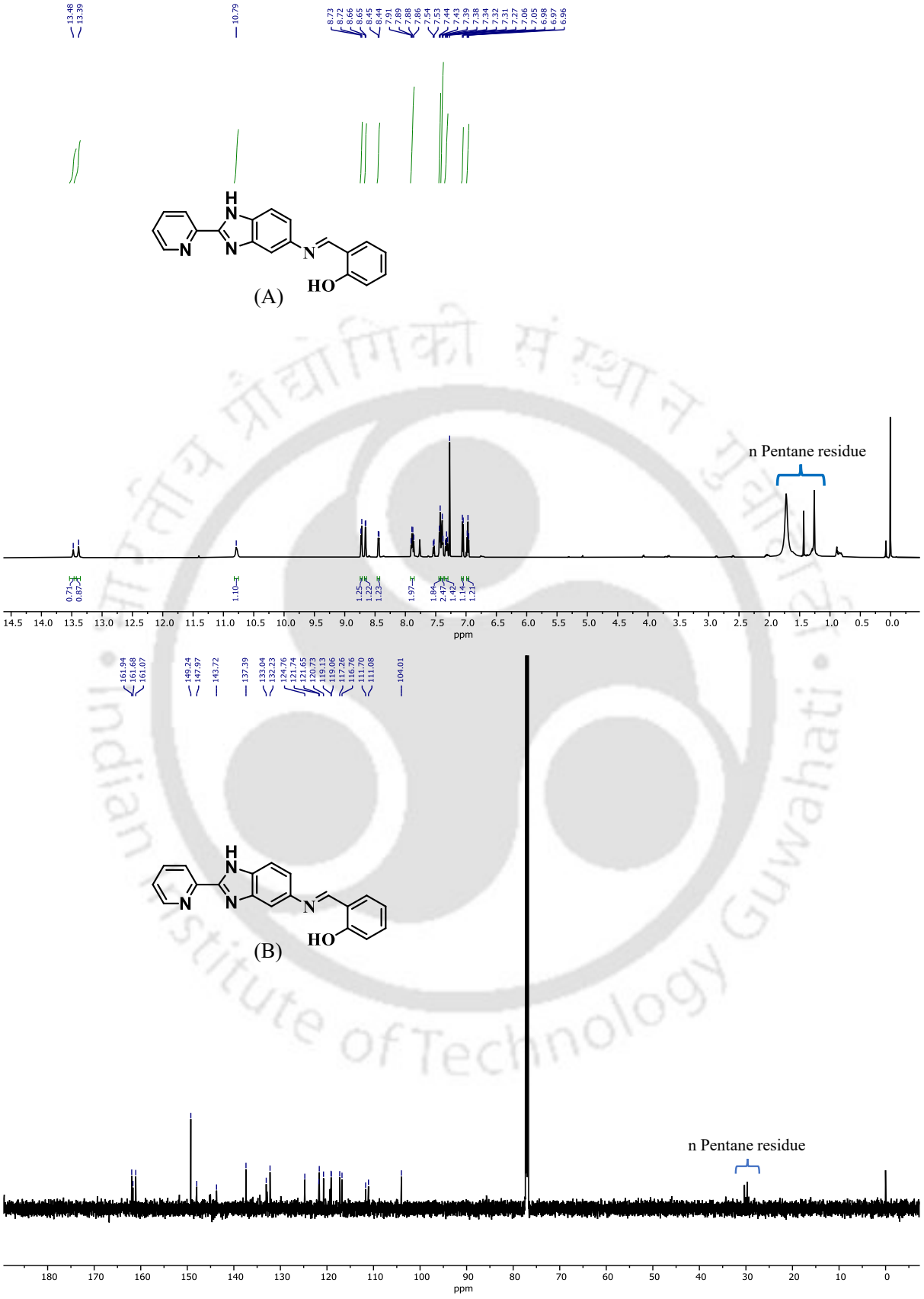


**Figure 3.37.** (A) $^{1}H$ and (B) $^{13}C$ (B) NMR of compound **3.4.**

### 3.4.12 HPLC trace of compound 3.2a

Compound **3.2a** was processed for HPLC analysis. Column used: Ascentis® express C18, 2.7 µm HPLC column, flow rate: 0.5 mL/min, mobile phase used: Optimised gradient of water/methanol. The gradient used:

0-3 min- 20% water:80% MeOH

3-5 min- 100% MeOH

5-10 min- 20% water:80% MeOH

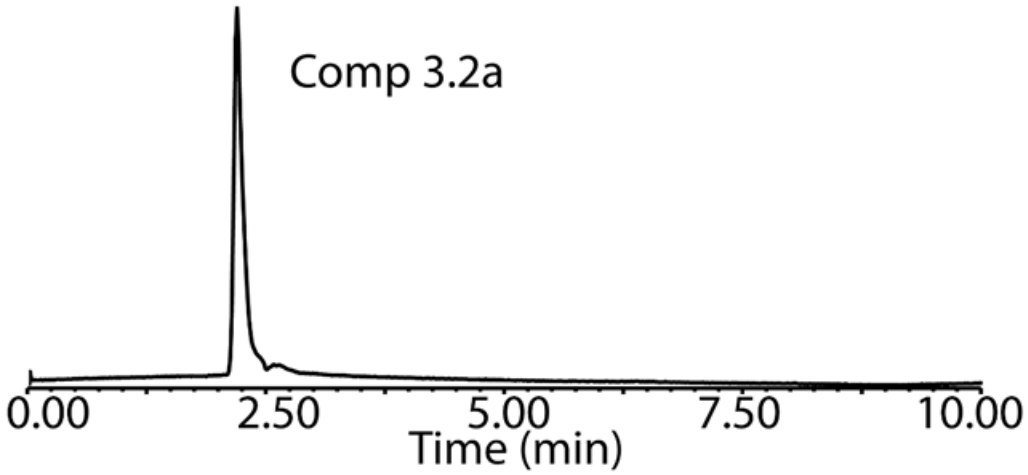


**Figure 3.38.** HPLC trace of compound **3.2a** with ~ 97% purity percentage.

### 3.5 References


1. Chao, X.; Johnson, T. G.; Temian, M.-C.; Docker, A.; Wallabregue, A. L.; Scott, A.; Conway, S. J.; Langton, M. J., Coupling Photoresponsive Transmembrane Ion Transport with Transition Metal Catalysis. *J. Am. Chem. Soc.* **2024,** *146* (7), 4351-4356.

2. Llopis-Lorente, A.; Schotman, M. J.; Humeniuk, H. V.; van Hest, J. C.; Dankers, P. Y.; Abdelmohsen, L. K., Artificial cells with viscoadaptive behavior based on hydrogel-loaded giant unilamellar vesicles. *Chem. Sci.* **2024,** *15* (2), 629-638.

3. Syed, A. J.; Anderson, J. C., Applications of bioluminescence in biotechnology and beyond. *Chem. Soc. Rev.* **2021,** *50* (9), 5668-5705.

4. Gartland, S. A.; Johnson, T. G.; Walkley, E.; Langton, M. J., Inter-Vesicle Signal Transduction Using a Photo-Responsive Zinc Ionophore. *Angew. Chem. Int. Ed.* **2023,** *62* (38), e202309080.

5. Kocyła, A.; Tran, J. B.; Krężel, A., Galvanization of protein–protein interactions in a dynamic zinc interactome. *Trends Biochem Sci* **2021,** *46* (1), 64-79.

6. Mi, P., Stimuli-responsive nanocarriers for drug delivery, tumor imaging, therapy and theranostics. *Theranostics* **2020,** *10* (10), 4557.

7. Llopis-Lorente, A.; Shao, J.; Ventura, J.; Buddingh′, B. C.; Martinez-Manez, R.; van Hest, J. C.; Abdelmohsen, L. K., Spatiotemporal Communication in Artificial Cell Consortia for Dynamic Control of DNA Nanostructures. *ACS Cent. Sci.* **2024,** *10* (8), 1619-1628.

8. Deplazes-Zemp, A., Artificial cell research as a field that connects chemical, biological and philosophical questions. *Chimia* **2016,** *70* (6), 443-443.

9. Xu, C.; Hu, S.; Chen, X., Artificial cells: from basic science to applications. *Mater. Today* **2016,** *19* (9), 516-532.

10. Lu, Y.; Allegri, G.; Huskens, J., Vesicle-based artificial cells: materials, construction methods and applications. *Mater. Horiz.* **2022,** *9* (3), 892-907.

11. Wang, T.; Guo, L.; Jiang, Z.; Chen, S.; Xu, S.; Zhang, Y.; Zhang, J.; Li, R.; Peng, T., Ru-pincer complex-bridged Cu-porphyrin polymer for robust (photo) electrocatalytic H2 evolution via single-atom active sites. *Adv. Funct. Mater.* **2021,** *31* (50), 2107290.

12. Fares, M.; Wu, X.; Ramesh, D.; Lewis, W.; Keller, P. A.; Howe, E. N.; Pérez-Tomás, R.; Gale, P. A., Stimuli-Responsive Cycloaurated "OFF-ON" Switchable Anion Transporters. *Angew. Chem. Int. Ed.* **2020,** *59* (40), 17614-17621.

13. Paul, R.; Dutta, D.; Mukhopadhyay, T. K.; Müller, D.; Lala, B.; Datta, A.; Schwalbe, H.; Dash, J. A Non-B DNA Binding Peptidomimetic Channel Alters Cellular Functions. *Nat. Commun.* **2024**, *15* (1), 5275.

14. Gutsmann, T.; Heimburg, T.; Keyser, U.; Mahendran, K. R.; Winterhalter, M., Protein reconstitution into freestanding planar lipid membranes for electrophysiological characterization. *Nat. Protoc.* **2015,** *10* (1), 188-198.

15. McCall, K. A.; Huang, C.-c.; Fierke, C. A. Zinc and Health: Current Status and Future Directions. *J. Nutr.* **2000**, *130* (5), 1437S−1446S.

16. Wojciechowska, A.; Daszkiewicz, M.; Bieńko, A. Polymeric Zn(II) and Cu(II) Complexes with Exobidentate Bridging l-Tyrosine: Synthesis, Structural and Spectroscopic Properties. *Polyhedron* **2009**, *28* (8), 1481−1489.

17. Makam, P.; Yamijala, S. S. R. K. C.; Tao, K.; Shimon, L. J. W.; Eisenberg, D. S.; Sawaya, M. R.; Wong, B. M.; Gazit, E. Non-Proteinaceous Hydrolase Comprised of a Phenylalanine Metallo-Supramolecular Amyloid-Like Structure. *Nat. Catal.* **2019**, *2* (11), 977−985.

18. Hoefel, D.; Grooby, W. L.; Monis, P. T.; Andrews, S.; Saint, C. P., A comparative study of carboxyfluorescein diacetate and carboxyfluorescein diacetate succinimidyl ester as indicators of bacterial activity. *J. Microbiol. Methods.* **2003,** *52* (3), 379-388.

19. Hettie, K. S.; Klockow, J. L.; Glass, T. E., Three-input logic gates with potential applications for neuronal imaging. *J. Am. Chem. Soc.* **2014,** *136* (13), 4877-4880.

20. Shivaji Padmor, M.; Vishwakarma, P.; Tothadi, S.; Pratihar, S., Cooperative Bimetallic Co− Mn Catalyst: Exploiting Metallo-Organic and Hydrogen Bonded Interactions for Rechargeable C-/N-Alkylation. *ChemCatChem* **2023,** *15* (20), e202300828.

21. Wang, T.; Guo, L.; Pei, H.; Chen, S.; Li, R.; Zhang, J.; Peng, T., Electron-rich pincer ligand-coupled cobalt porphyrin polymer with single-atom sites for efficient (photo) electrocatalytic CO2 reduction at ultralow overpotential. *small* **2021,** *17* (45), 2102957.

22. Langton, M. J.; Keymeulen, F.; Ciaccia, M.; Williams, N. H.; Hunter, C. A., Controlled membrane translocation provides a mechanism for signal transduction and amplification. *Nat. Chem.* **2017,** *9* (5), 426-430.

23. Sharma, R.; Sarkar, S.; Chattopadhayay, S.; Mondal, J.; Talukdar, P., A Halogen-Bond-Driven Artificial Chloride-Selective Channel Constructed from 5-Iodoisophthalamide-based Molecules. *Angew. Chem. Int. Ed.* **2024,** *63* (19), e202319919.

24. Gartland, S. A.; Johnson, T. G.; Walkley, E.; Langton, M. J., Inter-Vesicle Signal Transduction Using a Photo-Responsive Zinc Ionophore. *Angew. Chem. Int. Ed.* **2023,** *62* (38), e202309080.

25. Malla, J. A.; Upadhyay, A.; Ghosh, P.; Mondal, D.; Mondal, A.; Sharma, S.; Talukdar, P., Chloride Transport across Liposomes and Cells by Nontoxic 3-(1 H-1, 2, 3-Triazol-1-yl) benzamides. *Org. Lett.* **2022,** *24* (23), 4124-4128.

26. Dey, S.; Patel, A.; Haloi, N.; Srimayee, S.; Paul, S.; Barik, G. K.; Akhtar, N.; Shaw, D.; Hazarika, G.; Prusty, B. M.; Kumar, M.; Santra, M. K.; Tajkhorshid, E.; Bhattacharjee, S.; Manna, D., Quinoline Thiourea-Based Zinc Ionophores with Antibacterial Activity. *J. Med. Chem.* **2023**, *66* (16), 11078−11093.

27. Chen, Y.; Barba-Bon, A.; Grüner, B.; Winterhalter, M.; Aksoyoglu, M. A.; Pangeni, S.; Ashjari, M.; Brix, K.; Salluce, G.; Folgar-Cameán, Y.; Montenegro, J.; Nau, W. M.,

Metallacarborane Cluster Anions of the Cobalt Bisdicarbollide-Type as Chaotropic Carriers for Transmembrane and Intracellular Delivery of Cationic Peptides. *J. Am. Chem. Soc.* **2023,** *145* (24), 13089-13098.

28. Montal, M.; Mueller, P., Formation of Bimolecular Membranes from Lipid Monolayers and a Study of Their Electrical Properties. *Proc. Natl. Acad. Sci.* **1972,** *69* (12), 3561-3566.

29. Lide, D. R., Ed., CRC Handbook of Chemistry and Physics, 87th ed. *Taylor and Francis: Boca Raton, FL* **2007**.

30. Wang, P. S. P.; Nguyen, J. B.; Schepartz, A., Design and High-Resolution Structure of a β3-Peptide Bundle Catalyst. *J. Am. Chem. Soc.* **2014,** *136* (19), 6810-6813.

31. Makam, P.; Yamijala, S. S. R. K. C.; Tao, K.; Shimon, L. J. W.; Eisenberg, D. S.; Sawaya, M. R.; Wong, B. M.; Gazit, E., Non-proteinaceous hydrolase comprised of a phenylalanine metallo-supramolecular amyloid-like structure. *Nat. Catal.* **2019,** *2* (11), 977-985.

# *Chapter 4*

## *Development of molecular communication system using $Zn^{2+}$ selective supramolecular nanochannel to induce photo-regulated catalysis*

### 4.1 Background and objective of the present work:

As mentioned in the earlier section, metal ion transporters hold the most promising potential for applications in artificial cell mimicry. The molecular communication systems have emerged as a promising approach to replicate cellular communication pathways using engineered nanochannels and synthetic biomolecules to transmit and amplify chemical signals across the cell membranes. This approach holds significant potential for developing intelligent cellular-like platforms that enable controlled information exchange for targeted therapy, biosensing, synthetic cell-to-cell co-ordination and others.[1] Cellular communication, especially through signal transduction via ion channels and transport proteins, plays a critical role in coordinating cellular activities and maintaining homeostasis. These molecular-level coordinated pathways regulate various cellular functions such as proliferation, differentiation and apoptosis.[2, 3] The intricate signaling networks comprising ligand-receptor interactions, secondary messenger-mediated cascading reactions, and feedback loops enable cells to dynamically sense and respond to internal or external stimuli. The stimulus-mediated signal transduction is one of the fascinating aspects of the cellular communication system.[4] For example, in plant cells, the precursor of protochlorophyllide oxidoreductase (pPOR) is imported into plastids in a protochlorophyllide dependent manner. Inside plastids, POR catalyzes the light-dependent conversion of protochlorophyllide to chlorophyllide, a key step in chlorophyll biosynthesis and photosynthesis.[5] This process illustrates a hierarchical signal cascade with mass transport and light-dependent enzyme-gated catalytic activation.

Recent studies have demonstrated the development of inter-vesicle and transmembrane signaling systems capable of transmitting signals with or without directly transferring ions or signaling molecules.[6] However, a significant limitation of these systems is the lack of controllability once mass transport across the membrane triggers a downstream chemical reaction; the reaction occurs independently and cannot be externally regulated. We hypothesize that designing supramolecular nanochannel-based synthetic ion transport systems, which can regulate ion-mediated chemical reactions only in the presence of light and a precatalyst within the intravesicular environment, could be an effective strategy for developing photo-responsive molecular communication systems. This strategy could also be used as a valuable tool for replicating cellular functions. The $Zn^{2+}$ serves as an important signaling cofactor as it plays a pivotal role in various cellular processes, including enzyme activity, immune response and DNA synthesis.[7] Therefore, incorporating $Zn^{2+}$ as a chemical signal opens up a new avenue for replicating cellular functions.

In this study, we report the development of a photo-responsive molecular communication system by integrating a nanochannel-forming synthetic $Zn^{2+}$ transporter with a protoporphyrin IX (PPIX)-based $Zn^{2+}$ mediated catalytic module to monitor the ion transport-regulated biochemical transformation under red light. The tripodal compound self-assembled to form supramolecular nanochannels within the lipid bilayers to selectively transport $Zn^{2+}$ from the extravesicular to the intravesicular environment. The complexation of transported $Zn^{2+}$ with the PPIX resulted in the formation of a catalytic system to promote singlet oxygen ($^1O_2$) mediated oxidation of tryptophan (Trp) amino acid to N-formyl kynurenine (Nfk) exclusively in the presence of red light within the intravesicular environment. The PPIX-$Zn^{2+}$ mediated selective transformation of Trp to Nfk in the presence of red light mimics the indoleamine 2,3-dioxygenase 1 (IDO1) enzyme activity.

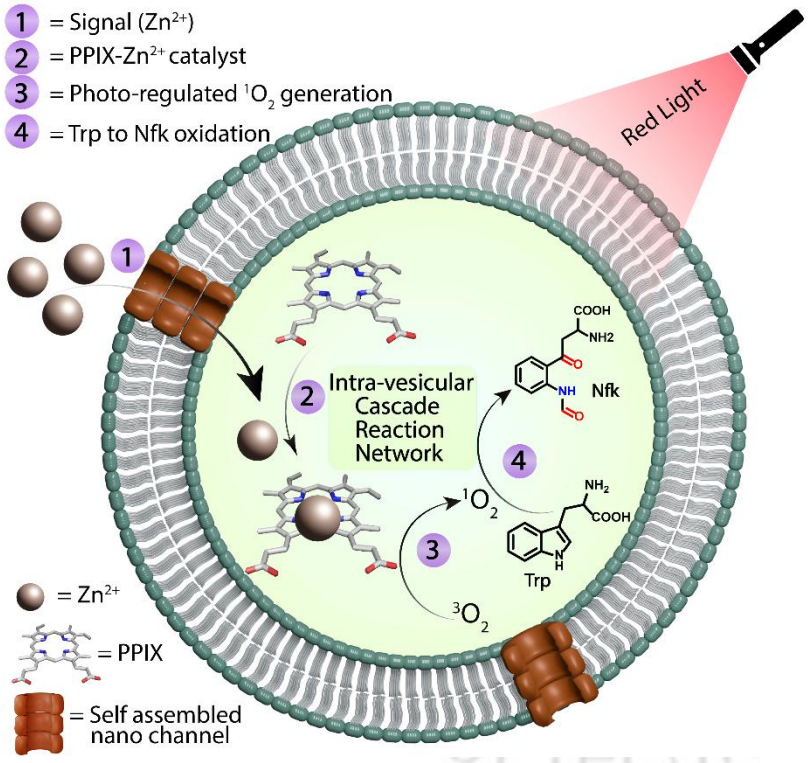


**Figure 4.1.** A schematic representation illustrating the crucial role of supramolecular ion-channels in facilitating the influx of $Zn^{2+}$ and in situ complexation of $Zn^{2+}$ with PPIX, which initiates a photo-regulated cascade reaction network, leading to the significant increase in photo-regulated reactive oxygen species (ROS) generation and the subsequent oxidation of Trp to Nfk.

## 4.2 Results and Discussion

### 4.2.1 Synthesis of ion transporters

The 2-(pyridin-2-yl)-1H-benzo[d]imidazole is a known sensor of $Zn^{2+}$, particularly due to the interaction be-tween the imidazole and pyridyl nitrogen atoms with the $Zn^{2+}$.[8] However, due to its lower lipophilicity (logP 1.95), it cannot be directly used as a transmembrane transporter of $Zn^{2+}$. Hence, to develop potent transmembrane $Zn^{2+}$ transporters, we synthesized tripodal and dipodal thiourea derivatives of 2-(pyridin-2-yl)-1H-benzo[d]imidazole. The reactions of 1,3,5-triethyl-2,4,6-tris(isothiocyanatomethyl)benzene with 2-(pyridin-2-yl)-1H-benzo[d]imidazol-6-amine and other aryl amines yielded compounds **4.1a–d**. (Figure 4.2) Similarly, the reactions of 1,3-bis(isothiocyanatomethyl)benzene with the same ligand yielded the dipodal compounds **4.2a**. Compounds **4.1a**, **4.1b, 4.1c**, and 4.2a were synthesized to investigate the role of thiourea, 2-(pyridin-2-yl)-1H-benzo[d]imidazole, and tripodal moieties in $Zn^{2+}$ transport activities.

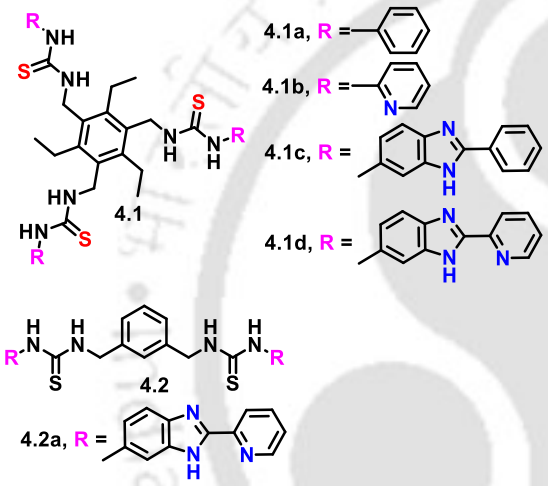


**Figure 4.2.** Structural representation of the synthesized compounds.

### 4.2.2 Ion transport studies:

The detailed ion transport study of the synthesized compounds was evaluated using the large unilamellar vesicles (LUVs) of egg yolk phosphatidylcholine (EYPC) and cholesterol (Chol) (8:2 molar ratio) by encapsulating pentapotassium salt of magnesium green (MgG) (Figure 4.3A). The LUVs were prepared in 10 mM HEPES buffer containing 100 mM NaCl, 50 µM MgG and 100 µM EDTA at pH 7.0 and were suspended in 10 mM HEPES buffer containing 100 mM NaCl, 100 µM EDTA at pH 7.0. The compound screening assay showed higher $Zn^{2+}$ transport efficacy for compound **4.1d** (~85%) compared to its related derivatives, **4.1a-4.1c** and **4.2a**, highlighting it as a promising candidate for further investigation and potential applications (Figure 4.3B). The lower $Zn^{2+}$ transport efficacy of compounds **4.1c** and **4.2a** in comparison to compound **4.1d** suggests the importance of the 2-(pyridin-2-yl)-1H-benzo[d]imidazole and tripodal moieties in $Zn^{2+}$ recognition and transport.

The concentration-dependent MgG assay of compound **4.1d** showed a half-maximal effective concentration ($EC_{50}$) of 44.83 ± 1.74 nM (compound 3d: lipid = 1: $5.58\times10^{8}$) and the Hill coefficient (n) value of 1.87 ± 0.09. (Figure 4.3C and D) The Hill coefficient (~2) suggests that compound **4.1d** exhibits positive cooperativity in forming supramolecular channels within the hydrophobic environment of the lipid bilayers.[9] The critical aggregation constant (CAC) value of compound **4.1d**, calculated from the concentration-dependent transport study, was around 15 nM (Figure 4.8). This indicates that supramolecular channels of compound **4.1d** begin to form within the lipid bilayer of the vesicles at concentrations greater than 15 nM. The cation selectivity study performed for compound **4.1d** revealed the selectivity for $Zn^{2+}$ among tested cations ($Zn^{2+}$, $Cu^{2+}$, $Ni^{2+}$, $Mn^{2+}$, $Mg^{2+}$, $Fe^{3+}$, $Co^{2+}$) (Figure 4.3E and 4.9). However, no difference in $Zn^{2+}$ transport efficacy was observed in anion selectivity studies ($ZnCl_2$, $ZnBr_2$, $Zn(NO_3)_2$, $ZnSO_4$) (Figure 4.3F and 4.10). The lucigenin-based ion transport studies using EYPC/CHOL-LUV⊃lucigenin clearly demonstrated that compound **4.1d** does not facilitate $Cl^-$ transport across the lipid bilayer (Figure 4.11). The UV-Vis absorption spectroscopy-based titration study revealed the binding constant of compound **4.1d** (10 μM) with $Zn^{2+}$ (0-85 μM) to be around 7439 ± 3 $M^{-1}$ (Figure 4.12).

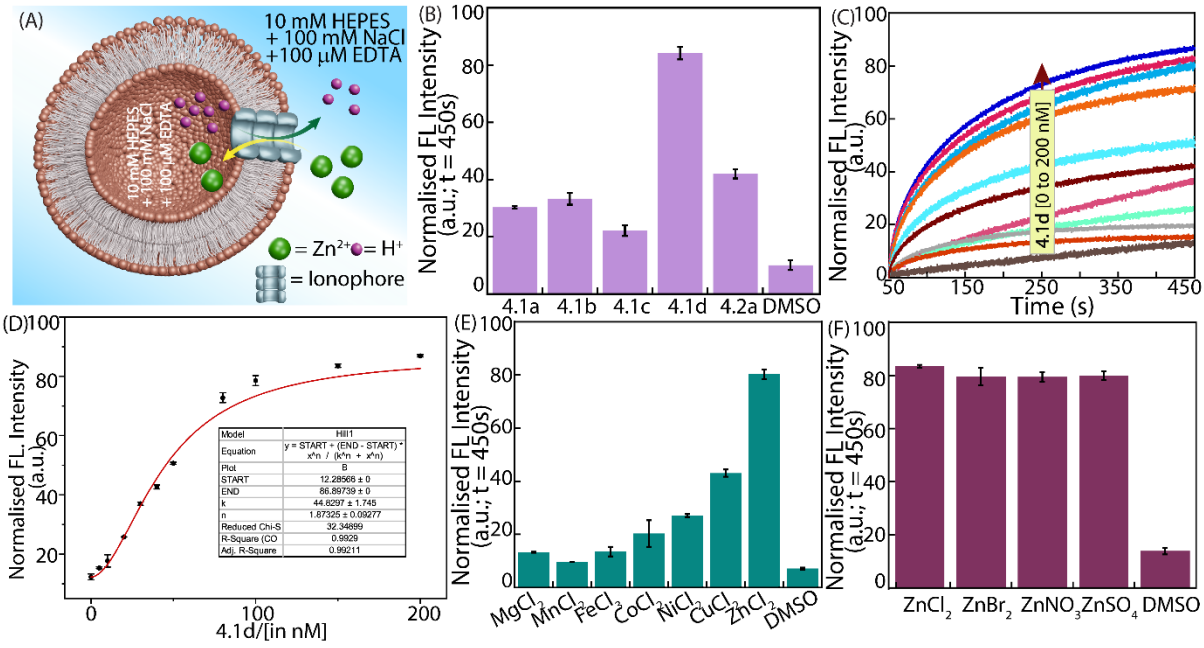


**Figure 4.3.** (A) Schematic representation of ion transport studies across EYPC/Chol-LUVs⊃MgG. (B) Evaluation of the $Zn^{2+}$ transport activity of the synthesized compounds (50 nM) across EYPC/Chol-LUVs⊃MgG prepared in 10 mM HEPES buffer, 100 mM NaCl, 100 μM EDTA, 50 μM MgG, pH 7.0, and dispersed in 10 mM HEPES buffer, 100 mM NaCl, 100 μM EDTA, pH 7.0. The LUVs were equilibrated with $ZnCl_2$, and a pulse of compound **4.1d**

was added to initiate the ion transport studies. (C) Concentration-dependent $Zn^{2+}$ transport activities of compound **4.1d**. (D) Concentration-dependent transmembrane $Zn^{2+}$ transport efficacy of compound **4.1d** across EYPC/Chol-LUV⊃MgG. The $EC_{50}$ value was calculated using the Hill equation. (E) Cation and (F) anion transport selectivity of compound **4.1d** (50 nM) across EYPC/Chol-LUVs⊃MgG.

### 4.2.3 Ion transport mechanism:

Mechanistic studies were performed using MgG-loaded liposomes in the presence of FCCP ($H^+$ carrier) and valinomycin ($K^+$ uniporter).[4] However, no significant change in the fluorescence of MgG was observed with or without FCCP, suggesting the involvement of $H^+$ during the compound **4.1d**-mediated $Zn^{2+}$ transport process (Figure 4.4A). Additionally, ion transport by compound **4.1d** was assessed using the pH-sensitive fluorescein dye, where an increase in the fluorescence intensity across the EYPC/CHOL-LUV⊃fluorescein indicated $H^+$ efflux (Figure 4.13). Therefore, both FCCP- and fluorescein-based ion transport assays confirmed that compound **4.1d** transports $Zn^{2+}/H^+$ via an antiport mechanism. The valinomycin-based ion transport studies showed an unvaried transport efficacy of compound **4.1d** with and without the $K^+$ ion uniporter, suggesting the non-involvement of $OH^-$ ions during the compound **4.1d**-mediated $Zn^{2+}$ transport process (Figure 4.4 B). The carboxyfluorescein-based leakage assay confirmed no vesicle disruption by compound **4.1d** (Figure 4.14). To further investigate the transport pathways, the Chol-dependent and U-tube-based transport assays were performed. In the cholesterol dependency assay, LUVs with varying EYPC: Chol ratios (6:4 and 8:2) were used to modulate membrane rigidity (Figure 4.15). As carrier-mediated transport is typically cholesterol-sensitive, the unchanged activity of compound **4.1d** supports a channel-based mechanism. In the U-tube assay, compound **4.1d** failed to transport $Zn^{2+}$ across the non-polar phase, whereas clioquinol, a known $Zn^{2+}$ carrier, enabled $Zn^{2+}$ transportation (Figure 4.16). Together, these results strongly support a channel-mediated rather than a carrier-based mode of $Zn^{2+}$ transport for compound **4.1d**.

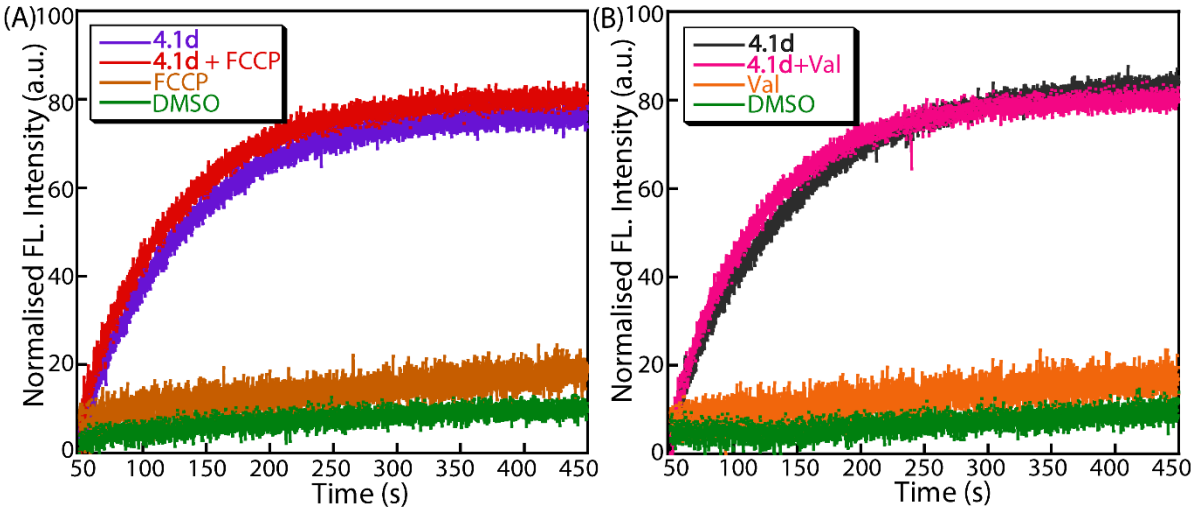


**Figure 4.4** (A) The $Zn^{2+}$ transport activity of compound **4.1d** (50 nM) in the absence and presence of FCCP (1 nM) across EYPC/CHOL-LUVs⊃MgG. (B) Ion transport activity of compound **4.1d** (50 nM) in the absence and presence of valinomycin (12 pM) across EYPC/CHOL-LUV⊃MgG. Val = valinomycin. DMSO (10 µL) was used as a control.

### 4.2.4 Ion transport pathway:

The FESEM images revealed that compound **4.1d** forms nanowire-like structures in a hydrophobic environment (chloroform) and spherical agglomerates in a hydrophilic environment (water) (Figure 4.17). These solvent-dependent morphology differences suggest a characteristic self-assembly pattern of compound **4.1d** in the hydrophobic medium. The 2D-NOESY measurement of compound **4.1d** (in DMSO-$d_6$) revealed a strong spatial correlation between the pyridyl aromatic proton ($\delta$ 7.51 ppm) and the thiourea N–H proton ($\delta$ 9.49 ppm) (Figure 4.5 A and B). Additionally, cross-peaks were observed between the benzylic proton ($\delta$ 4.68 ppm) and the ethyl group proton ($\delta$ 2.80 ppm) with the pyridyl aromatic proton ($\delta$ 7.49 ppm). These observations suggest a probable self-assembled architecture in which the pyridyl arms of two molecules engage in interlocking non-covalent interactions. In contrast, the remaining arms orient to form a potential channel-like cavity, which could facilitate ion transport. To further investigate the channel-forming ability, the real-time change in current at a constant voltage in the presence of compound **4.1d** was monitored through an electrophysiological experiment.[10] The bilayer lipid membranes (BLM) of diphytanoyl phosphatidylcholine (DPhPC) were prepared over the orifice in the Teflon foil connecting two electrolyte chambers containing $ZnCl_2$ (0.5 M) solution. After the addition of compound **4.1d** (4 µM) in both chambers, we detected repetitive opening-closing events at different holding

potentials, which confirmed the formation of an ion channel within the planar lipid bilayer (Figure 4.5 C). Additional measurements of current against voltage (I–V plot) were further monitored using a symmetrical $ZnCl_2$ (0.5 M) solution (Figure 4.19). A linear increase in current with increasing voltage was observed, indicating ohmic behavior. The measured single-channel conductance (G) of 54 ± 11 pS indicates the formation of ion channels with a pore diameter of 1.5 Å, according to a simple pore model.

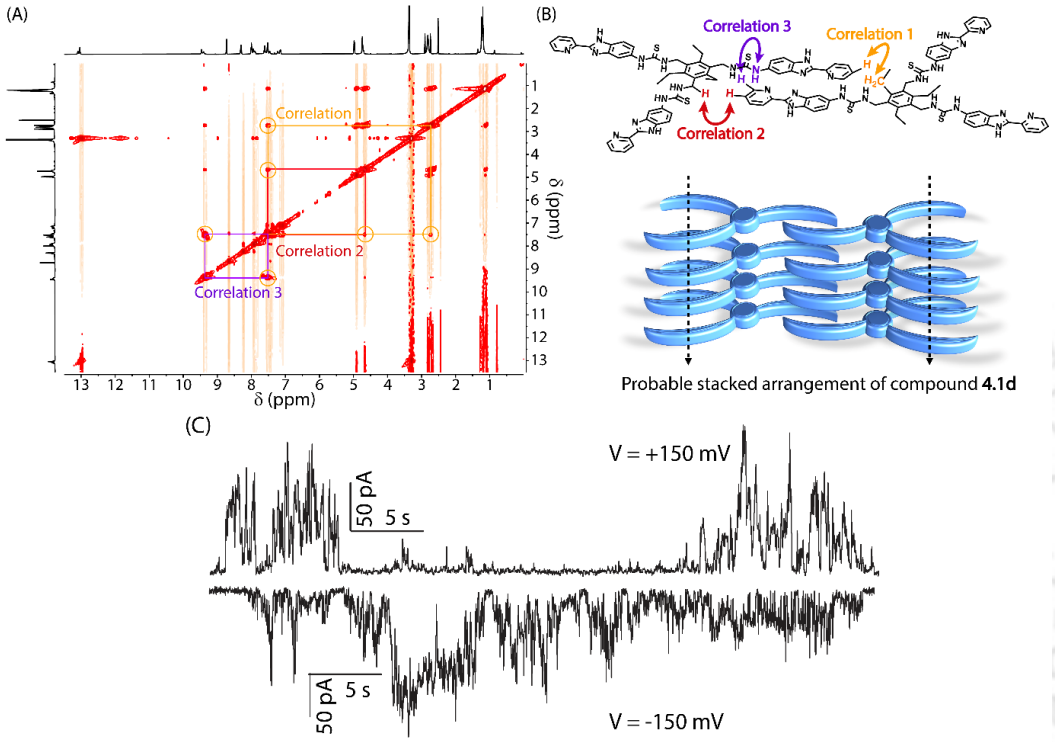


**Figure 4.5** (A) and (B) NOESY spectra of compound **4.1d** in DMSO-$d_6$ solvent. (C) Ion conductance measurements across the BLM at +150 mV and -150 mV in the presence of compound **4.1d** in a symmetrical solution of $ZnCl_2$ (0.5 M) in water.

### 4.2.5 $Zn^{2+}$ mediated photo-regulated catalysis:

Metalloporphyrins are essential biomolecules with catalytic properties that play vital roles in physiological functions within living systems. Metalloporphyrins are also used in molecular catalysis, water splitting, and photodynamic therapy.[11] The zinc-porphyrin has been identified as a reactive ROS generator under red light,[12] which can be utilized for carrying out reactions within the compartmentalized structures, such as LUVs. We observed that the complexation of PPIX with $Zn^{2+}$ generates ROS upon exposure to red light (8 watts, 400-700 nm). This ROS generation efficacy was measured using the 7′-dichlorofluorescin diacetate ($H_2$DCFDA) assay ($\lambda_{ex}$ = 485 nm, $\lambda_{em}$ = 522 nm). The enhancement of fluorescence intensity at 522 nm due to the

conversion of $H_2$DCFDA to 2',7'-dichlorofluorescein (DCF) was only observed in the presence of both PPIX and $Zn^{2+}$ upon photo irradiation (Figure 4.20). No significant DCF fluorescence enhancement was observed with PPIX alone, indicating that $Zn^{2+}$ binding significantly enhances the ROS generation aptitude of PPIX. UV-Vis and fluorescence-based titration studies of PPIX with $Zn^{2+}$ showed no metalation under the experimental conditions (Figure 4.21). All four Q bands (500–700 nm) of PPIX remained intact, suggesting no $Zn^{2+}$ incorporation into the porphyrin ring of PPIX.[13] However, a partial decrease in the Soret band (400 nm) and a significant reduction in fluorescence intensity at 640 nm indicated either complexation of $Zn^{2+}$ with the carboxylate groups of PPIX or adopting a weakly bound, 'sitting-atop' geometry above the porphyrin ring, without coordination to the core nitrogen atoms. These $Zn^{2+}$ binding modes may significantly alter the porphyrin ring's electronic structure, thereby enhancing its ROS-generating capacity upon photoactivation.[14]

To investigate the ROS-mediated catalytic activities of PPIX-$Zn^{2+}$ complex, the reactions were performed in the presence of Trp amino acid, both with and without red light in 20 mM HEPES buffer at pH 7.0. Upon optimization, we observed that red light (8-watt, 580-670 nm) achieves better photo-oxidation in just 3–4 hours, whereas white light (8-watt, 400 nm -700 nm) requires approximately 24 hours to reach similar efficiency, highlighting the superior effectiveness of wavelength-specific excitation for $Zn^{2+}$-PPIX mediated photo oxidation (Figure 4.22). It is noteworthy that white light consists of a broad range of wavelengths; however, only a limited portion overlaps with the absorption band of $Zn^{2+}$-PPIX. This restricted spectral overlap results in weaker excitation and diminishes photooxidation efficiency, especially compared to the selective activation provided by red light. Additionally, exposure to white light can promote increased nonspecific photodegradation of $Zn^{2+}$-PPIX, reducing its effectiveness, as confirmed by HPLC analysis. (Figure 4.23) Interestingly, after 4 h of red light exposure, HRMS analysis detected the formation of Nfk ($[M+H]^+$ = 237.0905) only in the reaction mixture containing Trp and the PPIX-$Zn^{2+}$ complex. Nfk is known to undergo hydrolysis to kynurenine (Kyn) in the presence of trichloroacetic acid (TCA).[15] The resulting Kyn was subsequently quantified using UV-vis spectroscopy following derivatization with p-dimethylaminobenzaldehyde (p-DMAB). The UV-Vis spectral analysis revealed a significant enhancement of the peak at 480 nm, corresponding to the formation of the imine complex of p-DMAB with Kyn (Figure 4.6C).[16] The time-dependent HPLC analysis confirmed increasing Kyn formation with light exposure (retention time of 2.8 min), while no significant amount of

Kyn was detected in the absence of light (Figure 4.24). The HRMS analysis of the eluted solution corresponding to the peak of 2.8 min (retention time) showed $[M+H]^+$ = 209.0914, indicating

the identity of Kyn (Figure 4.6 B). The Kyn formation was further validated by nuclear magnetic resonance (NMR) spectroscopy (Figure 4.25). Additional reactions of Trp with the PPIX-$Zn^{2+}$ complex in the presence of different ROS quenchers were performed to investigate the mechanism of Trp-to-Kyn formation. The DABCO, known as a $^1O_2$ scavenger,[16] completely suppressed both the HPLC peak at 2.8 min and the absorbance peak at 480 nm, suggesting that the conversion of Trp to Kyn proceeds via $^1O_2$ under red light (Figure 4.6 A and 4.26). Additional photo-regulated oxidation studies with the PPIX-$Zn^{2+}$ complex and tyrosine showed dimerization, and with methionine demonstrated mono-oxidation to methionine sulfoxide (Table 4.1 and Figure 4.27). However, no detectable oxidation of histidine was observed under similar reaction conditions.

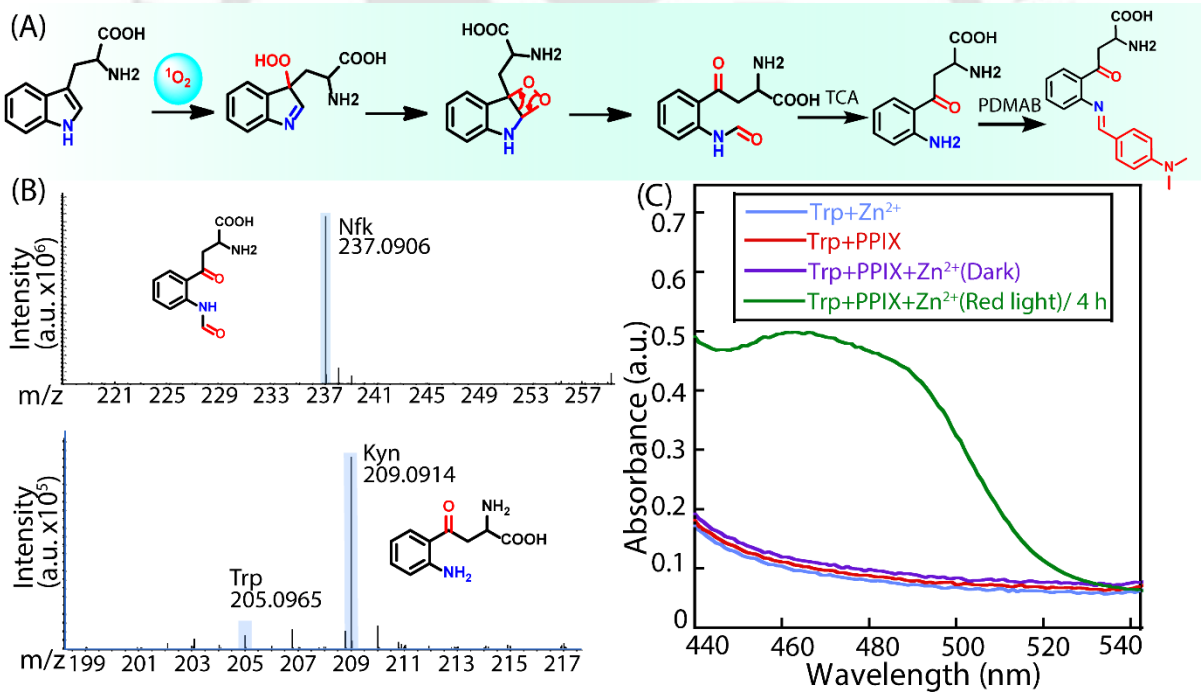


**Figure 4.6.** (A) Mechanistic scheme for Trp to kyn via Nfk through $^1O_2$ oxidation method. (B) Obtained HRMS spectra for Nfk and Kyn as products. (C) UV-vis absorbance spectra for the detection of kyn generation.

This finding provided a unique opportunity to develop a photo-regulated, $Zn^{2+}$ dependent molecular communication system. The EYPC/CHOL LUV⊃PPIX/Trp were prepared in 20 mM HEPES buffer at pH 7.0. The LUVs were suspended in 20 mM HEPES buffer at pH 7.0,

and compound **4.1d**, along with $Zn^{2+}$, was added to the extravesicular solution (Figure 4.7A). After prolonged exposure (4 h) to red light, the LUVs were lysed with 20% Triton X-100 (20 µL) (Figure 4.28). HPLC and UV-Vis spectral analyses indicated the conversion of Trp to Kyn in the vesicular environment. Control experiments without compound **4.1d**, $Zn^{2+}$, Trp, or light showed no significant formation of kyn. The time-resolved HPLC analysis confirmed a gradual increase in the Kyn formation, supporting Kyn formation via transmembrane $Zn^{2+}$ transport by compound **4.1d** and $^1O_2$-mediated oxidation under light within a confined vesicular environment (Figure 4.7B). We also conducted a similar reaction under alternating 60 min light and dark cycles for a total duration of 300 min. The HPLC and UV-Vis spectral analysis showed that light-dependent Trp to Kyn conversion is associated with the photo-induced $^1O_2$ generation by the in-situ generated PPIX-$Zn^{2+}$ complex within the vesicles (Figure 4.7C and 4.29). The indoleamine-2,3-dioxygenase (IDO1)- mediated catabolism of Trp to Nfk via the kynurenine pathway is involved in various physiological processes, including the immune response.[15] Hence, this photo-regulated molecular communication system acts as an artificial enzyme to mimic the catalytic conversion of Trp to Nfk within the vesicles.

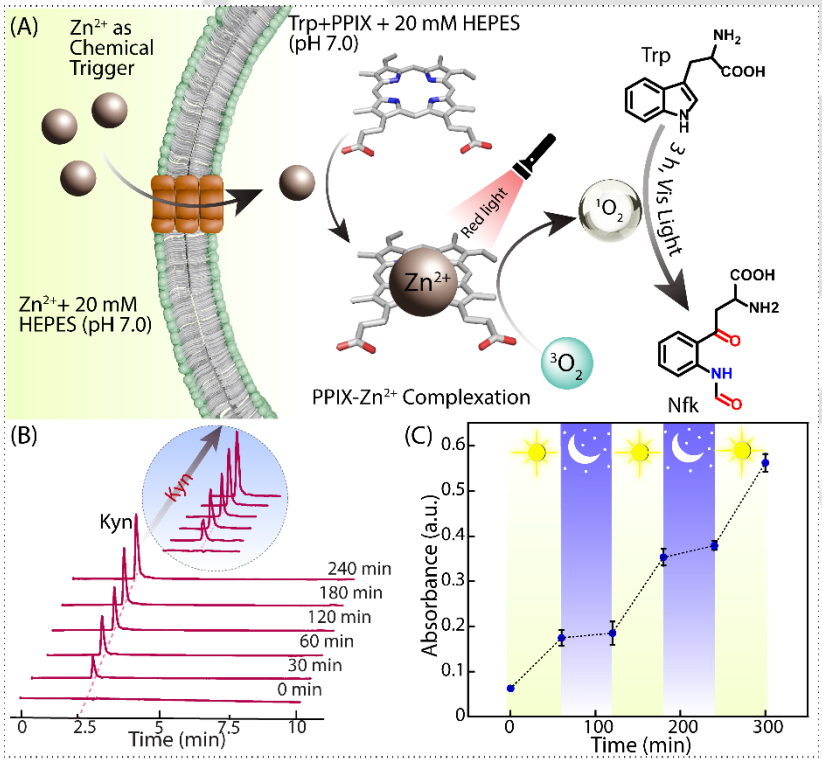


**Figure 4.7.** (A) Schematic illustration shows the in-situ complexation of $Zn^{2+}$ with PPIX, initiating light-regulated catalysis that significantly increases the generation of ROS and leads to the oxidation of Trp to Nfk. (B) HPLC analysis at different time intervals demonstrates the

production of Kyn within the EYPC/Chol-LUVs⊃Trp/PPIX system in the presence of compound **4.1d** and $Zn^{2+}$. (C) Stepwise red light irradiation ON/OFF experiment using EYPC/Chol-LUVs⊃Trp/PPIX in 20 mM HEPES buffer, pH 7.0, with compound **4.1d** and $Zn^{2+}$ to detect kyn generation.

### 4.3 Summary:

In this chapter, we report the development of a photo-responsive molecular communication system that utilizes a synthetic transmembrane metal-ion transporter. The 2-(pyridin-2-yl)-1H-benzo[d]imidazol-6-amine-based tripodal compound **4.1d**, self-assembled within the lipid bilayer to form supramolecular channels that selectively transport $Zn^{2+}$ with a half-maximal effective concentration of 45 nM and a Hill coefficient value of 1.87. Detailed mechanistic studies demonstrated that the $Zn^{2+}/H^{+}$ antiport process transports ions across the lipid bilayer. Electrophysiological measurements validated the development of supramolecular ion channels, exhibiting a single-channel conductance of 54 ± 11 pS. This conductance aligns with a simple pore model with a 1.5 Å pore diameter in a symmetrical 0.5 M $ZnCl_2$ solution. Due to the selective $Zn^{2+}$ transport ability of compound **4.1d**, this metal ion was utilized as a chemical signal to form $Zn^{2+}$-PPIX complex inside the vesicles, which acted as a photosensitizer. Upon exposure to red light, the PPIX-$Zn^{2+}$ complex generates $^1O_2$. Consequently, the PPIX-$Zn^{2+}$ complex was used to facilitate a $^1O_2$-mediated enzyme-like oxidation reaction within the vesicles, converting Trp to Nfk. Hence, this molecular communication system presents a unique biomimetic approach where $Zn^{2+}$ serves not only as a transportable ion but also as a functional chemical signal that triggers an enzyme-like oxidation reaction solely under red light. Overall, by integrating $Zn^{2+}$ ions, a channel-based synthetic ion transporter, PPIX, and photo-regulated ROS generation and oxidation reactions within a confined liposomal environment, we successfully mimic cell-like behavior, especially spatiotemporally controlled signal-induced oxidative cascades.

### 4.4 Experimental section:

**4.4.1 General methods:** As mentioned in the previous chapter.

**4.4.2 Synthesis and characterisation of compounds:**

**4.4.2.1 Synthesis of 1, 3, 5-triethyl-2, 4, 6-tris(isothiocyanatomethyl)benzene** – To a stirring solution of 1,3,5-tris(bromomethyl)-2,4,6-triethylbenzene (200 mg, 0.45 mmol) in dry DMF solvent, were added tetra butyl ammonium bromide (TBAB) (585 mg, 1.81 mmol), potassium

thiocyanate (308 mg, 3.17 mmol) and sodium iodide (55 mg, 0.36 mmol) at room temperature under $N_2$ atmosphere. Then the reaction mixture was continued to stir for 2- 3 hours at 80 °C.

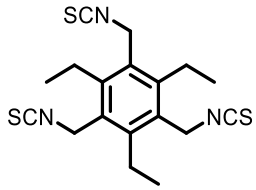


The progress of the reaction was monitored by TLC analysis. After completion of the reaction, the unwanted salts were filtered through the filter paper. The filtrate was diluted with water (50 mL), and the organic layer was extracted with ethyl acetate (2 × 50 mL). The combined organic layers were dried over anhydrous $Na_2SO_4$ and concentrated under reduced pressure. The crude reaction mixture was purified by column chromatography using a solvent gradient of ethyl acetate/hexane, yielding a white solid with 58% yield. Characterization of the compound was matched according to the reported procedure.[17]

**4.4.2.2 Synthesis of 2-phenyl-1*H*-benzo[d]imidazol-5-amine** − Benzoyl chloride (1.44 g, 10.24 mmol) was added to a stirring solution of 4-nitrobenzene-1,2-diamine (1.54 g, 10.06 mmol) and $Et_3N$ (1.5 mL, 10.76 mmol) in THF (100 mL) at 10 °C. The mixture was stirred overnight while slowly warming to room temperature. The mixture was diluted with water and extracted

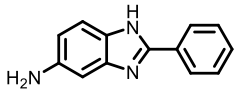


into ethyl acetate, and the product was recrystallized from acetonitrile as yellow crystals. To the obtained product (10 mmol), $BF_3$ etherate (1.5 mL, 12.92 mmol) was added, and the mixture was stirred in 1,4-dioxane (150 mL) and refluxed for 3 h. After cooling, the mixture was diluted with water and extracted with ethyl acetate. The product was purified on a silica gel column using hexanes/ethyl acetate (7:3), followed by recrystallization from ethyl acetate/hexanes, affording pale-yellow crystals (yield: 92%). Further, it was reduced catalytically over 0.5 g of 10% palladium-on-charcoal at normal pressure and room temperature to obtain the desired product (light yellow solid). Characterisation was matched according to the reported procedure.[18]

**4.4.2.3 Synthesis of 2-(pyridin-2-yl)-1*H*-benzo[d]imidazol-5-amine** − A mixture of an appropriate derivative of *o*-phenylenediamine, the corresponding carboxylic acid, and 5-20 equiv. of polyphosphoric acid was stirred in an oil bath at 180 °C for 2 h. The solution was

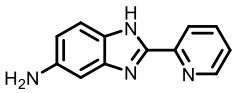

cooled and poured in a thin stream into rapidly stirred water. The pH was adjusted to 9 with sodium hydroxide. The solid was collected by filtration, dissolved in hot ethanol, and treated with charcoal. The ethanol was evaporated again, and the residue was recrystallized to obtain 2-Pyridin-2-yl-1*H*-benzimidazol, a white solid. To the solution of 2-Pyridin-2-yl-1H-benzoimidazol in concentrated $H_2SO_4$, concentrated $HNO_3$ was added dropwise between 0 and 10 °C. The mixture was stirred at room temperature for 2 h and then poured into ice water. Cautious neutralization with 50% NaOH provided a solid, which was filtered off and crystallized from MeOH to yield the desired product. 5-Nitro-2-pyridin-2-yl-1(3)*H*-benzimidazol as a light-yellow solid. 100 mg of nitro derivative was dissolved in 4 mL of absolute ethanol, and the solution was reduced catalytically over 0.5 g of 10% palladium-on-charcoal at normal pressure and room temperature. After the uptake of hydrogen was complete, the catalyst was removed by filtration, and the solvent was evaporated in vacuo. Upon recrystallization, the pure compounds were obtained. 2-Pyridin-2-yl-3H-benzoimidazol-5-ylamine as a light-yellow solid (yield: 78%). Characterisation was done according to the reported procedure.[8]

**4.4.2.4 General procedure for synthesising tripodal compound 4.1a-4.1d** − To the stirring solution of 3, 5-triethyl-2, 4, 6-tris(isothiocyanatomethyl)benzene (1.0 mmol) in DMF, different amines (3.0 mmol) were added and stirred overnight. The reactions were monitored through TLC. After completion of the reaction, ice-water was added, and the mixture was extracted with ethyl acetate (3 × 20 mL), then reduced under a rotary evaporator to obtain the crude solid. Column chromatography (hexane: ethyl acetate) was performed to purify the product, and further characterizations were performed for the same.

**4.4.2.4.1 Synthesis of 1,1',1''-((2,4,6-triethylbenzene-1,3,5-triyl)tris(methylene))tris(3-phenylthiourea) (4.1a)** −Compound **2** (0.1 mmol) and aniline (0.3 mmol) were used in the reaction following the general protocol mentioned above. The obtained crude solid was purified through column chromatography (hexane/ethyl acetate). Purified compound obtained as a pale-yellow solid in 60% yield.

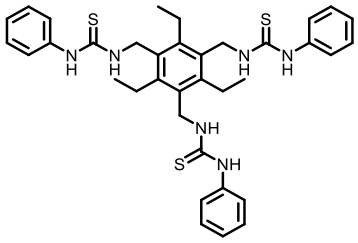

Characterisation: **$^{1}$H NMR** (400 MHz, DMSO-$d_6$) $\delta_{ppm}$: 9.42 (s, 3H), 7.54 (d, $J$ = 7.4 Hz, 8H), 7.31 (t, $J$ = 7.9 Hz, 7H), 7.09 (t, $J$ = 7.4 Hz, 3H), 4.73 (d, $J$ = 4.0 Hz, 6H), 2.78 (q, $J$ = 10.65 Hz, 6H), 1.18 (t, $J$ = 7.34 Hz, 9H).**$^{13}$C NMR** (151 MHz, DMSO) $\delta_{ppm}$: 180.56, 144.44, 140.06, 132.55, 128.90, 124.41, 123.04, 42.56, 23.32, 16.92. **HRMS**: ESI calc. for $C_{36}H_{42}N_6S_3$ $[M+H]^+$: 655.2706, found: 655.2706.

**4.4.2.4.2 Synthesis of 1,1',1''-((2,4,6-triethylbenzene-1,3,5-triyl)tris(methylene))tris(3-(pyridin-2-yl)thiourea) (4.1b)** − Compound **2** (0.1 mmol) and 2-aminopyridine (0.3 mmol) were used in the reaction following the general protocol mentioned above. The obtained crude solid was purified through column chromatography (hexane/ethyl acetate). Purified compound obtained as a white solid in 78% yield.

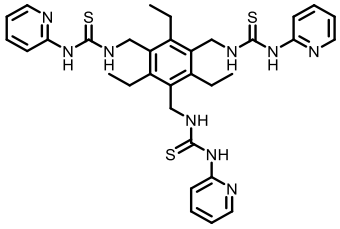

Characterisation: **$^{1}$H NMR** (600 MHz, DMSO-$d_6$) $\delta_{ppm}$: 11.72 (t, $J$ = 4.5 Hz, 3H), 10.69 (s, 3H), 7.72 (m, 3H), 7.59 (dd, $J$ = 5.2, 1.9 Hz, 3H), 7.14 (d, $J$ = 8.4 Hz, 3H), 6.79 (dd, $J$ = 7.2, 5.1 Hz, 3H), 4.86 (d, $J$ = 4.4 Hz, 6H), 2.83 (q, $J$ = 7.5 Hz, 6H), 1.19 (t, $J$ = 7.4 Hz, 9H). **$^{13}$C NMR** (151 MHz, DMSO) $\delta_{ppm}$: 179.32, 154.20, 145.28, 144.31, 139.56, 132.51, 118.19, 113.14, 43.63, 23.11, 16.57. **HRMS**: ESI calc. for $C_{33}H_{39}N_9S_3$ $[M+H]^+$: 658.2563, found: 658.2567.

**4.4.2.4.3. Synthesis of 1-(2-phenyl-1*H*-benzo[d]imidazol-5-yl)-3-(2,4,6-triethyl-3,5-bis((3-(2-phenyl-1*H*-benzo[d]imidazol-6-yl)thioureido)methyl)benzyl)thiourea (4.1c)** − Compound **2** (0.1 mmol) and 2-phenyl-1*H*-benzo[d]imidazol-5-amine (0.3 mmol) were used in the reaction following general protocol mentioned above. The crude solid was purified through column chromatography (hexane/ethyl acetate) to obtain a pale-yellow solid in 54% yield.

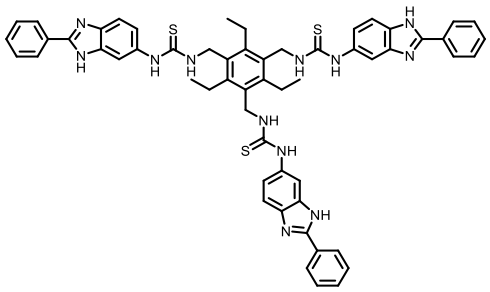

Characterisation: **$^{1}$H NMR** (600 MHz, DMSO-$d_6$) $\delta_{ppm}$: 12.90 (s, 3H), 9.46 (s, 3H), 8.15 (d, $J$ = 7.6 Hz, 5H), 8.11 (m, 1H), 7.82 (m, 2H), 7.65 – 7.43 (m, 13H), 7.12 (d, $J$ = 97.9 Hz, 4H), 6.80 (d, $J$ = 74 Hz, 1H), 4.98 (s, 2H), 4.74 (s, 4H), 2.80 (q, $J$ = 12.96, 6H), 1.20 (t, $J$ = 8.01 Hz, 9H). **$^{13}$C NMR** (151 MHz, DMSO) $\delta_{ppm}$: 180.93, 152.10, 145.61, 144.10, 132.99, 130.47, 130.31, 129.61, 129.45, 128.24, 126.76, 42.72, 23.04, 16.59. **HRMS**: ESI calc. for $C_{57}H_{54}N_{12}S_3$ $[M+H]^+$: 1003.3829, found: 1003.3800.

**4.4.2.4.4 Synthesis of 1-(2-(pyridin-2-yl)-1*H*-benzo[d]imidazol-5-yl)-3-(2,4,6-triethyl-3,5-bis((3-(2-(pyridin-2-yl)-1*H*-benzo[d]imidazol-6-yl)thioureido)methyl)benzyl)thiourea (4.1d)** − Compound **2** (0.1 mmol) and 2-(pyridin-2-yl)-1H-benzo[d]imidazol-5-amine (0.3 mmol) were used in the reaction following general protocol mentioned above. The crude solid was purified through column chromatography (hexane/ethyl acetate) to obtain a pale-yellow solid in 54% yield.

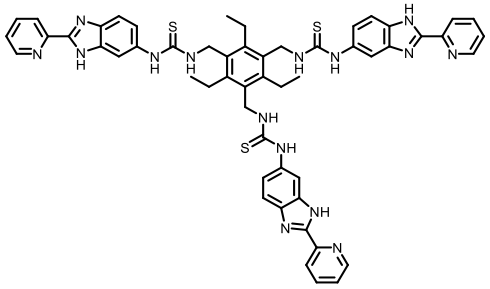

Characterisation: **$^{1}$H NMR** (400 MHz, DMSO-$d_6$) $\delta_{ppm}$: 13.07 (d, $J$ = 24.5 Hz, 3H), 9.49 (d, $J$ = 23.7 Hz, 3H), 8.72 (d, $J$ = 4.7 Hz, 3H), 8.29 (d, $J$ = 7.5 Hz, 3H), 7.99 (t, $J$ = 7.4 Hz, 3H), 7.89 (d, $J$ = 16.6 Hz, 3H), 7.61 (d, $J$ = 8.6 Hz, 2H), 7.55 – 7.44 (m, 7H), 7.22 (d, $J$ = 8.7 Hz, 1H), 7.14 (d, $J$ = 9.0 Hz, 2H),4.98 (s, 2H), 4.76 (s, 4H), 2.86 – 2.78 (m, 6H), 1.21 – 1.18 (m, 9H). **$^{13}$C NMR** (151 MHz, DMSO) $\delta_{ppm}$: 180.98, 151.55, 149.85, 148.88, 145.62, 144.10, 137.99, 135.61, 132.99, 129.59, 128.28, 125.10, 121.76, 119.37, 107.02, 42.76, 23.04, 16.59. **HRMS**: ESI calc. for $C_{54}H_{51}N_{15}S_3$ $[M+H]^+$: 1006.3687, found: 1006.3628.

**4.4.2.5 Synthesis of 1-(3-((3-(2-( pyridin-2-yl) - 1*H*-benzo [d] imidazol-5-yl)thioureido)methyl) benzyl)-3-(2-(pyridin-2-yl) -1*H*-benzo[d]imidazol-6-yl) thiourea (4.2a)** −To the stirring solution of 1,3-bis(isothiocyanatomethyl)benzene (0.5 mmol) in dry DMF 2-(pyridin-2-yl)-1H-benzo[d]imidazol-5-amine (1 mmol) was added dropwise and stirred for overnight. Reaction was monitored through TLC till completion. Afterwards, the compound was extracted with ethyl acetate (20 mL × 3) and reduced under pressure. The resulting solid was purified through column chromatography (ethyl acetate/hexane). A pale yellow solid was obtained in moderate yield (58%).

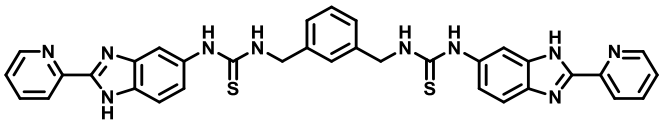

Characterisation: **$^{1}$H NMR** (600 MHz, DMSO-$d_6$) $\delta_{ppm}$: 13.12 (d, $J$ = 34.8 Hz, 2H), 9.70 (d, $J$ = 35.5 Hz, 2H), 8.73 (s, 2H), 8.31 (d, $J$ = 6.8 Hz, 2H), 8.13 (s, 1H), 8.04 (s, 1H), 7.99 (t, $J$ = 7.8 Hz, 2H), 7.69 (s, 1H), 7.66 (d, $J$ = 6.8 Hz, 2H), 7.52 (d, $J$ = 7.9 Hz, 3H), 7.33 (t, $J$ = 6.87 Hz, 1H), 7.29 (s, 1H), 7.24 (d, $J$ = 6.7 Hz, 2H), 7.19 (d, $J$ = 8.3 Hz, 1H), 7.15 (d, $J$ = 8.7 Hz, 1H), 4.76 (s, 4H). **$^{13}$C NMR** (151 MHz, DMSO) $\delta_{ppm}$: 181.43, 151.94, 151.60, 149.88, 148.82, 144.41, 141.97, 139.75, 138.04, 135.41, 133.29, 128.66, 126.67, 126.25, 125.15, 121.76, 119.75, 112.54, 108.32, 47.82. **HRMS**: ESI calc. for $C_{34}H_{28}N_{10}S_2$ $[M+H]^+$: 641.2013, found: 641.1979.

### 4.4.3 Methodology of ion transport studies:

**4.4.3.1 Preparation of EYPC/Chol-LUV⊃MgG vesicles —** To conduct the MgG fluorescence-based ion-transport studies, we took EYPC (50 mg/mL in deacidified $CHCl_3$) and cholesterol (CHOL; 25 mg/mL in deacidified $CHCl_3$) in a clean, dry glass vial in a molar ratio of 8:2. The solution was evaporated for 6 hours under reduced pressure to form a thin lipid film. After that, we rehydrated the film with 10 mM HEPES buffer containing 100 mM NaCl and 100 µM EDTA and 50 µM MgG dye at pH 7.0. The resulting suspension was vortexed six to seven times over 1 hour. Next, we performed 6-7 freeze-thaw cycles followed by 10 minutes of constant vortexing. We then extruded the lipid suspension 19–21 times using a mini extruder with a 200 nm pore size to achieve a uniform liposome size of 200 nm. Finally, we removed the unencapsulated MgG dye using the gel filtration technique (Sephadex G-50) and 10 mM HEPES buffer containing 100 mM NaCl at pH 7.0 as the eluting solution. This process yielded a final lipid concentration of 25 mM (assuming 100% lipid regeneration).[6]

**4.4.3.2 Transport assays with EYPC/Chol-LUV⊃MgG vesicles —** For the MgG-based ion transport assay, in a clean and dry fluorescence cuvette (3 mL), 10 mM HEPES buffer containing 100 mM NaCl, pH 7.0 (1930 µL), EYPC/Chol-LUV⊃MgG (40 µL), and $ZnCl_2$ (final concentration 1 mM) were added. The cuvette was placed under slow stirring conditions in a fluorescence spectrophotometer for about 3 min to equilibrate. The fluorescence was evaluated as a function of time ($\lambda_{em}$ = 531 nm, $\lambda_{ex}$ = 506 nm). At 50 s, 10 µL of compound was added to the cuvette solution to initiate the transport studies. Finally, the vesicles were completely lysed at 450 s by adding 20 µL of 20% Triton X-100. The transport studies for the compounds were performed in repetition at various concentrations of compound **4.1d** (5 nM to 200 nM). The fluorescence intensity measurement was continued for a further 50 s. The normalized % transport efficiency (%EE) at t = 450 s was considered for the particular transport efficiency of the compounds.

Transport activity, $T_{MgG} = (\frac{F_t - F_0}{F_\infty - F_0} \times 100)$ %

**4.4.3.3. Critical aggregation concentration measurements —** The critical aggregation concentration (CAC) of compound **4.1d** was determined using its concentration-dependent $Zn^{2+}$ transport properties. A distinct inflection point was observed through the linear fitting after analysing the % transport ($Zn^{2+}$) in the lower concentration range. Below 10 nM, the slope of the linear fit was 0.58 ± 0.05, while above 10 nM, the slope increased to 0.92 ± 0.08. The change in slope at the inflection point suggests the initiation of supramolecular nanochannels (> 10 nM) under liposomal conditions.

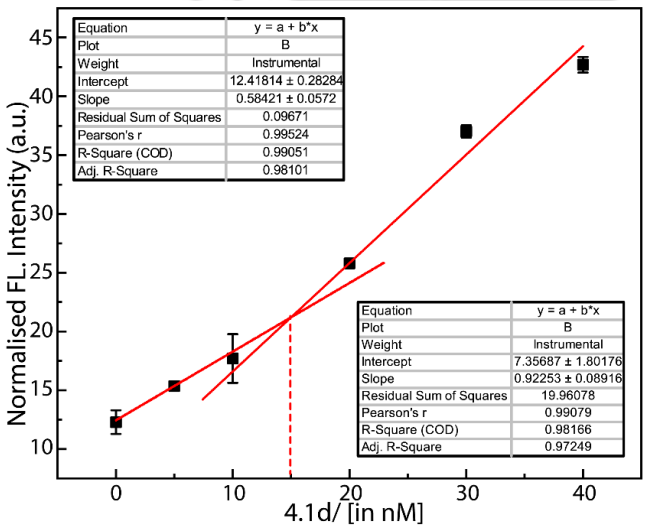


**Figure 4.8.** Measurement of CAC values of compound **4.1d** calculated from the concentration-dependent $Zn^{2+}$ ions transport properties across EYPC/Chol-LUV⊃MgG.

**4.4.3.4. Cation selectivity studies across EYPC/Chol-LUV⊃MgG vesicles —** For the cation selectivity studies, a similar procedure was followed for preparing vesicles and measuring ion transport activities, as mentioned in the previous section. For the fluorescence assay, 10 mM HEPES buffer containing 100 mM NaCl, pH 7.0 (1930 µL), EYPC/Chol-LUV⊃MgG (40 µL), and $M_xCl_y$ salt (1 mM final conc.) ($MgCl_2$, $MnCl_2$, $FeCl_3$, $CoCl_2$, $NiCl_2$, $CuCl_2$, $ZnCl_2$) were taken in a clean fluorescence cuvette (3 mL). The cuvette was placed in the spectrofluorometer under slow stirring conditions for ~3 min. The MgG fluorescence intensity was recorded as a function of time ($\lambda_{em}$ = 531 nm, $\lambda_{ex}$ = 506 nm). At 50 s, 10 µL of compound **4.1d** was added to the cuvette solution (final concentration 50 nM) to initiate the transport studies. Finally, the vesicles were lysed entirely by adding 20 µL of 20% Triton X-100 at 450 s, and the fluorescence intensity measurement was continued for a further 50 s. The studies on cation selectivity were conducted multiple times.

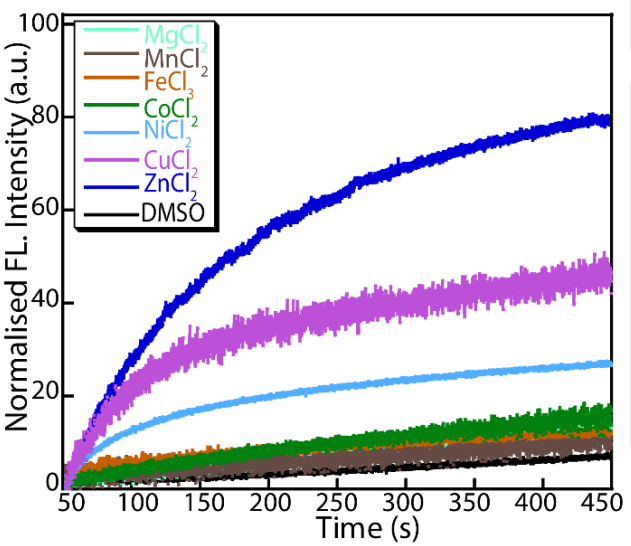


**Figure 4.9.** Comparison of the cation transport activity of compound **4.1d** (50 nM) across the bilayers of EYPC/Chol-LUV⊃MgG. The intravesicular solution was 10 mM HEPES buffer containing 100 mM NaCl, 100 µM EDTA, and MgG dye at pH 7.0, and the extravesicular solution was 10 mM HEPES buffer containing 100 mM NaCl and 100 µM EDTA at pH 7.0 and 1 mM $M_xCl_y$ (where M = $Mg^{2+}$, $Mn^{2+}$, $Fe^{3+}$, $Co^{2+}$, $Ni^{2+}$, $Cu^{2+}$, and $Zn^{2+}$). DMSO (10 µL) was used as a control.

**4.4.3.5 Anion selectivity studies across EYPC/Chol-LUV⊃MgG vesicles —** For the anion selectivity studies, a similar procedure was followed for preparing vesicles and measuring ion transport activities, as mentioned in the previous section. For the fluorescence assay, 10 mM

HEPES buffer containing 100 mM NaCl, pH 7.0 (1930 µL), EYPC/Chol-LUV⊃MgG (40 µL), and $Zn_xB_y$ (1 mM final concentration of $ZnCl_2$, $ZnBr_2$, $ZnSO_4$, and $Zn(NO_3)_2$ ) were taken in a clean fluorescence cuvette (3 mL). The cuvette was placed in a spectrofluorometer under slow stirring conditions for ~3 min. The MgG fluorescence intensity was monitored as a function of time ($\lambda_{em}$ = 531 nm, $\lambda_{ex}$ = 506 nm). At 50 s, 10 µL of compound **4.1d** (final conc. 50 nM) was added to the cuvette solution to initiate the transport studies. Finally, the vesicles were lysed by adding 20 µL of 20% Triton X-100 at 450 s, and the fluorescence intensity measurement was continued for a further 50 s. The studies on anion selectivity were conducted multiple times.

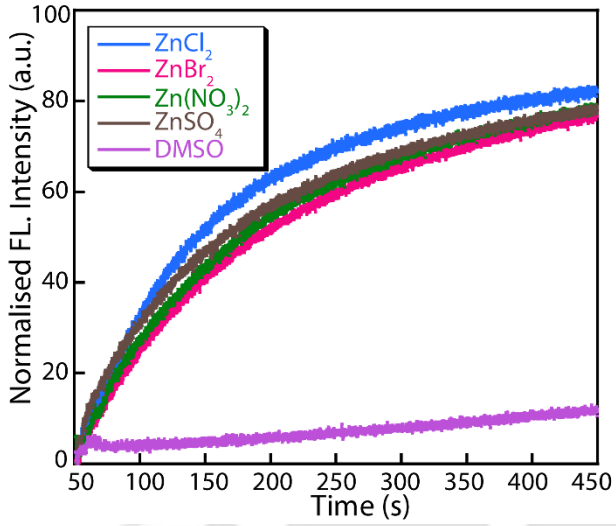


**Figure 4.10.** Comparison of the anion transport activity of compound **4.1d** (50 nM) across the bilayers of EYPC/Chol-LUV⊃MgG in the presence of different zinc salts. The intravesicular solution was 10 mM HEPES buffer containing 100 mM NaCl, 100 µM EDTA, and MgG dye at pH 7.0, and the extravesicular solution was 10 mM HEPES buffer containing 100 mM NaCl and 100 µM EDTA at pH 7.0 and 1 mM $Zn_xB_y$ ($ZnCl_2$, $ZnBr_2$, $ZnSO_4$, and $Zn(NO_3)_2$). DMSO (10 µL) was used as a control.

**4.4.3.6 Investigation of $Cl^-$ ion transport ability of the compound across the EYPC/Chol-LUVs⊃lucigenin —** To study ion transport using lucigenin fluorescence, large unilamellar vesicles (LUVs) composed of egg yolk phosphatidylcholine (EYPC) and cholesterol (CHOL) were prepared. EYPC (50 mg/mL in deacidified $CHCl_3$) and CHOL (25 mg/mL in deacidified $CHCl_3$) were mixed in a clean glass vial in an 8:2 molar ratio. The organic solvent was evaporated under reduced pressure for 6 hours, forming a uniform thin lipid film. The lipid film was hydrated by adding 800 µL of 20 mM HEPES buffer containing 1 mM lucigenin and 100 mM $NaNO_3$ (pH 7.0). The resulting suspension was subjected to six to seven vortex cycles

over one hour to ensure homogeneity, followed by 17–19 freeze-thaw cycles. Subsequently, the suspension underwent constant vortexing for 10 minutes to encapsulate lucigenin within the lipid bilayer. Using a mini extruder, the lipid suspension was extruded through a 200 nm polycarbonate membrane (Avanti Polar Lipids). This extrusion process was repeated 19–21 times (ensuring an odd number of passes) to obtain uniformly sized LUVs. Unencapsulated lucigenin dye was removed by size-exclusion chromatography using a Sephadex G-50 column equilibrated with 20 mM HEPES buffer containing 100 mM $ZnCl_2$ (pH 7.0) to get the final lipid concentration of 25 mM (assuming 100% lipid regeneration). For the fluorescence-based transport assay, 1940 µL of 20 mM HEPES buffer containing 100 mM $ZnCl_2$ (pH 7.0) and 50 µL of the EYPC/CHOL-LUV⊃lucigenin LUV suspension was transferred to a quartz fluorescence cuvette. The sample was maintained at room temperature under slow stirring. Fluorescence emission was monitored using a spectrophotometer at 455 nm excitation and 505 nm emission. After recording the baseline fluorescence for 50 seconds, 10 µL of compound **4.1d** (from a DMSO stock solution) was added to initiate ion transport. At 450 seconds, the vesicles were lysed by adding 20 µL of 20% Triton X-100 solution, and fluorescence was recorded until 500 seconds to determine the endpoint.

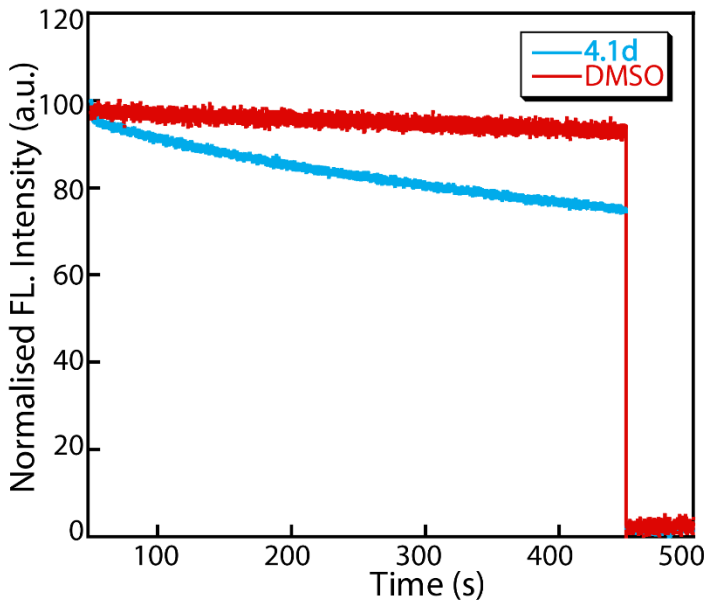


**Figure 4.11.** Chloride ion transport activity of compound **4.1d** (10 µM) across EYPC/Chol-LUV⊃lucigenin, with DMSO (10 µL) as the control.

**4.4.3.7 Binding affinity of 3d with $Zn^{2+}$ —** The binding affinity of compound **4.1d** for $Zn^{2+}$ was examined through UV-Vis titration of the water medium. In this experiment, a 10 µM solution of compound **4.1d** was titrated with $ZnCl_2$, resulting in a gradual decrease in

absorbance with each addition of $Zn^{2+}$ ions. The association constant ($K_a$) for the interaction was determined using the Bindfit v0.5 program by fitting the absorbance data to a 1:1 binding model. Under the experimental conditions, the calculated (average of three measurements) $K_a$ was $(7.44 \pm 0.20) \times 10^3$ $M^{-1}$.

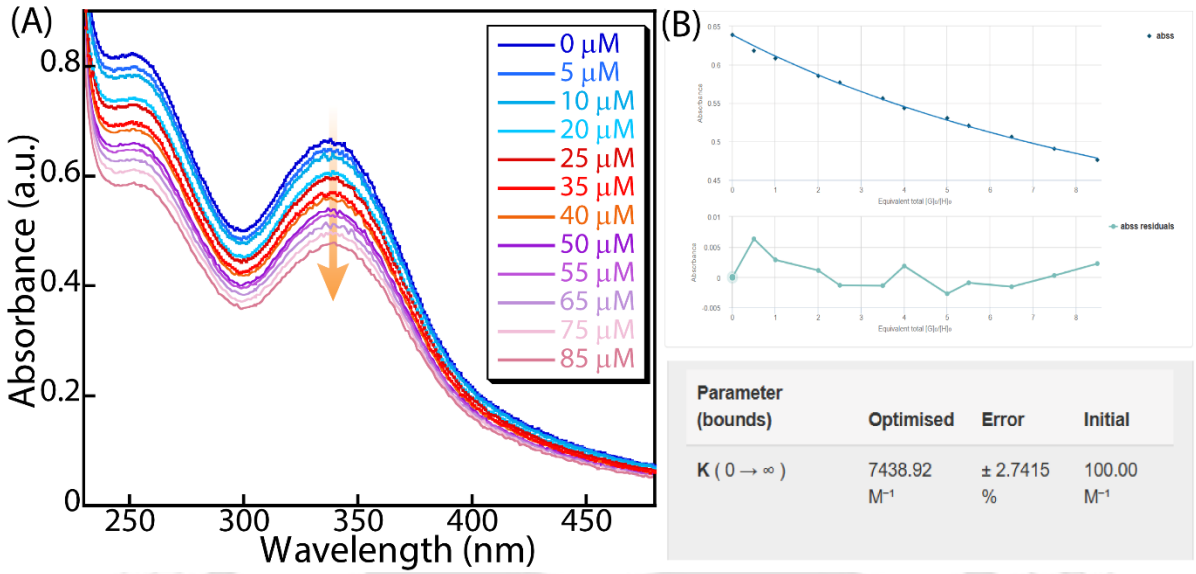


**Figure 4.12.** Representative UV-Vis absorbance titration spectra of compound **4.1d** (10 µM) with varying concentrations of $Zn^{2+}$ ions (0-85 µM). (B) Calculation of binding constant using the BindFit 0.5 program.

**4.4.3.8 Ion transport study across EYPC/Chol-LUV⊃MgG in the presence of FCCP —** For the FCCP assay, the vesicles were prepared similarly as mentioned in the earlier section using 10 mM HEPES, 100 mM NaCl, 100 µM EDTA buffer pH 7.0. In a clean fluorescence cuvette (3 mL), 10 mM HEPES buffer containing 100 mM NaCl, pH 7.0 (1930 µL), EYPC/Chol-LUV⊃MgG (40 µL), $Zn^{2+}$ (final concentration 1 mM), and FCCP (1.0 nM) were taken. The cuvette was placed in the spectrofluorometer under slow stirring conditions for ~3 min. The fluorescence intensity was recorded over time ($\lambda_{em}$ = 531 nm, $\lambda_{ex}$ = 506 nm). At 50 s, 10 µL of compound **4.1d** was added to the cuvette solution (final concentration 50 nM) to initiate the transport studies. Finally, the vesicles were fully lysed by adding 20 µL of 20% Triton X-100 at 450 s, and the fluorescence intensity was measured for an additional 50 s. The control experiment was performed in the presence of DMSO and only FCCP. The FCCP assay was performed in multiple.

**4.4.3.9 Fluorescein-based assay to monitor pH modulation along with $Zn^{2+}$ transportation across EYPC/Chol-LUVs⊃fluorescein vesicles —** To conduct the fluorescein-based ion

transport measurements for monitoring pH changes along with $Zn^{2+}$ transport process within the vesicles, LUVs were prepared similarly as mentioned in the earlier section using 10 mM fluorescein dye in 10 mM HEPES buffer containing 100 mM NaCl at pH 6.0. In a clean fluorescence cuvette (3 mL), 10 mM HEPES buffer containing 100 mM NaCl, pH 6.0 (1930 µL), EYPC/Chol-LUV⊃fluorescein (40 µL), and $ZnCl_2$ (final concentration 3 mM) were added. The cuvette was placed under slow stirring conditions in a fluorescence spectrophotometer for about 3 min to equilibrate. The fluorescence was evaluated over time ($\lambda_{em}$ = 520 nm, $\lambda_{ex}$ = 495 nm). At 50 s, compound **4.1d** (1 µM) was added to the cuvette solution to initiate the transport studies. Similarly, the transport studies were also performed with various extravesicular buffers of different pH (pH 6.5 and 7.0). The normalized fluorescence intensity was determined by using the equation below,

$$I_{rel} = \frac{I_t}{I_{min}}$$

where $I_t$ is the fluorescence intensity at time t, and $I_{min}$ is the fluorescence minima of the particular kinetics.

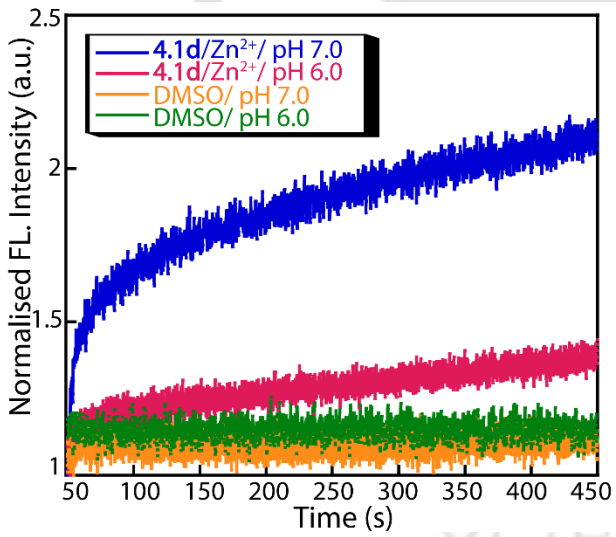


**Figure 4.13.** Measurement of intravesicular pH modulation upon addition of compound **4.1d** across EYPC/Chol-LUV⊃fluorescein suspended in 10 mM HEPES buffer containing 100 mM NaCl at pH 6.0/7.0 after the addition of 3 mM $ZnCl_2$ and 1 µM compound **4.1d** in the extravesicular environment. The intravesicular solution was 10 mM HEPES buffer containing 100 mM NaCl, pH 6.0.

**4.4.3.10 Ion transport study across EYPC/Chol-LUV⊃MgG in the presence of valinomycin —** For the valinomycin assay, the liposomes were prepared similarly as mentioned in the earlier section using 10 mM HEPES, 100 mM KCl, 100 μM EDTA, pH 7.0. In a clean fluorescence cuvette (3 mL), 10 mM HEPES buffer containing 100 mM NaCl, pH 7.0 (1930 μL), EYPC/Chol-LUV⊃MgG (40 μL), $Zn^{2+}$ (final concentration 1 mM), and valinomycin (12 pM) was taken. The cuvette was placed in the spectrofluorometer under slow stirring conditions for ~3 min. The fluorescence intensity was recorded over time ($\lambda_{em}$ = 531 nm, $\lambda_{ex}$ = 506 nm). At 50 s, 10 μL of compound **4.1d** was added to the cuvette solution (final concentration 50 nM) to initiate the transport studies. Finally, the vesicles were fully lysed by adding 20 μL of 20% Triton X-100 at 450 s, and the fluorescence intensity was measured for an additional 50 s. The control experiment was performed in the presence of DMSO and only valinomycin. The valinomycin assay was performed in multiple.

**4.4.3.11 Vesicle leakage assay across EYPC−LUV⊃carboxyfluorescein —** A thin lipid film was prepared by evaporating a solution of 154 μL of EYPC (50 mg/mL stock in chloroform), and 39 μL cholesterol (25 mg/mL stock in chloroform) in vacuo for 6 h.[19] After that, the lipid film was hydrated with 500 μL buffer (10 mM HEPES, 10 mM NaNO3, 50 mM carboxyfluorescein (CF), pH 7.0) for 1 h with occasional vortexing of 4−5 times and then subjected to a freeze-thaw cycle (≥ 15 times). The vesicle solution was extruded through a polycarbonate membrane with 200 nm pores 19 times (an odd number) to give vesicles with a mean diameter of ~200 nm. The extracellular dye was removed with size exclusion chromatography (Sephadex G-50) with 10 mM HEPES buffer (100 mM NaCl, pH 7.0.) Final concentration: ~25 mM EYPC-CHOL lipid; intravesicular solution: 10 mM HEPES, 10 mM $NaNO_3$, 50 mM CF, pH 7.0; extravesicular solution: 10 mM HEPES, 100 mM NaCl, pH 7.0.

**4.4.3.12 Carboxyfluorescein leakage assay —** In a clean and dry fluorescence cuvette, 50 μL of the above lipid solution and 1930 μL of 10 mM HEPES buffer, 100 mM NaCl, pH 7.0, were taken and kept in a slowly stirring condition by a magnetic stirrer equipped with the fluorescence instrument (at t = 0 s). The CF fluorescence emission intensity time course, $F_t$, was observed at $\lambda_{em}$ = 517 nm ($\lambda_{ex}$ = 492 nm). Compound **4.1d** was added at t = 50 s, and at t = 450 s, 20 μL of 20% Triton X-100 was added to lyse the vesicles and achieve 100% CF release. This study confirmed that the integrity of the bilayer membranes remains intact at varying concentrations of compound **4.1d**.

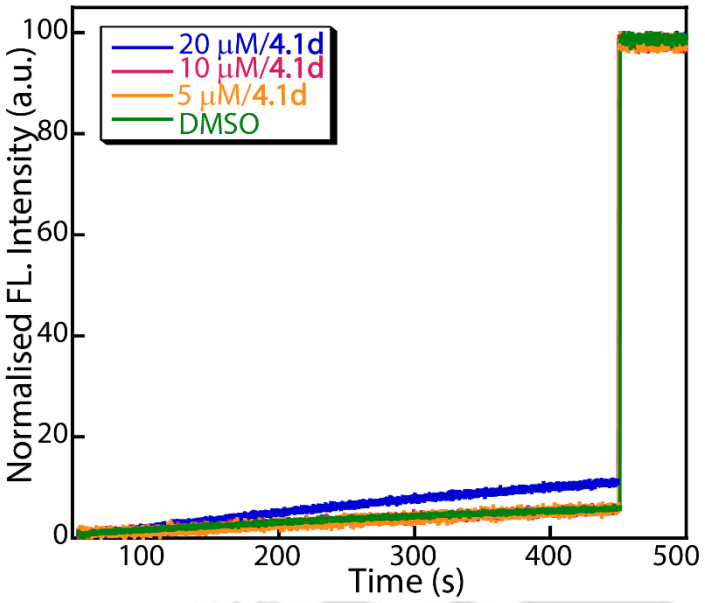


**Figure 4.14.** Vesicle leakage assay of compound **4.1d** using EYPC/Chol-LUV⊃CF. DMSO (10 μL) was used as a control.

**4.4.3.13. Ion transport study across EYPC/Chol-LUV⊃MgG vesicles for cholesterol dependency assay —** To get an insight into channel or carrier-like behaviour of the potent compound, the cholesterol dependency assay was performed across EYPC/Chol-LUV⊃MgG. The vesicles were prepared according to the previously mentioned procedure with varying cholesterol concentrations. The LUVs with 8:2 and 6:4 molar ratios of EYPC/Chol were prepared, encapsulating 10 mM HEPES buffer containing 100 mM NaCl, 100 μM EDTA, and 50 μM MgG at pH 7.0. In a clean fluorescence cuvette (3 mL), 10 mM HEPES buffer containing 100 mM NaCl, pH 7.0 (1930 μL), EYPC/Chol-LUV⊃MgG (40 μL) of an 8:2 ratio, and $Zn^{2+}$ (final concentration 1 mM) were taken. The cuvette was placed in the spectrofluorometer under slow stirring conditions for ~3 min. The fluorescence intensity was recorded over time ($\lambda_{em}$ = 531 nm, $\lambda_{ex}$ = 506 nm). At 50 s, 10 μL of compound **4.1d** was added to the cuvette solution (final concentration 50 nM) to initiate the transport studies. Finally, the vesicles were fully lysed by adding 20 μL of 20% Triton X-100 at 450 s, and the fluorescence intensity was measured for an additional 50 s. The same procedure was followed for measuring transport across EYPC/Chol-LUVs with a 6:4 ratio. DMSO control (10 μL) was measured with both 8:2 and 6:4 ratio-based vesicles. [20]

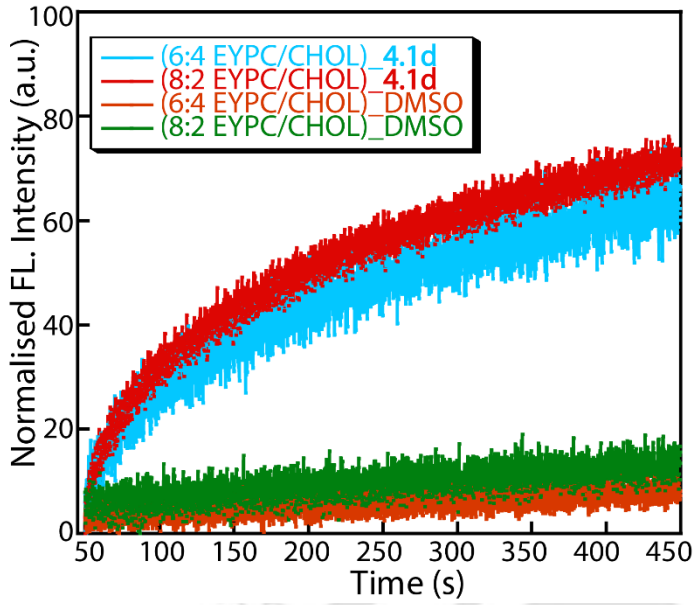


**Figure 4.15.** Cholesterol concentration-dependent $Zn^{2+}$ transport activity of compound **4.1d** (50 nM) using EYPC/Chol-LUV⊃MgG with a molar ratio of 8:2 and 6:4 (EYPC/Chol). The vesicles were prepared using 10 mM HEPES buffer containing 100 mM NaCl, 100 µM EDTA and MgG dye at pH 7.0, and suspended in 10 mM HEPES buffer containing 100 mM NaCl and 100 µM EDTA at pH 7.0. DMSO (10 µL) was used as a control.

**4.4.3.14 U-Tube assay for compound 4.1d –** The classical U-tube experiment was performed to confirm the mechanistic pathway for the $Zn^{2+}$ transport by compound **4.1d**. The lipid bilayer was mimicked using chloroform (12 mL) as the organic layer. The compound **4.1d** (2 mM) in chloroform was placed at the bottom of the U-tube under mild stirring conditions. The left arm of the tube was filled with 20 mM HEPES and 0.1 M $ZnCl_2$ solution (12 mL), and the right arm with 20 mM HEPES and 0.1 M aqueous $NaNO_3$ solution (12 mL). Arsenazo-III, a metal-ion-sensing dye (20 µM), was added to the receiver arm to detect $Zn^{2+}$. The $Zn^{2+}$ binding to arsenazo-III dye (20 µM; $\lambda_{max}$ = 545 nm) showed a significant shift in UV-Vis spectra ($\lambda_{max}$ = 600 nm). The $Zn^{2+}$ concentration at the receiver end was monitored using a UV-Vis spectrophotometer after 72 h. The obtained spectra suggested that after 72 h, no significant amount of $Zn^{2+}$ was carried to the receiver end of the U tube. Hence, compound **4.1d** could not act as a carrier through an apolar phase ($CHCl_3$). A similar study was performed in the presence of clioquinol (CQ, 2 mM), a $Zn^{2+}$ carrier.

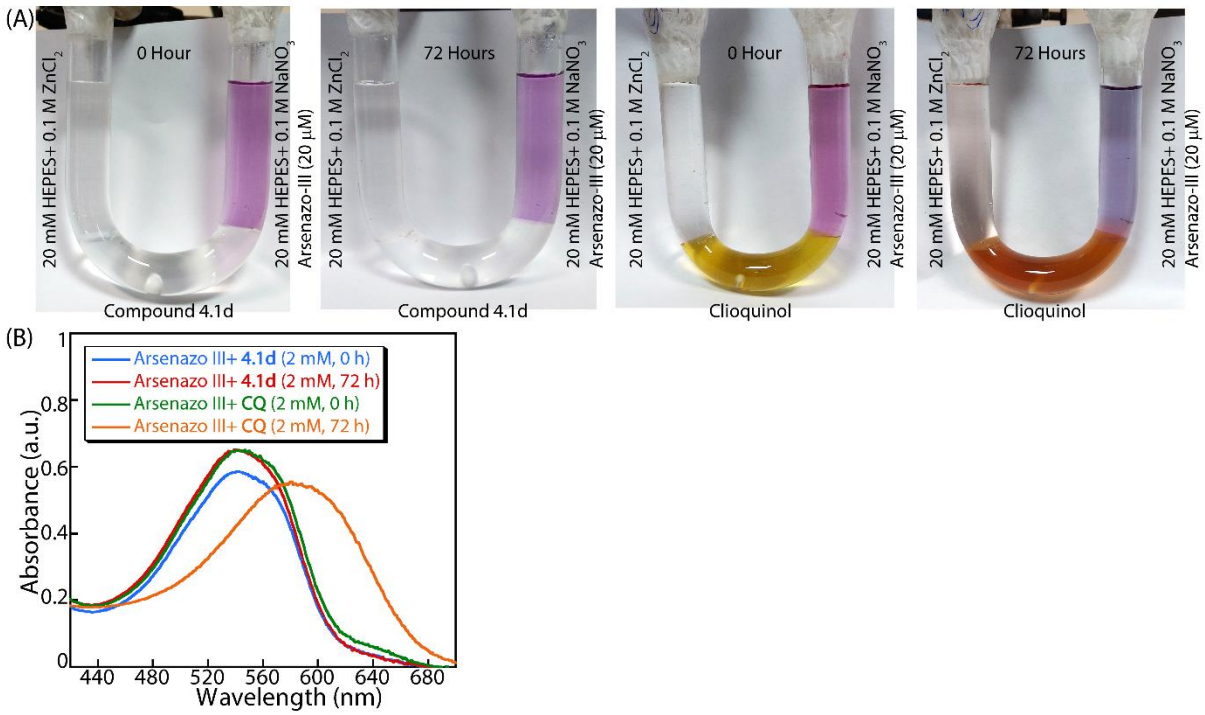


**Figure 4.16.** U-tube assay of compound **4.1d** and clioquinol (CQ; control). (B) UV-Vis absorbance spectra of arsenazo-III dye-containing solution from the receiver end of the U-tube in the presence of compound **4.1d** and CQ at 0 and 72 h.

### 4.4.4 Field emission scanning electron microscopy (FESEM) analysis:

To understand the effect of solvent polarity on the self-assembly properties of the compound, we conducted a morphological study using FESEM. Compound **4.1d** (1 mM) solutions in water and $CHCl_3$ were prepared, drop-casted onto a FESEM sample, and dried at room temperature. Before analysis, the samples were stacked onto the FESEM grid and coated with gold solution.[21]

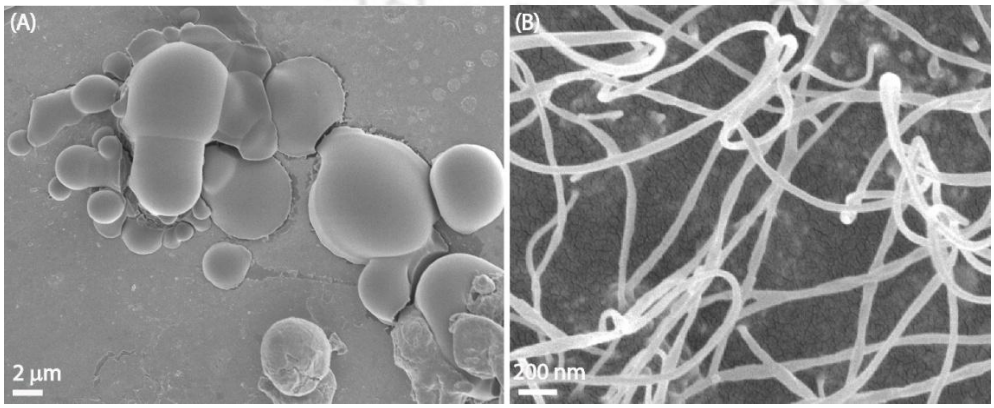


**Figure 4.17.** Morphological analysis using FESEM of compound **4.1d** in (A) hydrophilic ($H_2O$) and (B) hydrophobic ($CHCl_3$) environment.

### 4.4.5 NOESY spectra of the compound:

The NOESY spectrum of compound **4.1d** was recorded in DMSO-$d_6$. To elucidate the molecular basis of the channel-forming behaviour of tripodal compound **4.1d**, we explored its self-assembly properties under varying solvent environments. Morphological studies revealed that in aqueous solution, compound **4.1d** formed spherical aggregates, whereas in chloroform, it self-organized into nanofiber-like architectures. To investigate the origin of solvent-dependent self-assembly patterns, the 2D-NOESY NMR experiment was performed in DMSO-$d_6$, a solvent in which **4.1d** is sufficiently soluble to enable spectral acquisition. Despite the high polarity and solubilizing nature of DMSO, we observed three distinct cross-peaks, suggesting close spatial proximity between protons located on different arms, consistent with intermolecular interactions in solution. While DMSO does not fully replicate the hydrophobic environment of chloroform ($CHCl_3$) or a lipid bilayer, notable correlations between arm-to-arm interactions are still observed. This observation suggests that such interactions represent favourable contact sites even in relatively polar solvents like DMSO. In hydrophobic environments, these interactions likely become even more dominant. As a result, they are expected to play a key role in driving the formation of the observed nanofibrous morphology. These findings collectively suggest a model in which arm-mediated intermolecular associations act as key nucleation points for higher-order organization, linking molecular self-assembly with functional channel activity.

### 4.4.6 Black lipid membrane conductance measurements:

A solvent-free black lipid membrane (BLM) was formed as previously mentioned. Briefly, a thin Teflon foil (20 µm; Goodfellow) with a 50-100 µm orifice was sandwiched between two homemade Delrin half-cells. The orifice in the Teflon foil was pre-painted with 3 µL of hexane/hexadecane on both sides, dried for 20 minutes, and filled with 2.5 mL of buffer on each side. Before forming the lipid bilayer, about 10 µL (size of the surface around 1×1 $cm^2$) of a 1 v% 1,2-diphytanoyl-sn-glycero-3-phosphocholine (diPhyPC) in pentane was added to the buffer surface. After 5-10 minutes drying, the bilayer was formed by lowering and raising the buffer level using a 5 mL pipette. The ion conductance measurements were performed with Ag-AgCl reference electrodes with a diaphragm (Metrohm, Filderstadt, Germany). One electrode (GND) was connected to the ground, and the other electrode (Active) was connected to the head-stage of an Axopatch 200B amplifier that was used for the conductance measurements in the voltage clamp mode. Signals were filtered by an onboard low-pass Bessel filter at 1 kHz and recorded onto a computer hard drive with a sampling frequency of 2 kHz.

The conductance was obtained from the averaged ion current for a series of voltage steps. All measurements were taken from at least three independent measurements. Compound **4.1d** (1 mM) was prepared in DMSO and diluted accordingly. To accelerate equilibrium, we added compound **4.1d** (4 µM) on both sides of the membrane with equimolar concentrations (equilibrated for 1 h). For single-channel conductance (G) measurements, both chambers (GND and Active) were filled with a symmetrical solution containing 0.5 M $ZnCl_2$ in water. Channel formation in the presence of compound **4.1d** was confirmed by the distinctive channel opening and closing events after applying voltages. All data were analysed by the ClampFit 9 software (Molecular Devices). The complete data traces were recorded over a long period, and from a large trace, a small portion is presented in the manuscript and the Supporting Information.

**Calculation of ion channel diameter—** The pore size is estimated from the measured single-channel pore conductance G and is proportional in first order to the bulk conductivity kappa to the pore area $S = \frac{\pi d^2}{4}$ and inversely proportional to the pore length L.

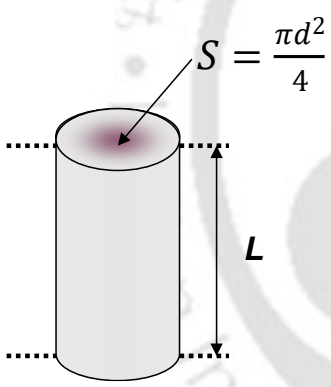


$G = \kappa\frac{\pi d^2}{4L}$; $\kappa = \sum_{i=1}^{N} c_i\rho_i$

Where our experimentally measured (from I-V plot) conductance G = 54 pS, d = diameter of the pore, L = length of the channel = 40 Å, $c_i$ = concentration of the ion *i,* [mol/m$^3$] and $\rho_i$ = specific conductance of the ion *i*, [S·m$^2$/mol]. Using published values for $\rho_{Zn(II)}$ = specific conductance of the $Zn^{2+}$ = 52.8 × 10$^{-4}$ [S·m$^2$/mol] and $\rho_{Cl(I)}$ = specific conductance of the $Cl^-$ ion = 76.31 ×10$^{-4}$ [S·m$^2$/mol].[22] We obtained the κ = bulk conductivity = 12.9 S/m for a concentration of $ZnCl_2$ = 0.5 M. Inverting the equation yields the pore diameter (d) = 1.5 Å.

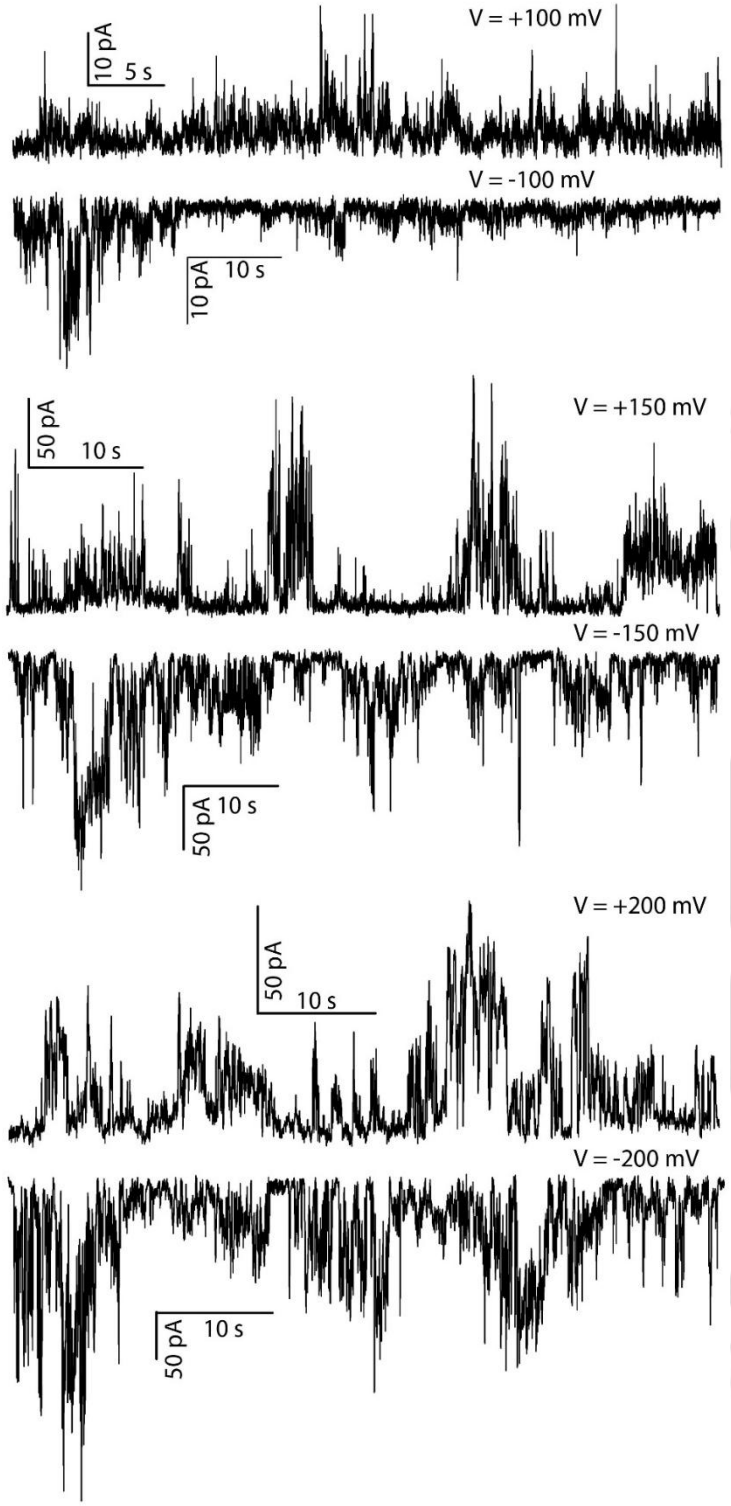


**Figure 4.18.** Ion conductance measurements of compound **4.1d** (4 μM) were recorded at +100 mV, -100 mV, +150 mV, -150 mV, +200 mV, and -200 mV under symmetrical $ZnCl_2$ solutions (0.5 M).

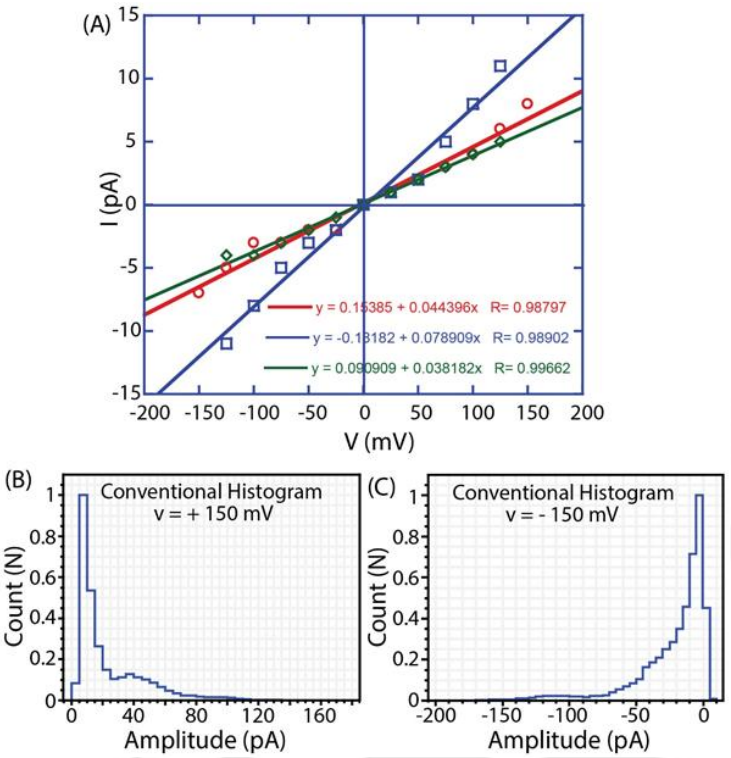


**Figure 4.19.** (A) I–V plots of compound **4.1d** in symmetrical $ZnCl_2$ solution (0.5 M). This curve presents the average of a highly fluctuating ion current. Histograms of the fluctuating ion current for (B) +150 mV and (C) -150 mV in a symmetrical $ZnCl_2$ solution (0.5 M). The pronounced peak was observed at around 40 pA and 20 pA at +150 mV and -150 mV, respectively. This peak we identified as a stable single channel. Less pronounced are multiple of them.

### 4.4.7 ROS detection by $H_2$DCFDA Dye:

To evaluate reactive oxygen species (ROS) generation upon $Zn^{2+}$–PPIX complex, a fluorescence-based assay using 2′,7′-dichlorofluorescein diacetate ($H_2$DCFDA) was performed. The assay was conducted in 20 mM HEPES buffer (pH 7.0), wherein 40 µM $H_2$DCFDA was incubated with various combinations of 20 µM PPIX and 50 µM $Zn^{2+}$. Fluorescence spectra were recorded at $\lambda_{ex}$ = 485 nm and $\lambda_{em}$ = 522 nm. After 1 hour of incubation, only the sample containing $H_2$DCFDA, PPIX, and $Zn^{2+}$ exhibited a distinct fluorescence emission peak at 522 nm, indicative of ROS production. No significant fluorescence was observed in the control samples. [23]

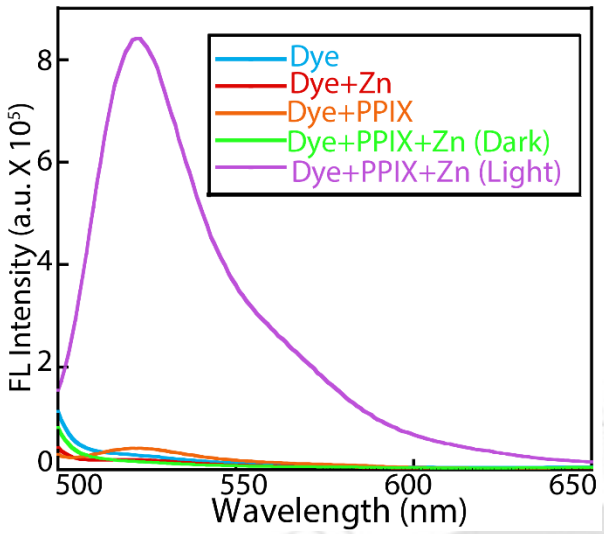


**Figure 4.20.** ROS detection assay by $H_2$DCFDA dye in 20 mM HEPES buffer, pH 7.0.

### 4.4.8 PPIX- $Zn^{2+}$ interaction study:

To investigate the interaction between PPIX and $Zn^{2+}$, both absorption and fluorescence spectroscopic analyses were conducted. Samples containing 20 µM PPIX and 50 µM $Zn^{2+}$ were prepared in 20 mM HEPES buffer (pH 7.0). In the UV-Vis absorption spectra, a notable decrease in the Soret band at 400 nm was observed. Typically, PPIX metalation results in the reduction of the four distinct Q-bands (500–700 nm) to two peaks. However, in our measurements, all four Q-bands remained diminished yet intact, indicating that $Zn^{2+}$ interacts with PPIX without inducing metalation. Fluorescence emission spectra were recorded with excitation at 400 nm and emission monitored at 640 nm. A marked decrease in emissions intensity at 640 nm was observed in the presence of $Zn^{2+}$, suggesting the formation of a $Zn^{2+}$–PPIX complex, consistent with non-metalating binding.

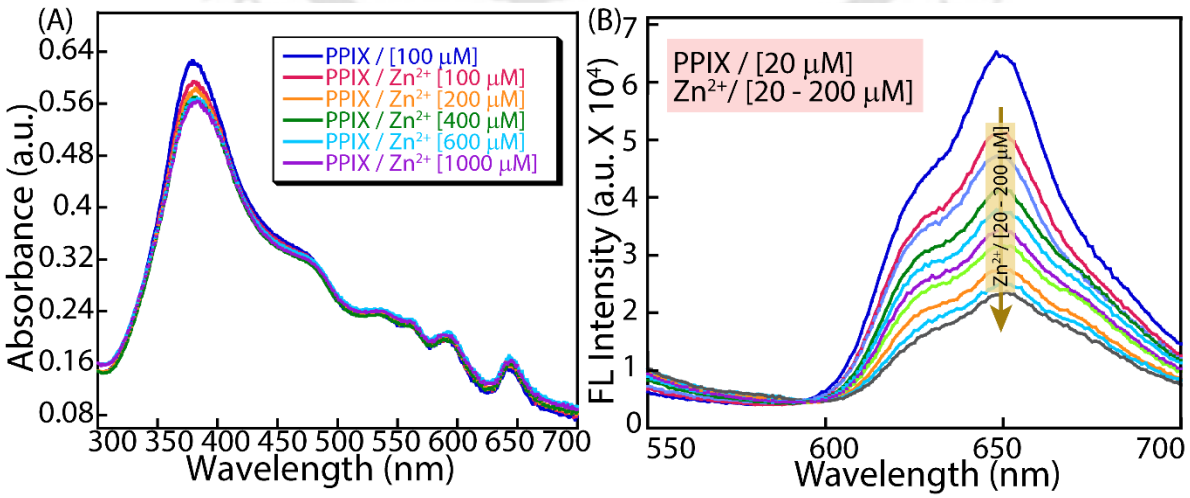


**Figure 4.21.** UV-Vis (A) and fluorescence-based (B) PPIX and $Zn^{2+}$ interaction studies in aqueous medium.

### 4.4.9 Kynurenine detection assay (Oxidation of Trp to Kyn):

We performed a UV-Vis spectrophotometric-based assay to detect the formation of kynurenine (Kyn) from tryptophan (Trp) in the presence of a PPIX-$Zn^{2+}$ complex. The reaction mixtures contained 50 µM PPIX, 100 µM $Zn^{2+}$, and 1 mM Trp in 20 mM HEPES buffer (pH 7.0), combined in various permutations and exposed to white (4 h and 24 h) and red light (4 h). Following light treatment, samples were quenched by adding 100 µL of 30% (w/v) trichloroacetic acid and incubated at 65 °C for 30 minutes. Subsequently, 2% (w/v) p-dimethylaminobenzaldehyde (pDMAB) in acetic acid was added, and the absorbance spectra were recorded using a UV-Vis spectrophotometer. A distinct absorption peak at ~480 nm was observed only in the sample containing all three components (PPIX, $Zn^{2+}$, and Trp) under light exposure, confirming the formation of Kyn. Control samples lacking one or more components, as well as the complete mixture kept in the dark, showed no significant peak at this wavelength, indicating that light exposure is crucial for the reaction to proceed.[10]

It is noteworthy that exposure to red light significantly increased kynurenine formation, whereas the same duration of white light produced only about 30% as much kynurenine. Achieving a comparable level of product formation with white light required approximately 24 hours.

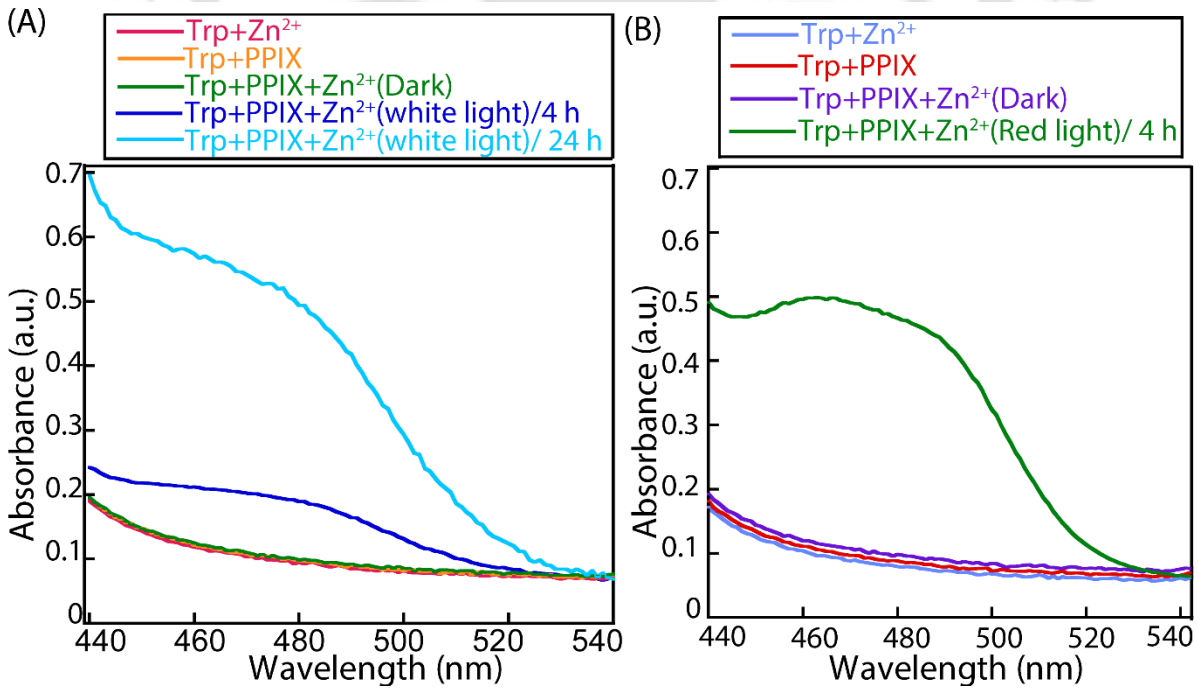


**Figure 4.22.** UV-Vis spectral analyses for Kyn detection under varying conditions of Trp, PPIX, $Zn^{2+}$, with (A) visible light and (B) red light exposure.

White light contains many wavelengths, but the intensity and overlap with $Zn^{2+}$-PPIX's absorption bands are relatively low, leading to weaker excitation and reduced photooxidation efficiency compared to targeted red light. Additionally, white light can cause more nonspecific photodegradation of the $Zn^{2+}$-PPIX complex, further diminishing its effectiveness. Photodegradation was further confirmed through HPLC analysis of PPIX.

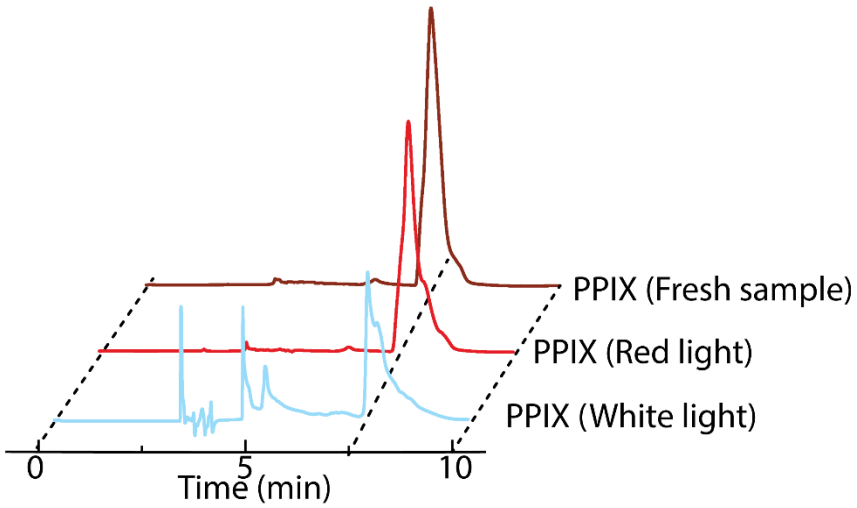


**Figure 4.23.** HPLC analysis of PPIX photodegradation under different light exposure after 8 h.

In 20 mM HEPES buffer (pH 7.0), 50 µM PPIX was incubated with white and red light for 8 h. Another fresh PPIX sample was used as a control, and HPLC analysis of the photo-irradiated and untreated samples was conducted under conditions similar to those in other cases.

### 4.4.10 HPLC analysis for the detection of kynurenine:

The PPIX-$Zn^{2+}$ complex-mediated Kyn formation in the presence of light was quantified by HPLC using an acetonitrile/water mobile phase. The assay monitored the oxidation of Trp to Kyn, a characteristic of indoleamine 2,3-dioxygenase 1 (IDO1) enzyme activity, by measuring absorbance at 365 nm with a UV detector. Reaction mixtures containing Trp (1 mM), protoporphyrin IX (PPIX, 20 µM), and $Zn^{2+}$ (50 µM) were prepared in various combinations in 1 mL of 20 mM HEPES buffer (pH 7.0). Samples were exposed to red light for 3 hours. Following light exposure, each sample was treated with 100 µL of 30% (w/v) trichloroacetic acid (TCA) and incubated at 65 °C for 30 minutes. The resulting mixtures were filtered through 0.2 µm PTFE syringe filters to remove particulates prior to HPLC injection. A control sample containing Trp, PPIX, and $Zn^{2+}$ was maintained in the dark under identical conditions. For time-dependent analysis, samples containing Trp, PPIX, and $Zn^{2+}$ were subjected to red light

exposure for 30, 60, 120, 180, and 240 min. Post-treatment, these samples were processed identically for HPLC analysis. Column used: Ascentis® express C18, 2.7 µm HPLC column, flow rate: 1.0 mL/min, mobile phase used: Optimised gradient of water/acetonitrile. The gradient used:

0-3 min- 20% water:80% $CH_3CN$

3-5 min- 100% $CH_3CN$

5-10 min- 20% water:80% $CH_3CN$

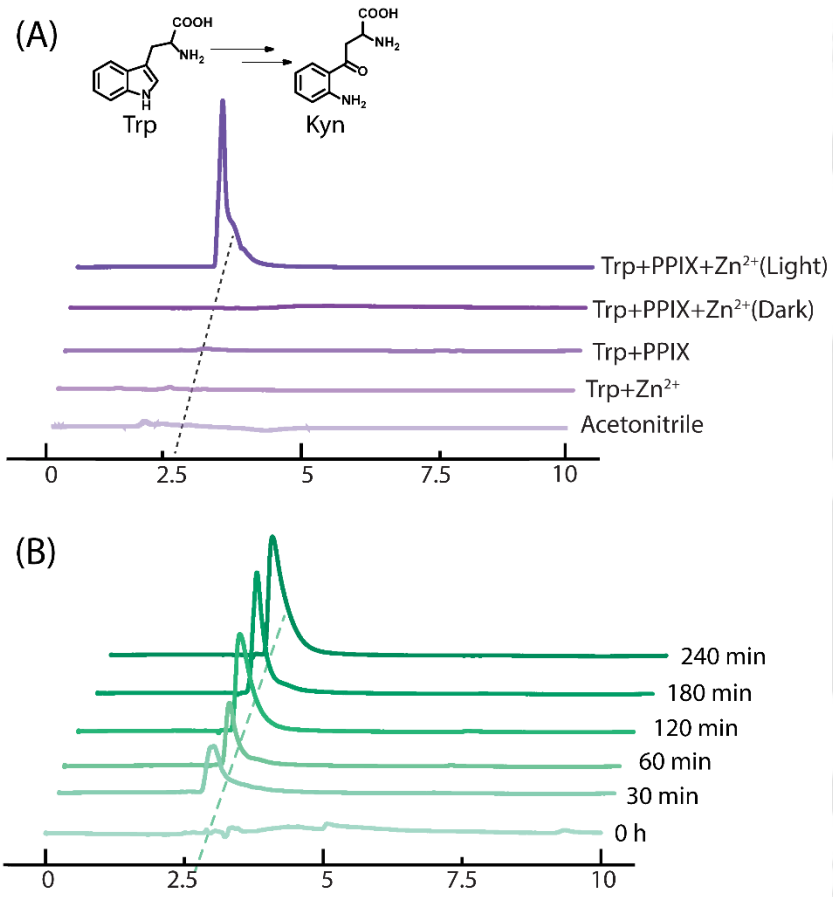


**Figure 4.24.** (A) Control studies using HPLC for Kyn formation (different combinations of Trp, PPIX, $Zn^{2+}$ and light). (B) Time-dependent HPLC analysis of Kyn generation from Trp (1 mM) under red light irradiation in HEPES buffer (pH 7.0) containing PPIX (20 µM) and $Zn^{2+}$ (50 µM).

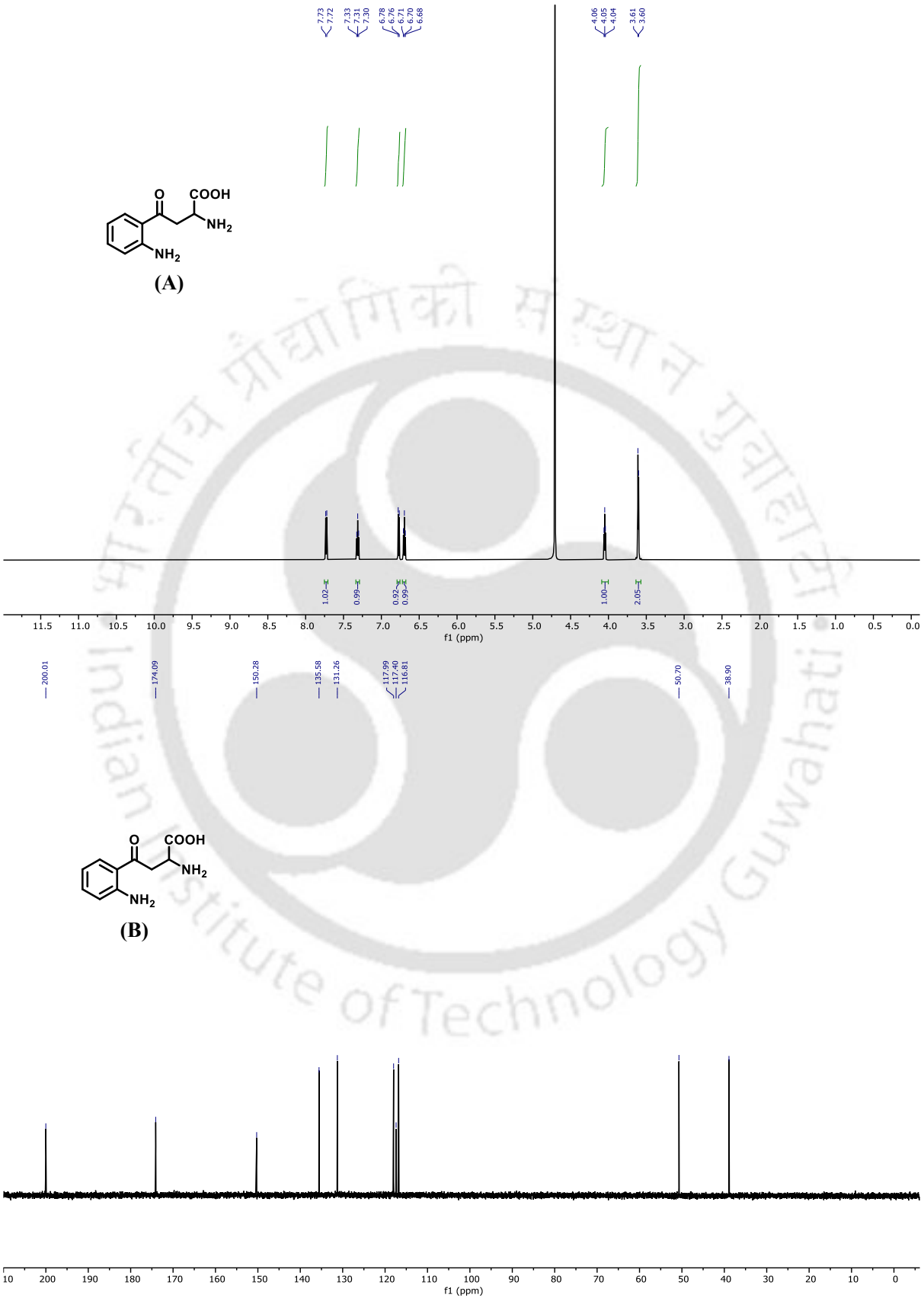


**Figure 4.25.** (A) $^{1}H$ and (B) $^{13}C$ NMR of Kyn.

### 4.4.11 ROS scavenging analysis:

To investigate the generation of oxidative species from the PPIX-$Zn^{2+}$ complex upon light irradiation, a ROS scavenging assay was performed using 1,4-diazabicyclo[2.2.2]octane (DABCO), ethanol[24], and catalase[25], known as $^1O_2$, hydroxyl (OH·), and peroxide radical scavengers, respectively. Samples were prepared in 20 mM HEPES buffer (pH 7.0) containing 20 µM PPIX, 1 mM Trp, and 50 µM $Zn^{2+}$. To probe the role of different ROS species, samples were supplemented with quenchers—DABCO (100 mM), ethanol (50 mM), and catalase (50 mM)—prior to irradiation. The mixtures were irradiated with red light for 3 h. Following the above-mentioned procedure (section 8), samples were prepared for Kyn detection using both UV and HPLC.

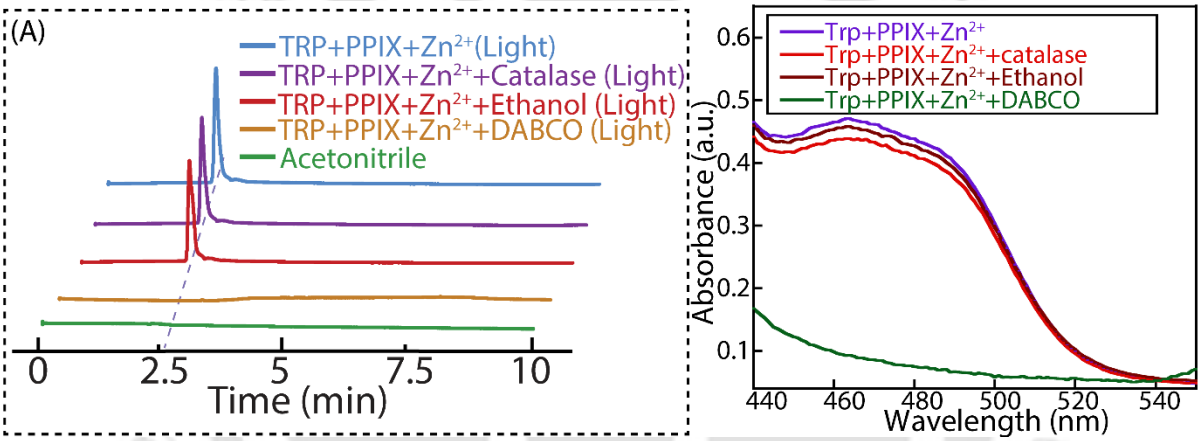


**Figure 4.26.** Detection of Kyn in samples containing Trp, PPIX, and $Zn^{2+}$ in 20 mM HEPES buffer (pH 7.0), treated with DABCO (100 mM), catalase (50 mM), and ethanol (50 mM) in (A) HPLC analysis and (B) UV-Vis absorbance spectra.

### 4.4.12 ROS-mediated oxidation reaction of different amino acids:

ROS-mediated oxidation reactions were also carried out in the presence of another substrate like Tyrosine (Tyr), Histidine (His) and Methionine (Met) in 20 mM HEPES buffer, pH 7.0, under red light (580 nm- 670 nm) conditions. HRMS of samples were recorded after 4 h of treatment for detecting the product as represented in the following table:

**Table 4.1** HRMS data detected in ROS-mediated substrate in 20 mM HEPES buffer, pH 7.0.

| Substrate | Product | HRMS $[M+H]^+$ | ESI MS detected |
|---|---|---|---|
| **Tryptophan** | N-formyl kynurenine | 237.087 | 237.0905 |
| **Tyrosine** | Di-tyrosine | 361.1394 | 361.1413 |
| **Methionine** | Methionine sulfoxide | 166.0532 | 166.0530 |
| **Histidine** | ND | - | - |

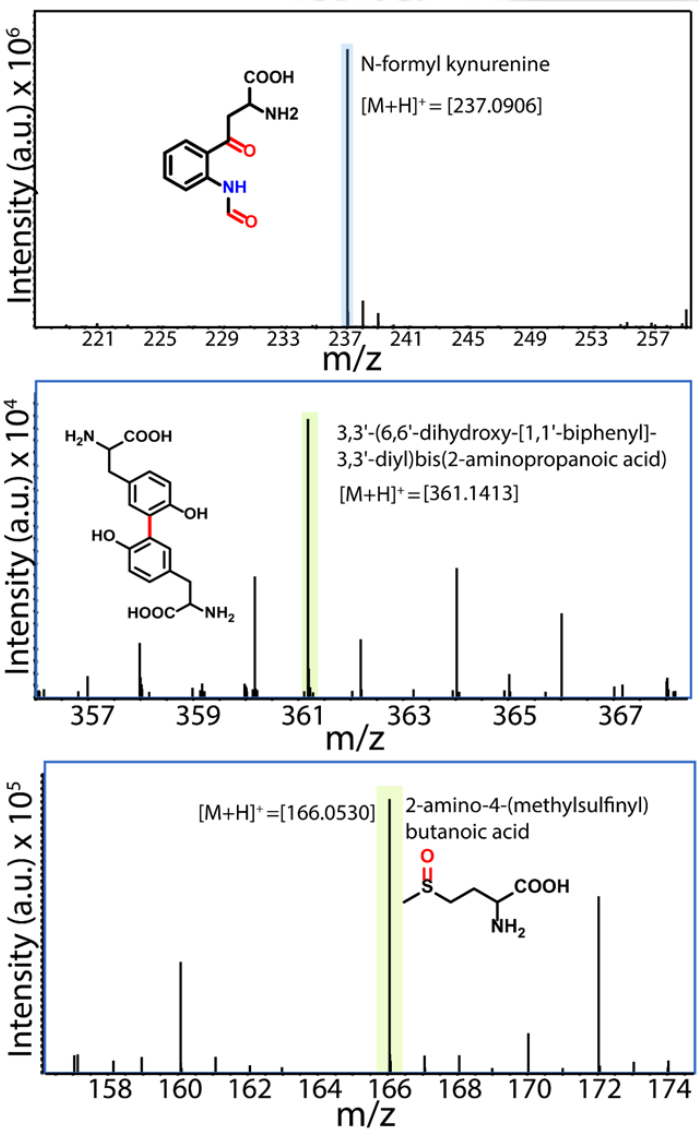


**Figure 4.27**. HRMS spectrum of the ROS-mediated reaction product showing the molecular ion peak consistent with the expected oxidized product.

**4.4.13 HPLC analysis for the detection of kynurenine under liposomal environment:**

**4.4.13.1 Preparation of EYPC/Chol-LUV⊃ PPIX/TRP −**

A thin lipid film was prepared by evaporating a solution of 308 µL of EYPC (50 mg/mL stock in chloroform) and 78 µL cholesterol (25 mg/mL stock in chloroform) in vacuo for 6 h. After that, lipid film was hydrated with 1000 µL buffer (20 mM HEPES, pH 7.0) containing 100 µM PPIX, 2 mM Trp for 1 h with occasional vortexing of 4−5 times and then subjected to freeze-thaw cycle (≥ 5 times). The vesicle solution was vortexed for 15 minutes for thorough mixing. The obtained solution was divided into 4 parts, each having 250 µL of vesicle solution (final vesicle concentration assumed: 25 mM).

**4.4.13.2 Kyn detection in EYPC/Chol-LUV ⊃PPIX/TRP −** The obtained liposomal aliquots were treated with $Zn^{2+}$, compound **4.1d**, and red light for 4 hours in HEPES buffer pH 7.0. Post photo-irradiation, resulted vesicle solutions were lysed using 20 µL of 20% Triton-X and centrifuged at 10000 rpm for 5 min to obtain the supernatant part. The resulting solutions were filtered through 0.2 µm PTFE syringe filters to remove particulates. Further treatment was done according to the earlier section to detect kyn in HPLC.

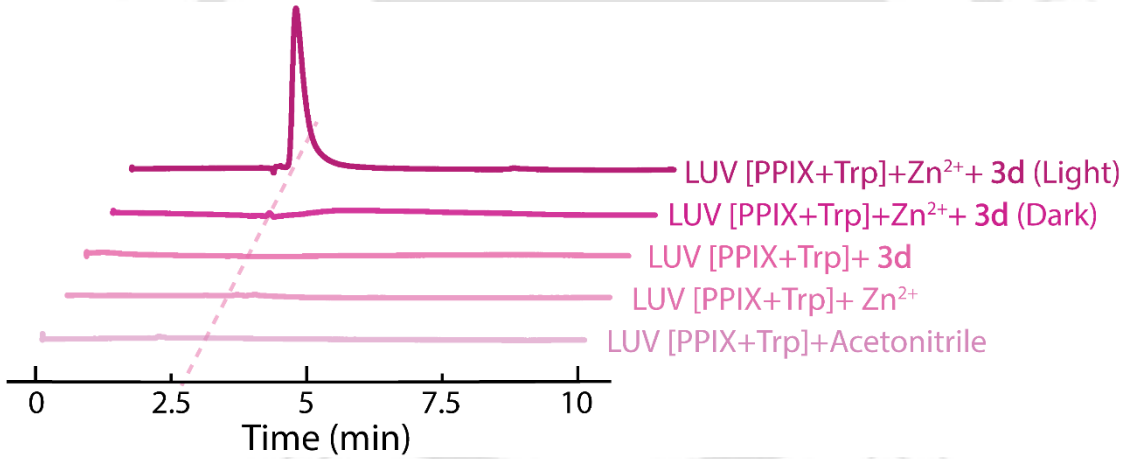


**Figure 4.28.** HPLC analysis for kynurenine detection in EYPC/Chol-LUVs⊃TRP/PPIX with compound **4.1d** and $Zn^{2+}$ treatment.

**4.4.14 Alternate light and dark treatment of EYPC/Chol-LUV⊃PPIX/Trp:**

LUVs were prepared according to the earlier-mentioned procedure with a final lipid concentration of 25 mM (2 mL). Compound **4.1d** was equilibrated with the prepared LUV solution, followed by the addition of $Zn^{2+}$ ions. The resulting mixture was gently stirred and subsequently exposed to alternating red light and dark conditions for a period of 60 min each. At the end of every 60 min interval, a 300 µL aliquot was withdrawn and lysed using 20 µL of

20% Triton X-100. Subsequently, these samples were analysed for kyn using HPLC and UV Vis absorbance study as mentioned in the earlier section.

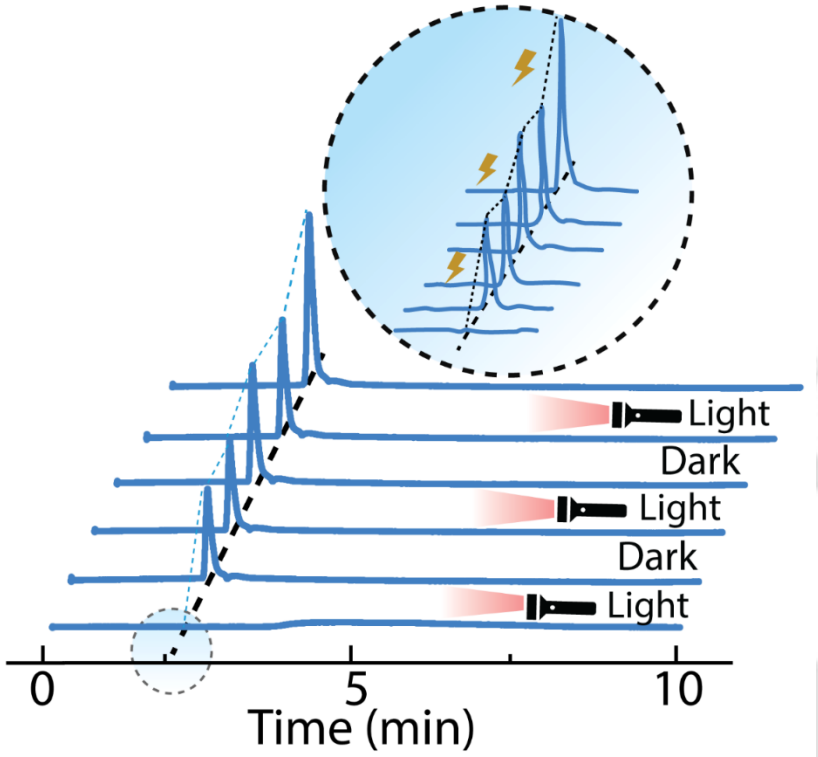


**Figure 4.29.** HPLC analysis for kyn detection in EYPC/Chol-LUVs⊃TRP/PPIX treated with compound **4.1d** and $Zn^{2+}$ under alternate light and dark conditions at a 60 min interval.

### 4.4.15 NMR spectra of the synthesized compounds:

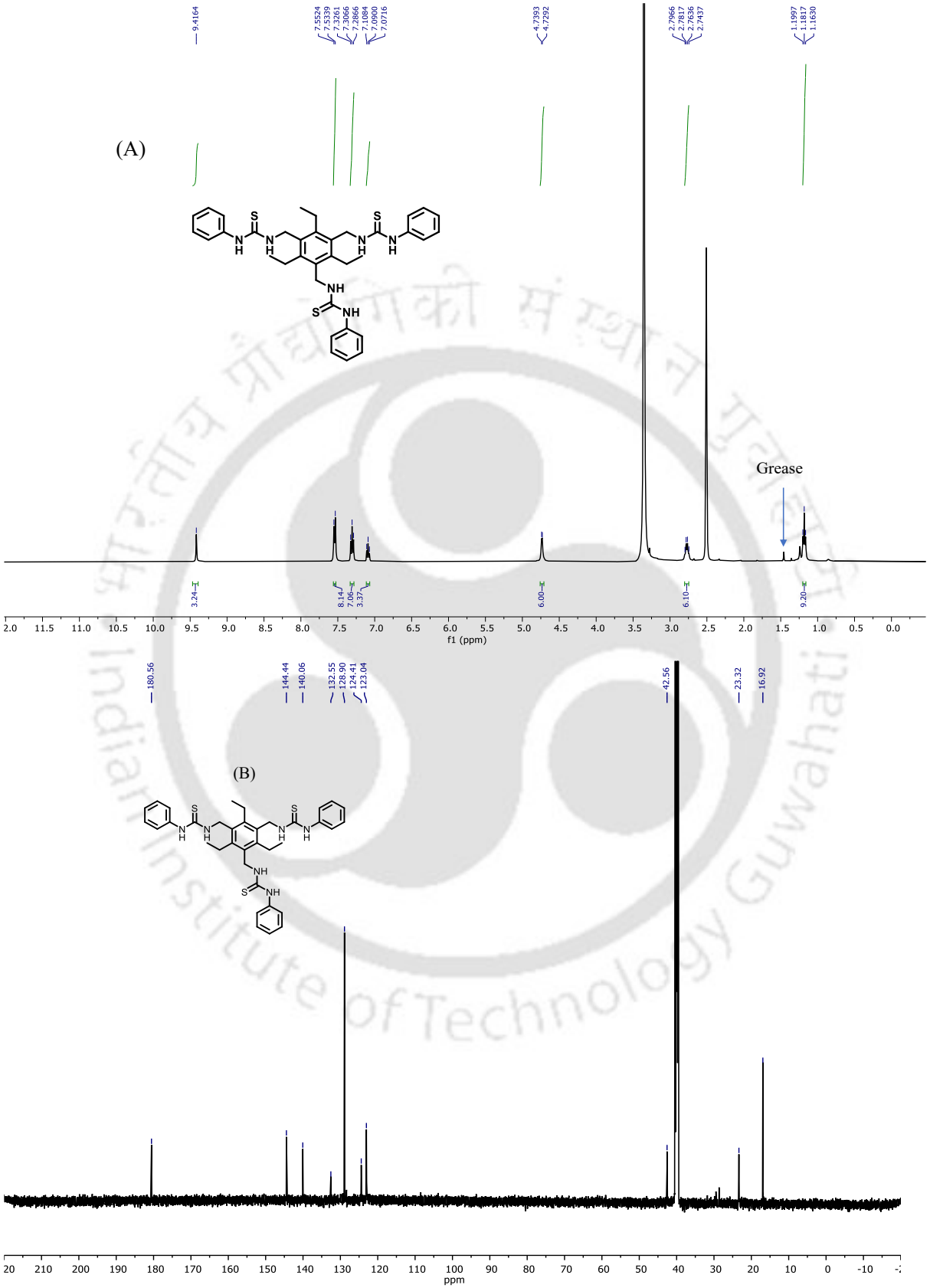


**Figure 4.30.** $^{1}$H (A) and $^{13}$C NMR (B) of compound **4.1a** in DMSO-$d_6$.

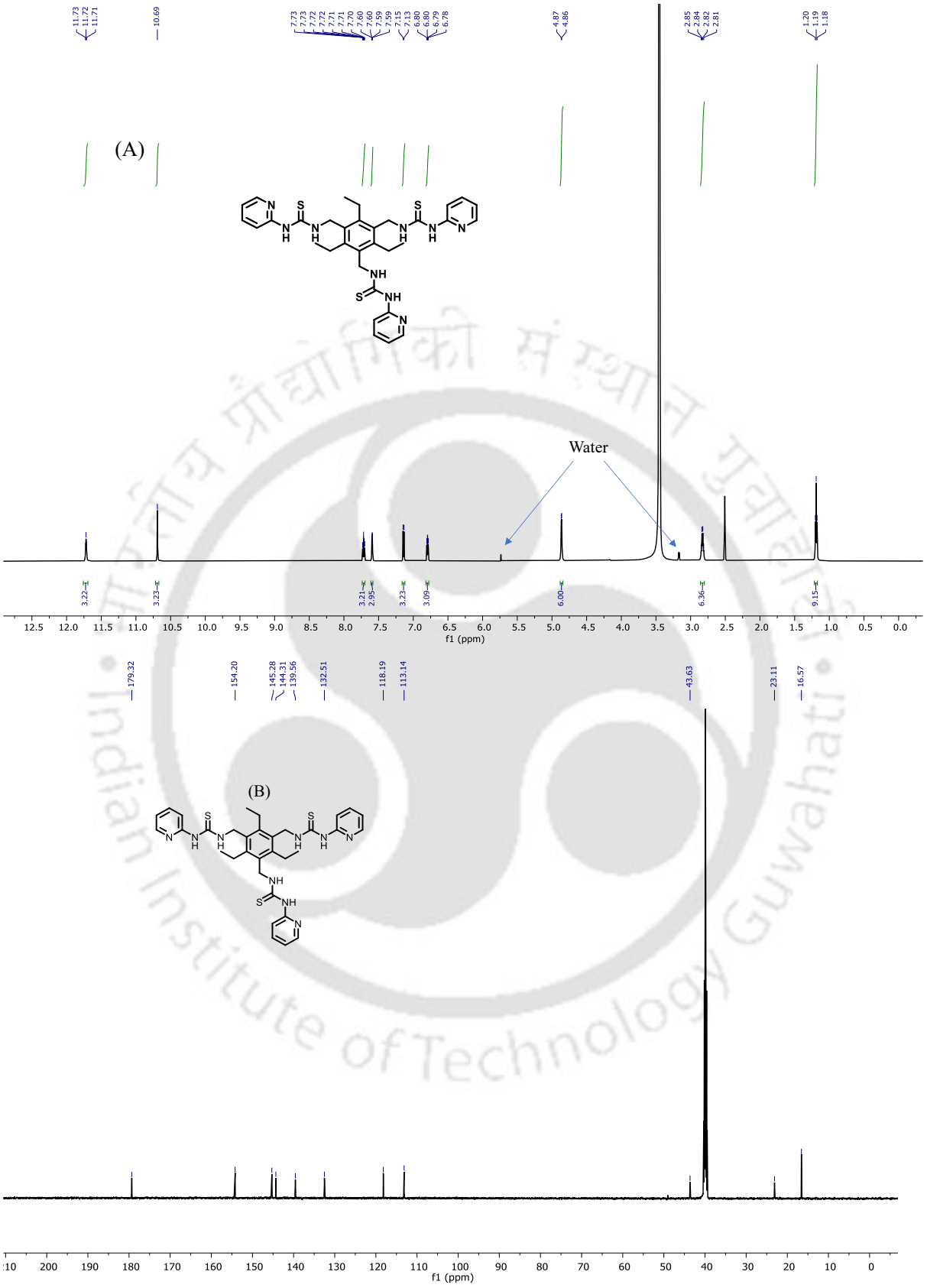


**Figure 4.31.** $^{1}$H (A) and $^{13}$C NMR (B) of compound **4.1b** in DMSO-$d_6$.

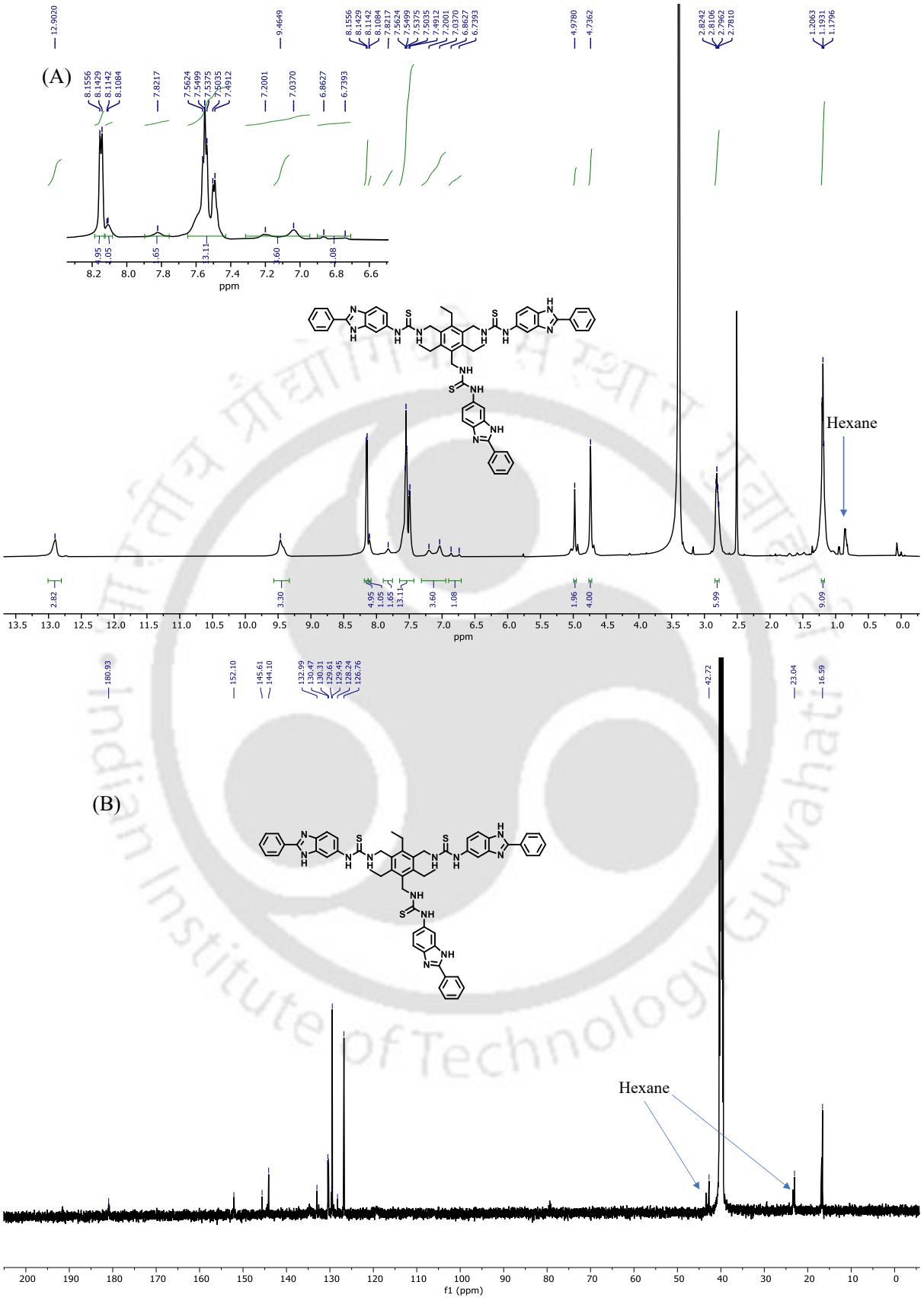


**Figure 4.32.** $^{1}$H (A) and $^{13}$C NMR (B) of compound **4.1c** in DMSO-$d_6$.

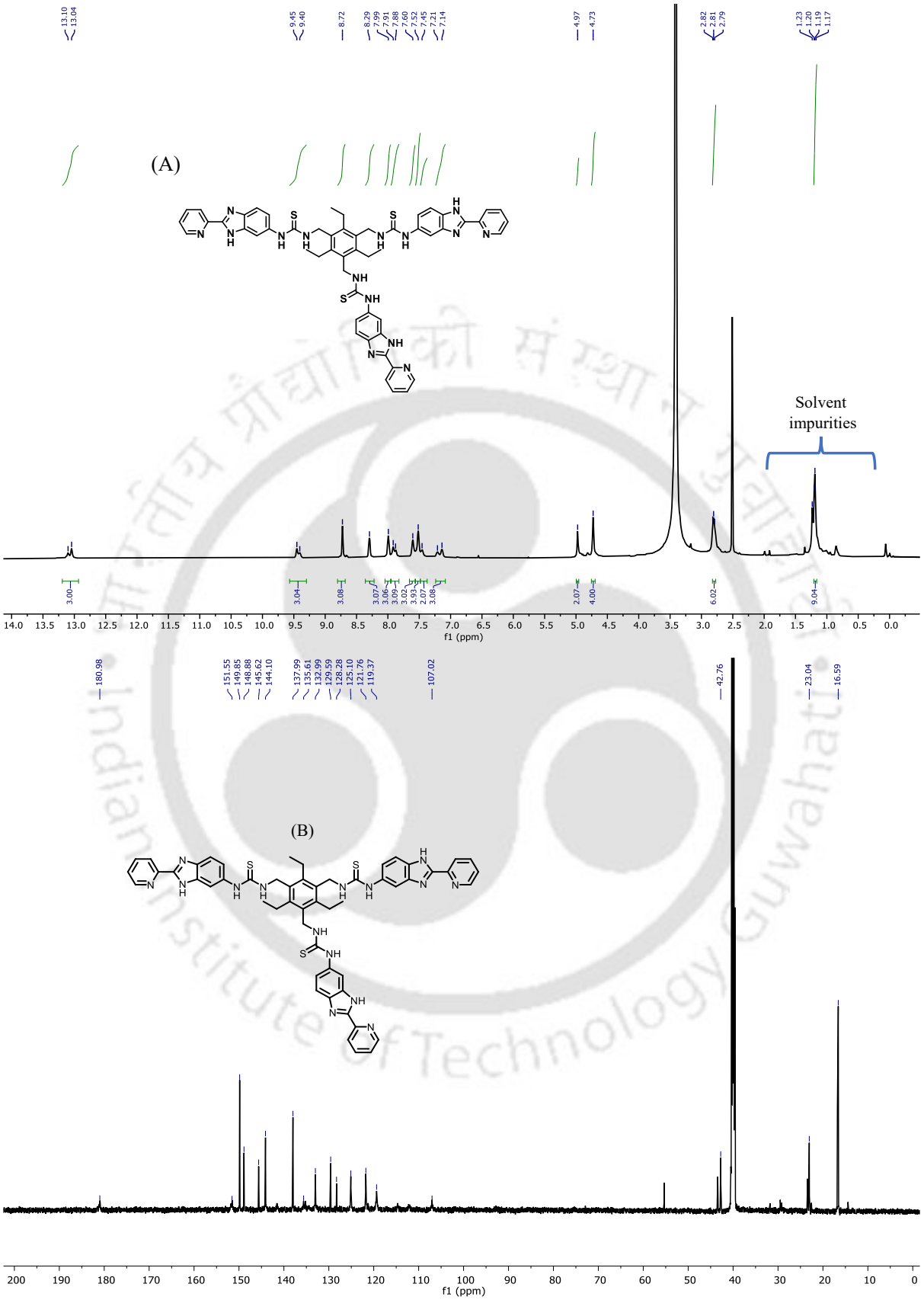


**Figure 4.33.** $^{1}$H (A) and $^{13}$C NMR (B) of compound **4.1d** in DMSO-$d_6$.

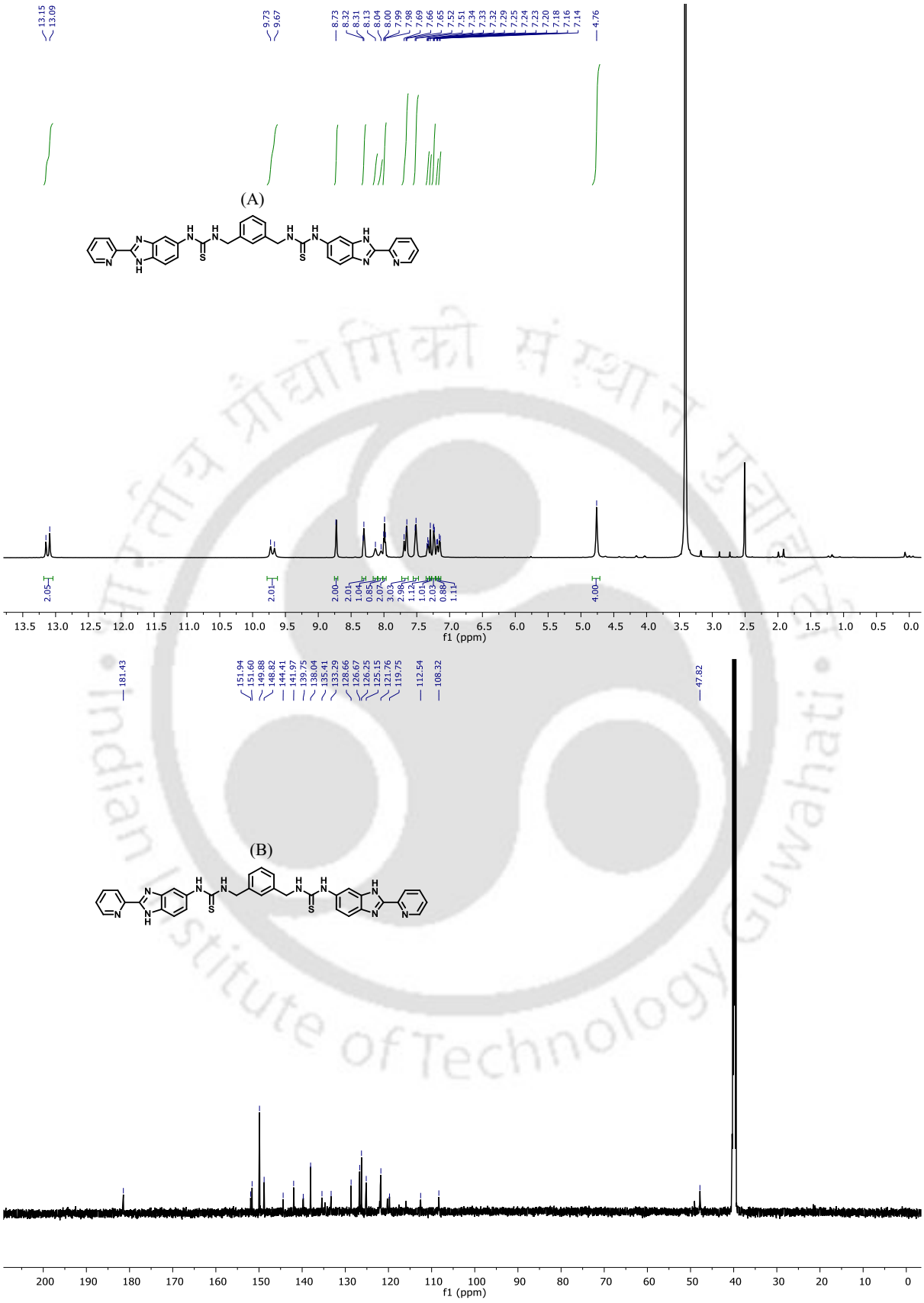


**Figure 4.34.** $^{1}$H (A) and $^{13}$C NMR (B) of compound **4.2a** in DMSO-$d_6$.

### 4.4.16. HPLC trace of compound 4.1d

Compound **4.1d** was processed for HPLC analysis. Column used: Ascentis® express C18, 2.7 µm HPLC column, flow rate: 0.5 mL/min, mobile phase used: Optimised gradient of water/methanol. The gradient used:

0-5 min- 20% water:80% MeOH

5-10 min- 100% MeOH

10-15 min- 20% water:80% MeOH

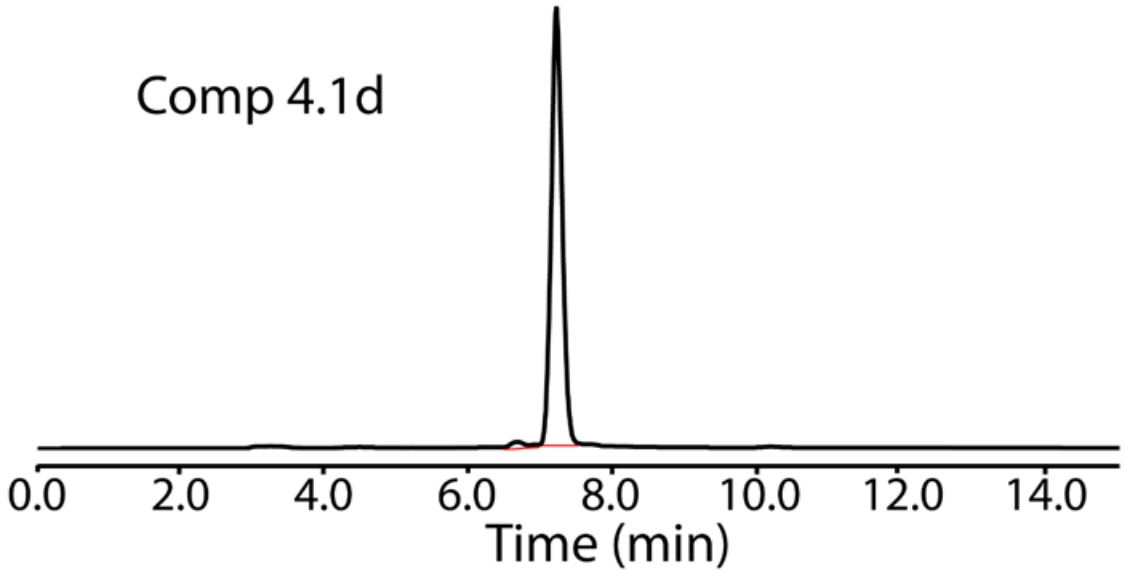


**Figure 4.35.** HPLC trace of compound **4.1d** with ~ 98% purity percentage.

**4.5 References:**

1. Shi, K.; Song, C.; Wang, Y.; Chandrawati, R.; Lin, Y., Engineering receptor-mediated transmembrane signaling in artificial and living cells. Commun. Mater. **2023,** 4 (1), 65.

2. Mustafa, M.; Ahmad, R.; Tantry, I. Q.; Ahmad, W.; Siddiqui, S.; Alam, M.; Abbas, K.; Moinuddin; Hassan, M. I.; Habib, S., Apoptosis: a comprehensive overview of signaling pathways, morphological changes, and physiological significance and therapeutic implications. Cells **2024,** 13 (22), 1838.

3. Su, J.; Song, Y.; Zhu, Z.; Huang, X.; Fan, J.; Qiao, J.; Mao, F., Cell–cell communication: new insights and clinical implications. STTT **2024,** 9 (1), 196.

4. Srimayee, S.; Prusty, B. M.; Kar, M. K.; Winterhalter, M.; Manna, D., Supramolecular Ion Channels to Engineer $Zn^{2+}$ Ion Transport Mediated Chemical-to-Optical Signal Transduction. Angew. Chem. Int. Ed. **2025**, e202501634.

5. Silva, P. J.; Cheng, Q., An alternative proposal for the reaction mechanism of light-dependent protochlorophyllide oxidoreductase. ACS Catal. **2022,** 12 (4), 2589-2605.

6. Gartland, S. A.; Johnson, T. G.; Walkley, E.; Langton, M. J., Inter-Vesicle Signal Transduction Using a Photo-Responsive Zinc Ionophore. Angew. Chem. Int. Ed. **2023,** 62 (38), e202309080.

7. Chen, B.; Yu, P.; Chan, W. N.; Xie, F.; Zhang, Y.; Liang, L.; Leung, K. T.; Lo, K. W.; Yu, J.; Tse, G. M., Cellular zinc metabolism and zinc signaling: from biological functions to diseases and therapeutic targets. STTT **2024,** 9 (1), 6.

8. Schiffmann, R.; Neugebauer, A.; Klein, C. D., Metal-Mediated Inhibition of Escherichia c oli Methionine Aminopeptidase: Structure− Activity Relationships and Development of a Novel Scoring Function for Metal− Ligand Interactions. J. Med. Chem. **2006,** 49 (2), 511-522.

9. Paul, R.; Dutta, D.; Mukhopadhyay, T. K.; Müller, D.; Lala, B.; Datta, A.; Schwalbe, H.; Dash, J., A non-B DNA binding peptidomimetic channel alters cellular functions. Nat. Commun. **2024,** 15 (1), 5275.

10. Gutsmann, T.; Heimburg, T.; Keyser, U.; Mahendran, K. R.; Winterhalter, M., Protein reconstitution into freestanding planar lipid membranes for electrophysiological characterization. Nat. Protoc. **2015,** 10 (1), 188-198.

11. Li, X.; Lei, H.; Xie, L.; Wang, N.; Zhang, W.; Cao, R., Metalloporphyrins as catalytic models for studying hydrogen and oxygen evolution and oxygen reduction reactions. Acc. Chem. Res. **2022,** 55 (6), 878-892.

12. Rajasree, S. S.; Li, X.; Deria, P., Physical properties of porphyrin-based crystalline metal–organic frameworks. Commun. Chem. **2021,** 4 (1), 47.

13. Lavado, A. S.; Chauhan, V. M.; Zen, A. A.; Giuntini, F.; Jones, D. R. E.; Boyle, R. W.; Beeby, A.; Chan, W. C.; Aylott, J. W., Controlled intracellular generation of reactive oxygen species in human mesenchymal stem cells using porphyrin conjugated nanoparticles. Nanoscale **2015,** 7 (34), 14525-14531.

14. Restrepo-Acevedo, A.; Murillo, M. I.; Orvain, C.; Thibaudeau, C.; Recberlik, S.; Verget, L.; Gómez Vidales, V.; Gaiddon, C.; Mellitzer, G.; Le Lagadec, R., Protoporphyrin IX-Derived Ruthenium (II) Complexes for Photodynamic Therapy in Gastric Cancer Cells. Inorganic Chemistry

**2025,** 64 (19), 9684-9702.

15. Pradhan, N.; Akhtar, N.; Nath, B.; Peña-García, J.; Gupta, A.; Pérez-Sánchez, H.; Kumar, S.; Manna, D., Inhibition of immunosuppressive indoleamine 2, 3-dioxygenase by targeting the heme and apo-form. ChemComm **2021,** 57 (3), 395-398.

16. Grigalavicius, M.; Mastrangelopoulou, M.; Berg, K.; Arous, D.; Ménard, M.; Raabe-Henriksen, T.; Brondz, E.; Siem, S.; Görgen, A.; Edin, N. F. J., Proton-dynamic therapy following photosensitiser activation by accelerated protons demonstrated through fluorescence and singlet oxygen production. Nat. Commun. **2019,** 10 (1), 3986.

17. Akhtar, N.; Pradhan, N.; Saha, A.; Kumar, V.; Biswas, O.; Dey, S.; Shah, M.; Kumar, S.; Manna, D., Tuning the solubility of ionophores: glutathione-mediated transport of chloride ions across hydrophobic membranes. Chem. Commun. **2019,** 55 (58), 8482-8485.

18. Patrick, D. A.; Gillespie, J. R.; McQueen, J.; Hulverson, M. A.; Ranade, R. M.; Creason, S. A.; Herbst, Z. M.; Gelb, M. H.; Buckner, F. S.; Tidwell, R. R., Urea derivatives of 2-aryl-benzothiazol-5-amines: a new class of potential drugs for human African trypanosomiasis. J. Med. Chem. **2017,** 60 (3), 957-971.

19. Malla, J. A.; Upadhyay, A.; Ghosh, P.; Mondal, D.; Mondal, A.; Sharma, S.; Talukdar, P., Chloride Transport across Liposomes and Cells by Nontoxic 3-(1 H-1, 2, 3-Triazol-1-yl) benzamides. Org. Lett. **2022,** 24 (23), 4124-4128.

20. Chattopadhayay, S.; Ghosh, A.; Kumar Mukhopadhyay, T.; Sharma, R.; Datta, A.; Talukdar, P., Supramolecular Barrel-Rosette Ion Channel Based on 3, 5-Diaminobenzoic Acid for Cation-Anion Symport. Angew. Chem. Int. Ed. **2023,** 62 (46), e202313712.

21. Sharma, R.; Sarkar, S.; Chattopadhayay, S.; Mondal, J.; Talukdar, P., A Halogen-Bond-Driven Artificial Chloride-Selective Channel Constructed from 5-Iodoisophthalamide-based Molecules. Angew. Chem. Int. Ed. **2024,** 63 (19), e202319919.

22. Lide, D. R., Ed., CRC Handbook of Chemistry and Physics, 87th ed. Taylor and Francis: Boca Raton, FL **2007**.

23. Dey, S.; Patel, A.; Haloi, N.; Srimayee, S.; Paul, S.; Barik, G. K.; Akhtar, N.; Shaw, D.; Hazarika, G.; Prusty, B. M., Debasis Manna, Quinoline thiourea-based zinc ionophores with antibacterial activity. J. Med. Chem. **2023,** 66 (16), 11078-11093.

24. Weinstain, R.; Savariar, E. N.; Felsen, C. N.; Tsien, R. Y., In vivo targeting of hydrogen peroxide by activatable cell-penetrating peptides. J. Am. Chem. Soc. **2014,** 136 (3), 874-877.

25. Lou, Z.; Zhang, Y.; Liang, X.; Cao, M.; Ma, Y.; Chen, P. R.; Fan, X., Deep-Red and Ultrafast Photocatalytic Proximity Labeling Empowered In Situ Dissection of Tumor-Immune Interactions in Primary Tissues. J. Am. Chem. Soc. **2025,** 147 (11), 9716-9726.

## 5. Thesis conclusion

In this thesis, we have successfully demonstrated the diverse applications of synthetic ionophores in both therapeutic and non-therapeutic domains. A brief literature review of naturally occurring ionophores and ion channels, along with reported synthetic ionophores and stimulus-responsive systems, was presented in **Chapter 1**. To explore the effect of stimuli, we synthesized a proanionophore with an RGD peptide-appended bis-thiourea-based moiety as a chloride ion transporter, which showed apoptosis activity upon release triggered by elevated GSH and ROS in **chapter 2**. We observed that the RGD-attached pro-ionophore showed greater selectivity for the diseased A375 cell line than for the normal HEK293T cell line. In **chapter 3**, we showcased a chemical-to-optical signal conversion process through a synthetic molecular ion channel as a molecular communication network. In this chapter, we synthesized a salicylaldehyde-based imine derivative that serves as a $Zn^{2+}$ ion channel, with $Zn^{2+}$ acting as our chemical signal. Inside the vesicle, Tyr binds to the $Zn^{2+}$ ion, conferring esterase-like activity that converts non-fluorescent AHPTS to fluorescent HPTS, thereby generating an optical signal. In **chapter 4**, we have a tripodal pyridyl-benzimidazole moiety that acts as a $Zn^{2+}$ ion channel to initiate a photoregulated oxidation reaction inside the vesicle. The transported $Zn^{2+}$ ion binds to PPIX to generate ROS, specifically $^1O_2$, which has been used to convert Trp to Nfk upon red light irradiation. The IDO1 enzyme in our biological system facilitates the formation of Nfk from Trp. Hence, this **chapter 4** also showcases a molecular communication network activating upon photo-irradiation. Overall, in this thesis, we have explored the classical therapeutic aspects of synthetic ionophores as anticancer agents, multi-stimuli-responsive pro-ionophores, and synthetic transporters as molecular communication systems for mimicking natural signal transduction phenomena.

## 6. Future prospects

The origins of synthetic ion transporters date back to the late twentieth century, when researchers sought to mimic natural ionophores and incorporate biological principles into artificial systems. Since then, the discipline has expanded dramatically; what began as basic carriers has evolved into complex, precisely tuned structures designed not only for efficient transportation but also with clear applications in medicine and technology. Over time, researchers have added layers of complexity as they investigate how light, pH, or redox cues can be utilised to turn transport on and off, giving these molecules a level of control similar to natural regulation. Interestingly, the lack of transition-metal- or metal-based synthetic

ionophores or channels reveals a gap that can be filled to expand functional diversity. Beyond transport, these systems can replicate signal transduction events in which ion fluxes encode information, linking synthetic chemistry and biological communication channels. Extending this approach, the creation of molecular communication systems based on synthetic ionophores paves the way for decoding complicated biological processes and implementing logic operations at the molecular level. These discoveries not only deepen our understanding of ion transport but also bring us closer to the creation of artificial cells, in which synthetic components work together to replicate life-like processes.

## Stimuli-responsive release of active anionophore from RGD-peptide-linked proanionophore

S. Srimayee, S. R. Badajena, N. Akhtar, M. K. Kar, S. Dey, P. Mohapatra and D. Manna, *Chem. Commun.*, 2023, **59**, 12759 **DOI:** 10.1039/D3CC02451B

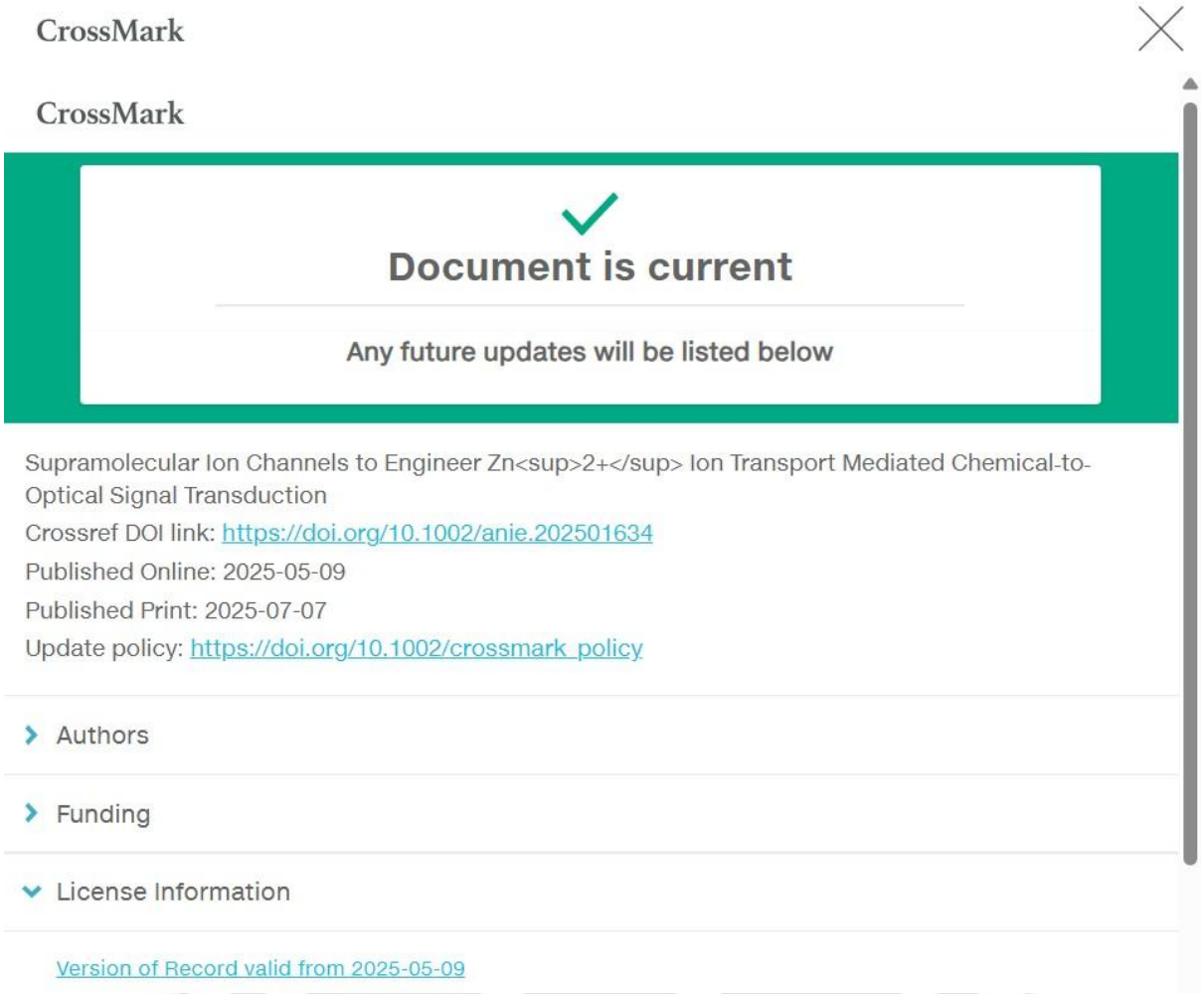

# Publications


1. **Srimayee, S.**$^{+}$, Prusty, B. M.$^{+}$, Kar, K. M., Winterhalter, M., Manna, D., Sterically Geared Tripodal Pyridyl benzimidazole Self-Assembly Forms $Zn^{2+}$ Ion Channels to Induce Photoregulated Catalysis., *Chemical Communication*, **2026**. (Just accepted)
2. Prusty, B. M., **Srimayee, S.,** Manna, D.*, Temporally Controlled Interconversion Between Suprasome and Supracube Structures to Regulate Catalytic Activities., *Chemistry A European Journal*,**2026**.
3. Kar, K. M., **Srimayee, S.,** Prusty, B. M., Kumar, R., Manna, D.*, Photoregulated Inter-Vesicle Signalling System: Transforming $Zn^{2+}$ Signals to $Cl^{-}$ Signals Using Synthetic Ion Transporters., *ACS Applied Bio Materials*, **2026**.
4. **Srimayee, S.**$^{+}$**,** Prusty, B. M.$^{+}$, Kar, K. M., Winterhalter, M., Manna, D., Supramolecular Ion Channels to Engineer $Zn^{2+}$ Ion Transport Mediated Chemical-to-Optical Signal Transduction, *Angewandte Chemie International Edition*, **2025**.
5. Prusty, B. M., **Srimayee, S.,** Karn, R., Haloi, N., Winterhalter, M., Manna, D., Supramolecular Nanochannels: Suprasome-Mediated Delivery of Ionophore to Regulate Transmembrane $Zn^{2+}$ Ion Transport, *Chemistry A European Journal***, 2025**.
6. Karn, R., Biswas, S., **Srimayee, S**., Patel, A., Chauhan, S., Manna, D., Metal-responsive fluorophore and amikacin-conjugated heparin for bacterial cell imaging and antibacterial applications. *ACS Infectious Disease.*, **2024**.
7. Kar, K. M.; Mahata, R.$^{+}$; **Srimayee, S.**$^{+}$**;** Haloi, N.; Kumar, R.; Lindahl, E.; Santra, K. M.; Manna, D., β-Carboline-based light and pH dual stimuli-responsive ion transporters induce cancer cell death. *Chemical Communication* **2024**, 60, 8419-8422.
8. Patra, K. A., Roy, A., Gomila, M. R., Kundu, S., **Srimayee, S.**, Halder, D., Manna, D., Saha, I., Binding of Linear Anions and Formation of Anion Encapsulated Dimeric Assembly by Cis-5,15-bis(3,5-trifluoromethylphenyl)calix[4]pyrrole. *European Journal of Organic Chemistry*, **2024**, 27 (29).
9. Das, S., Karn, R., Kumar, M., **Srimayee, S.,** Manna, D., A chloride-responsive molecular switch: driving ion transport and empowering antibacterial properties. *Organic Biomolecular Chemistry*, **2024**, 22 (1), 114-119.
10. Dey, S., Patel, A., Haloi, N., **Srimayee, S.,** Paul, S., Barik, G. K., Akhtar, N., Shaw, D., Hazarika, G., Prusty, B. M., Kumar, M., Santra, M. K., Tajkhorshid, E.*, Bhattacharjee, S.*, and Manna, D.*, Quinoline Thiourea-Based Zinc Ionophores with Antibacterial Activity, *Journal of Medicinal Chemistry*, **2023**, 66, 11078-11093.
11. **Srimayee, S.,** Badajena, R. S., Akhtar, N., Kar, K. M., Dey, S., Mohapatra. P.,* Manna, D.*, Stimuli-responsive release of active anionophore from RGD-peptide-linked proanionophore, *Chemical Communication*, **2023**, 59, 12759-12762.
12. Patra, K. A., **Srimayee, S.,** Halder, D., Roy, A., Mukherjee, S., Kundu, S., Hossain, M., Saha, R., Lee, C.H., Manna, D.*, Saha, I*, Transmembrane fluoride anion transport by meso-3,5-bis(trifluoromethyl)phenyl picket calix[4]pyrrole. *Chemical Communication*, **2023**, 59, 7407-7410.